REPORT DOCUMENTATION PAGE	Form Approved OMB NO. 0704-0188

1. REPORT DATE (DD-MM-YYYY)	2. REPORT TYPE	3. DATES COVERED (From - To)
05-01-2017	Final Report	28-Sep-2015 - 27-Dec-2016

4. TITLE AND SUBTITLE
Final Report: Positrons on Demand

5a. CONTRACT NUMBER

5b. GRANT NUMBER
W911NF-15-C-0217

5c. PROGRAM ELEMENT NUMBER

6. AUTHORS
MicroPET, Inc.

5d. PROJECT NUMBER

5e. TASK NUMBER

5f. WORK UNIT NUMBER

7. PERFORMING ORGANIZATION NAMES AND ADDRESSES
MicroPET, Inc.
750 Battery Street, 7th Floor

San Francisco, CA 94111 -0000

8. PERFORMING ORGANIZATION REPORT NUMBER

9. SPONSORING/MONITORING AGENCY NAME(S) AND ADDRESS (ES)
U.S. Army Research Office
P.O. Box 12211
Research Triangle Park, NC 27709-2211

10. SPONSOR/MONITOR'S ACRONYM(S)
ARO

11. SPONSOR/MONITOR'S REPORT NUMBER(S)
67717-LS-DRP.3

12. DISTRIBUTION AVAILIBILITY STATEMENT
Approved for Public Release; Distribution Unlimited

13. SUPPLEMENTARY NOTES
The views, opinions and/or findings contained in this report are those of the author(s) and should not contrued as an official Department of the Army position, policy or decision, unless so designated by other documentation.

14. ABSTRACT
MicroPET has bounded the performance and scaling characteristics of an approach to synthesizing short-lived positron emitting isotopes based on anisotropic plasma jets that are generated by intense, sub-picosecond laser pulses focused into pulsed supercritical hydrogen jets. While these jets produce multi-MeV protons, the fluxes and energies achievable with currently available lasers are inadequate to generate useful quantities of the radioisotopes. Future efforts will explore radiofrequency quadrupole linear accelerators as an alternative proton source to create the first synthetic system to produce positron emitting biomolecules at the point of care

15. SUBJECT TERMS
positron, radioisotope, tomography, pharmacokinetics

16. SECURITY CLASSIFICATION OF: a. REPORT	b. ABSTRACT	c. THIS PAGE	17. LIMITATION OF ABSTRACT	15. NUMBER OF PAGES	19a. NAME OF RESPONSIBLE PERSON
UU	UU	UU	UU		Peter Haaland
					19b. TELEPHONE NUMBER
					571-389-9901

Standard Form 298 (Rev 8/98)
Prescribed by ANSI Std. Z39.18

Report Title

Final Report: Positrons on Demand

ABSTRACT

MicroPET has bounded the performance and scaling characteristics of an approach to synthesizing short-lived positron emitting isotopes based on anisotropic plasma jets that are generated by intense, sub-picosecond laser pulses focused into pulsed supercritical hydrogen jets. While these jets produce multi-MeV protons, the fluxes and energies achievable with currently available lasers are inadequate to generate useful quantities of the radioisotopes. Future efforts will explore radiofrequency quadrupole linear accelerators as an alternative proton source to create the first synthetic system to produce positron emitting biomolecules at the point of care.

Enter List of papers submitted or published that acknowledge ARO support from the start of the project to the date of this printing. List the papers, including journal references, in the following categories:

(a) Papers published in peer-reviewed journals (N/A for none)

Received Paper

TOTAL:

Number of Papers published in peer-reviewed journals:

(b) Papers published in non-peer-reviewed journals (N/A for none)

Received Paper

TOTAL:

Number of Papers published in non peer-reviewed journals:

(c) Presentations

Number of Presentations: 0.00

Non Peer-Reviewed Conference Proceeding publications (other than abstracts):

Received	Paper
12/27/2016	1 A. J. Goers1, L. Feder1, J. Murray1, G. A. Hine1, F. Salehi1, D. Woodbury1, J.J. Su1, D. Papadopoulos1, A. Zigler2, P. D. Haaland3, and H. M. Milchberg1. Proton acceleration by multi-terawatt laser interaction with a near-critical density hydrogen jet, Advanced Accelerator Concepts (APS). 01-AUG-16, National Harbor, MD. : ,
12/27/2016	2 Andy Goers, George Hine, Linus Feder, FatholahSalehi, Bo Miao, Daniel Woodbury, and Howard Milchberg. PHYSICSProton acceleration by multi-TW interaction with a near-critical density hydrogen jet, American Physical Society Division of Plasma Physics Meeting. 31-OCT-16, San Jose, CA. : ,
TOTAL:	**2**

Number of Non Peer-Reviewed Conference Proceeding publications (other than abstracts):

Peer-Reviewed Conference Proceeding publications (other than abstracts):

Received	Paper
TOTAL:	

Number of Peer-Reviewed Conference Proceeding publications (other than abstracts):

(d) Manuscripts

Received	Paper
TOTAL:	

Number of Manuscripts:

Books

Received Book

TOTAL:

Received Book Chapter

TOTAL:

Patents Submitted

Patents Awarded

Awards

Graduate Students

NAME	PERCENT_SUPPORTED	Discipline
George Hine	1.00	
Daniel Woodbury	1.00	
Linus Feder	1.00	
FTE Equivalent:	**3.00**	
Total Number:	**3**	

Names of Post Doctorates

NAME	PERCENT_SUPPORTED
Andrew Goers	1.00
FTE Equivalent:	**1.00**
Total Number:	**1**

Names of Faculty Supported

NAME	PERCENT_SUPPORTED	National Academy Member
Howard Milchberg	0.05	Yes
FTE Equivalent:	**0.05**	
Total Number:	**1**	

Names of Under Graduate students supported

NAME	PERCENT_SUPPORTED	Discipline
Dan Younis	1.00	Physics
Patrick Daschbach	1.00	Electrical Engineering
FTE Equivalent:	**2.00**	
Total Number:	**2**	

Student Metrics

This section only applies to graduating undergraduates supported by this agreement in this reporting period

The number of undergraduates funded by this agreement who graduated during this period: 0.00

The number of undergraduates funded by this agreement who graduated during this period with a degree in science, mathematics, engineering, or technology fields:...... 0.00

The number of undergraduates funded by your agreement who graduated during this period and will continue to pursue a graduate or Ph.D. degree in science, mathematics, engineering, or technology fields:...... 0.00

Number of graduating undergraduates who achieved a 3.5 GPA to 4.0 (4.0 max scale):...... 0.00

Number of graduating undergraduates funded by a DoD funded Center of Excellence grant for Education, Research and Engineering:...... 0.00

The number of undergraduates funded by your agreement who graduated during this period and intend to work for the Department of Defense 0.00

The number of undergraduates funded by your agreement who graduated during this period and will receive scholarships or fellowships for further studies in science, mathematics, engineering or technology fields:...... 0.00

Names of Personnel receiving masters degrees

NAME

Total Number:

Names of personnel receiving PHDs

NAME

Total Number:

Names of other research staff

NAME	PERCENT_SUPPORTED
Jao Jiang Su	1.00
FTE Equivalent:	**1.00**
Total Number:	**1**

Sub Contractors (DD882)

1 a. University of Maryland - College Park

1 b. Office of Research Administration
3112 Lee Building 7809 Regents Dr
College Park MD 207425141

Sub Contractor Numbers (c):
Patent Clause Number (d-1): 52.227-11
Patent Date (d-2): 5/1/14 12:00AM
Work Description (e): Laser-driven proton acceleration from near critical density cluster jets
Sub Contract Award Date (f-1): 10/26/16 12:00AM
Sub Contract Est Completion Date(f-2): 12/30/16 12:00AM

---

1 a. University of Maryland - College Park

1 b. 3112 Lee Building
College Park MD 207425141

Sub Contractor Numbers (c):
Patent Clause Number (d-1): 52.227-11
Patent Date (d-2): 5/1/14 12:00AM
Work Description (e): Laser-driven proton acceleration from near critical density cluster jets
Sub Contract Award Date (f-1): 10/26/16 12:00AM
Sub Contract Est Completion Date(f-2): 12/30/16 12:00AM

---

1 a. University of Maryland - College Park

1 b. 3112 Lee Building
7809 Regents Drive
College Park MD 207425141

Sub Contractor Numbers (c):
Patent Clause Number (d-1): 52.227-11
Patent Date (d-2): 5/1/14 12:00AM
Work Description (e): Laser-driven proton acceleration from near critical density cluster jets
Sub Contract Award Date (f-1): 10/26/16 12:00AM
Sub Contract Est Completion Date(f-2): 12/30/16 12:00AM

Inventions (DD882)

5 **Cryogenic targets for radionuclide activation**

Patent Filed in US? (5d-1) N
Patent Filed in Foreign Countries? (5d-2) N
Was the assignment forwarded to the contracting officer? (5e) N
Foreign Countries of application (5g-2):

5a: Peter Haaland

5f-1a: MicroPET

5f-c: 649 Mission St, Suite 213,
San Francisco CA 94105

Scientific Progress

This project has identified a new mechanism for proton acceleration from sub-picosecond laser interactions with supercritical gas jets. Although the process starts with target-normal sheath acceleration the physics responsible for ion acceleration is mostly due to intense, transient magnetic fields whose collapse drives a directed, multi-MeV flux of ions to a suitable target. Particle-in-cell simulations in 2 and 3 dimensions, anchored by experimental data at lower pulse energies (up to 500 mJ, between 50 and 400 fs, 3 micron focus, Ti:Sapphire pulses) define the performance and scaling attributes of a PET synthesis system based on laser acceleration of protons. MicroPET has discovered that the laser requirements (2-3J/pulse, 200-500 Hz repetition rate) are just beyond the state of the art for commercially feasible laser systems.

Technology Transfer

We are pursuing collaborations with Mass General Hospital / Harvard Medical School and Starfire Technology for the next phase of development.

POSITRONS ON DEMAND

Final Technical Report
ARO Contract F911NF-15-C-0217

26 December 2016

MicroPET, Inc.
649 Mission Street, Suite 213
San Francisco, CA 94105-4127

REPORT DOCUMENTATION PAGE

Form Approved
OMB No. 0704-0188

1. REPORT DATE *(DD-MM-YYYY)*
12/26/2016

2. REPORT TYPE
Final Technical Report

3. DATES COVERED *(From - To)*
28 SEP 2015 - 26 DEC 2016

4. TITLE AND SUBTITLE
Positrons On Demand

5a. CONTRACT NUMBER
W911NF-15-C-0217

5b. GRANT NUMBER

5c. PROGRAM ELEMENT NUMBER

6. AUTHOR(S)
MicroPET, Inc.
649 Mission Street, Suite 213
San Francisco, CA 94105-4127

5d. PROJECT NUMBER

5e. TASK NUMBER

5f. WORK UNIT NUMBER

7. PERFORMING ORGANIZATION NAME(S) AND ADDRESS(ES)
MicroPET, Inc.
649 Mission Street, Suite 213
San Francisco, CA 94105-4127

8. PERFORMING ORGANIZATION REPORT NUMBER
PODM-FR

9. SPONSORING/MONITORING AGENCY NAME(S) AND ADDRESS(ES)
DARPA/BTO, 675 North Randolph Street, Arlington, VA 22203-2114
ARO/RDRL-ROP-L, P.O. Box 12211, Research Triangle Park, NC 27709-2211

10. SPONSOR/MONITOR'S ACRONYM(S)

11. SPONSOR/MONITOR'S REPORT NUMBER(S)

12. DISTRIBUTION/AVAILABILITY STATEMENT
Approved for public release; distribution unlimited.

13. SUPPLEMENTARY NOTES

14. ABSTRACT
Report developed under contract W911NF-15-C-0217. This final report characterizes the performance and scaling characteristics of a laser-driven plasma proton accelerator for generation of biomolecular imaging tracers with short-lived radioisotopes. New mechanisms for the generation of quasi-neutral plasma jets based on sub-picosecond irradiation of supercritical hydrogen fluid jets are described and are suitable for generation of positron emitting isotopes with modest but essential increases in commercially available laser pulse energies and repetition rates.

15. SUBJECT TERMS
positron, radioisotope, laser, plasma, tomography, pharmacokinetics

16. SECURITY CLASSIFICATION OF: a. REPORT	b. ABSTRACT	c. THIS PAGE	17. LIMITATION OF ABSTRACT	18. NUMBER OF PAGES	19a. NAME OF RESPONSIBLE PERSON
					Dr. Peter Haaland
					19b. TELEPHONE NUMBER *(Include area code)*
Unclassified	Unclassified	(U)	None	282	571 289 9901

REPORT DOCUMENTATION PAGE	*Form Approved* *OMB No. 0704-0188*

1. REPORT DATE *(DD-MM-YYYY)*
12/26/2016

2. REPORT TYPE
Final Technical Report

3. DATES COVERED *(From - To)*
28 SEP 2015 - 26 DEC 2016

4. TITLE AND SUBTITLE
Positrons On Demand

5a. CONTRACT NUMBER
W911NF-15-C-0217

5b. GRANT NUMBER

5c. PROGRAM ELEMENT NUMBER

6. AUTHOR(S)
MicroPET, Inc.
649 Mission Street, Suite 213
San Francisco, CA 94105-4127

5d. PROJECT NUMBER

5e. TASK NUMBER

5f. WORK UNIT NUMBER

7. PERFORMING ORGANIZATION NAME(S) AND ADDRESS(ES)
MicroPET, Inc.
649 Mission Street, Suite 213
San Francisco, CA 94105-4127

8. PERFORMING ORGANIZATION REPORT NUMBER
PODM-FR

9. SPONSORING/MONITORING AGENCY NAME(S) AND ADDRESS(ES)
DARPA/BTO, 675 North Randolph Street, Arlington, VA 22203-2114
ARO/RDRL-ROP-L, P.O. Box 12211, Research Triangle Park, NC 27709-2211

10. SPONSOR/MONITOR'S ACRONYM(S)

11. SPONSOR/MONITOR'S REPORT NUMBER(S)

12. DISTRIBUTION/AVAILABILITY STATEMENT
Approved for public release; distribution unlimited.

13. SUPPLEMENTARY NOTES

14. ABSTRACT
Report developed under contract W911NF-15-C-0217. This final report characterizes the performance and scaling characteristics of a laser-driven plasma proton accelerator for generation of biomolecular imaging tracers with short-lived radioisotopes. New mechanisms for the generation of quasi-neutral plasma jets based on sub-picosecond irradiation of supercritical hydrogen fluid jets are described and are suitable for generation of positron emitting isotopes with modest but essential increases in commercially available laser pulse energies and repetition rates.

15. SUBJECT TERMS
positron, radioisotope, laser, plasma, tomography, pharmacokinetics

16. SECURITY CLASSIFICATION OF: a. REPORT	b. ABSTRACT	c. THIS PAGE	17. LIMITATION OF ABSTRACT	18. NUMBER OF PAGES	19a. NAME OF RESPONSIBLE PERSON / 19b. TELEPHONE NUMBER *(Include area code)*
Unclassified	Unclassified	(U)	None	282	Dr. Peter Haaland / 571 289 9901

Executive Summary 3

Chapter 1: Laser/Chamber Configuration 5

Vacuum Vessel 5

Pumps 6

Gas Jet Target 7

Laser 8

Summary 11

Chapter 2: A flexible target 12

Pulsed gas jets 12

Summary 19

Chapter 3: Interferometric Characterization of the Quasi-Neutral Plasma Jet 20

Principle of femtosecond interferometry 20

Experimental setup for third harmonic interferometry 23

Frequency tripling apparatus 23

Design of the wave front division interferometer 24

References 25

Chapter 4: Plasma Optimization Design Study Report 26

Overview – Objectives 26

Physics of energy transfer to multi-MeV protons 27

MicroPET Optimization Study: 36

The role of plasma density gradients 37

Effect of peak density to critical density ratio: 39

Effect of aspect ratio: 43

Summary: 45

Chapter 5: Resolving proton energy with CR39 (acrylate) targets 47

Etching Procedure and Proton Pit Counting 51

References: 52

Chapter 6 : Intercomparison of Thomson Parabola and CR-39 ion energy spectra 53

Thomson Parabola 53

Comparison with CR39 detection 55

Conclusion 55

Chapter 7: Solid target design 56

Overview 56

Carbon-11 production from Boron-Nitride Target 58

Conclusion: 61

Chapter 8: Scaling of Proton Divergence and Flux: Implications for Isotope Production 62

^{11}C production rates and quasi-neutral plasma jet requirements 63

Laser and primary target characteristics that optimize the directed flux of energetic protons 66

Study of C11 conversion efficiency and input to system design 75

Chapter 9: N_2/O_2 target design and interaction scaling report 79

Gas or Liquid N_2 with trace O_2? 79

Target interaction scaling with plasma jet characteristics 82

Conclusion 84

Appendices 84

Executive Summary

This report presents results of the *Positrons on Demand* project that explored the performance and scaling characteristics of a new approach to on-site synthesis of biomolecular imaging reagents. The positron-emitting isotopes of atoms such as C, N, and O that occur naturally in biomolecules have half-lives of a few minutes, limiting the useful specific activity of imaging ligands that are synthesized in remote cyclotron facilities. This project aimed to produce multi-MeV protons using a quasi-neutral plasma jet that was in turn generated by focusing a brief, intense laser pulse on a hydrogen gas jet. These protons would subsequently bombard a radioisotope precursor that is then incorporated into an imaging reagent with microfluidic chemical synthesis tools. A compelling feature of this approach is that neutrons are not produced in the proton source, obviating the need for massive shielding and expensive infrastructure that constrain cyclotron facilities.

The interplay of laser pulse energy, duration, focus, target density and target geometry constrain the effective production of protons with sufficient energy to produce radioisotopes. This interplay has been quantitatively evaluated using 2- and 3-dimensional particle-in-cell simulations and verified experimentally. It is decidedly nonlinear. Pulsed supercritical hydrogen jets maintain their fluid properties several diameters from a nozzle exit plane; these homogeneous targets provide suitable densities and density gradients for the generation of multi-MeV protons. Sub-picosecond laser pulses focused within the hydrogen jet generate plasma waveguides that are extraordinarily stable and reproducible. The pulse length and energy are optimal for production of energetic protons when the light is just fully absorbed by the relativistic plasma.

Based on their penetration through a 4-micron thick aluminum foil and the diameter of the pits produced in etched bis-allyl carbonate (CR-39) we find evidence of forward-directed 3-5 MeV protons following irradiation of a supercritical hydrogen jet with 200fs, 0.5J laser pulses. However, laser pre-pulses and power limitations in Howard Milchberg's laboratory at the University of Maryland prevented generation of adequate proton currents and energies to produce ^{11}C from ^{14}N as originally planned. The mechanism of target-normal sheath acceleration is insufficient to account for these experimental results. Rather, the evolution of strong magnetic fields in the transient plasmas were found to account for most of the forward-directed ion acceleration. This new mechanism, essentially a picosecond z-pinch, can produce sufficient proton fluxes and energies for generation of positron emitting isotopes. However, the combined requirements of pulse energies of 2-3 joules, pulse widths of 200-600 fs, and repetition rates of several hundred Hertz are beyond today's state of the art for commercially viable lasers. The available facility at

UMD is limited to pulse energies < 0.5J, repetition rates of < 10 Hz, and pre-pulse intensities of 10^{-4}. Advances in laser technology to deliver economical, robust performance capable of completing the MicroPET vision are possible, but beyond the scope of this project. The company is exploring evolving laser technology but sees a near-term alternative using recent advances in radio-frequency quadrupole linear accelerators as a swifter alternative to the laser driven plasma for compact, economical, neutron-free generation of positron emitting biomolecular ligands.

The company has invented a new source for the efficient production of ^{11}C and other radioisotopes. This invention will be described separately in a confidential communication to the Government.

Summarizing, MicroPET has bounded the performance and scaling characteristics of an approach to synthesizing short-lived positron emitting isotopes based on anisotropic plasma jets that are generated by intense, sub-picosecond laser pulses focused into pulsed supercritical hydrogen jets. While these jets produce multi-MeV protons, the fluxes and energies achievable with currently available lasers are inadequate to generate useful quantities of the radioisotopes. Future efforts will explore radiofrequency quadrupole linear accelerators as an alternative proton source to create the first synthetic system to produce positron emitting biomolecules at the point of care.

Chapter 1: Laser/Chamber Configuration

This program will explore design options for a compact, light-weight, neutron-free, laser proton accelerator. These concepts will be formulated and tested in apparatus based on the 25 TW laser system at the University of Maryland. This chapter summarizes the characteristics of the apparatus and how they will be used to design of a complete isotope production system.

Vacuum Vessel

The vacuum chamber is shaped for complete characterization of the optical pulses, parametric optimization of the gas jet target, and flexible measurement of proton fluxes and energy distributions produced in quasi-neutral plasma jets. The layout for the chamber is shown in figure 1 below.

The chamber is a stainless-steel box (1.2 x 0.7 x 0.46 meters) with welded Conflat® flanges at the perimeter to incorporate optical windows and diagnostics. The top face of the chamber is transparent polycarbonate to enable viewing of the complete optical train, and the bottom (not shown) has a twelve inch Conflat® flange bolted to the vacuum pumps. Polycarbonate outgases water, plasticizers, and other contaminants that interfere with experiments, however these impacts are mitigated by maintaining a small flow of purge gas that sweeps desorbed material from the chamber. The purge gas is N_2 boil-off from liquid nitrogen.

Purge gas flows enable unconventional chamber materials such as the polycarbonate plate window. The plasma jet source could be manufactured entirely of polycarbonate or other injection-molded polymer, providing lighter weight and completely obviating the prospect of neutron generation by ion-metal collisions. An injection molded chamber could also be produced with more complex geometry and at lower cost than with welded steel.

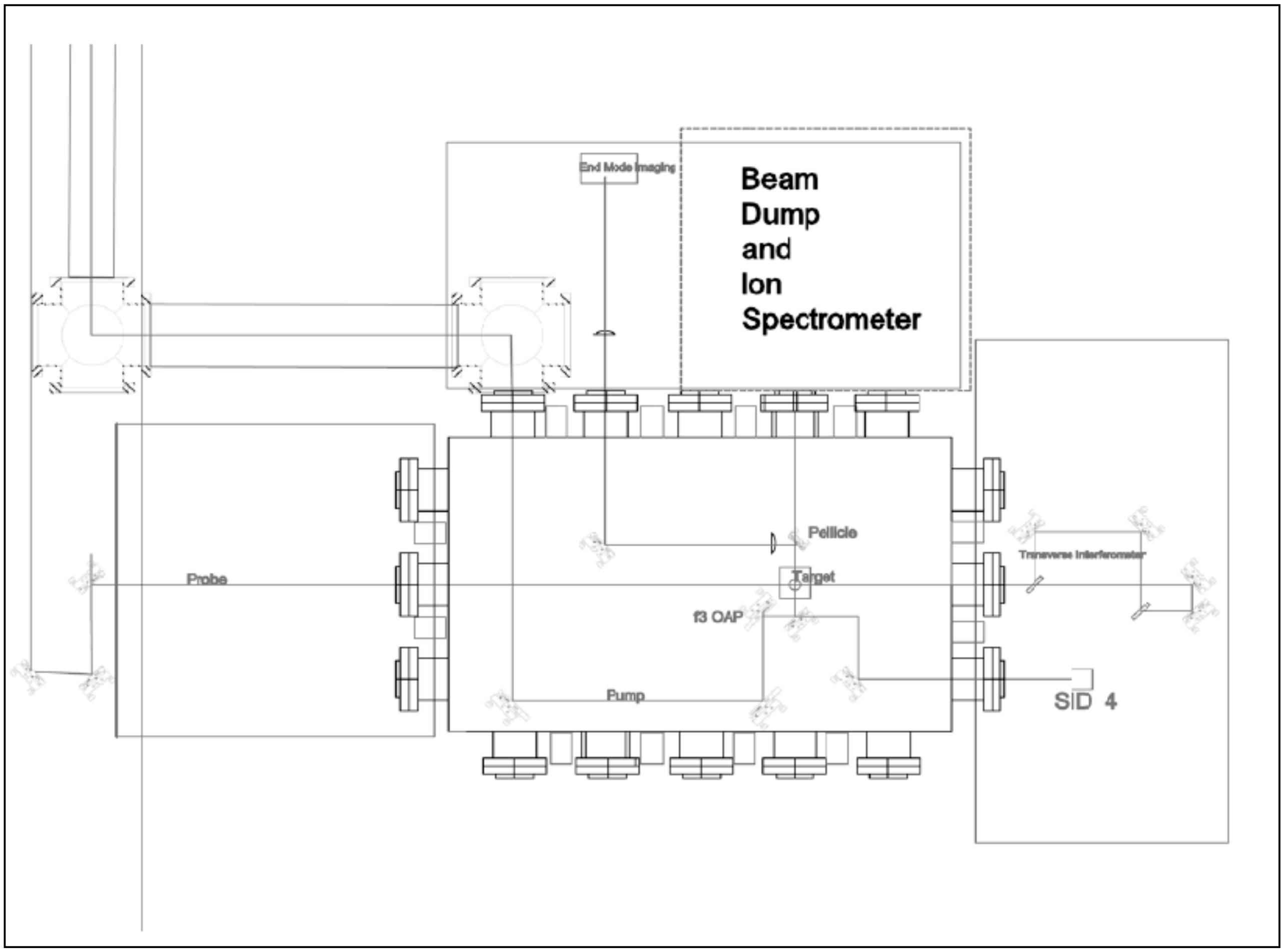

Figure 1: Top view of the proof-of-concept vacuum chamber. The expanded, high energy pulses enter the main chamber and are compressed by two gratings, then focused on the target by an off-axis parabolic mirror. Beam diagnostics, an interferometric probe for measurement of gas jet profiles, and a port for characterization of the proton fluxes and energies are also shown.

A polymeric vacuum chamber also provides flexibility in the configuration of the window through which energetic protons will pass to activate gaseous or liquid radionuclide precursors. The small solid angle of the quasi-neutral plasma jet and the ability to shrink the geometry once characteristic length and time scales are quantified may enable differential pumping of a cylindrical aperture leaving only the disposable polymeric window of the precursor cartridge between the proton beam and the precursors.

Pumps

The pumping capacity of the system must handle both the purge gas flow at steady state and the pulsed load of the low duty-cycle target gas jet. In the current configuration, this is accomplished with a roots blower backed by a roughing pump. This configuration which works well for 10 Hz gas jets with ~1ms pulse widths and 7 MPa backing pressure at -160C. Optimization of the gas jet using computational fluid dynamics to shape the nozzle, described in the next chapter, can relax the pumping requirements. High intensity experiments commonly use turbomolecular pumps backed by oil-free scroll or diaphragm pumps to avoid contamination. However, the turbomolecular pump can be saturated by the pulsed gas jet doses. A roughing-backed roots blower provides more flexibility when significant average gas mass flows are required. Oil backflow is obviated by maintaining a steady bleed of clean nitrogen gas and keeping the chamber pressure in the viscous flow regime (pressure ~ 0.25 Pa). Larger duty cycles may result from recent evidence (Goers et al., PRL 115, 194802 (2015)) of multi-MeV electron production at lower intensities and higher repetition rates; these may require different pump configurations.

A catalytic or sorption trap for hydrogen and oil-free pumps may permit virtually closed-cycle operation, reducing logistical complexity and operating costs for a point-of-care system.

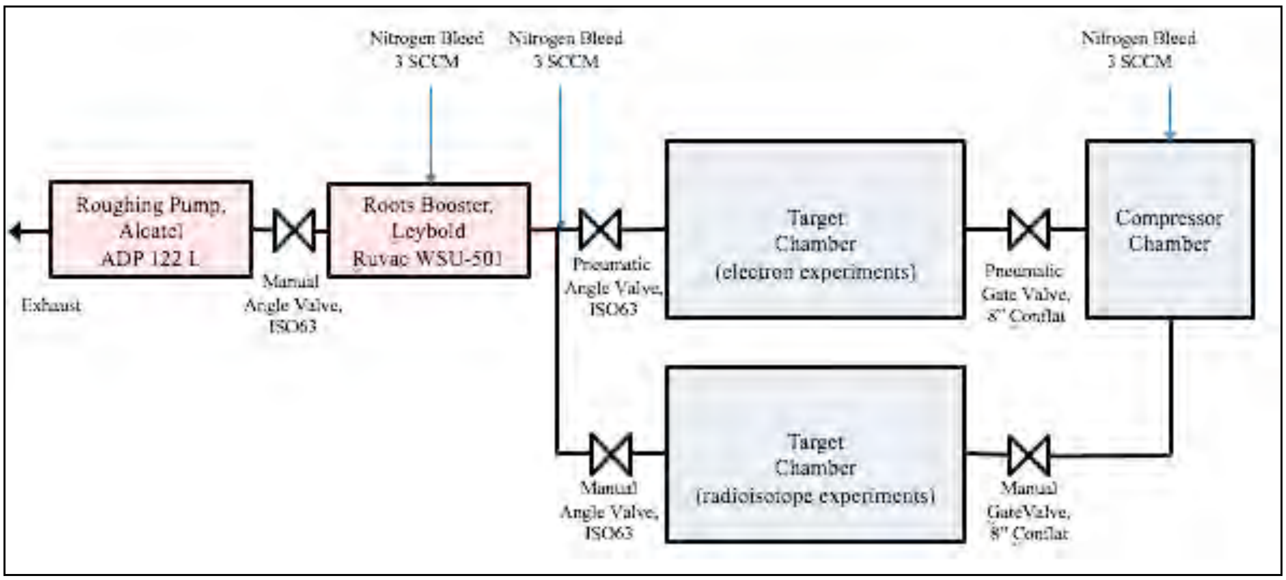

Figure 2: Layout of the vacuum system. The chirped laser pulse is compressed in a separate, valved chamber through which nitrogen is flowed at a few standard cm^3 per minute. Two target chambers are connected to a roots blower backed by a roughing pump. The continuous nitrogen bleed rigorously prevents backflow of oil vapor from the pumps and sweeps any adsorbed contaminants from the optics.

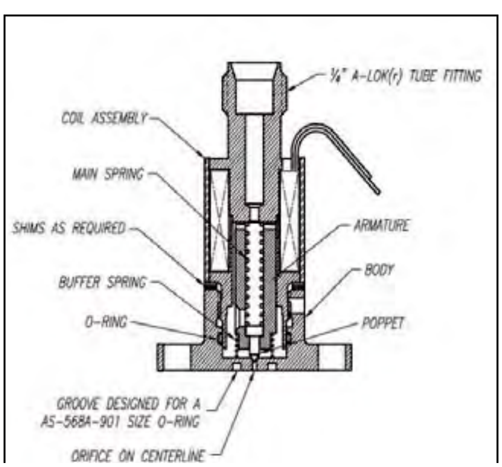

Gas Jet Target

The proof-of-concept chamber has a target gas source controlled by a fast solenoid valve with a metal poppet to seal at cryogenic temperatures. A cross-section of this valve is shown in figure 3 below. The shape of the nozzle and the thermodynamics of the expansion control the time-dependent density profile in the target region. Prior work at UMD has concentrated on flat and conical nozzles, which produce sonic flows. Alternative nozzle configurations to shape the flow field and enhance clustering of hydrogen will be described in the next Milestone Report.

Figure 3: Cross-section of the Parker series 99 solenoid valve used to pulse high-pressure, low temperature hydrogen gas through a needle or nozzle.

The maximum backing pressure for the Parker valve is 7 MPa, however we have identified a suitable valve (Clark-Cooper EH30) that operates at pressures up to 70 MPa. If the nozzle and pump configuration is compatible this will increase the target density by an order of magnitude. A cross-section of this valve is shown in figure 4.

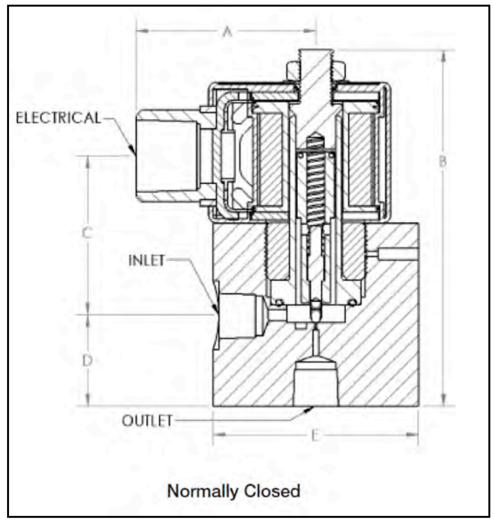

Figure 4: Cross-section of the 7 MPa EH30 valve planned for jet experiments.

A minimum opening time of a few hundred microseconds is required to fully develop the nozzle flow, however timescales for condensation and expansion must also be considered in a search for the optimal gas target. We seek to optimize both the target density and density gradient in the laser focal volume. Nozzle geometry, stagnation pressure and temperature, and the nucleation of hydrogen clusters are degrees of freedom to be discussed in the next chapter.

Laser

A comprehensive description of the laser system to be used in the proof-of-concept demonstration is provided in an excerpt from Andy Goers' dissertation (Appendix I). The output of the current system is 40fs, 800nm, 900 mJ optical pulses at 10 Hz. To generate the plasma jets the electric field at the target must be greater than about 10^{18}W/cm^2. With 900 mJ/pulse we need a very small focus and a short pulse duration to achieve these intensities. Figure 5, reproduced from Goers' thesis (Appendix I) shows the full width at half maximum as a function of group delay dispersion, with a minimum pulse width of ~40 fs.

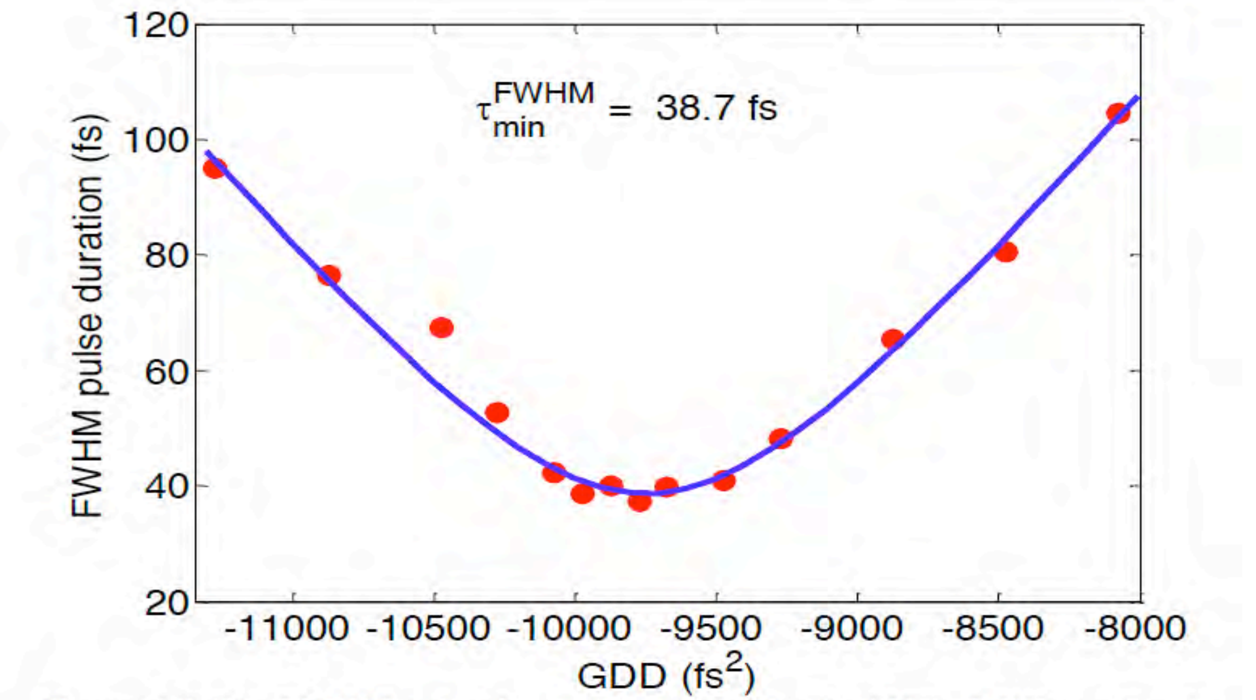

Figure 2.8. The FWHM pulse duration measured by the SHG FROG as a function of GDD applied by the Dazzler along with a least squares fit to a hyperbola.

Figure 5: Figure 2.8 from Andy Goers' dissertation).

The UMD team has also optimized the spatial focus and coherence of the light pulse, as seen in the phase front and focal spot measurement in figure 6 and the inverted field autocorrelation fringes in figure 7. Complete descriptions of the methods used to obtain these results are found in the appendix.

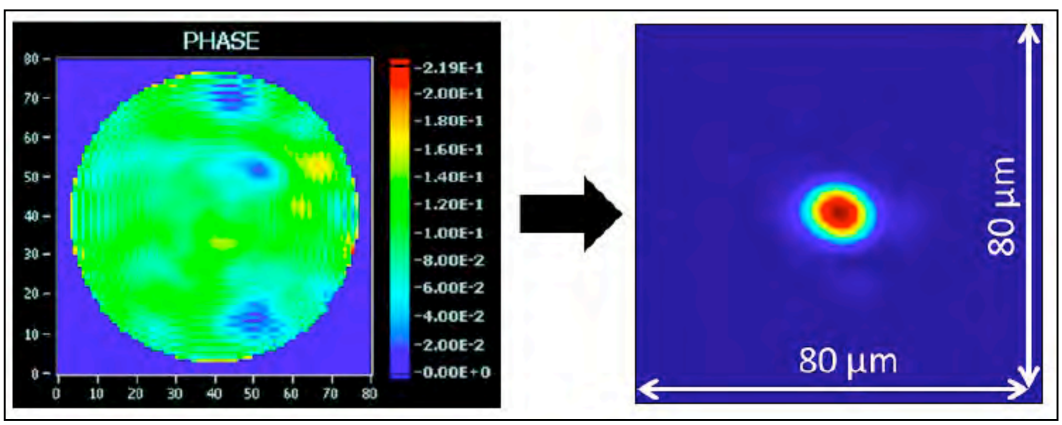

Figure 6: Measured phase front and focal spot for a ~40fs, 800nm pulse. (Appendix figure 2.12 for details).

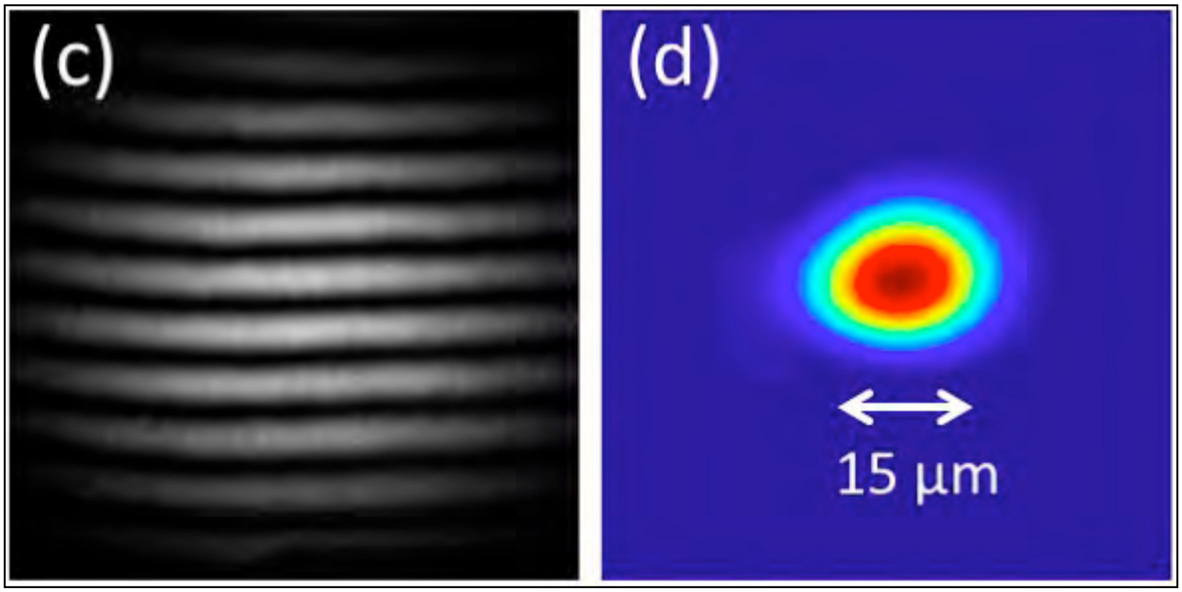

Figure 7: Inverted field fringe pattern and focal spot size from figure 2.14 of the Appendix.

Our proposal describes the challenge of pre-pulses in some detail. The current laser system has pre-pulses whose amplitudes are ~10^{-4} times those of the main pulses and that precede it by 18 and 50 ps, as seen in figure 8. This implies pre-pulse intensities of ~10^{14} W/cm^2 which are sufficient to ionize the gas target before arrival of the main pulse.

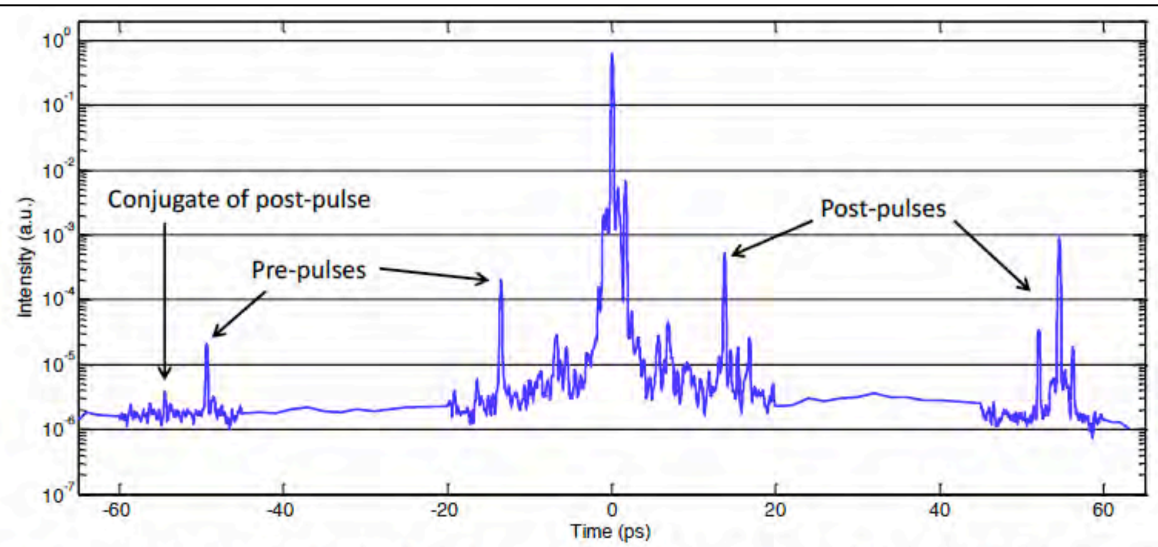

Figure 2.10. Sample third order autocorrelation trace of the amplified pulse. Higher resolution scans are shown around areas with known pulse structure.

Figure 8: Pre- and post-pulse laser intensities. (Figure 2.10 in Appendix 1).

Summary

This chapter summarizes the characteristics of the experimental chamber and laser for MicroPET's point-of-care radioisotope generator. The chamber is designed to enable efficient optimization of both the sub-picosecond laser pulse and the density profile of the pulsed jet of H_2. Flowing purge gas provides options for a completely polymeric vacuum chamber, which provides advantages in cost, neutron-free operation, and geometric flexibility.

The 25TW, 10 Hz laser system that will be used to study quasi-neutral plasma jet formation in pulsed hydrogen jets is also described based on the recent (Nov 2015) dissertation of Andy Goers (Appendix I). The experimental chamber is large and flexible enough to fully characterize the optical pulses, gas jets, and quasi-neutral plasmas whose optimization is a central part of the Positrons on Demand program.

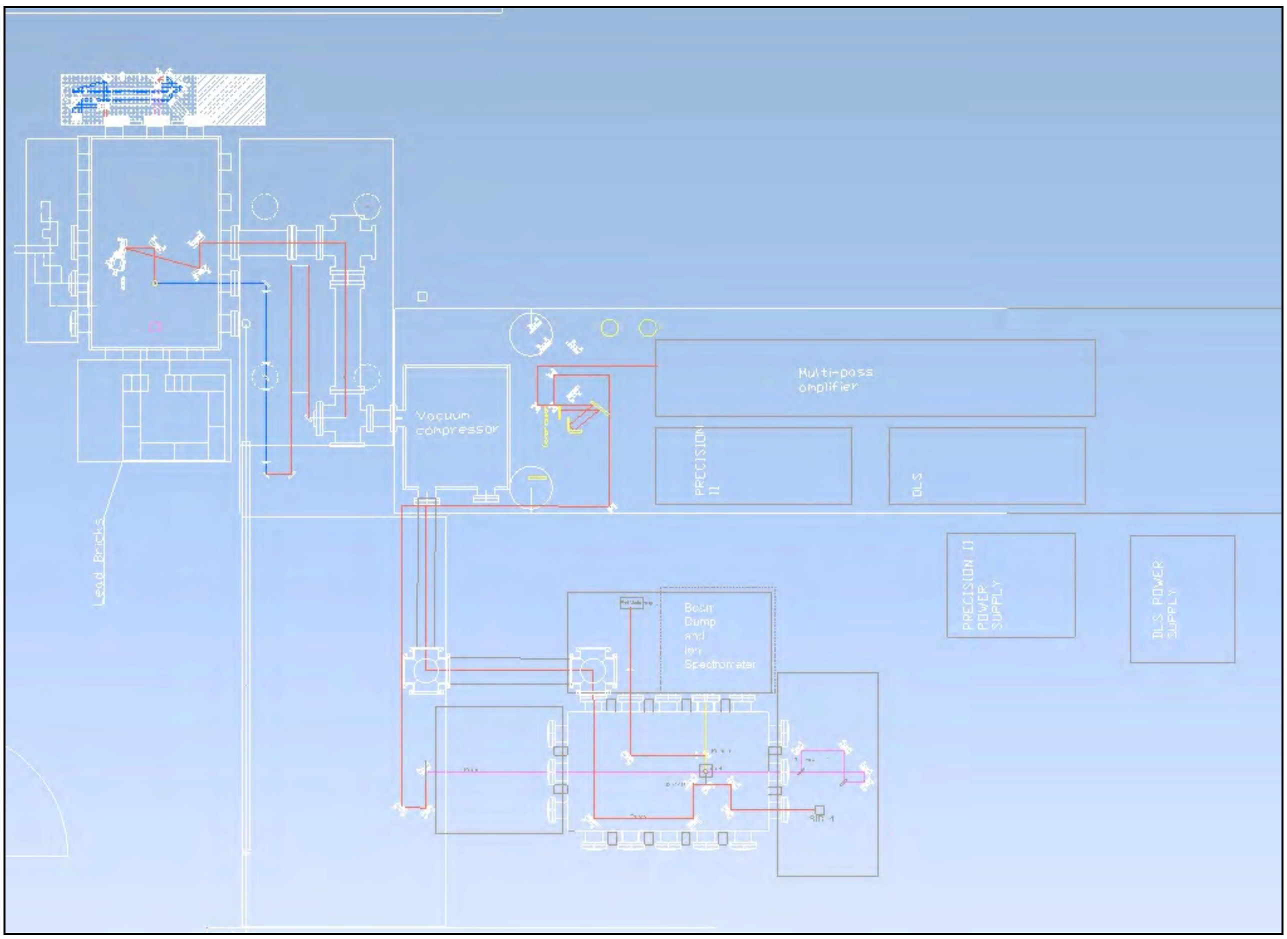

Figure 9: Complete overview of the 25 TW laser experimental configuration in the Milchberg laboratory at UMD College Park.

Chapter 2: A flexible target

The objective of the *Positrons on Demand* program is to produce generic positron-emitting radioisotopes at the point of care for imaging by positron emission tomography. These isotopes are created by impinging energetic (5-15 MeV) protons on a precursor material such as a mixture of $^{14}N_2$ and $^{16}O_2$ to generate short-lived tracers such as $^{11}CO_2$ ($t_{1/2}$= 20.4 minutes). Conventional production using cyclotrons, high beam currents, and relatively large batches results in neutron radiation hazards, heavy and expensive shielding, and logistical complexity that limits the availability of isotopic reagents other than those containing ^{18}F. This challenge applies especially to new ligands that probe neurochemistry *in vivo*.

Energetic protons from which these radioisotopes can be produced have been generated with lasers impinging on solid targets. However, solid targets are complicated by the need for precise optical alignment in vacuum, variability of target thickness and composition, deposition of binder material on optical surfaces, and mechanical complexity. We have chosen to develop a target based on a supercritical pulsed fluid jet which has the following advantages:

1. No ions other than H^+ are produced by the high-energy laser pulse;
2. Optical surfaces are not damaged or coated with refractory material that is generated from solid targets;
3. Movement or alignment of the target is not required to provide a reproducible target density profile and composition at useful pulse repetition rates of 10Hz or more;
4. Pumping requirements are simplified because the gas load is proportional to the duty cycle of the pulsed valve, which in our case is 0.02 or less;
5. The low average flow rate of clean gas reduces the impact of impurities and surface contaminants; and
6. The mechanical simplicity of the pulsed valve permits a compact vacuum chamber to house the fluid jet, laser optics, and precursor substrate.

Pulsed gas jets

We have determined through simulation and a thorough review of the plasma physics literature that control of the neutral density and its gradients at the edges of a thin target are crucial constraints on the efficient conversion of photon energy to proton acceleration. Figure 1 below shows a set of profiles for helium gas with a stagnation temperature and pressure of 20C and 30 MPa (300 bar) reported by Scylla *et al.* *(Rev. Sci. Instrum. 83, 033507 (2012); doi: 10.1063/1.3697859).* The number density of gas behind this 30 MPa jet is between 6 and 7 x 10^{21} based on the helium equation of state. Figure 2, taken from the same reference, shows that the profiles remain pseudo-Gaussian with density gradients extending over 250-270 microns. The high stagnation pressure requires a valve with an open time of tens of milliseconds and a multi-stage pumping system with a roots blower and backing pumps.

Our experimental configuration cools hydrogen gas to -160^{o}C, so that the stagnation pressure and temperature correspond to supercritical conditions. At 7 MPa backing pressure the hydrogen molecular gas density is 4.5 x 10^{21} cm^{-3}, yielding an atomic number density (9 x 10^{21}) greater than that found at 30 MPa with the room temperature helium described in reference 1. Cooling is also important because the non-ideal fluid properties, including the Joule-Thomson coefficient, viscosity, volume expansivity, and sound speed are significantly different for a supercritical fluid undergoing expansion than they are for an ideal gas.

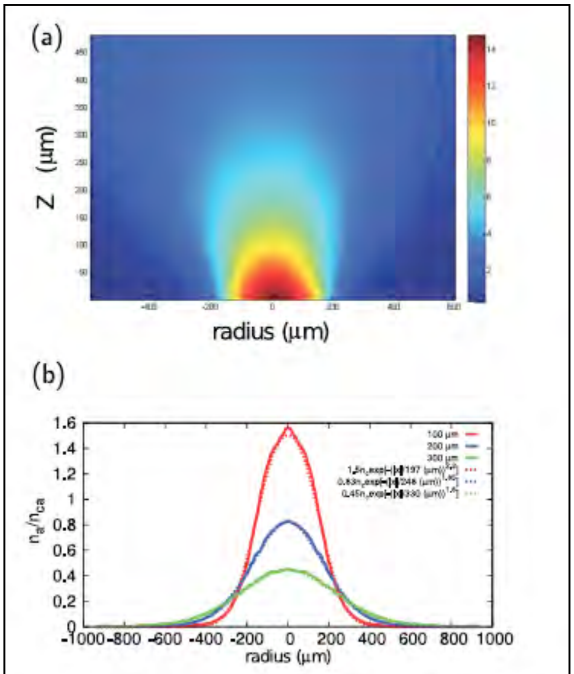

FIG. 3. Data extraction from interferograms obtained with a 400 μm-cylindrical nozzle pressurized at p = 300 bar. (a) Phase shift distribution (colormap in radian) from CWT. (b) Neutral He profiles n_a normalized to the atomic critical density n_{ca} at 100 (red line), 200 (blue line), and 300 μm above a 400 μm sonic nozzle from Abel-inversion. The dotted lines indicate the best exponential fits.

Figure 1: Figure 3 from reference (1) showing the spatial density profile of He gas with stagnation conditions of 20^{o}C and 30 MPa. The scale on the lower panel is in terms of n_{ca}=1.68 x $10^{21}cm^{-3}$.

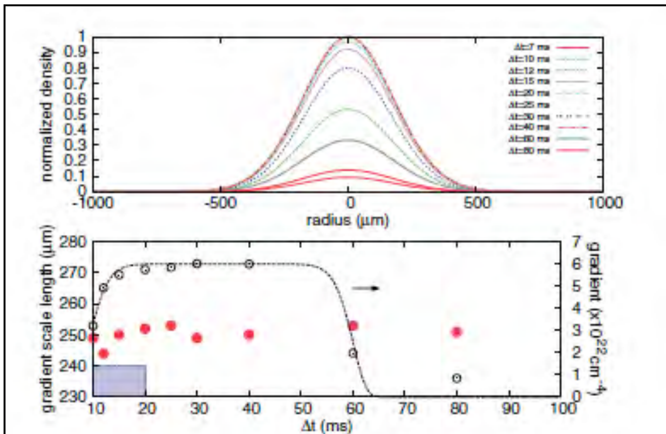

FIG. 7. Profile evolution for different Δt using the same nozzle as in Figure 6. (Top) radial profiles normalized to the peak density at 25 ms. (Bottom) gradient calculated as the peak density over the gradient scale length (black empty dots), and gradient scale lengths from gaussian fits of the profiles (red dots). The blue region indicates the opening time of the valve. The interpolated dashed line is an indication to guide the reading.

Figure 2 Time-dependent radial density profiles. (Sylla et al. Rev. Sci. Instrum. 83, 033507 (2012); doi: 10.1063/1.3697859). The maximum gradient is 3 x $10^{22}cm^{-4}$.

We hypothesized that the real gas properties of supercritical hydrogen would affect the shape and density of the pulsed fluid jet. Table I summarizes a selection of these properties for the helium used in reference 1 alongside hydrogen at less than 1/4th of the stagnation pressure and two temperatures. We have constructed a two-color interferometric microscope to image both the neutral jet profile and the plasmas that results from pulsed laser irradiation. The interferometer was described in detail in our Milestone 3 report.

Table I : Selected fluid properties for pulsed jets	**He @ 300K, 30 MPa**	**H_2 @ 300K, 7 MPa**	**H_2 @ 110K, 7 MPa**
Density (kg/m^3)	42	20	35
Number Density (molecules/cm^{-3})	6×10^{21}	1.6×10^{21}	4.5×10^{21}
Viscosity (μPa-s)	20	9.5	5
Joule-Thomson coefficient (K/MPa)	-0.6	-0.33	0.4
Sound Speed (m/s)	1130	1350	920
Heat Capacity C_p (kJ/kg-K)	5.2	14.5	12.9
Heat Capacity Ratio C_p/C_v = [redacted]	1.64	1.41	1.71
Volume expansivity (K^{-1})	.0292	.003	.01

The low viscosity, volume expansivity, and the positive value of the Joule-Thomson coefficient all facilitate stable jets of supercritical fluid in the zone near the nozzle exit.

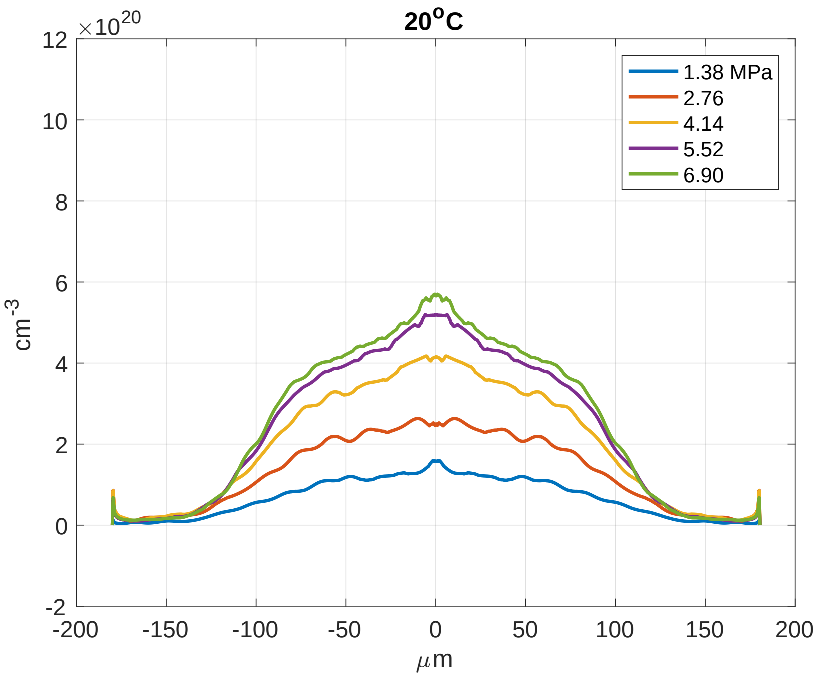

Figure 3: H_2 number density profiles 50 μm from the exit plane of a room temperature jet with stagnation pressures from 1.4 to 6.9 MPa (200 to 1000 psi) emerging from a 160 μm nozzle. The density of atoms in the laser driven plasma are twice these values.

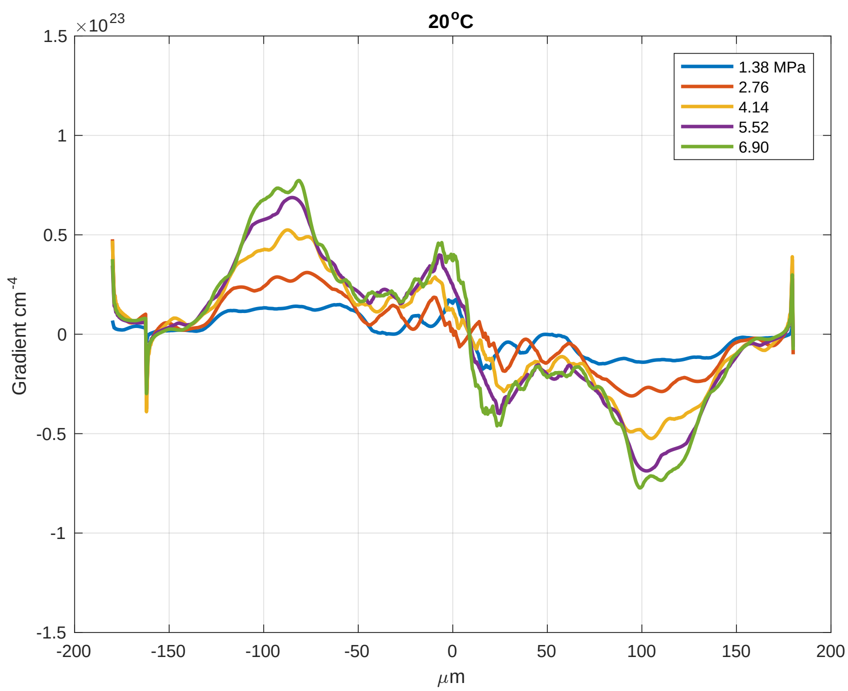

Figure 4: Room temperature density gradients for the profiles shown in the preceding figure. Systematic control of the gradients at the boundary is accomplished through adjustment of the stagnation pressure.

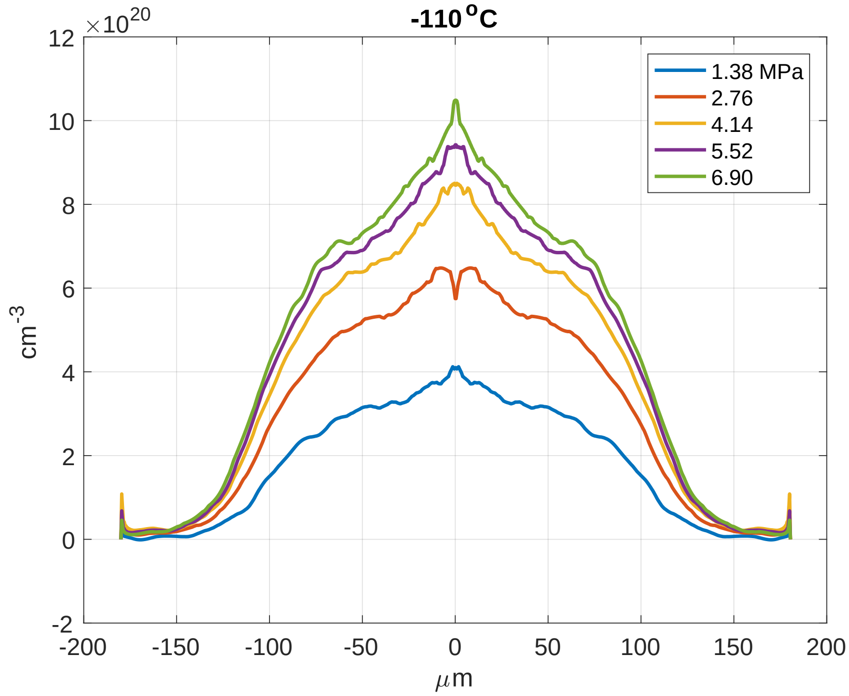

Figure 5: H_2 number density profiles with a stagnation temperature of -160°C; all remaining conditions are as cited in figure 3. The peak in the center is an artefact of numerical Abel inversion.

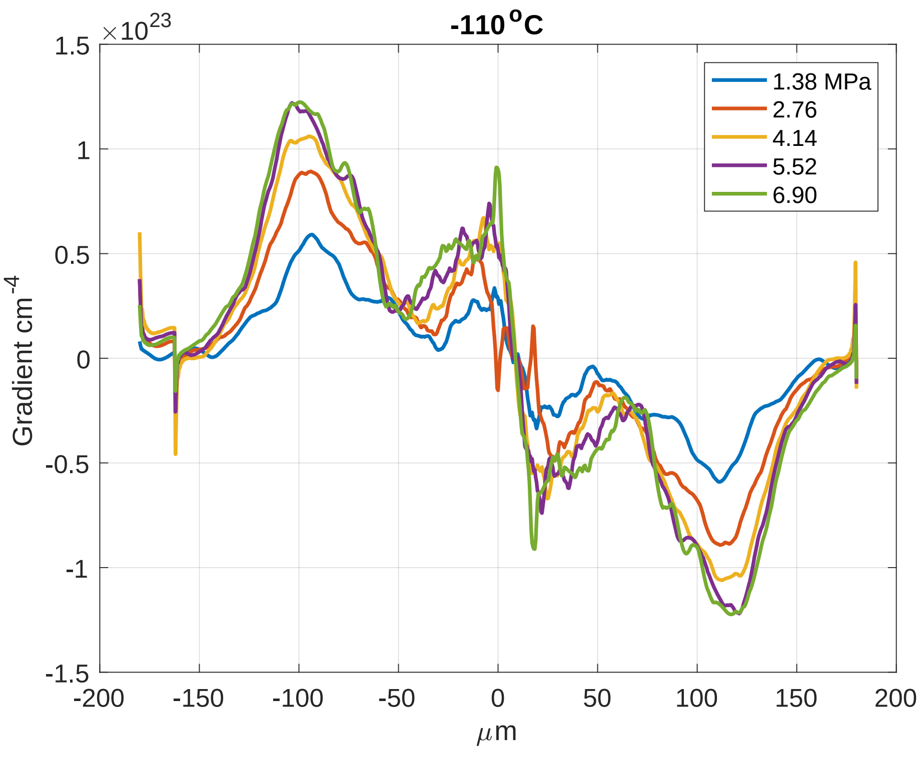

Figure 6: Density gradients of the jet's edges -160°C are about four times those reported for He (eight times if one considers the atomic density of the resulting plasmas).

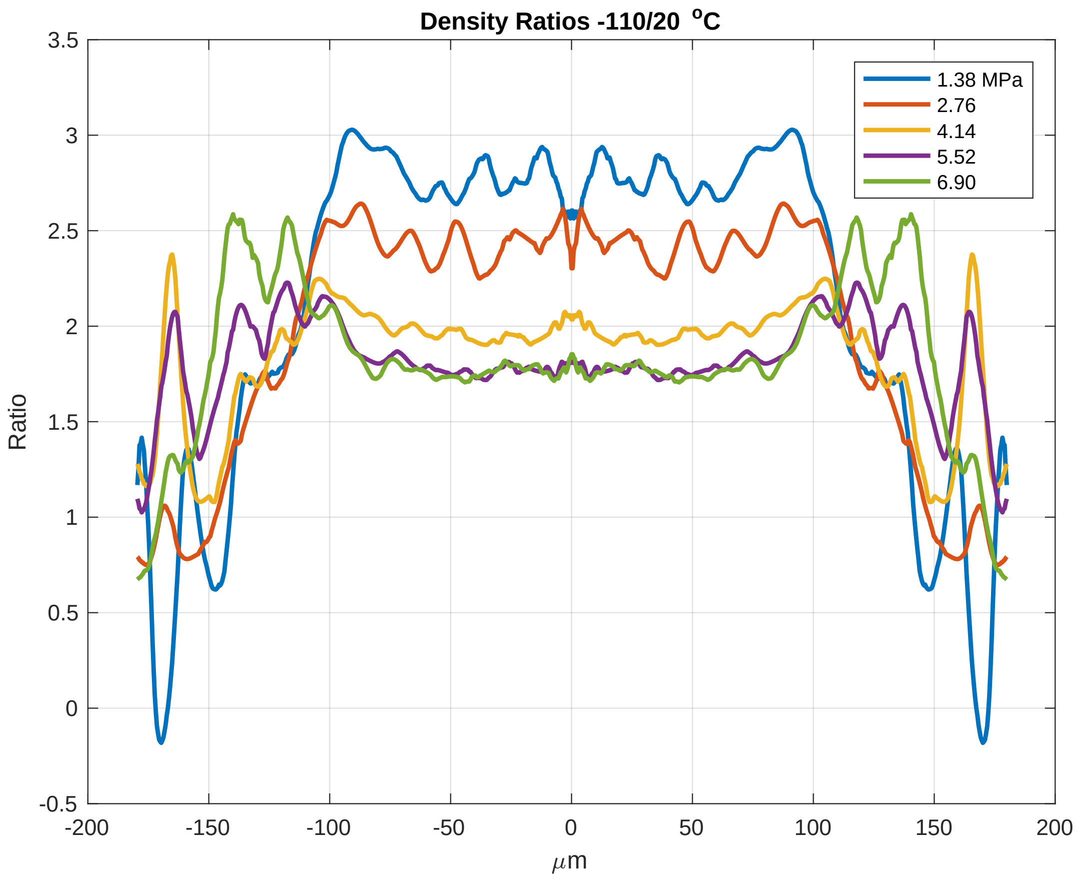

Figure 7: Ratio of number densities at -160°C and 20°C are temperature dependent because the dynamics of expanding jets vary with both pressure and temperature.

The atomic number density produced in the first femtoseconds of the incident laser pulse is twice the values shown in figures 3-7 because the H_2 is fully ionized to 2 protons and 2 early in the pulse. In other words, we observe densities up to 2 x 10^{21} atoms per cubic centimeter and density gradients of as much as 2.5 x 10^{24} cm^{-}

In addition to control of the target gas density and density gradient we find that the performance of the valve and jet are extremely reproducible. The density profiles are extracted by averaging 50 discrete-pulse interferograms; shot-to-shot variability is only a few percent, small enough to maintain excellent alignment of the gas and high power laser pulses.

The profile of the gas pulse stabilizes about 300 μs after the valve is opened and remains constant for a millisecond; ample time to produce the quasi-neutral plasma jet. The fast opening and closing of the pulsed valve is made possible by the lower stagnation pressure (7 versus 30 MPa for the configuration in ref. 1), and this in turn decreases vacuum pumping requirements in our system design.

Another feature of the current approach is the ability to adjust the thickness of the target. The conical nozzle used to generate the profiles in figures 3-7 has an inner diameter of 160 μm; 50 μm from the exit plane the width of the jet is only 220 μm. The smallest commercially available nozzle has an inner diameter of 60 μm, so a target thickness of as little as 100 μm is feasible without significant change to the experimental configuration. Even narrower nozzles are possible using laser machining methods, though we expect that these will not be necessary.

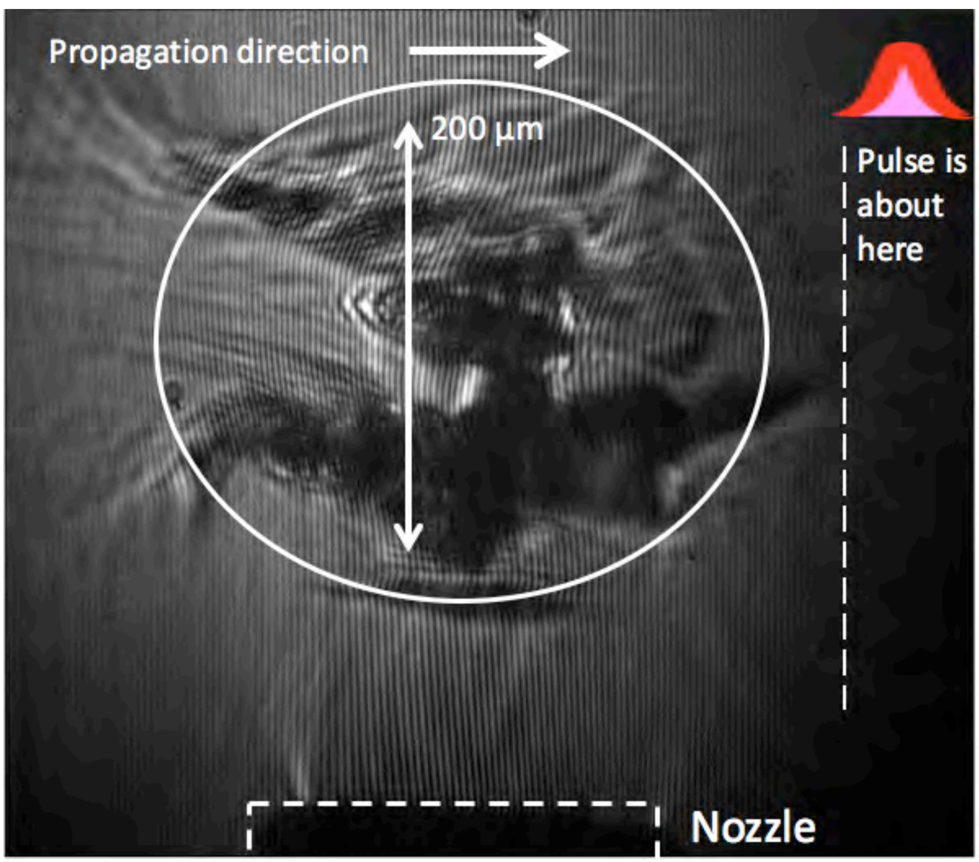

Figure 8: Interferometric image (266nm) of a transient hydrogen plasma (-165C, 7MPa stagnation conditions) using a 500mJ, 400fs, 800nm laser pulse.

Summary

This chapter outlines the successful characterization of a pulsed supercritical hydrogen jet that serves as the target for creation of energetic proton bursts that in turn produce positron emitting isotopes. Independent control of the target density, density gradients, and spatial extent of the jet have been demonstrated over ranges appropriate to reproducible generation of directed energetic protons from terawatt laser pulses.

Chapter 3: Interferometric Characterization of the Quasi-Neutral Plasma Jet

The fluxes and energy spectra of ions accelerated by a high intensity laser pulse impinging on a dense plasma depend dramatically the target density profile. The *Positrons on Demand* project requires an effective method for the measurement of neutral gas and plasma density profiles for optimization of the ion source parameters. We have selected femtosecond transverse interferometry[1,2], which has been used effectively for nearly 30 years, as the primary method for plasma and neutral gas density measurements. The high plasma densities used in the experiments (~10^{21} cm^{-3}) we have chosen require an ultraviolet probe wavelength to limiting the confounding effects of plasma refraction. Here we describe a frequency tripling apparatus that generates femtosecond pulses at 266 nm along with a photon-efficient wave-front division interferometer.

Principle of femtosecond interferometry

Figure 1 provides an overview of the system with a raw interferogram from which hydrogen molecule density has been extracted. The femtosecond probe beam is derived from the main pump beam, assuring that the two are synchronized. The probe beam is directed through the plasma orthogonal to the pump pulse and acquires a phase shift with respect to a reference portion of the beam which does not pass through the plasma. This phase shift is recorded by imaging the plane of the plasma onto a CCD while interfering the signal and reference portions of the beam. The phase shift image is then extracted through Fourier transform techniques[3]. The ultrashort nature of the probe captures a “snapshot” of the plasma with a temporal resolution of approximately the probe pulse duration.

Each pixel on the phase image corresponds to the phase accumulated along a chord through the plasma so that the 2D phase measurement, $\Delta\phi(x,y)$, is given by

$$\Delta\phi(x,y) = \frac{2\pi}{\lambda}\int (n(x,y,z)\text{-}1)\,dz \quad (1)$$

where λ is the vacuum probe wavelength, $n(x,y,z)$ is the target refractive index, and z is the probe propagation direction. When measuring large phase shifts such as occur when working with high density gas jets and plasmas, an appropriate fringe spacing ensures that the phase shift between adjacent fringes is not more than 2π radians. Otherwise, the extracted phase is ambiguous and

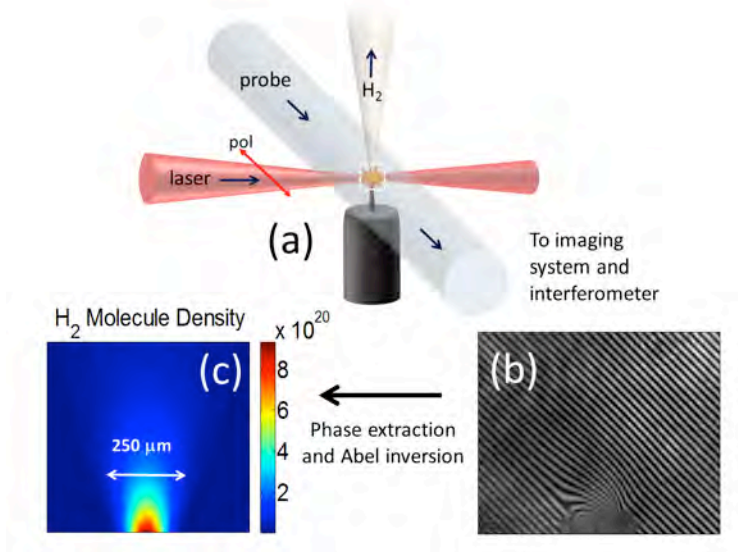

Figure 1. Experimental setup of neutral gas measurement using transverse interferometry (a) with a sample raw interferogram (b) and extracted density profile (c).

inaccurate extraction results. This ambiguity can be eliminated by using a high fringe density or by minimizing the phase gradients through tuning of the probe wavelength.

If cylindrical symmetry is assumed about some axis of the phase image, the Abel transform can be used to invert the phase shift integral and give the refractive index in terms of the measured phase shift. Taking the symmetry axis as the x axis, Abel inversion gives

$$n(r,y)\text{-}1 = -\frac{\lambda}{2}\int_r^{r_0}\left(\frac{d\Delta\phi(x,y)}{dx}\right)\frac{dx}{\sqrt{x^2\text{-}r^2}}\,. \quad (2)$$

The Abel transform can be computed numerically using Fourier or Hankel transform methods[4,5], or analytically if the measured phase shift follows an appropriate functional form.

The density of the hydrogen gas jet target can be measured by timing the probe beam to pass through the gas jet just prior to the arrival of the main, high intensity beam. The refractive index of this neutral gas is linearly proportional to the density, $N(r,y)$ and the molecular polarizability, α of the gas:

$$n(r,y)\text{-}1 = N(r,y)*2\pi\alpha. \quad (3)$$

If the neutral gas density is fixed, shorter wavelengths will experience a larger phase shift per equations (1) and (3). When working with high density targets, this means a longer wavelength may be preferable to avoid large phase gradients which make reliable phase extraction impossible.

For measuring plasma densities, the Abel inverted refractive index can be related to the plasma density via

$$n(r,y)\text{-}1 \approx \frac{\omega_p(r,y)^2}{2\omega^2} = \frac{N_e(r,y)e^2\lambda^2}{2\pi m_e c^2}$$

where $\omega_p = \sqrt{4\pi N_e e^2/m_e}$ is the plasma frequency, ω is the laser frequency, N_e is the plasma electron density, e is the elementary charge, and m_e is the electron mass. This formula for the refractive index assumes a sufficiently under dense plasma ($\omega_p \ll \omega$). Note that here for a fixed plasma density the total phase shift scales as $\Delta\phi \propto \lambda$ so that a shorter wavelength probe will acquire a smaller total phase shift. Therefore, using a higher frequency probe at high density will reduce probe phase shift as well as probe refraction.

The transverse probe line design for *Positrons on Demand* was evaluated using probe wavelengths at the second, third, or fourth harmonic of Ti:Sapphire. In principle, plasma density measurements using transverse interferometry should be possible for all plasma densities up to the critical density, N_{cr}, of the transverse probe where $N_{cr} = \frac{m_e\omega^2}{4\pi e^2}$. In practice, probe absorption and deflection by plasma density gradients normally limit the effective maximum density to around 10% of the probe critical density[1]. A second harmonic probe was used in previous experiments and found to exhibit strong absorption and phase gradients too large to be extracted using our phase extraction algorithms. A probe at the third harmonic of Ti:Sapphire ($\lambda = 266\ nm$) has an associated critical density of $1.58{\times}10^{22} cm^{-3}$ and, therefore, is capable of probing plasma densities near the critical density of our Ti:Sapphire pump laser ($N_{cr} = 1.74{\times}10^{21} cm^{-3}$). The fourth harmonic of Ti:Sapphire, while exhibiting a proportionately higher critical density, was suboptimal because it is strongly absorbed in the atmosphere, requiring an interferometer housed entirely in vacuum. Further, the yield of a fourth harmonic assembly was estimated at approximately 1%, 8-10x less than that for readily available nonlinear crystals used to generate the 266 nm pulses.

Experimental setup for third harmonic interferometry

Frequency tripling apparatus

The femtosecond probe beam is derived from the 25 TW peak power Ti:Sapphire laser pulse used as the main drive beam for ion acceleration experiments. This means the pump and probe are synchronized and can be delayed with respect to each other with femtosecond resolution. About 10 mJ is split from the 1.2 J beam using a 1% transmitting beam splitter after the final amplifying stage. The ~10 mJ probe beam is then compressed using a single grating pulse compressor with about 50% efficiency, then sent through a micrometer controlled delay line and a frequency tripling apparatus.

The third harmonic assembly is based on a two stage conversion design with a calcite plate to compensate group velocity dispersion as detailed by Enqvist.[6] Figure 2 shows a schematic of the assembly. The probe beam is sent through a BBO crystal cut for Type I phase matching of second harmonic generation (SHG) at the fundamental wavelength, $\lambda = .800\, nm$. Next, the fundamental and second harmonic beams are orthogonally polarized. Type I phase matching of sum frequency generation ($\omega + 2\omega = 3\omega$) in a second BBO crystal (THG) provides efficient conversion to the third harmonic. A zero-order quartz wave plate placed between the two crystals ensures that the fundamental and second harmonic polarizations are parallel. The wave plate acts as a half wave plate for the fundamental and, therefore, a full wave plate for the second harmonic, yielding parallel polarizations.

Finally, the group velocity of the fundamental beam is faster than that of the second harmonic in both SHG crystal and the wave plate. This leads to walk off between the fundamental and second harmonic. Without compensation, the two pulses would not overlap temporally in the second BBO crystal. This temporal walk off is compensated using a birefringent calcite plate placed between the SHG crystal and the wave plate where the fundamental and second harmonic polarizations are orthogonal. The optical axis of the calcite compensator is aligned so the fundamental beam is polarized along the (slow) ordinary axis ($n = 1.649$) and the second harmonic is polarized along the (fast) extraordinary axis ($n = 1.497$). Tuning the incidence angle of the beams on the compensator plate allows fine scale adjustment of the delay between the fundamental and second harmonic pulses in the THG crystal.

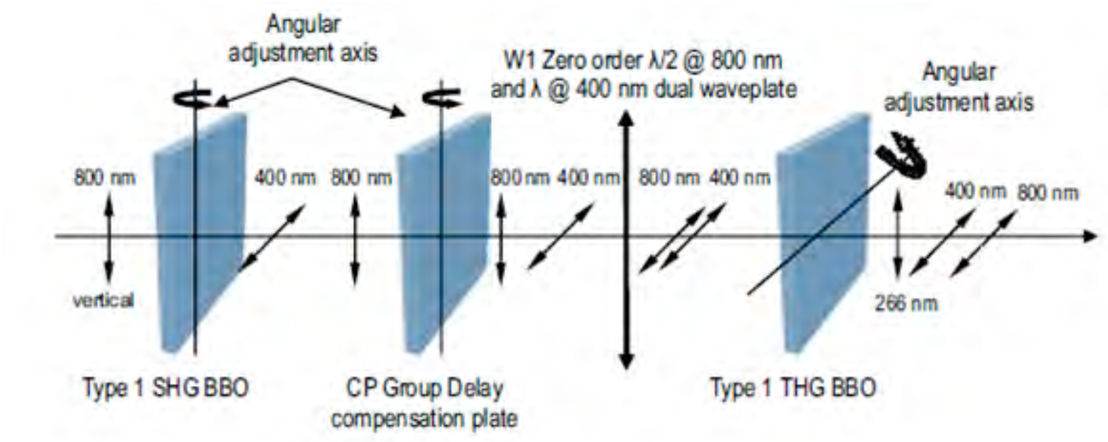

Figure 2. Schematic of the frequency tripling apparatus showing the polarization of the pulses as they travel through the assembly. Image credit: Eksma Optics www.eksmaoptics.com

This frequency tripling apparatus maintains a very compact footprint and has conversion efficiencies near 10%. With a 1 mJ input pulse energy this yields the ~100 μJ pulse energies at 266 nm to probe our high-density plasmas. Further, the collinear geometry makes the residual fundamental and second harmonic beams available for multi-wavelength probing experiments. For example, we use the fundamental ($\lambda = 800\,nm$) beam as the probe for interferometry of the neutral gas density profile while reserving the third harmonic probe for interferometry of the high-density plasma.

Design of the wave front division interferometer

A Nomarski interferometer based around a Fresnel biprism wave front division optic was designed and built to image the 266 nm probe beam. This design is compact setup and is much more photon-efficient than amplitude division interferometers. The absence of additional mirrors within the interferometer improves fringe stability and provides probe and reference path lengths which are automatically matched on a

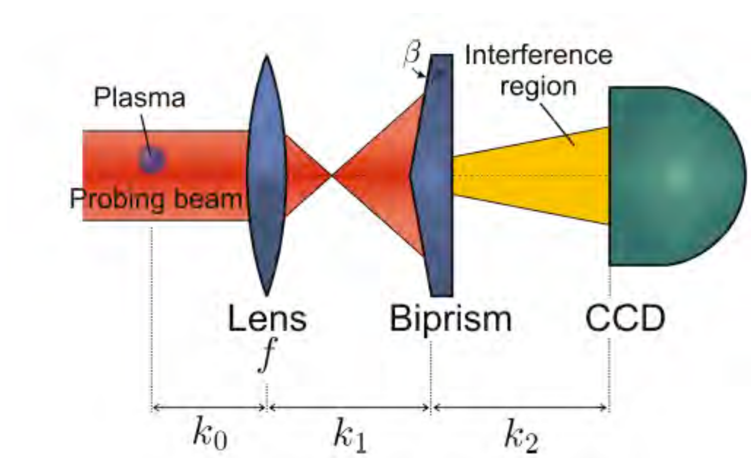

Figure 3. Schematic of the Nomarski interferometer with a Fresnel biprism as the wave front division optic. In our design $k_0 = 90\,mm, k_1 = 170\,mm,$ $k_2 = 280\,mm, f = 75\,mm,$ *and* $\beta = 1°$. *Image credit: Kalal et al. JKPS **56**, 287 (2010).*

femtosecond time scale. The theoretical description provided by Kalal *et al.* of this type of Nomarski interferometer was used to choose proper optics given our spatial and imaging constraints[7]. Their detailed description of the working principle of the interferometer is attached as an appendix.

The plane of the plasma is first imaged outside the target chamber using a confocal telescope with magnification M = 2. The Nomarski interferometer, shown schematically in Fig. 3, consists of a single lens, a shallow Fresnel biprism, and a UV sensitive CCD array. The lens images the plasma at five times magnification (10x total magnification) onto a 14 bit CCD (PCO Technology PCO ultraviolet) which has approximately 30% quantum efficiency at 266 nm. A 1 degree Fresnel biprism is placed 170 mm from the imaging lens and 95 mm from the focus of the probe beam. The introduction of the Fresnel biprism in the imaging system creates two spatially separated virtual foci. Interference between these virtual foci creates the fringe pattern on the CCD with the fringe spacing adjusted by changing the separation between the imaging lens and biprism. With the geometric layout shown in Fig. 3 and a ½" CCD sensor there are 100 fringes across the CCD, a theoretical resolution image of 2.4 μm, and a field of view 640 μm by 480 μm.

A representative image from the MicroPET diagnostic is shown in figure 4.

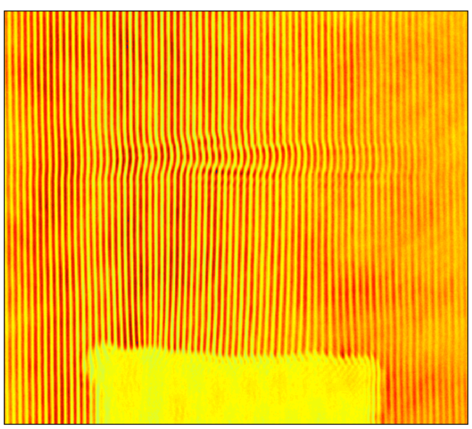

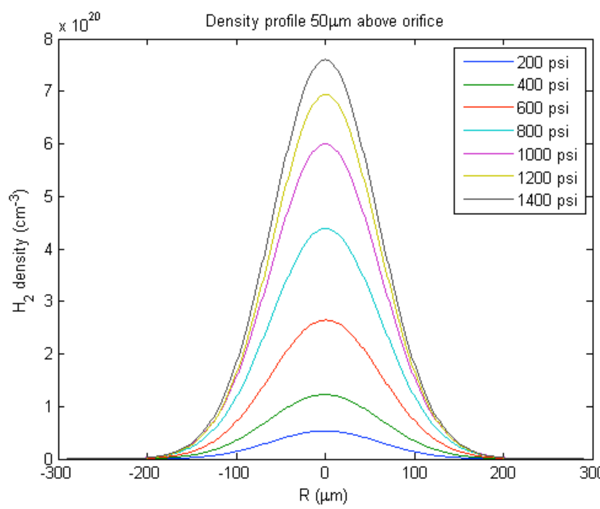

Figure 4: (left) 266 nm interferogram (400 μm edge lengths) of a transient plasma illustrating control of the fringe spacing for resolution of the plasma density profile. (right) Neutral density profile as a function of stagnation pressure at room temperature 50 microns in front of a 130 micron diameter nozzle extracted from a series of 400 nm interferograms. References

References

[1] M. Roth, J. Instrum. **6**, R09001 (2011).

[2] T.R. Clark and H.M. Milchberg, Phys. Rev. Lett. **78**, 2373 (1997).

[3] M. Takeda, H. Ina, and S. Kobayashi, J. Opt. Soc. Am. **72**, 156 (1982).

[4] M. Kalal and K.A. Nugent, Appl. Opt. **27**, 1956 (1988).

[5] D. Keefer, L. Smith, and S. Sudharsanan, J. Quant. Spectrosc. Radiat. Transf. **39**, 367 (1988).

[6] H. Enqvist, A Setup for Efficient Frequency Tripling of High-Power Femtosecond Laser Pulses., 2004.

[7] K. Milan, J. Korean Phys. Soc. **56**, 287 (2010).

Chapter 4: Plasma Optimization Design Study Report

Overview – Objectives

This chapter describes efforts to optimize production of PET radioisotopes from a new ion source driven by laser excitation of a quasi-neutral plasma jet. The optimization is performed over the laser, primary (H_2) and secondary (N_2:O_2 or BN) target characteristics and involves two distinct, coupled aspects: (i) transfer of power from the laser to quasi-neutral proton fluxes with energies above 5 MeV and (ii) conversion of the proton flux to positron-emitting radioisotopes. This chapter focuses on the first of these aspects.

The primary targets generated by the laser irradiation of high-density supercritical gas jets. This creates plasma densities up to and exceeding the critical density of Ti:Sapphire (Ti:Sa) laser pulses ($\approx 1.7 \times 10^{21} cm^{-3}$). The energy transfer from laser to the gas target and eventually to energetic protons differs significantly from the traditional and well-studied Target Normal Sheath Acceleration (TNSA) where the interaction of lasers with solid targets whose thickness is less than the laser pulse length and the plasma density is much greater than the critical density. Our analytic and computational studies of the interaction of the laser with our dense jet targets indicate new physical mechanisms that lead to more efficient ion acceleration. An important conclusion of the study is that optimal transfer of energy to multi-MeV protons occurs in a narrow range of conditions that depend on the laser parameters (intensity I, wavelength λ, pulse length T, focal spot size and location within the gas target) and gas target parameters (density profile, length, transverse size, and the ratio of density to its critical value).

Particle-in-Cell simulations using the parameters shown in Table 2 were performed in two and three dimensions. They indicate the following temporal sequence of laser-plasma target interactions:

1. The laser enters the neutral gas target and strips the electrons from H_2 yielding a fully ionized column of H^+ and e^- in less than 10^{-15}s (1 fs). This process extracts about 10 μJ from the incident pulse.
2. The laser field forms a beam localized in a single plasma channel that penetrates the target. The situation resembles a laser guided by a plasma waveguide formed by the ponderomotive force that expels the plasma radially.
3. The laser energy is depleted as it propagates through the channel and is deposited on the ambient electrons creating a hot multi-MeV electron gas over a length scale equal to the laser absorption length L_H that depends on the laser and plasma parameters.
4. The sharp density and temperature gradients created by the laser energy deposition in the channel boundaries create strong quasi-static magnetic and longitudinal electric fields at the boundaries of the channel and of the target.
5. The expansion of the electron cloud and the differential motion of electrons and ions in the electromagnetic fields in the plasma-vacuum interface at the end of the target create strong space charge electric fields transferring the electron energy to the protons.

Our primary challenge is optimizing energy transfer from the laser to a collimated proton flux whose energies exceed 5 MeV. Before addressing the solution to these challenges, we present briefly the results of a simulation run for parameters typical of the microPET project.

Physics of energy transfer to multi-MeV protons

A 2D PIC simulation code explores the interaction of a linearly polarized laser (E_y, B_z) laser with Gaussian radial intensity profile impinging on a plasma target with a super-Gaussian density distribution, the parameters for this run, labeled R19, are listed in Table 1 below. Fig.1 shows the layout for the simulation including the plasma density and laser magnetic fields .12 ps into the pulse. The laser is injected from the left boundary and propagates in free-space till it enters the gas target located at 40 μm at time t=.12 psec.

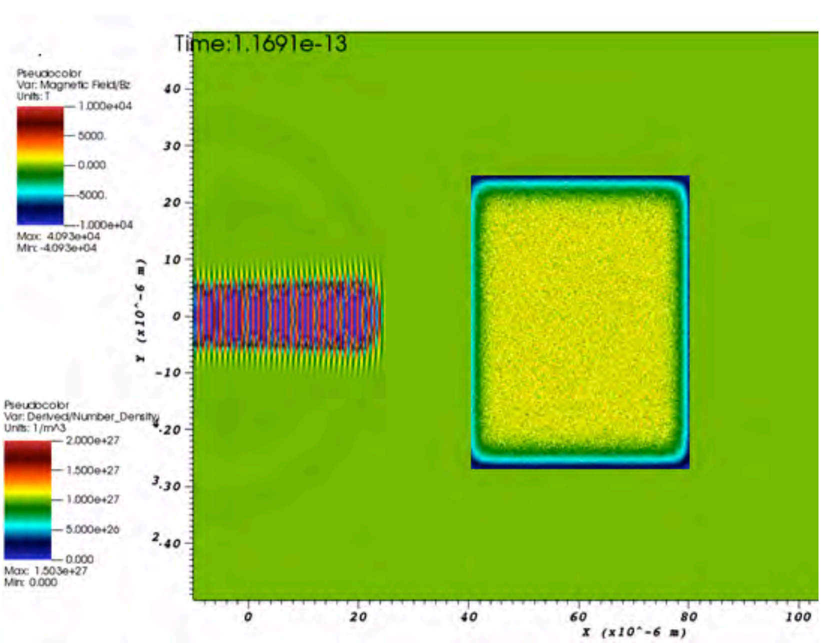

Figure 1: Simulation set-up. The laser pulse with Gaussian spatial and temporal profiles is introduced at the left boundary. The pulse propagates through free-space and enters the target at x=40 μm at t= .13 ps.

Table 1

Laser wavelength μm	1
Laser pulse length fs	300
Laser Peak intensity 10^{19} W/cm^2	2
Laser focal spot σ μm	2.97
Laser Energy per pulse J	1.44
Laser linear pulse energy J/μm	.314
a	3.82
Peak plasma density 10^{21} #/cm^3	1.11
n/n_c	1
Target profile	$e^{-(\frac{x-60}{20})^6} \times e^{-(\frac{y}{25})^6}$

Fig. 2 shows a time series of the evolving plasma density. The ponderomotive force of the laser pushes the plasma laterally and forms a plasma channel whose structure is maintained up to the end of the plasma target. Upon entering the target the laser pulse self-focuses (Fig. 2a) at t=.3 ps and the plasma waveguide guides the laser and the hot electrons towards the end of the plasma target. The plasma waveguide achieves its minimum width near the focal point, located close to x=52μm, and maintains its integrity to the end of the plasma target until at least. 9 ps after the laser pulse has exited the target. (Figs 2b-d). This is critical to achieving efficient proton acceleration. The plasma channel guides the laser pulse and the hot electrons towards the front of the target where the proton acceleration takes place.

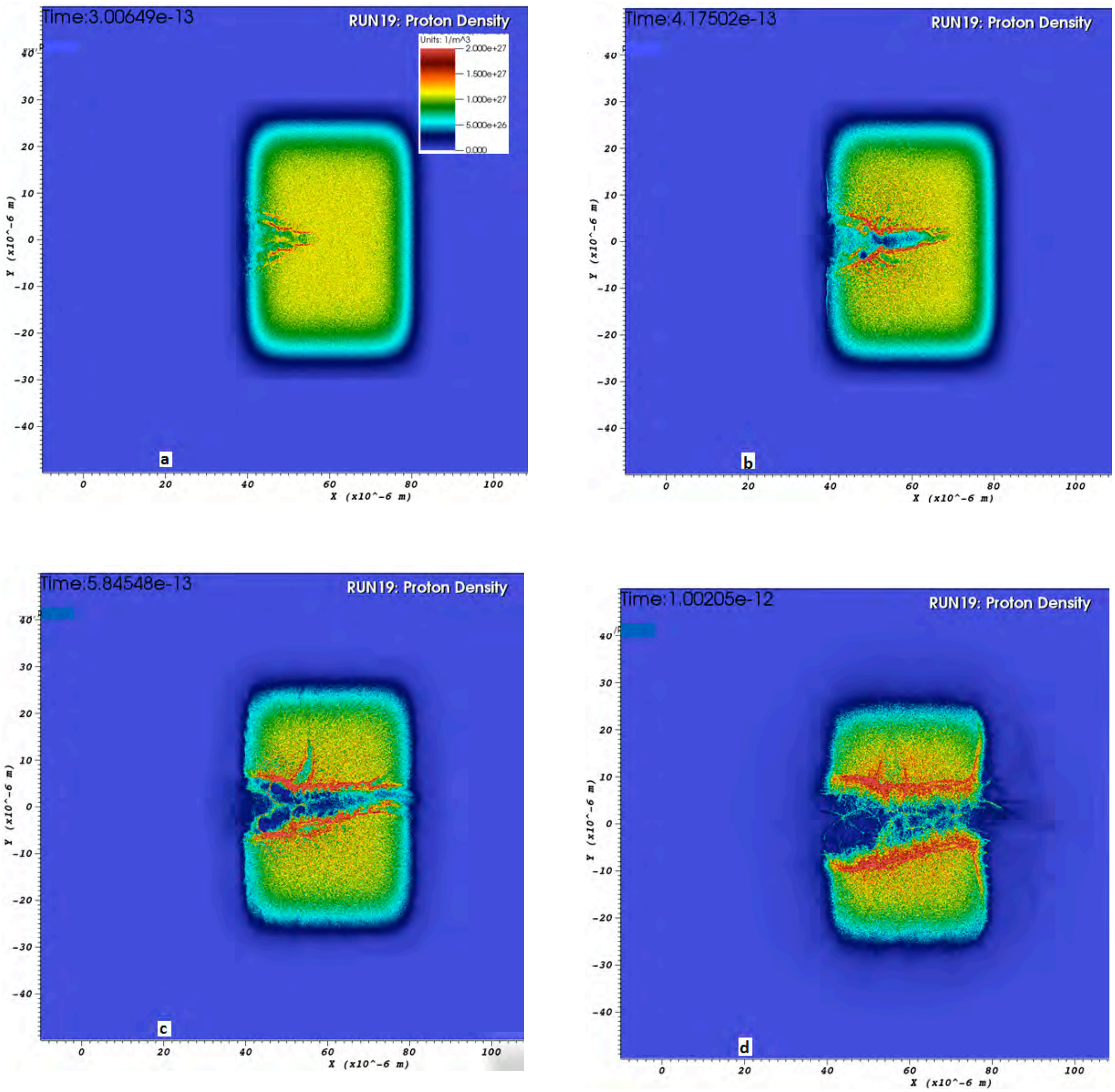

Figure 2: Temporal evolution of the plasma density in two-dimensions showing the formation of a plasma channel. Notice that the channel has a minimum size close to x=52 μm at t=.30 ps corresponding to the focal point of the laser. The memory of the focusing can be seen in Fig. 2b at t= .42 ps. The ponderomotive force of the laser results in a plasma channel that maintains its integrity throughout the simulation allowing the laser to propagate and deposit its energy to the electrons close to the target front.

The plasma density associated with the "walls" of the channel can be assessed from the images in figure 3. These show line plots of the plasma density as a function of y at t=.4 and 1 ps and at x= 45 and 75 μm. The "walls" of the waveguide have density more than three times the ambient plasma density, thereby acting as excellent guides.

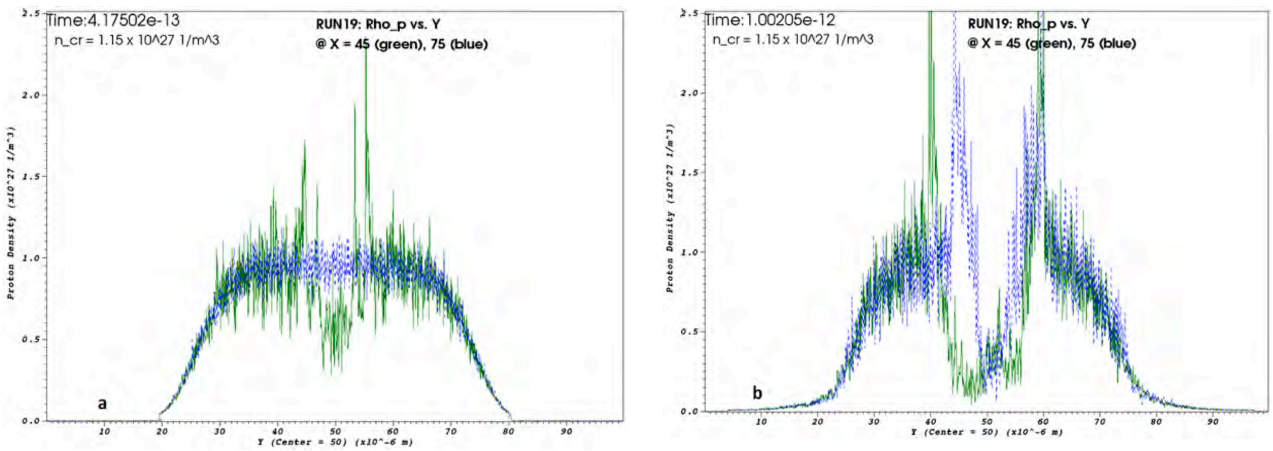

Figure 3: Line plots of the plasma density as a function of y at times t=.42 ps (a) and t=1 ps (b) at x=45 μm (green) and x=75 μm (blue). The figures indicate that plasma channel narrows with length and that the density of the channel walls reaches values of three times the critical density.

Figure 4 has line plots of the laser electric field amplitude E_y and the electrostatic field E_x generated by the laser-plasma interaction, as a function of x along the channel center y=0. Consistent with Fig. 2a, Fig. 4a shows the laser focusing at x= 52μm, before reaching the peak plasma density. The interaction of the laser with the plasma generates electrostatic fields with scale length of a few μm and amplitude of few MV/μm. The E_x fields have alternating positive and negative polarity inside the plasma target but positive polarity only near the outer target boundary. As seen in Fig. 4b charge separation potentials of 10-20 MeV are created between x=80-100 μm and maintained even after t=.6 ps when the laser energy is depleted.

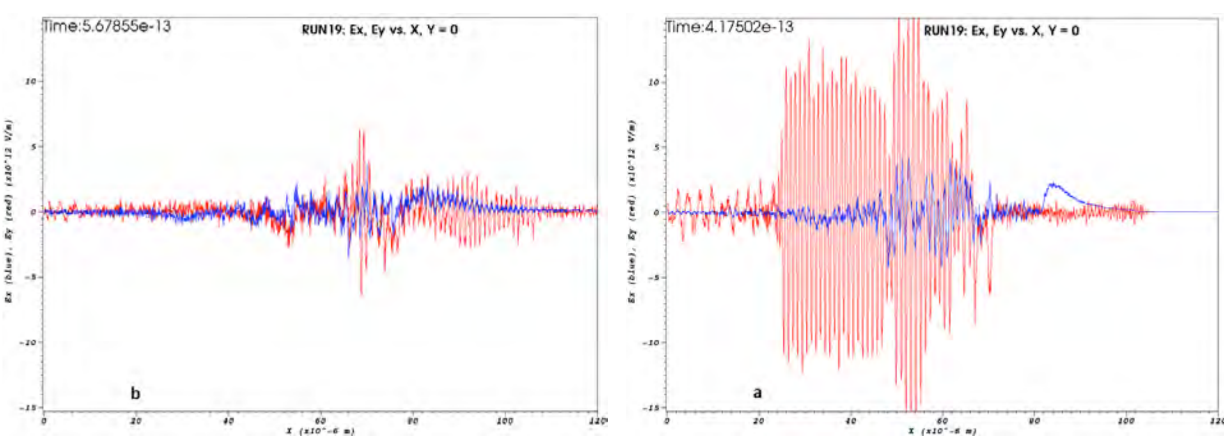

Figure 4: Line plots along of the laser field E_y (red line) and the electrostatic field E_x (blue line) at times t=.42 ps (a) and t=.57 ps (b). Spike-like E_x fields with alternating polarity and amplitude MV/μm are generated behind the laser front. These fields are responsible for electron heating and dissipation of the laser power. Starting at t=.42 ps an electrostatic field along the x-direction develops between 80-90 μm. In

addition to accelerating protons this field leads to reflection of hot electrons towards the negative x-direction. Large potential is maintained after the laser energy is depleted at t=.57 ps.

Complementary to the results described in Figs. 4 is the two-dimensional temporal evolution of the quasi-static electric field E_x shown in Figs. 5. The dominant components of the quasi-static electric field are located near the front and rear boundary of the target and appear as the front of the laser pulse reaches the front side of the target (Fig. 5a). This is consistent with the previous discussion of Fig. 4a. The electric field amplitude reaches peak values of 2.5 MV/μm on the front, 1 MV/μm on the rear side, and maintains significant amplitude up to .6 ps.

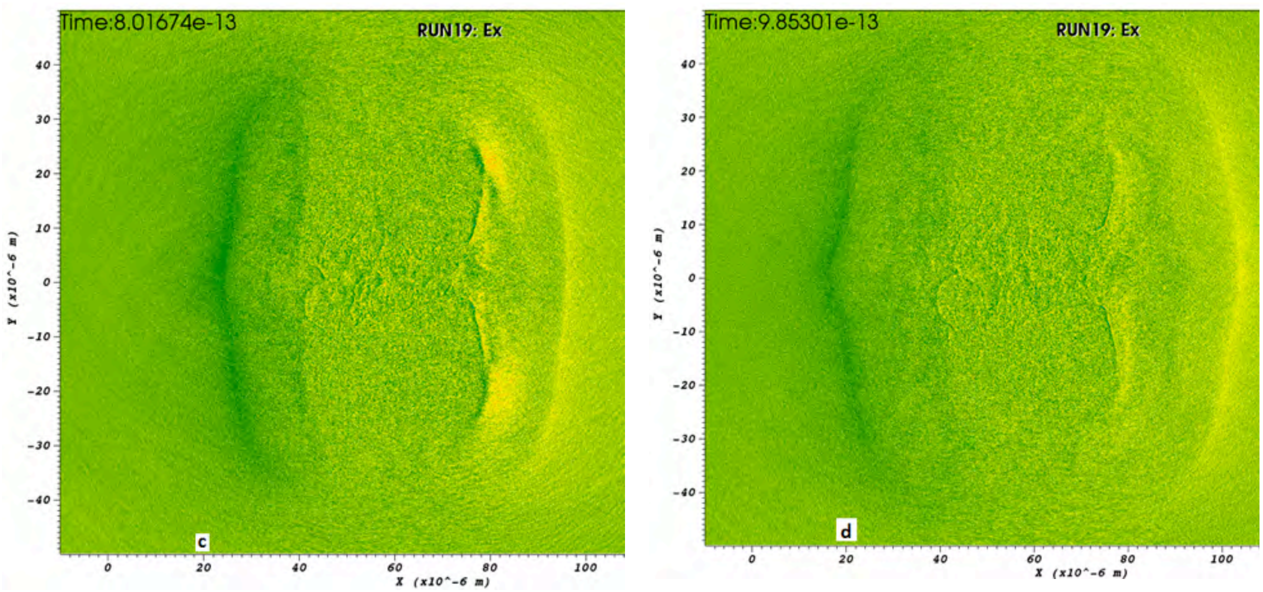

Figure 5: Temporal evolution of the quasi-static electric field (E_x) in two-dimensions. Notice that that they have planar structure and the dominant components are located near the front and the back of the target.

An important new aspect of the interaction is the appearance of quasi-static magnetic fields in the z-direction shown in Figs. 6. The quasi-static magnetic fields also appear simultaneously with the quasi-static electric field shown in Fig. 5a. By the time the laser pulse energy has been depleted they fill the channel and have strengths more than $5x10^3$ T (Figs. 6a-b). Now the laser contains approximately 15% of its initial energy, while quasi-static magnetic fields with opposite polarity across the y=0 line of the x-y plane near the channel entry at x=40-45 μm have been spontaneously generated. The quasi-static magnetic fields remain strong until the end of the run. The presence of quasi-static fields is very important in confining the heated electrons inside the plasma channel and controlling their energy transport near the front boundary. They are the controlling agent of the proton acceleration.

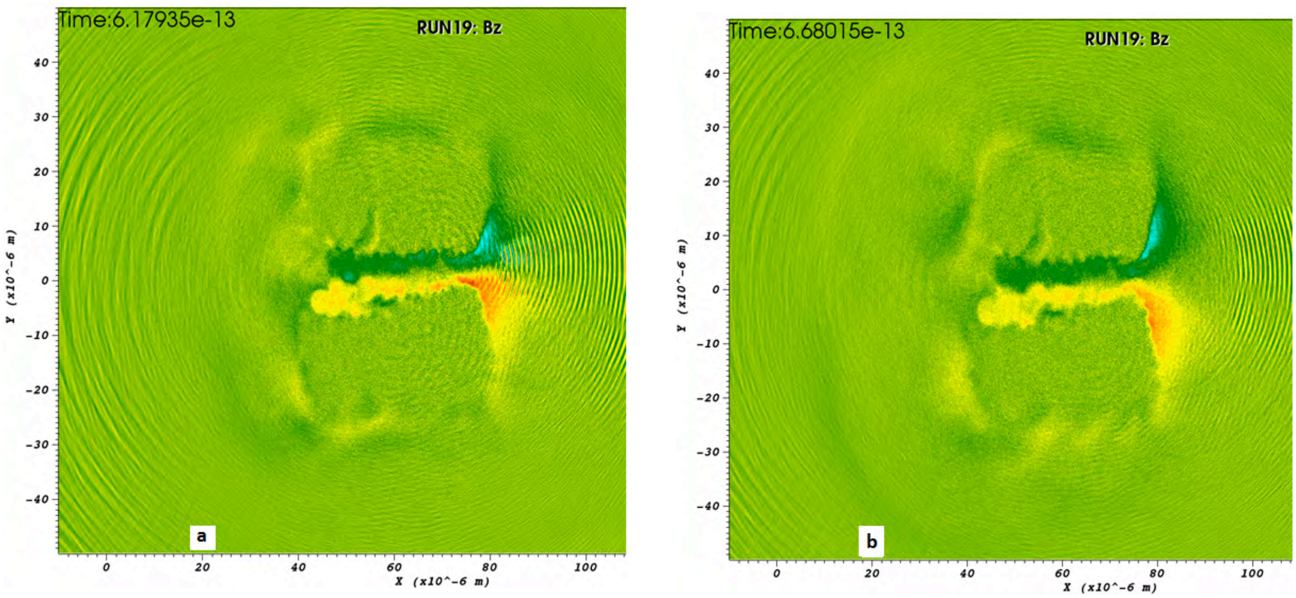

Figure 6: Quasi-static magnetic field in the z-direction following the depletion of the laser pulse energy. Notice that the fields persist to the end of the run.

Before discussing energy transfer to electrons and protons it is instructive to refer to Fig. 7 that shows the temporal evolution of energy partitioned among electromagnetic fields, electrons, and protons. It illustrates the time scales of significant changes in the interactions. At t=.60 ps the energy of the hot electrons reaches its maximum value of approximately 80% of the laser energy. The energy in quasi-static and electromagnetic fields energy is approximately 14%, with the remaining in 6 % in protons. Energy transfer from the energetic electrons to multi-MeV protons subsequently dominates the interaction, while the quasi-static fields control the extent of hot electron transport and induced charge separation.

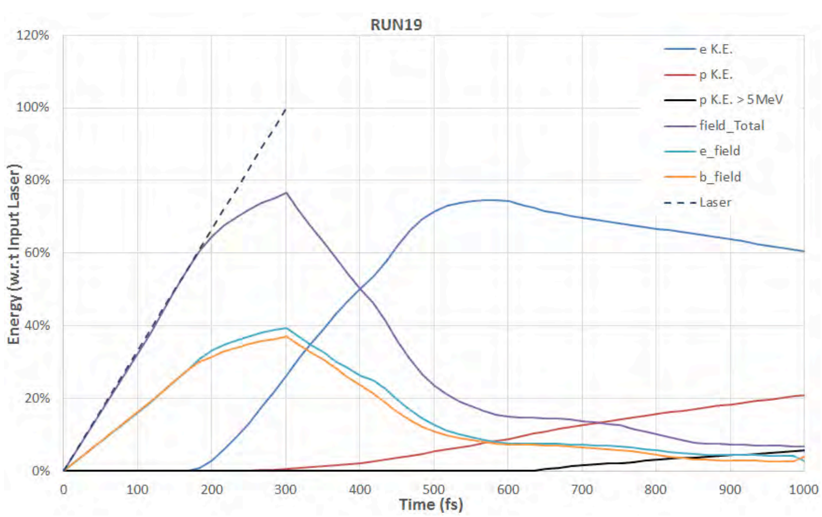

Figure 7: Temporal evolution of energy in key plasma and electromagnetic field components. Notice that energy transfer from the laser to relativistic electron heating is the dominant interaction till t=.6 ps, while energy transfer from relativistic electrons to protons in general and to protons with energy larger than 5 MeV at times t>.6 ps

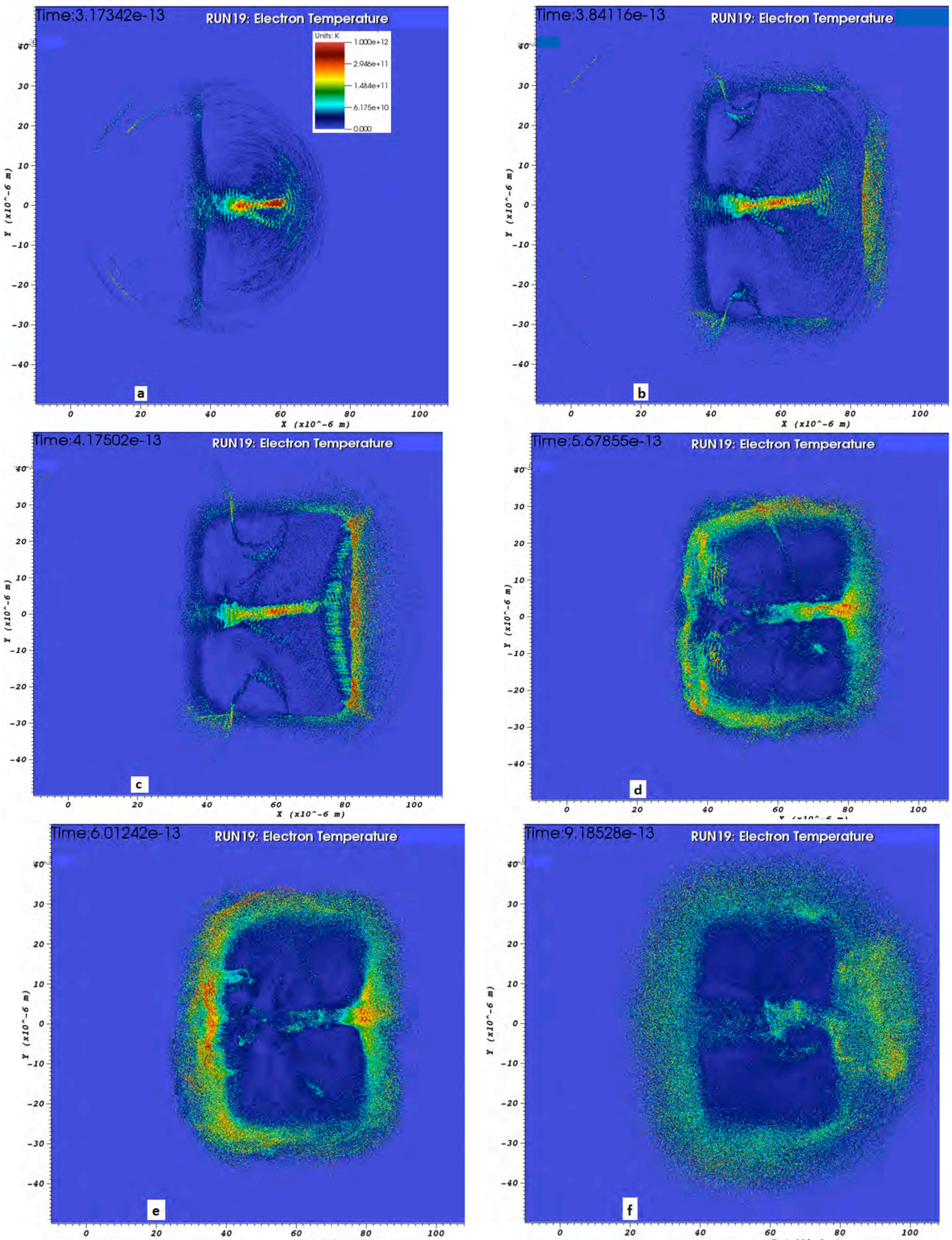

Figure 8: Figures a-d describe the dynamics and spatial distribution of hot electrons during the energy transfer from the laser to relativistic electrons. Figures e and f show the expansion of the multi-MeV electrons at the front of the target that controls the energy transfer from relativistic electrons to multi-MeV protons

Snapshots of spatial distributions of the electron energy are shown in Figs. 8. Fig. 8a shows electrons heated to several MeV by the laser pulse at t = .32 ps expanding about the focal point. Fig. 8b shows hot electrons close to the plasma target front. These electrons were heated by the laser pulse near the exit of the plasma channel, expanded laterally to occupy the width of plasma target, and subsequently stream backwards (Fig. 8c). The hot electron expansion and associated current are the cause of the strong planar quasi-static electric and magnetic fields shown in Figs 5 and 6. Starting at t =.56 ps the hot electrons are confined at the intersection of the plasma channel and outer plasma target boundary (Figs. 8d-f). Fig. 7 shows that t =.6 ps coincides with the start of significant proton acceleration. The electron heating by the laser at 400 fs is evident by the strong depletion of the laser energy shown in Fig. 7 (green line) between .3 and .6 ps. As seen in Figs. 8e,f the hot electrons are concentrated in the plasma waveguide and the target boundaries. Their expansion is the dominant process that controls proton acceleration.

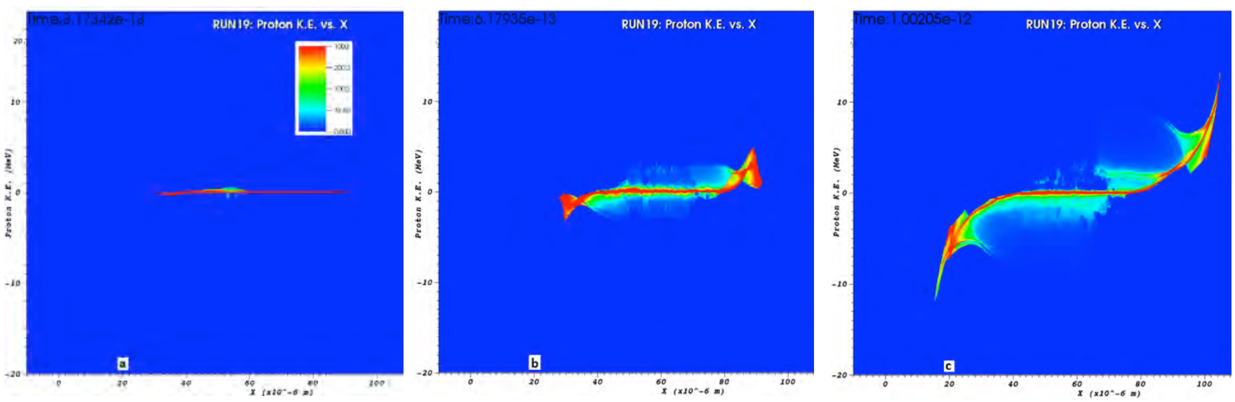

Figure 9: *Proton phase space in the x-direction at: (a) t=.38 ps indicating acceleration only at the rear of the target; (b) t=.61 ps when proton acceleration at the rear and front side are approximately equal; (c) t=1 ps showing that the acceleration at the front of the target dominates after t=.6 ps.*

The final set of simulations addresses the efficiency, dynamics, angular distribution and brightness of the MeV protons. Referring to the line that represents the normalized proton energy content in Fig.7 proton acceleration starts at t=.38 ps, its fraction of system energy increases linearly with time and at the end of the run at t=1 ps comprises 24% of the energy in the laser pulse. Acceleration of the forward moving protons with energy larger than 5 MeV (needed to create ^{11}C from ^{14}N) starts at .6 ps and saturates at .95 ps. Fig.9 shows the proton phase space in the x-direction for times .38 ps, .61 ps and 1 ps. Notice that the up to t=.58 ps the rear target acceleration dominates and creates a backward streaming proton flux. The acceleration at the front of the target dominates after t=.6 ps with maximum energy at the front reaching 14 MeV, while the energy at the back remains below 10 MeV.

Fig. 10 plots the proton energy distribution averaged over the entire space as a function of time. For times shorter than .6 ps the fields responsible for the proton acceleration are seen in Figs 5a,b with energetic protons accelerated mostly in the backward direction. At later times, especially after t=.8 ps, the protons are accelerated by the expansion of the hot relativistic electron front near x=80 μm as seen in Figs 8e,f and the corresponding E_x field seen in Figs 5c,d.

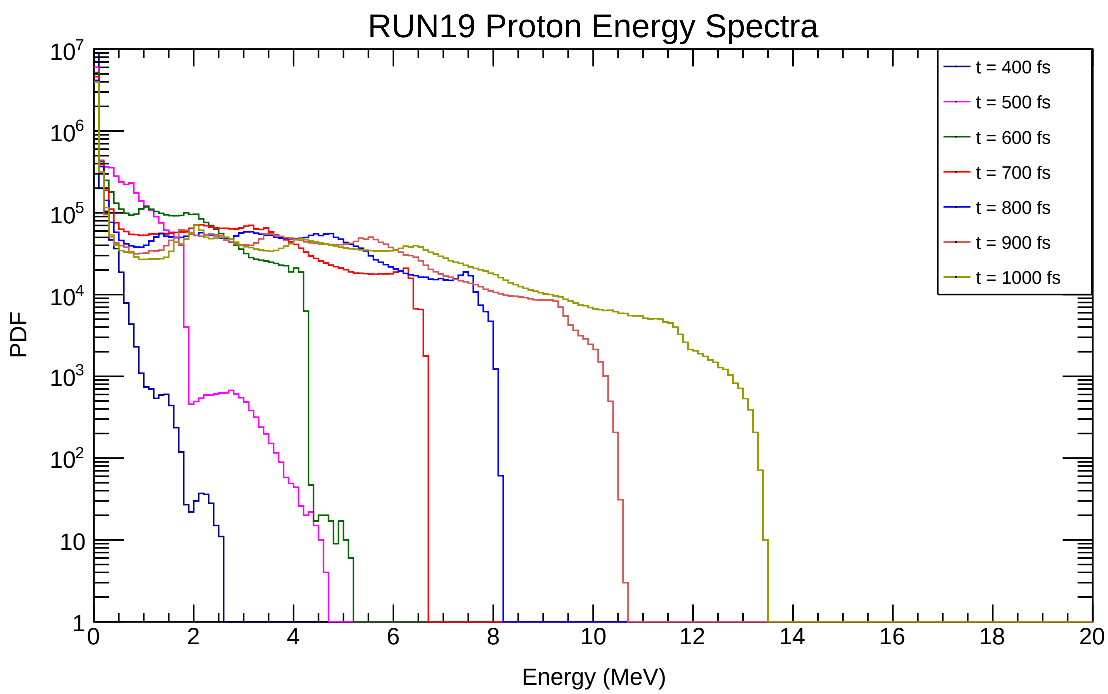

Figure 10: Temporal evolution of the proton energy distribution averaged over the simulation space.

Figure 11 displays two-dimensional proton density for protons with energy above 5 MeV and divergence angle below 20°. This is important for comparison with CR39 experimental design and measurements, as well as for choosing parameters for the secondary precursor target. The spatial distribution of the proton beam resembles that expected from a planar diode with lateral dimensions close to the lateral dimensions of the plasma target.

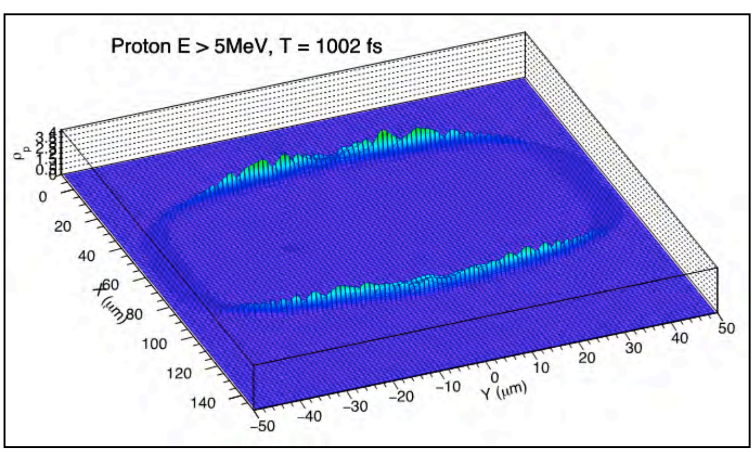

Figure 11: Proton density for E> 5 MeV and divergence angle smaller than 20°

MicroPET Optimization Study:

A major difference of the MicroPET proton acceleration scheme and most past laser proton acceleration studies is the use of a gaseous rather than solid primary target with controlled density profile parameters described in Milestone report #2. In the theoretical/computational studies for plasma optimization we modeled the primary target as plasma characterized by Gaussian or super-Gaussian distributions in the incident laser plane given by:

$$n(x,y) = \zeta n_c Exp[-(\frac{x-x_o}{L})^{\gamma}]Exp[-(y/\varepsilon L)^{\delta}]\,. \qquad (1)$$

In Eq. (1) n_c is the critical density, $.5<\zeta<2$, a parameter characterizing the ratio of the peak density to the critical density, ε is the ratio of the transverse to longitudinal size of the target, and γ and δ are the gradient lengths of the target with zero representing a Gaussian target. In all runs the value of L=20 μm. The laser was modeled with a Gaussian intensity profile with focal spot size σ at the entry of the target and parameters of RUN19 discussed in the previous section (Table 1). All lengths are in μm. The objective of the simulations was to study the impact on proton acceleration efficiency of varying the parameters of the primary target given by Eq. (1) by comparing the results with those of the benchmark simulation described in Section I. We focused on three attributes: Density gradients (γ, δ), Peak density to critical density ratio (ζ), and Aspect ratio (ε).

Table 2 Selected Parameters for PIC simulations

RUN ID	Plasma Target Parameters	proton K.E. > 5MeV	
		forward+/-20 °	K.E./Laser
RUN09	ζ=1, γ=δ=14, ε=1.25	1.29E+11	5.48%
RUN12	ζ=.75, γ=δ=14, ε=1.25	1.42E+11	8.01%
RUN15	ζ=1, γ=δ=6, ε=1	6.26E+09	1.46%
RUN18	ζ=1, γ=δ=0, ε=1.25	2.29E+10	2.49%
RUN19	ζ=1, γ=δ=6, ε=1.25	1.35E+11	5.64%
RUN20	ζ=.75, γ=δ=6, ε=1.25	1.44E+11	8.04%

Over 20 simulations with varied laser pulse and plasma target parameters were performed. Representative results that optimize the efficiency and support the key experimental diagnostics are presented here. Table 2 lists the parameters of the plasma target, the number of protons with energy higher than 5 MeV at the front exit of the target, and the fraction of the laser pulse energy transferred to kinetic energy of protons with energy larger than 5 MeV. Notice that RUN09 and RUN12 represent a plasma target with almost discontinuous front and back density profiles, in other words at the limit of infinite large density gradients. RUN19 and RUN20 are like Run09 and RUN12 except that they represent super-Gaussian density distribution with $\gamma=\delta=6$.This represents density gradients already achieved in the experiment and described milestone report 2. Referring to table 2 we note that gradients beyond $\gamma=\delta=6$ do not improve the efficiency. On the other hand, super-Gaussian (RUN19) is significantly more efficient than simple Gaussian (RUN18). Two other noteworthy facts appear in table 2. (i) Mildly subcritical targets (RUN12 and RUN20) are more efficient than critical density targets; and (ii) cylindrical targets ($\varepsilon=1$) are extremely inefficient (RUN15). We present below a comparative study of the key physics differences among the selected simulations runs that guide our planning of the experiments and the selection of the required diagnostic instrumentation.

The role of plasma density gradients

Figs 12-13 show comparison of the proton acceleration between R19 and R18. In addition to more energetic proton distribution for R19 conditions shown in Figs 12b, the proton phase space in the x-direction (Fig.13a) shows the front acceleration for R18 occurs between x=100-120 μm and between x=10-25 in the backward direction, causing significantly weaker fluxes.

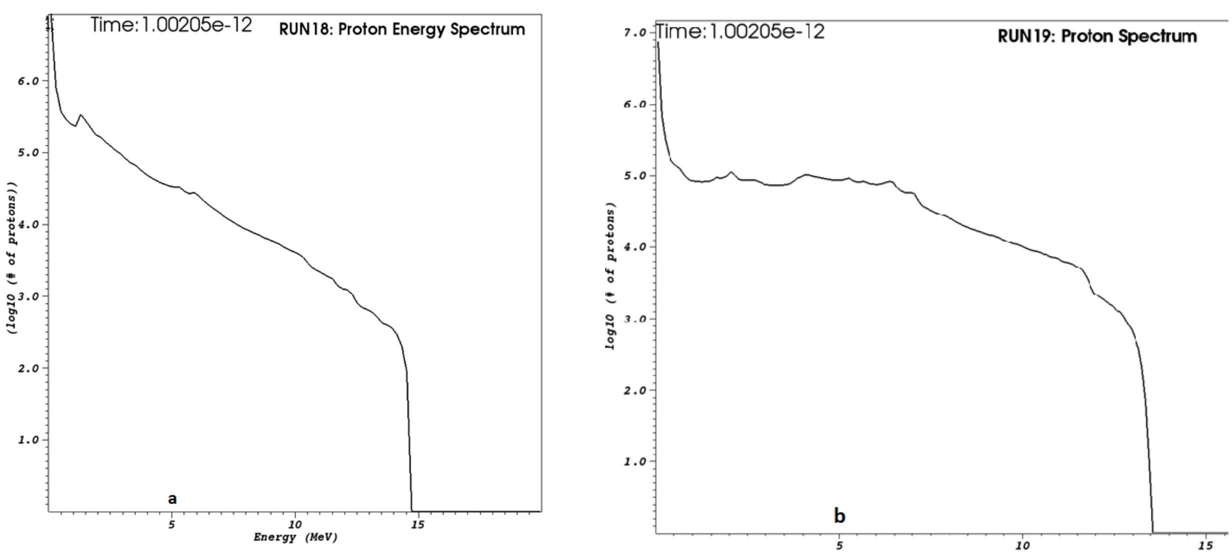

Figure 12: Proton energy distribution function averaged over the simulation volume for: (a) R18; (b) R19.

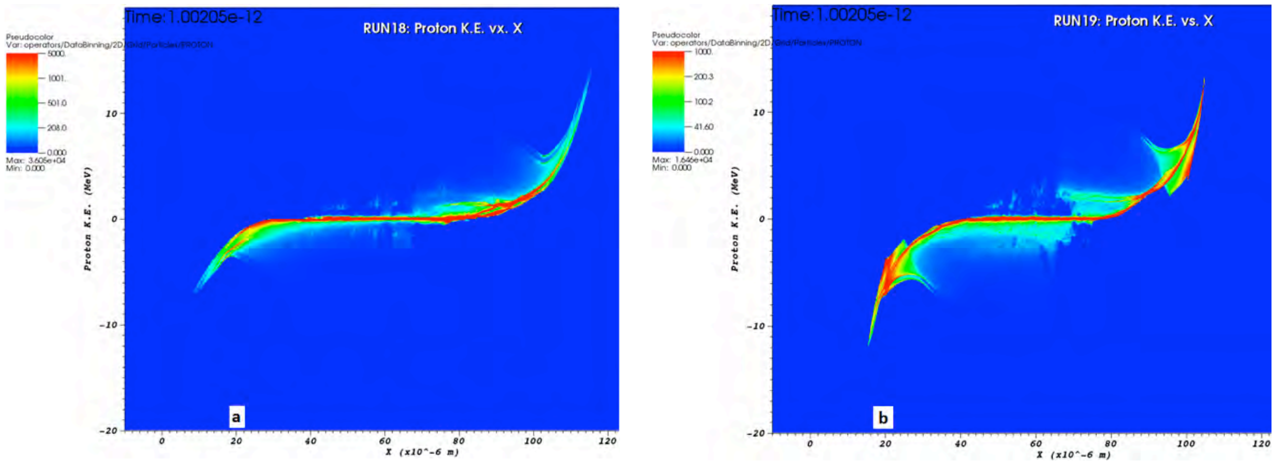

Figure 13: Phase space distributions for (a) R18 and (b) R19.

Figure 14 compares the electron temperature distributions between R19 and R18 during proton acceleration. The greater efficiency of the proton acceleration for R19 is due to both the location of the expanding hot electron cloud close to the front of plasma target and its significantly higher temperature. For comparison with experiment, the distribution of the total number of protons with energy above 3 MeV in Fig. 15 shows two locations with higher proton flux that correspond precisely to the location of the hot electrons seen in Fig.14a.

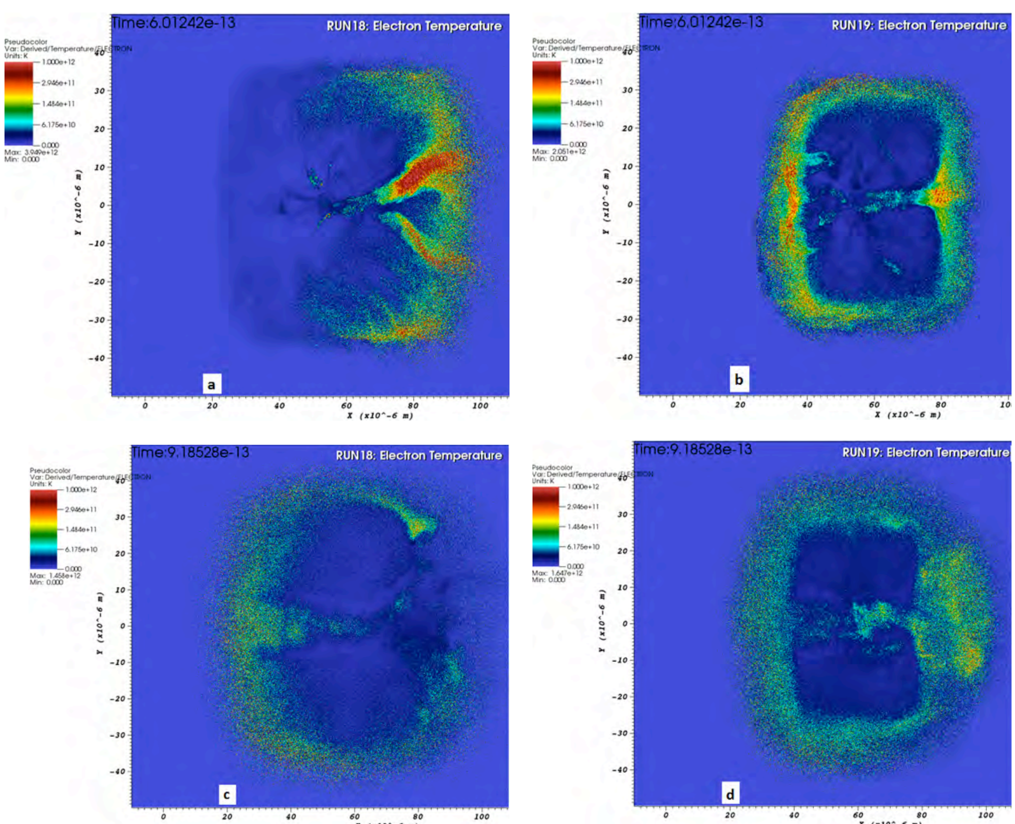

Figure 14: Hot electron temperature distribution in two dimensions for R18 and R19 at: (a) t= .6 ps; (b) t= .92 ps. Notice that at t=.6 ps, that marks the beginning of the forward proton acceleration, there are two hot electron spots surrounded by relatively low temperature electrons and the hot electrons have lost their energy by t=.92 ps. On the other hand, high electron temperatures are sustained in R19 driving the strong proton acceleration observed in Fig. 13b

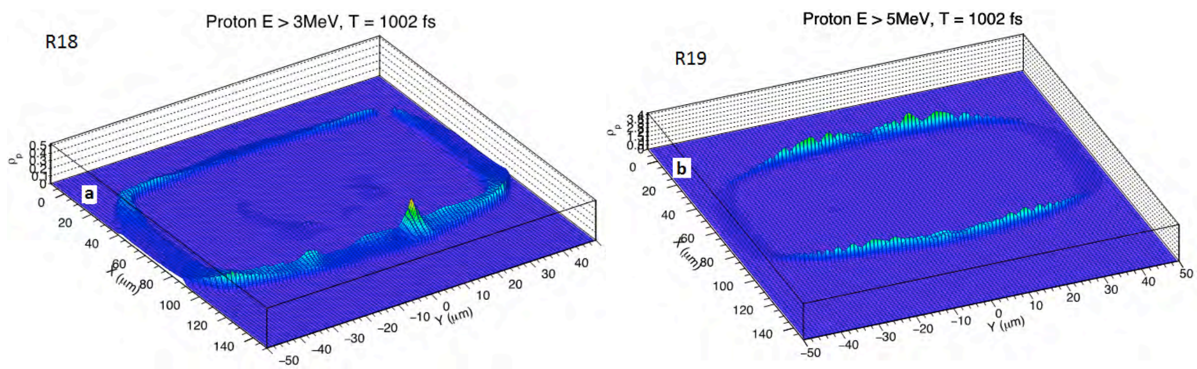

Figure 15: Two-dimensional proton density at t=1 ps for: (a) E>3 MeV protons in R18; (b) E>5 MeV protons in R19. Notice the hot spots in the R18 simulations corresponding to the location of hot electron temperature spots in Fig. 14a.

Fig. 16 shows the laser propagation channeling and the plasma channels for R18 where inefficient acceleration leads to the strong filamentation that is associated with the early time laser focusing.

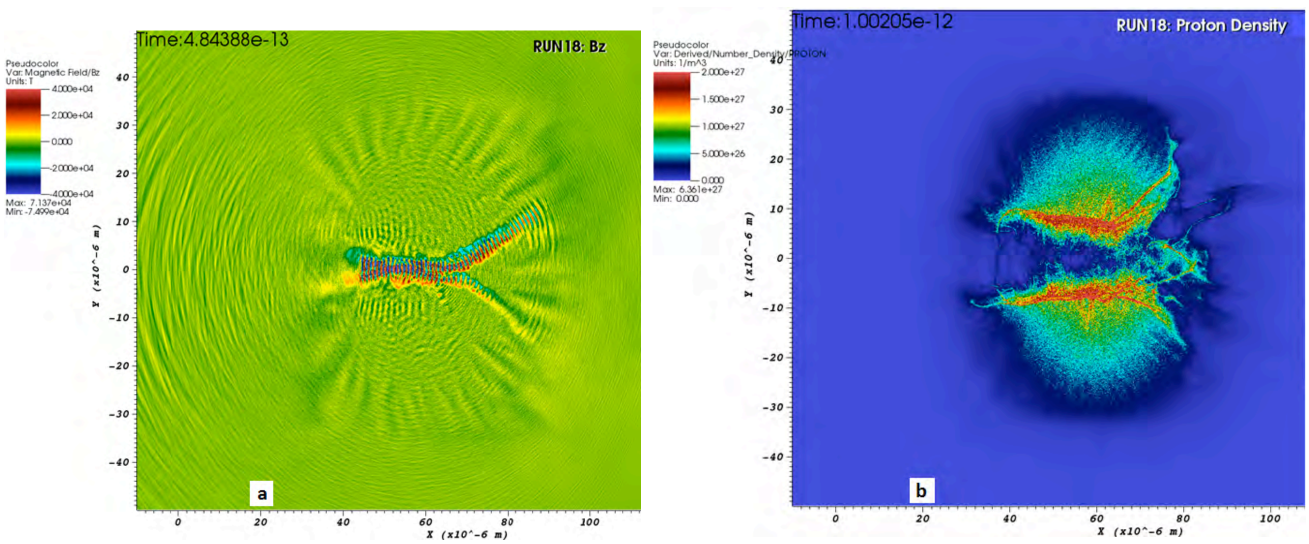

Figure 16: Consequences of filamentation resulting in poor matching of the laser to the plasma waveguide seen in: (a) laser guidance in filamentary channels; (b) formation of unmatched plasma channel as compared to Fig. 2 describing R19.

Effect of peak density to critical density ratio:

To study the effect of varying the parameter ζ we repeated the simulation discussed in Section 2 with all the parameters of R19 except for the ratio of peak to critical density. Run19 had a value of ζ=1, while R20 had ζ=.75. Fig 17 compares the temporal evolution of the proton distribution function averaged over the simulation volume. Notice that the acceleration efficiency of R20 start dominating after t=.6 ps and coincides with forward proton acceleration. This is confirmed by the details of the temporal evolution of the x-direction proton phase space (not shown here).

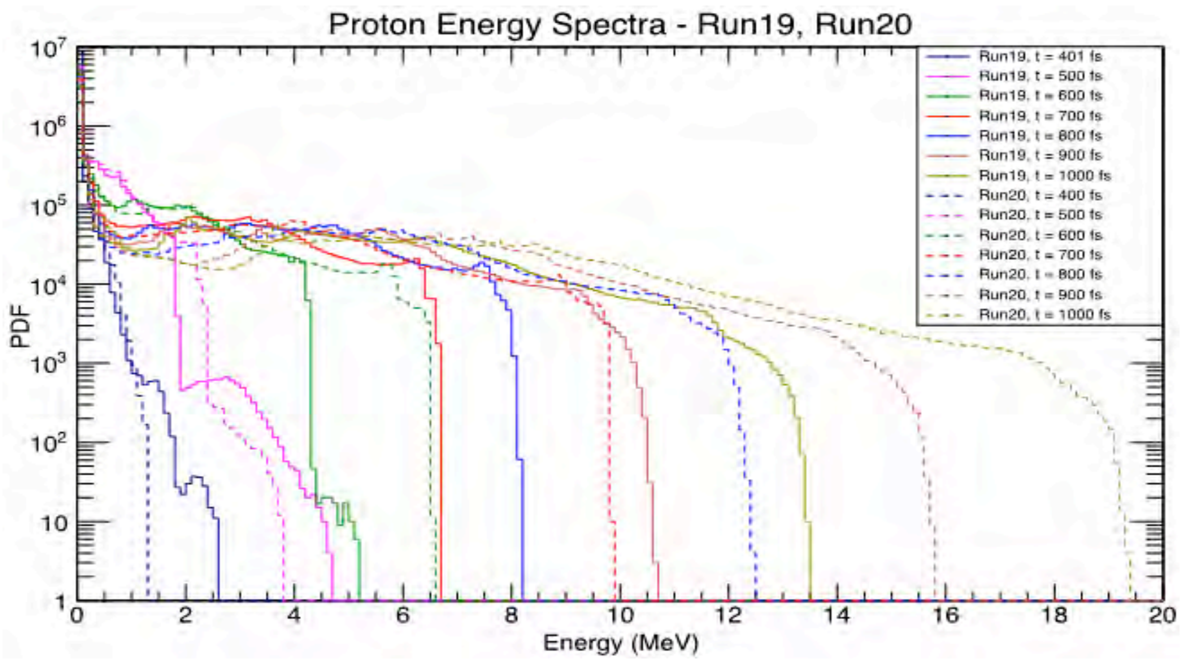

Figure 17: Temporal evolution of proton energy distribution function averaged over the simulation volume for R19 and R20 simulation runs indicating the greater efficiency of the subcritical R20 simulation parameters.

Figures 18 and 19 compare the proton phase space in the x-direction and the total number of

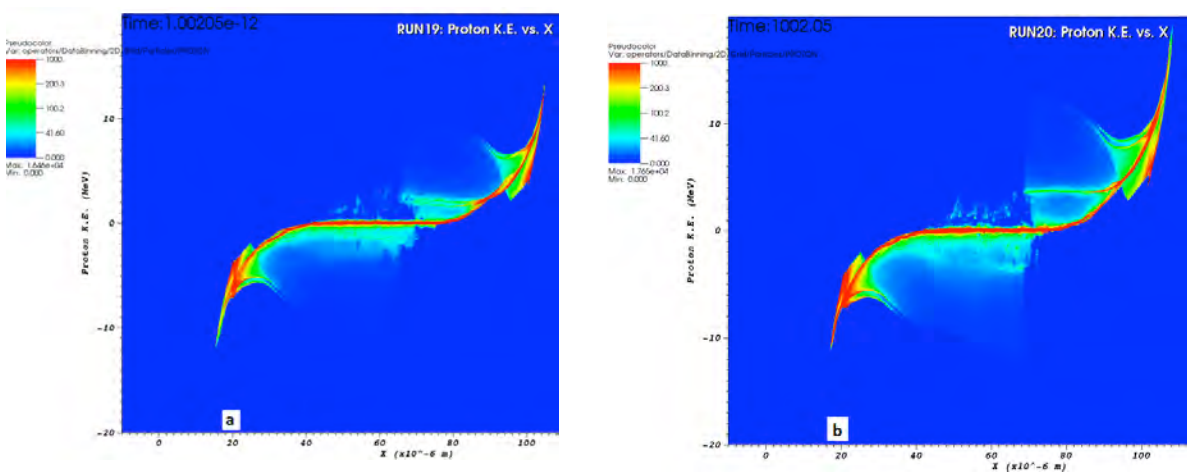

Figure 18: Proton phase space in the x-direction at t=1 ps for (a) R19; (b) R20. The predominance of forward acceleration related to the target front is apparent.

protons with energy larger than 5 MeV measured at each side of the plasma target for R19 and R20 at the end of the simulation. The higher efficiency of the proton acceleration for the under dense target R20, especially for forward directed protons is apparent.

The physics responsible for the difference in efficiency in the two cases can be traced back to:

(i) The fact that the focal point of the laser in the plasma is more than 10 μm deeper in the under dense plasma target used in R20. This is seen in Fig. 20 that compares the location of the focal point between the two simulation runs.

(ii) The group velocity of the laser pulse in the plasma is faster for the under dense plasma

(iii)

(iv)target allowing the laser pulse to penetrate deep into the target. This is seen in Fig.21 that shows that at t =.42 ps the laser has penetrated to the front of the plasma target for R20, while it is still close to the middle of the target for R19.

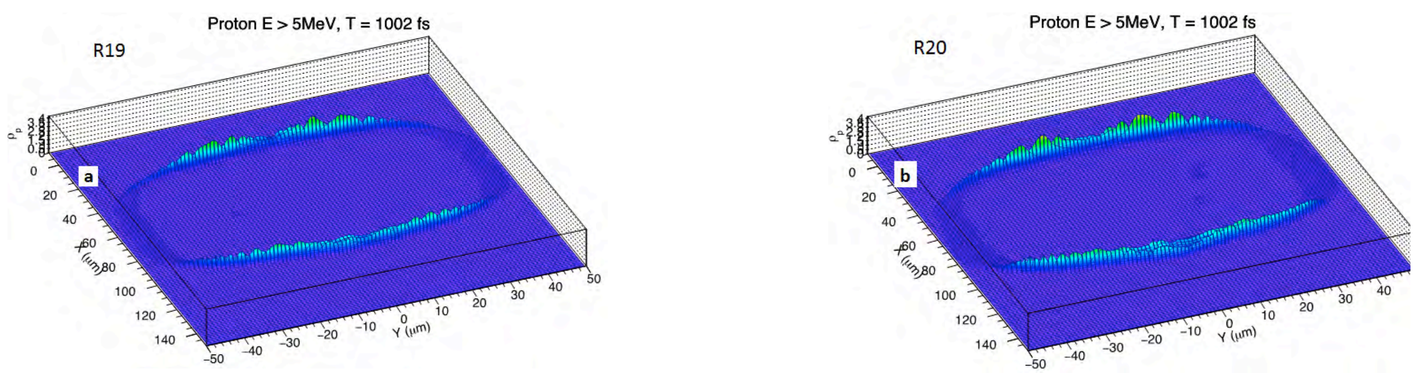

Figure 19: Two-dimensional proton density for E> 5 MeV at t=1 ps for: (a) R19; (b) R20.

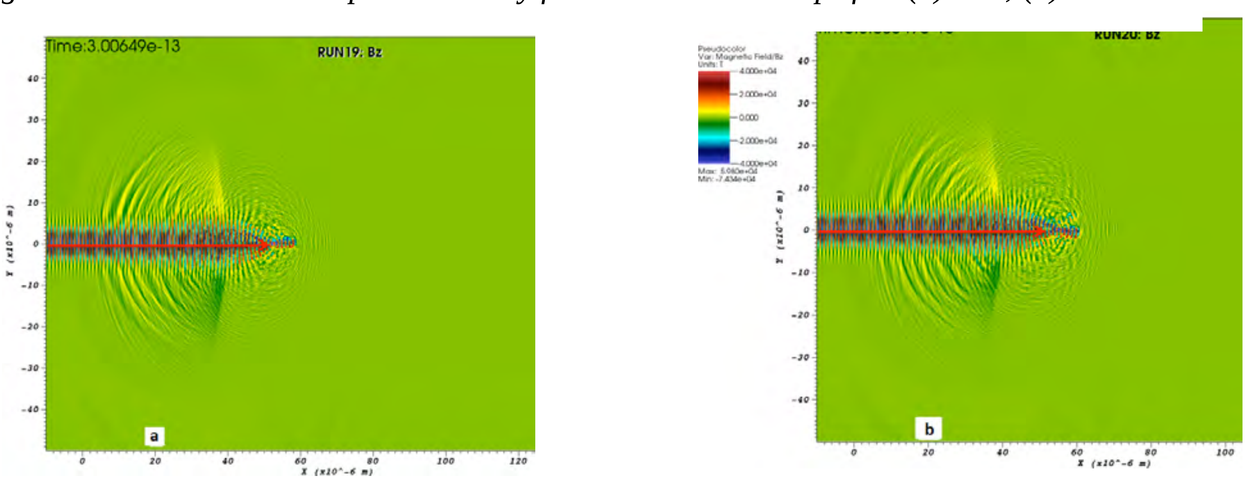

Figure 20: Spatial structure of laser pulse at time t=.3 ps for: (a) R19; (b) R20. It shows that the focal point (marked by the red arrow) for R19 occurs closer to the target entrance than for R20.

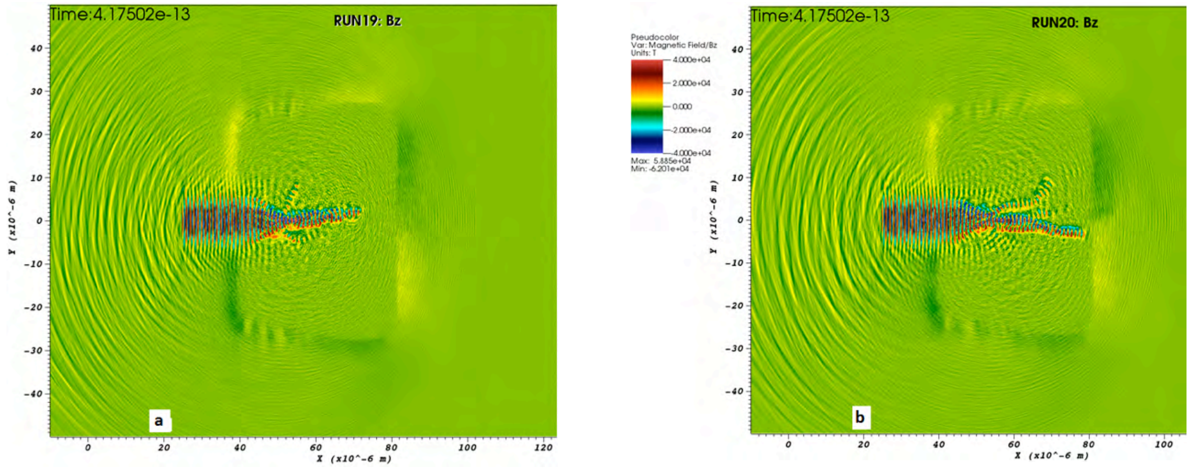

Figure 21: Spatial structure of laser pulse at time t=.42 ps for: (a) R19; (b) R20. It shows that the laser pulse has reached the vicinity of the target front for R20 while it is depleted just after the midpoint for R19. It is a consequence of the lower group velocity of the laser pulse for R19 and results in energy deposition further away from the front of the target than for R20.

The shifted location of the laser focus inside the plasma and of the group velocity of the laser pulse drive the efficiency of proton acceleration. The electron temperature and its lateral distribution at the plasma-vacuum interface associated with the front of the target also play important roles in the phase space of the resulting proton fluxes. It is this stage between 0.6 and 1 ps that maximum proton acceleration occurs. The temperature differences between the subcritical and the critical run in Fig.22 shows the spatial distribution of the electron temperature at the beginning of the strong proton acceleration phase at t=.6 ps and during the approach to maximum at t= .92 ps. The electron temperature and the temperature gradients are much stronger for R20 than R19. These factors result in efficient energy transfer from the hot electrons to protons during the expansion of the hot electron gas near the target front. The combined shifting of the laser focusing and the group velocity of the pulse resulted in depositing energy the of the laser power closer to the target front for the parameters of R20.

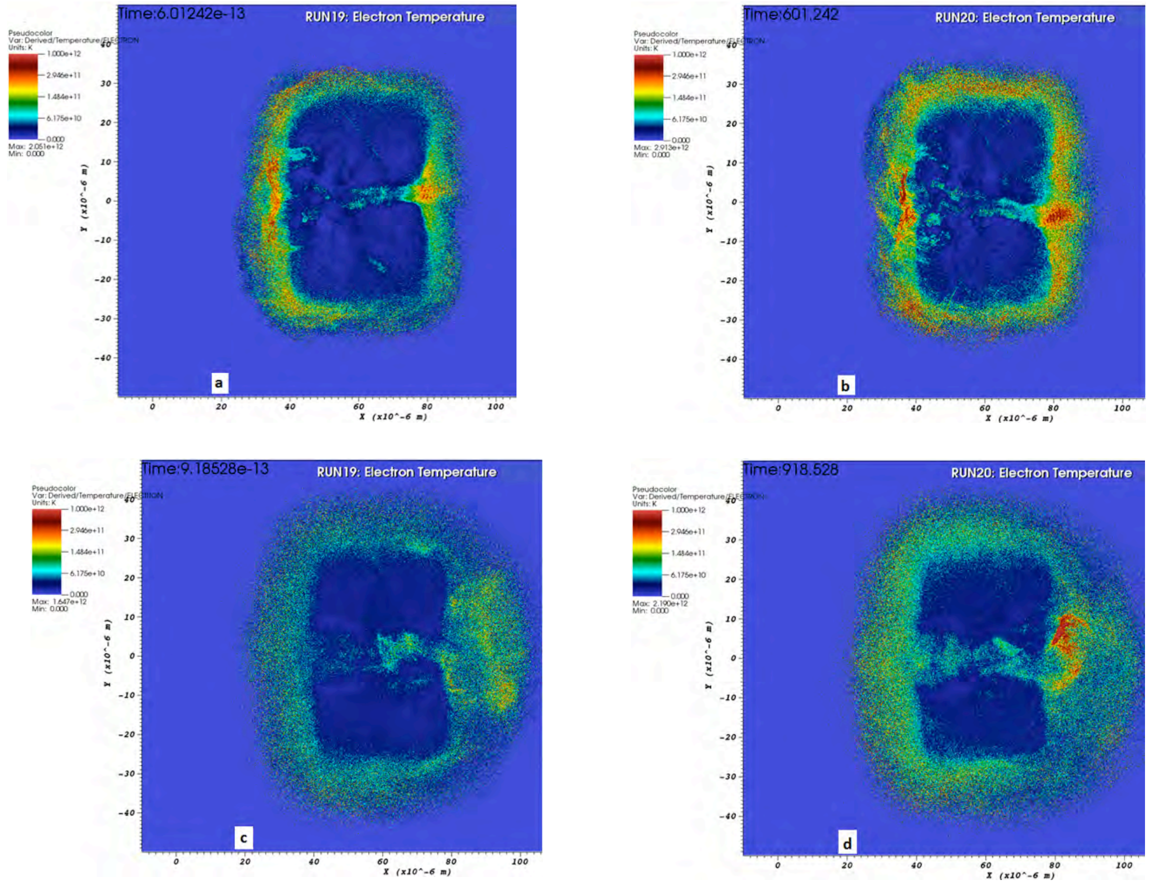

Figure 22: Spatial distribution of the hot electron temperature for R19 (a,c) and R20(b,d) at t=.6 ps and t=.92 ps. Notice that the higher electron temperature at the target front in the R20 simulation. Additionally, notice the confinement of hot electrons inside the plasma channel by the induced quasi-static magnetic fields.

Effect of aspect ratio:

The effect of aspect of ratio is resolved by comparing R19 and R15 where the value of $\varepsilon=1$ implies a target with cylindrical symmetry and a 20 μm radius of curvature. The other parameters were the same as in R19. The target is located at (x=0, y=0). Fig.23 show the volume averaged proton distribution function (Fig. 23a), the proton phase space (Fig. 23b) and the two-dimensional spatial distribution of protons (Fig. 23c).

The proton acceleration is significantly weaker compared to R19 and R20.

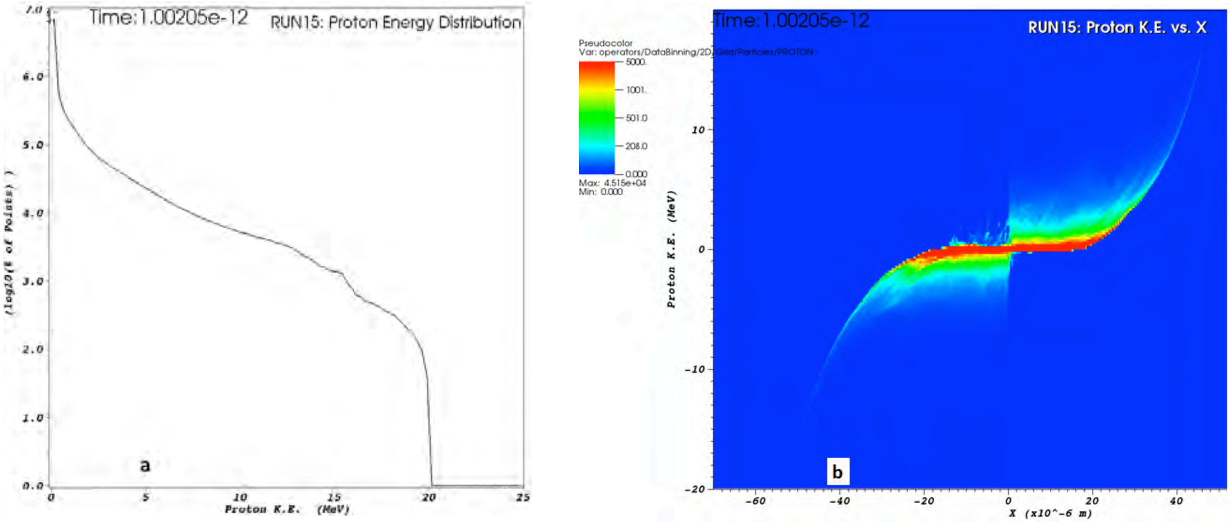

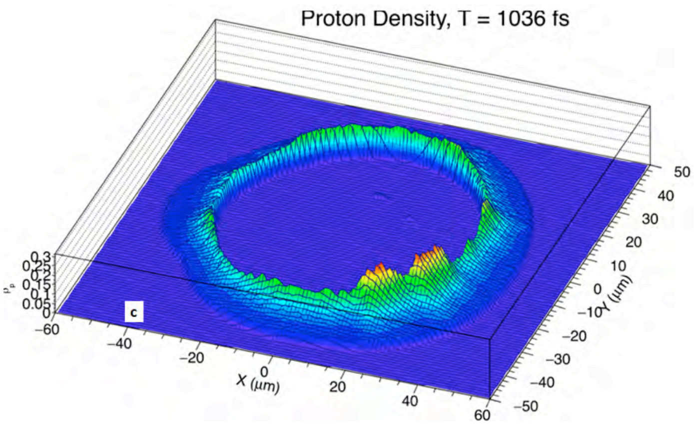

Figure 23: Proton acceleration signatures for the cylindrical plasma targets parameters of R15: (a) Volume averaged proton distribution function; (b) Proton phase space in the x-direction; (c) Two dimensional proton density for E>3 MeV.

It is however important from the diagnostic point of view and from the conceptual plasma target design to explore briefly the physics involved in the acceleration of cylindrically symmetric targets. Figs. 24 show the laser pulse interacting with the plasma target. Filamentation starts as soon as the laser pulse enters the target at t=.23 ps (Fig. 24a).

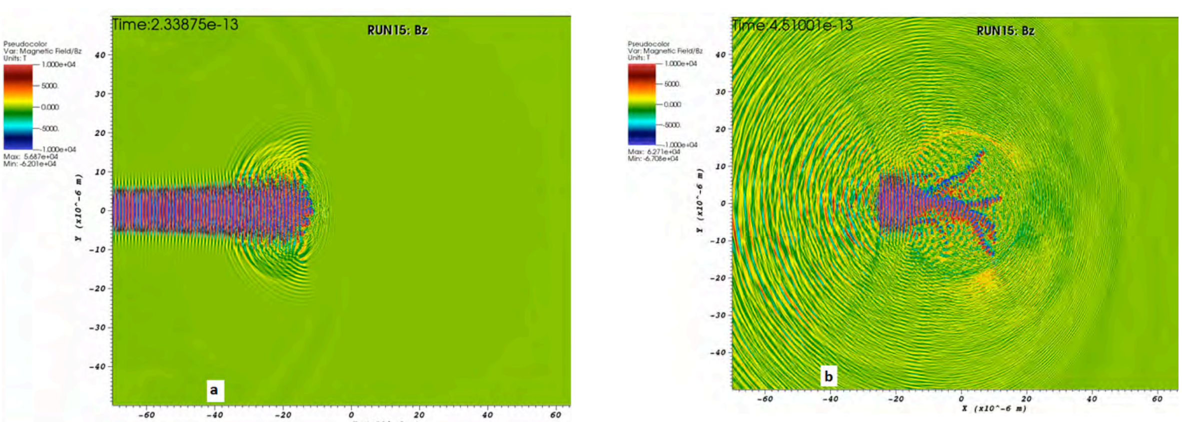

Figure 24: Laser pulse interaction with plasma target for R15 at (a) t=.23 ps; (b) t=.45 ps. Strong filamentation starts early and is completely developed by t=.45 ps.

The filamentation is caused by the planar laser front interacting with a curved target. The interaction is strong and creates several plasma channels (fig. 24b) that essentially destroy the plasma channel (Fig.25) and degrade energy transfer to protons.

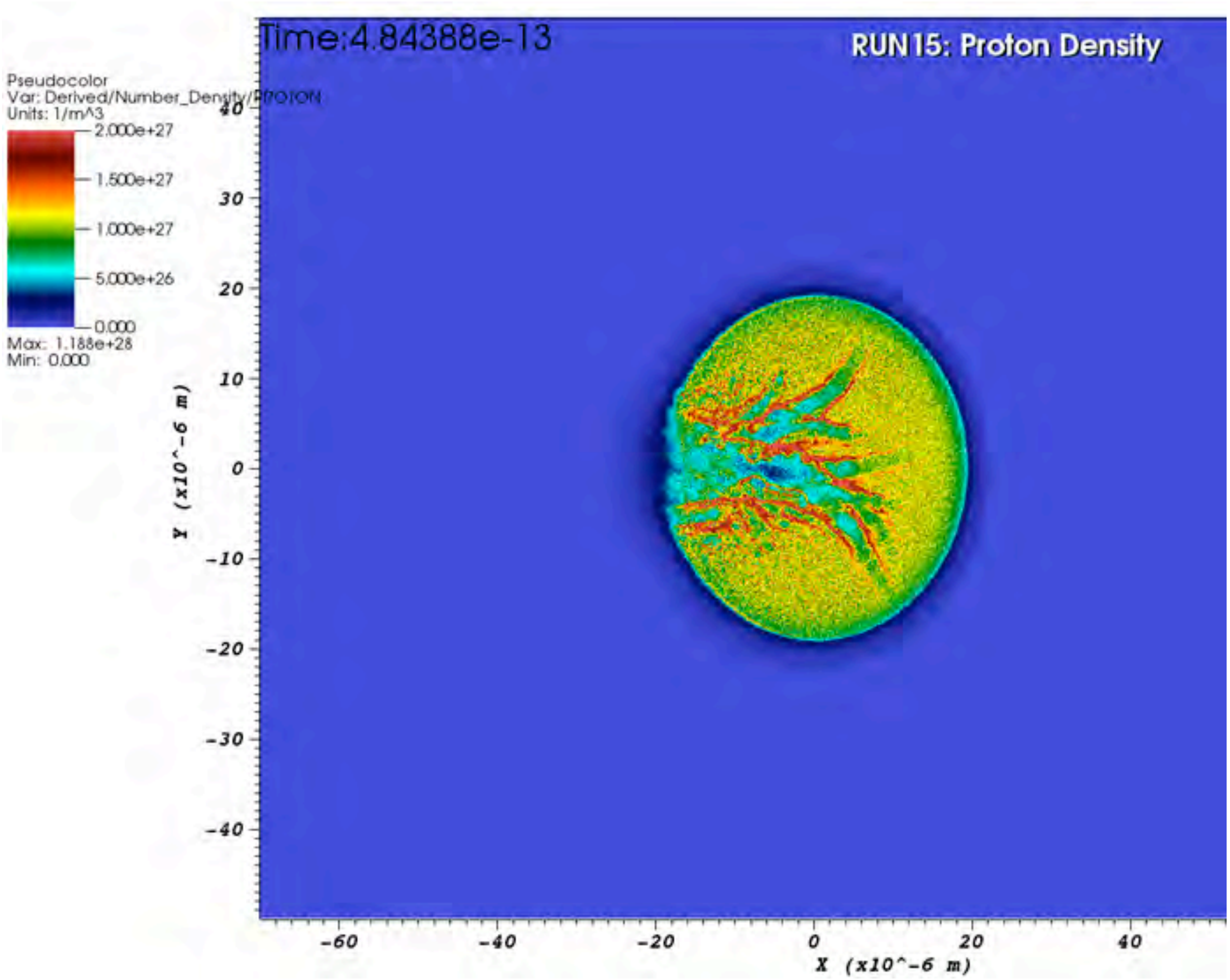

Figure 25: Filamentary plasma channel structure at t= .48 ps for R15 target parameters.

Summary:

We have examined the parameters that govern the efficiency of proton acceleration driven by the interaction of ultra-short, multi-TW Ti:Sapphire laser pulses with ionized, high-density gas jets. The analytic study complements the ongoing experimental program (Milestone reports 1-3). We performed fully-relativistic Particle-in-Cell (PIC) code numerical methods and analytical modeling. Useful features different from those found in the literature of lasers impinging on solid targets were found including:

- A plasma waveguide follows the laser focusing in the plasma target and guides the laser through the target;
- Strong, large amplitude (> $5x10^3$ T) azimuthal, quasi-stationary, self-generated magnetic fields surround the wall of the plasma channel and the plasma-vacuum interfaces;
- Multi-MeV electrons are heated by the laser-plasma interaction in the waveguide. The relativistic electrons are confined by the self-generated field and guided towards the plasma-vacuum boundaries;
- Dominant proton acceleration occurs by the expansion of the hot electron plasma at the plasma-vacuum boundaries. Although conceptually like Target-Normal Sheath Acceleration (TNSA), the expansion is modified by the effect of the magnetic field on the hot electrons at the plasma boundaries;
- Maximum proton acceleration occurs at the plasma-vacuum boundary with the highest electron temperature;
- Maximum proton acceleration at the front plasma-vacuum interface occurs when the laser energy deposition length L_H is comparable to the target length L;
- The energy deposition length L_H can be controlled by using a combination of focusing optics and plasma target profiles that focus the laser close to the middle of the target. Use of a slightly subcritical peak density results in pulse group velocity in the forward direction favoring hot electron generation close to the front boundary between the plasma and vacuum; and
- Filamentation can be inhibited by matching the numerical aperture of the input optics to the numerical aperture of the plasma waveguide, or by choosing the plasma target aspect ratio.

We conclude that high efficiency requires maximum laser energy to be transferred to hot electrons at the front boundary of the target. Key elements in achieving this are:

(i) Formation of stable plasma waveguides that guide the laser pulse over the entire channel length;
(ii) Energy deposition length from laser to hot electrons comparable to target length; and
(iii) Quasi-static azimuthal magnetic fields (B_z) that confine hot electrons inside the plasma channel.

Exploring and verifying these features is an integral part of the experimental program and its diagnostic instrumentation.

Chapter 5: Resolving proton energy with CR39 (acrylate) targets

The *Positrons on Demand* effort requires determination and control of the spectra of multi-MeV protons generated by the interaction of a laser pulse with the primary gas target. Diverse diagnostic techniques are used to measure the spectra of accelerated MeV protons, including radiochromic film (RCF) dosimetry, fluorescence, nuclear track recording, and magnetic spectrometry. We have determined that methods using allyl diglycol carbonate polymer (CR-39) recording media offer significant advantages in terms of accuracy, sensitivity and ease of operation.

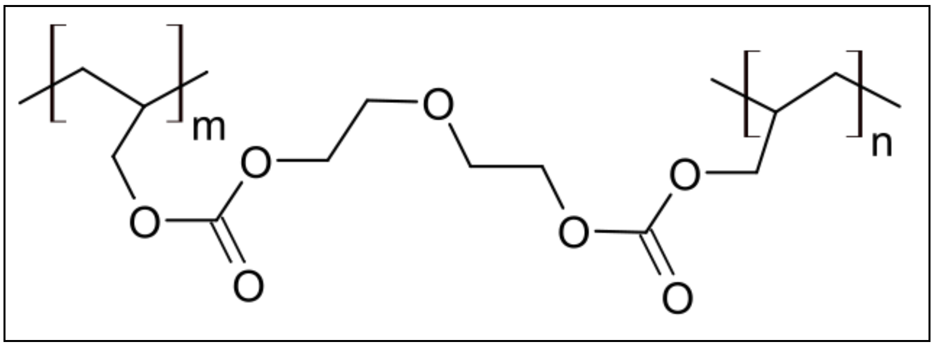

Figure 1: Chemical structure of Columbia Resin 39 (CR-39) allyl diglycol carbonate.

RCF dosimetry is composed of an active monomer layer that polymerizes when exposed to ionizing radiation or high-energy particles. The reaction results in a change of the film color and subsequent analysis using densitometry provides quantitative information on the dose of the absorbed radiation. The total yield of the impinging ions is calculated by comparing the exposed material's optical density with dose calibration curves for the specific type of film used, for example GafChromic MD-55, HS, and HD- 810 films [1,2].

Fluorescers or scintillators are materials whose atoms emit photons at a specific frequency following the absorption of energetic photons or particles. Calculation of the ion flux and spectrum requires from fluorescence requires knowledge of the quantum efficiency of the fluorescent process and estimates of the total fraction of emitted light that is collected. A typical scintillator with higher than average quantum efficiency is Saint Gobain's BC-400 which yields ~ 10^5 photons per 10 MeV proton. Although uncertainty in the quantum yield and optical collection terms are important limitations of this approach, the major challenge of these detection methods is that they are also sensitive to energetic electrons and photons.

CR-39 (allyl diglycol carbonate), is a clear plastic polymer that is commonly available with an optical polish in many shapes and sizes due to its widespread use as ophthalmic lenses. It was first suggested in 1978 that CR-39 be used for the detection of accelerated ions through the production of damage tracks [3]. As an ion propagates through the CR-39 material, it ionizes and destroys molecular bonds in a very localized area along its path. These damaged areas develop into visible cavities, or pits, by etching the exposed CR-39 in aqueous NaOH or KOH. The clear advantage of using CR39 plates for ion detection is their response to a single ion, enabling quantitative ion yield estimates. This quality was explicitly displayed by Hara *et al*., who extracted a single He ion from an accelerated beam and detected it with a CR-39 plate [4]. The etched pits can be observed on a micrometer spatial scale using conventional microscopes and at a sub-micron scale with atomic force microscopes, [5] facilitating high spatial resolution in a CR-39 detection system. However, these advantages come with the drawback of post-processing - the etching and counting of pits are a time consuming and meticulous process. This drawback prevents CR-39 from use in real time as an online diagnostic.

CR-39 can also be used to deconvolve the energy spectrum of ions due to their nonlinear loss of energy while propagating through the dielectric medium. As an ion travels through a dielectric, it loses its energy primarily by inelastic collisions with the material's atomic electrons. These collisions could result in ionization or excitation of the atomic electrons. These inelastic processes are quantified by the following formula for the energy lost per unit length:

$$\frac{dE}{dx} = -2\pi N_a r_e^2 m_e c^2 \rho \frac{Z}{A} \frac{z^2}{\beta^2} \left[\ln \left(\frac{2 m_e \gamma^2 v^2 W_{max}}{I^2} \right) - 2\beta^2 \right]$$

where:

$$W_{max} = \frac{2m_e c^2 \beta^2 \gamma^2}{1 + 2(^{m_e}/_{M_i})\sqrt{1+\beta^2\gamma^2} + (^{m_e}/_{M_i})^2}$$

$\beta = {}^{v}/_{c}$	: normalized ion velocity
$\gamma = {}^{1}/_{\sqrt{1-\beta^2}}$	: relativistic Lorentz factor
$N_a = 6.022\text{x}10^{23}\ \text{mol}^{-1}$	: Avogadro's number
$r_e = 2.817\text{x}10^{-13}\ \text{cm}$	: classical electron radius
$m_e = 9.11\text{x}10^{-31}\ \text{kg}$	: electron mass
$M_i = 2.67\text{x}10^{-27}\ \text{kg}$	: proton mass
$c = 3\text{x}10^{8}\ \text{m/s}$	: speed of light
$\rho = 1330\ \text{kg/m}^3$	: density of CR-39
$Z = 146$	: atomic number of CR-39
$A = 272$	: atomic weight of CR-39
$z = 1\ \text{e}$	: charge of a proton in units of e

As it decelerates in the CR-39 material, the slower moving ion has a larger collisional cross-section that increases its local energy deposition rate. This results in a nonlinear increase of the deposited energy as the ion propagates, culminating with peak deposition of energy in a thin layer where the ion stops -- the Bragg Peak. This can be seen in Fig. 2, which is a plot of a 20 MeV proton's energy loss as it propagates into CR-39.

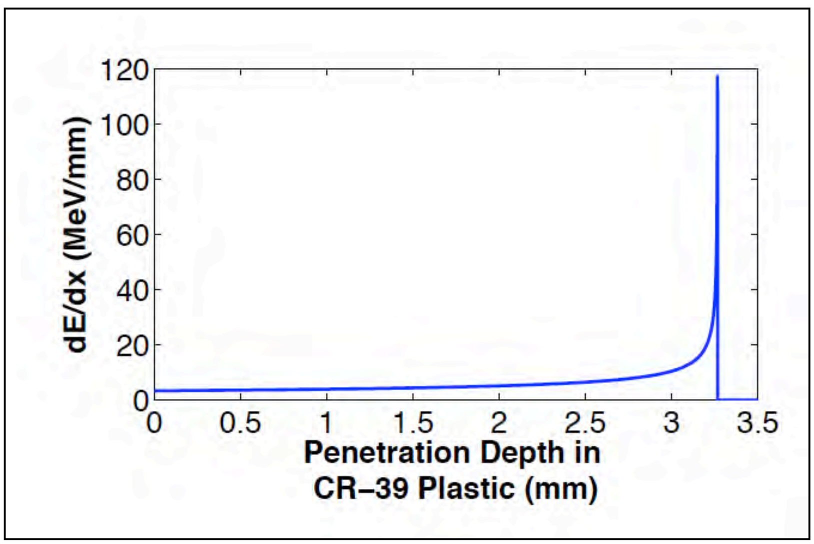

Figure 2: Energy loss in CR-39 for a 20 MeV proton with a Bragg Peak at 3.25 MeV.

Developing a visible response of the CR-39 to this energy deposition is obtained through chemical etching. It is characterized by the ratio of the etch rate near the damaged areas, called the track etch rate V_t, to the bulk material etch rate, V_b. If V_t is larger than V_b, it is possible for an etched track to develop and be observed under a microscope. This response increases with increasing charge of the ion, Z, or with decreasing velocity, $\beta = v/c$, due to an increase in the collisional cross-section of the ion with atomic electrons. It is predicted that observable tracks will form in CR-39's at a Z/β as small as 8-10 (ref. [3]). This minimum threshold of Z/β for an ion to produce an observable pit is the key to the determination of its energy. The functional dependence of Z/β on propagation distance remains relatively low until the proton nears the end of its trajectory. Over most of its path the energetic proton will not leave observable damage until near its Bragg Peak. This allows for the discrimination of protons with different energies corresponding to different depths of their respective Bragg Peaks. It's possible to achieve high energy resolution by observing the onset of proton-related damage in small depth increments while etching into a CR-39 plate.

For our goals, the CR-39 detection system can be based on a stack of five or more 50x50 mm^2, 0.2 or 0.5 mm thick plates that will be oriented 5-7 centimeters from the gas jet along the laser propagation direction. It will cover a significant solid angle and provide information on the emittance of the proton beam. To prevent possible damage by the laser beam, the stack of CR-39 layers will be covered by a thin (10-15micron) aluminum foil to prevent damage by scattered light from the laser pulse. The effect of the foil on the energy deposition will be included.

Energy deposition of mono-energetic, 1-25 MeV protons in CR-39 plastic is plotted versus penetration depth in figure 3. The Bragg peaks are clearly visible. Superimposed on this plot are the edges of five 1 mm thick CR39's (shown in black dashed lines) to display the spectral sensitivity of the detection system.

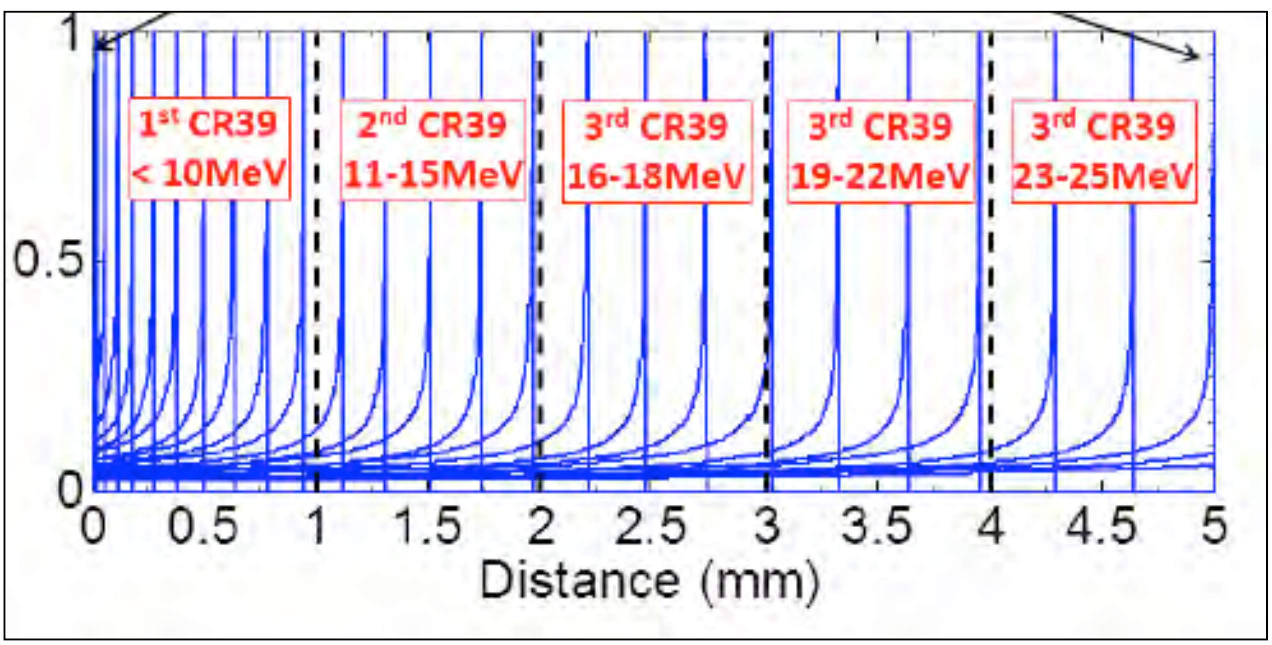

Figure 3: Energy deposition in stack of five 1 mm thick CR 39 plates for mono-energetic protons at

1 MeV increments from 1-25 MeV. The black arrows indicate 1 MeV and 25 MeV Bragg Peaks near zero and 5 mm depths, respectively.

After exposure to protons, each CR-39 dosimeter is etched for 5-6 hours at 80 degrees C and then analyzed. For finer spectral resolution, further etching in 5 hour increments up to a total of 20 hours can be done. It effectively moves the plane of detection by 50 micron increments deeper into the CR-39. Using this method energy resolution as fine as 0.1 MeV for 20 MeV protons can be obtained. Background noise level is subtracted using non-exposed CR-39 from the same vendor and manufacturing lot. Highly resolved energy spectra require this slow process, for a fast indication during the experiment; the exposed plates can be etched for 20 minutes at 90 degrees, rinsed with distilled water, and examined under a microscope.

An excellent review of the response of CR-39 nuclear track detector to 1-9 MeV protons is given in the attached report by Prof R.Petrasso *et al.* from MIT.

Etching Procedure and Proton Pit Counting

CR-39 plastic nuclear detectors are widely used for the detection of energetic ions since they are not sensitive to electrons and x-rays. After exposure to accelerated protons, each CR-39 is etched in a fresh 6N NaOH solution held at a constant temperature of 80**C +/-** 0.1deg. The glass container holding the NaOH solution and the hot plate along with the thermocouple probe, which provides the feedback for temperature stabilization, should be used. CR's must be well separated. Fresh solution is prepared and its temperature is stabilized for each set of CR-39 plates. The development must be performed with adequate ventilation.

Five to six hour etching increments were empirically found to provide proton pit sizes greater than 10 **μ**m and therefore easily resolved with optical microscopy or profilometry. The optical profilometer provides a careful measure of the widths of the CR-39 plates and the pits profiles.

The bulk-etching rate was found by several groups to be 10 **μ**m/hr; each 5 hr increment removes ~50 **μ**m of bulk material from each face of the CR-39 plates. After etching, each CR-39 is cleaned with distilled water and dried with dry air. The CR-39's can be viewed under an optical microscope at a magnification of 100 or with an optical profilometer. A 2-axis, computer-controlled actuator translates the CR-39 as images from a CCD camera record the entire surface. Standard image processing algorithms are applied to automate pit identification (e.g. Matlab Image Processing Toolbox or NIH Image). The energy of a detected proton is calculated by equating the distance traveled through the CR-39 plastic to the distance traveled by a proton of a certain energy to yield the Bragg peak at that location.

After the initial 5 hour etching period, the fine energy features can be identified by a gross change in yield between adjacent data points. In these cases, further etching of the corresponding CR-39 in as many as four, 5 hour increments can be carried out to obtain finer spectral resolution around each feature. The pit diameter also grows linearly with the etch time further, enabling identification of the protons whose Bragg peak occurs within each 50 **µ**m slice of CR-39.

Additional recent references on CR-39 track detection based on work by Killkenny *et al.* [7] and Petrasso *et al.* [8] as well as a thorough report from the MIT group are included as an appendix.

References:

1. D. S. Hey, "Use of **G**af**C**hromic film to diagnose laser generated proton beams," *Rev. Sci. Instrum.*, 79, p. 053501 (2008).
2. F. N**u**rnberg, "Radiochromic film imaging spectroscopy of laser-accelerated proton beams," *Rev. Sci. Instrum.,* **80**, p. 033301 (2009).
3. G. G. Cartwright, E. K. Shirk, and P. B. Price, "A nuclear-track-recording polymer of unique sensitivity and resolution." *Nucl. Instrum. Meth.*, **153**, p. 457 (1978).
4. K. Hara, M. Koh, T. Matsukawa, T. Tanii, and I. Ohdomari, "Single-ion detection using nuclear track detector **CR**-39 plastic," *Rev. Sci. Instrum.*, **70**, p. 4536, 1999.
5. S. Kar *et al*., "Analysis of latent tracks for **M**e**V** protons in **CR**-39," J. App. Phys., **101**, p. 044510 (2007).
6. W. R. Leo, Techniques for Nuclear and Particle Physics Experiments, 2nd ed. Berlin, Germany: Springer-Verlag, (1994).
7. Killkenny, J.D. *et al.*, "Empirical assessment of the detection efficiency of CR-39 at high proton fluence and a compact, proton detector for high-fluence applications", *Rev. Sci. Instrum.,* **85**, 043302 (2014).
8. Petrasso *et al.*, ""The response of CR-39 nuclear track detector to 1–9 MeV protons," *Rev. Sci.Instrum,* **82**, 103303 (2011). (minor erratum in *Rev. Sci. Instrum.* **85,** 119901 (2014).

Chapter 6 : Intercomparison of Thomson Parabola and CR-39 ion energy spectra

Thomson Parabola

A central challenge examined by this program involves understanding the relationships between laser and cryogenic fluid jet parameters and the energy distribution of ions in the quasi-neutral plasma jet that results from their interaction. In the most general case of a laser generated plasma, ions with varied charge-to-mass ratios can be produced. Characterizing the energy of these ions requires both magnetic and electric fields to separate species of different charge to mass ratios (q/m). MicroPET's approach produces a plasma jet whose only ions are protons; no charge state higher than +1 is feasible. While a mixture of H_2 and D_2 in the source would arguably produce ions with different q/m, pure D_2 that might be used to access different nuclear reactions would also produce ions with only one q/m ratio.

Sorting out the energy and mass/charge ratios of ion fluxes using parallel electric and magnetic fields was first described by J.J. Thomson in 1907. (J. J. Thomson, Philos. Mag. 13, 561 (1907) There are excellent papers on the resolution, dynamic range, design, and fabrication of Thomson parabola ion spectrometers in the literature. (J. A. Cobble , K. A. Flippo , D. T. Offermann , F. E. Lopez , J. A. Oertel et al., *Rev. Sci. Instrum.* 82 , 113504 (2011); doi: 10.1063/1.3658048), D. Jung et al., *Rev. Sci. Instrum.* 82, 013306 (2011)

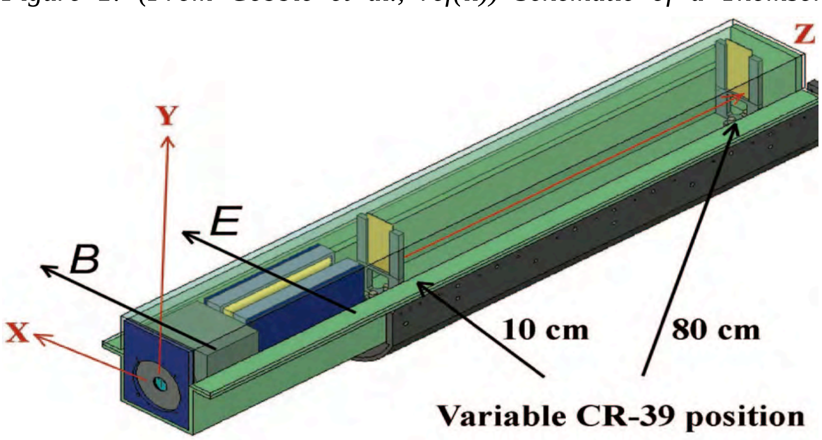

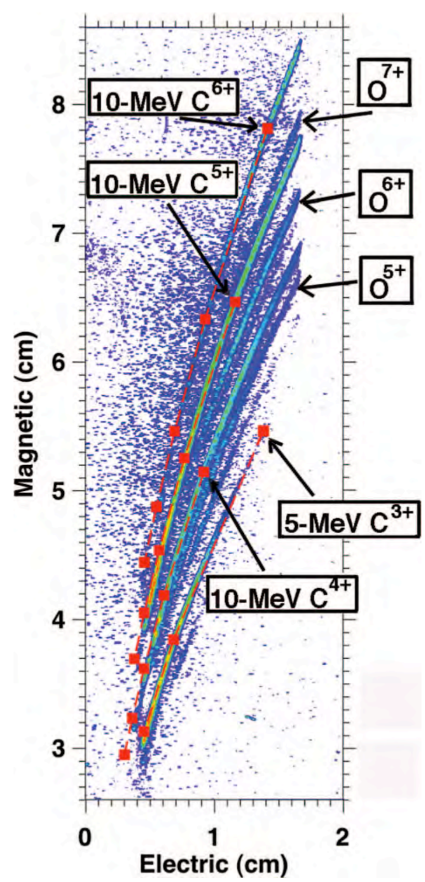

Figure 1: (From Cobble et al., ref(ii)) Schematic of a Thomson parabola ion spectrometer. An ion beam enters at the aperture on the left and drifts through parallel electric and magnetic fields before being imaged on a two-dimensional detector. Ions of a single mass-to-charge ratio produce a parabolic trace as seen from an ion beam produced by irradiation of a diamond-like carbon film at right.

This approach to characterizing ion energy spectra complements the method described in the Milestone 5 report, where the diameter and depth of the tracks in bis-allyl carbonate (CR-39) following a strong base etch are used to estimate ion energies. The latter approach has the advantage of very high detection efficiency but this comes at the expense of relatively long turnaround times, particularly for optimization experiments.

High energy resolution and dispersion provided by Thomson parabola spectrometers can simultaneously resolve protons and low atomic number ions with more than 100 MeV/nucleon. They are applying high electric and magnetic fields enable energy resolutions of **ΔE/E** < 5% at while separating different ion species at low energies on the detector plane. This approach benefits from the reliability of the static electric and magnetic fields as well as the inherent simplicity of the physics. The main factors contributing to the intrinsic resolution of a Thomson Parabola for a specific charge to mass ratio are the drift length and the pinhole size that limits and collimates the incoming ion beam, and the strength and length of the magnetic field along the ion propagation direction. Stronger, longer magnetic fields increase energy resolution by higher dispersion. A larger pinhole decreases resolution due to an increased ion beam spot size on the detector but increases the detected flux.

The intrinsic instrument resolution **ΔE/E** can be described in the nonrelativistic case by a parabolic equation using the energy range covered by the beam spot on the detector divided by its center energy. Separation of different charge to mass ratios depends on the electric field parameters and the drift together with the beam spot size on the detector. The intersection point of the upper and lower boundary of the respective parabola traces calculates the "merging" energy of two neighboring traces, where the boundaries are given by the beam spot size on the detector. It is obvious that the magnetic and electric field parameters must be increased to obtain extremely high energy resolution and separation of traces.

A typical Thomson Parabola spectrometer spans two vacuum compartments separated by a vacuum valve, where the first part forms the core of the TP with two magnets with a few centimeter gap. The field expands almost uniformly over the whole 20 cm with a very sharp drop off at the edges. Within the magnets, a pair of copper electrodes is separated by 2 cm to favor an extremely high potential of 40 kV without vacuum breakdown.

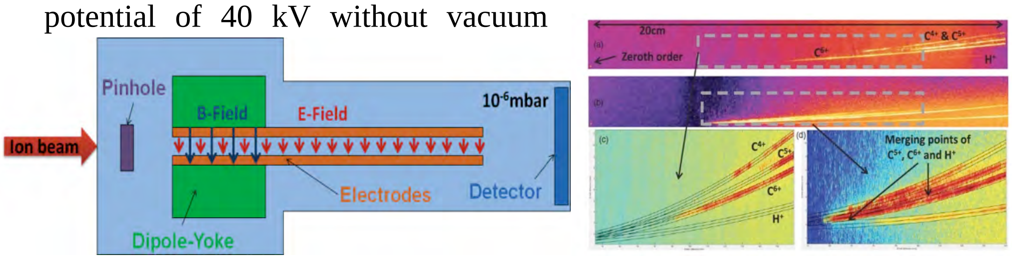

Figure 2: Schematic of the Thomson Parabola spectrometer reported in reference (left) and a sample spectrum from the laser driven plasma of a carbon target (right) showing the parabolic trajectories and separation of ions with different q/m ratios. (From Cobble et al.[2])

Comparison with CR39 detection

Spectral measurements performed with stacks of CR 39 and the Thompson Parabola are complementary. Whether by stacking thinner plates or estimating ion energy from the etched pit dimensions the CR-39 technique measures the whole beam angular distribution with coarse energy resolution.

The energy spectrum measured with the TP is continuous and has higher resolution, but it yields information only over a small solid angle that is set by geometric relationship between the ion source and the detector pinhole. Its properties are very sensitive also to alignment. Misalignment can prevent detection of the high-energy segment of the spectrum which may be concentrated at a specific angular trajectory.

Conclusion

A target whose plasma contains ions with more than one charge to mass ratio, such as would be produced by a polymer film or metallic foil, the Thomson Parabola ion spectrometer permits detailed understanding of the energy and composition of the ion flux that is not possible with etched CR-39 alone. The MicroPET approach produces only protons, with a charge to mass ratio that can only be one, so that the combined electric and magnetic fields are not needed to resolve energies of species with different q/m. A simple magnetic spectrometer (with no electric field drift) would suffice to measure ion energy distributions subject to the same alignment and angular divergence limits as the Thomson parabola. Moreover, the presence of a single q/m species means that ion energies inferred from etch pit diameter and depth avoid ambiguity where multiple species are present. Since these methods do not require precise alignment or a sampling aperture we have selected CR-39 diagnostics to characterize our ion energy

Chapter 7: Solid target design

Overview

Quasi-neutral plasma jets generate proton fluxes with energies more than 5 MeV. These jets result from irradiation of a high-density (.5-1.5x10^{21} H_2 cm^{-3}) primary gas target with sub-picosecond, intense (TW) laser pulses. This milestone report describes the generation of a PET radioisotope, ^{11}C, from a solid phase boron nitride (BN) target. The approach is straightforwardly generalized to other solid precursors given only the pertinent nuclear reaction cross-sections and plasma jet parameters.

Boron Nitride has equal numbers of boron and nitrogen atoms, but the ^{11}B isotope has only 80% natural abundance. Positron emitting ^{11}C atoms from the solid BN target are produced by nuclear reactions of both boron ($^{11}B(p,n)^{11}C$) and nitrogen ($^{14}N(p,\alpha)^{11}C$) whose cross sections as a function of proton energy are shown in Figures 1.

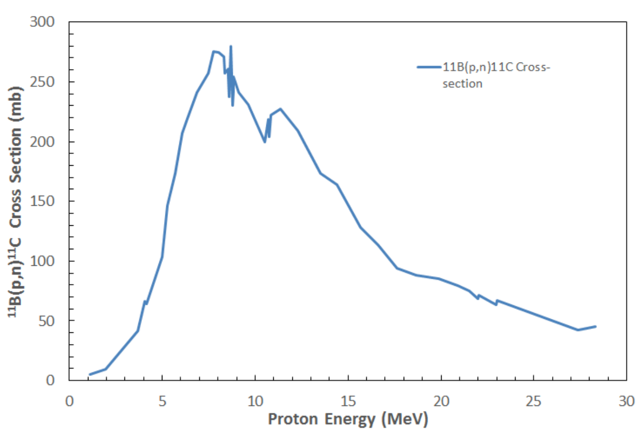

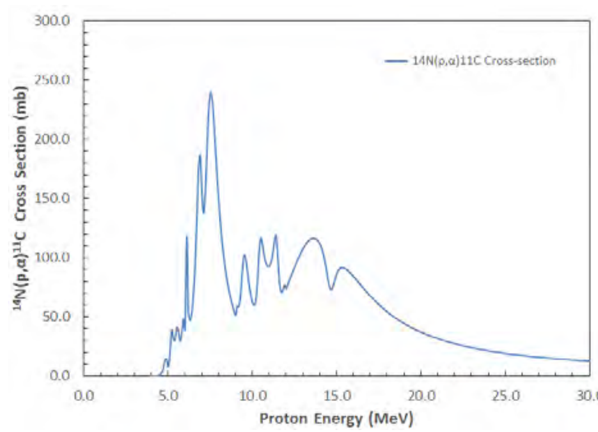

Figure 1: Cross sections (1mb = $10^{-31}m^2$) for production of ^{11}C from ^{11}B (left) and ^{14}N (right).

Isotope production is computed using the open-source GEANT4 code. GEANT4 is a software platform developed and maintained by an international consortium[1] that simulates the interaction of energetic particles with matter. It has been applied in high energy, nuclear, and accelerator physics, as well as medical and space science studies. The algorithms and numerical methods are described in detail in widely cited publications.[2,3,4] The code provides a complete set of tools for building geometry, assigning materials, running events, tracking particle histories, and visualization. It is complemented by the G4TENDL dataset that allows calculation of isotope yields for incident protons with energy up to 200 MeV.[5] The boundary conditions needed to run these calculations include the geometry and composition of the secondary target and the energies and flux of the incident protons. The proton energy distribution functions produced by quasi-neutral plasma jets are found using the methods described in previous milestone reports.

GEANT4 calculations yield N_1, the number of ^{11}C atoms produced inside the secondary target after one laser shot, as a well as the ^{11}C yield profile. The energy deposition per pulse from inelastic scattering is also produced. The activity, A_1, is calculated using the isotope half-life T per the equation

$$A_1 = \frac{N_1 \ln{(2)}}{\mathrm{T}}. \qquad \textbf{\{Eq. 1\}}$$

The ^{11}C half-life, T=20.4 minutes, is much longer the intra-pulse period 1/r where r is the laser repetition rate, (rT>>1), so the activity A after irradiating one half time (20.4 minutes) is:

$$A = A_1 \left(\frac{rT}{2\ln{(2)}}\right). \qquad \textbf{\{Eq. 2\}}$$

The activity A(*t*) after irradiating for time *t* is:

$$A(t) = A_1 \left(1 - e^{-\ln(2)t/T}\right)\left(\frac{rT}{\ln{(2)}}\right). \qquad \textbf{\{Eq. 3\}}$$

The GEANT4 calculations generate N_1 and A_1 for the proton energy flux in the plasma jet created by a single pulse using the design parameters of the solid target. Activation after irradiation time *t* is then computed using **{Eq. 3}**.

The number N of ^{11}C atoms required to achieve an activity level A in milliCuries, (mCi), can be found from **{Eq. 1}** and is:

$$N = \frac{1}{\lambda}\frac{dN}{dt} = \frac{A(mCi)(3.7x10^7 dps)}{\ln(2)/1.2x10^3} = 6.4x10^{10} A(mCi)$$

where dps indicates decays per second.

Carbon-11 production from Boron-Nitride Target

The proton fluxes from quasi-neutral plasma jets are anisotropic. We have therefore studied two prototypical secondary target geometries: a planar disc that subtends a solid angle of .38 steradian (sr), and an integrating sphere (4π =12.6 sr) that surrounds the interaction region. The former corresponds to a cone with an apex angle of 40^{o} and spans 3% of the available output. The proton energy distributions for the quasi-neutral jet produced under the conditions of table 1 are different for these two target geometries. The planar disc intercepts protons with a broader and higher average energy, as can be seen in figure 2.

Table 1: *Quasi-neutral jet production conditions*

Wavelength	Pulse duration	Peak Intensity	Pulse Energy	Plasma Density	Target Profile (μm)
1 μm	300 fs	2 10^{19} W/cm^2	1.4 J	8.4 10^{20} cm^{-3}	$e^{-((x-60)/20)^6} * e^{-(y/25)^6}$

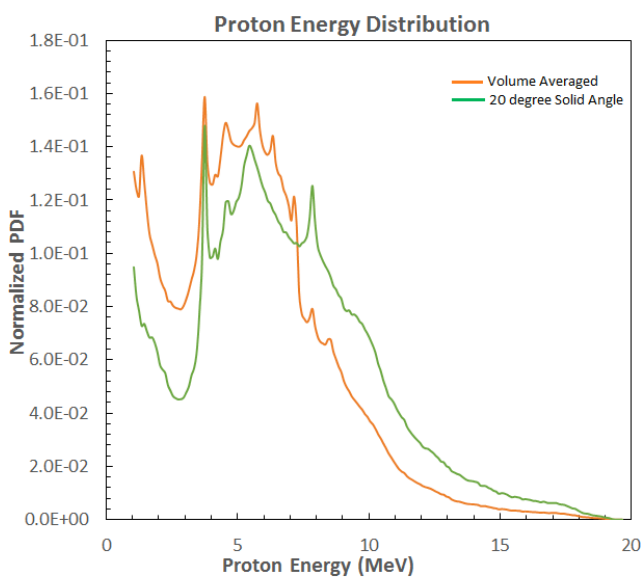

Figure 2a: Normalized ion energy distributions functions for collection in a .38 steradian solid angle oriented along the laser axis (green) and over the full sphere (orange).

The average energy of the entire proton flux (orange curve in figure 2) is 6.8 MeV. Protons moving in the forward direction (green curve in figure 2) have average energy of 7.3 MeV. The conversion efficiency from the laser pulse energy to protons with energies above 5MeV is 4.1% (5×10^{10} protons/pulse) in the forward direction and 8% (10^{11} protons/pulse) over 4π steradians. Figure 3 below shows the overlap of these energy distributions with the ^{11}B and ^{14}N nuclear cross-sections using the same color scheme.

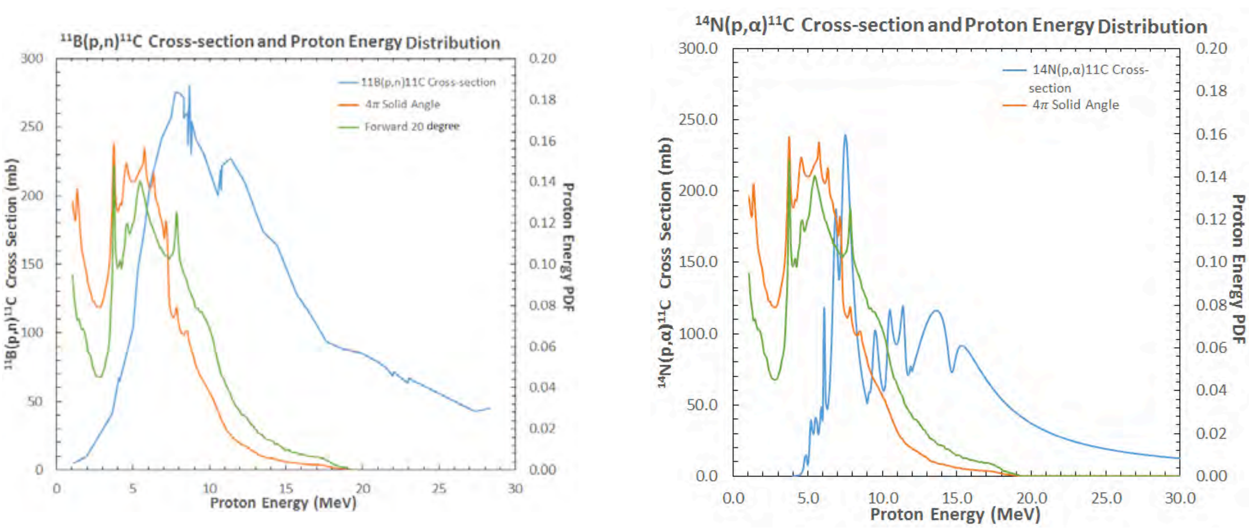

Figure 2b: The energy distribution of forward-directed protons (green) has better overlap with cross-sections for ^{11}B and ^{14}N and therefore greater efficiency for conversion to ^{11}C than the spatially average flux (orange).

The distribution functions and cross-sections shown in Figure 2b are used with GEANT4 to calculate the number of ^{11}C atoms per laser pulse as a function of the BN target thickness for both the planar and spherical secondary target. Figure 3 displays the contributions from ions of different energies to the yield of ^{11}C in the 0.38 sr cone and the complete spherical targets. 40% of the useful yield comes from 3% of the solid angle.

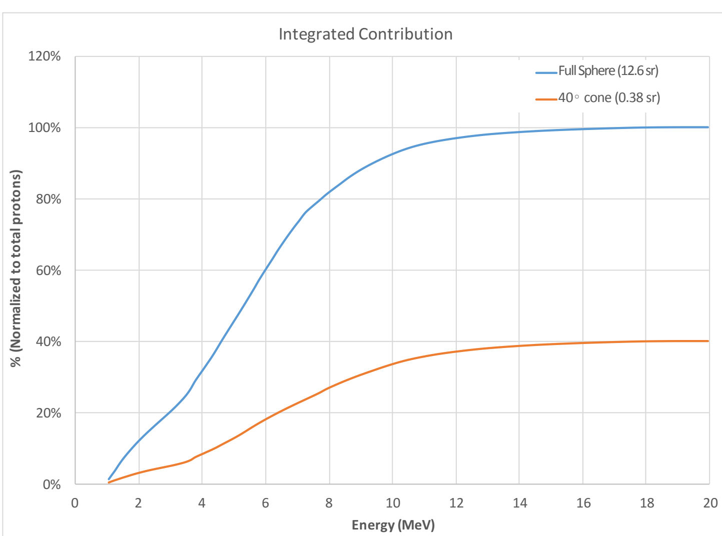

Figure 3: The contribution of ions with various energies to the production of ^{11}C showing that 40% of the useful yield is concentrated in 3% of the total solid angle.

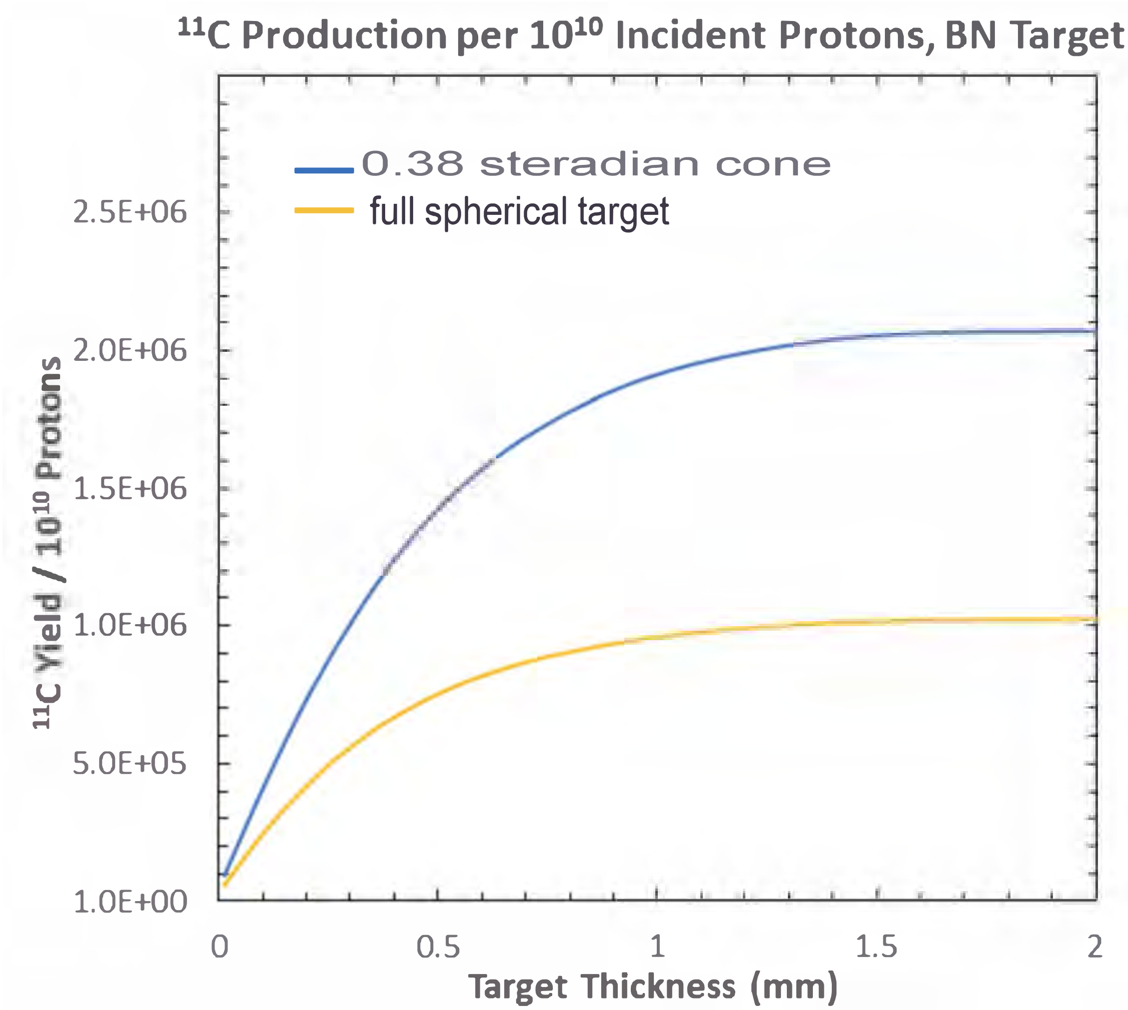

Figure 4: ^{11}C production rates normalized to the number of incident protons as a function of BN target thickness. The efficiency of the higher average energy of forward-directed protons in the quasi-neutral plasma jet is about twice as high in the smaller cone than in the full sphere.

Figure 4 leads to the important conclusion that a smaller secondary target with solid angle 0.38 sr produces ^{11}C thirteen times as efficiently -- (0.4*4π/.38) -- on a per-proton basis than complete sampling of the plasma jet over 4π sr. A second observation from Figure 4 is that a 1.3mm thick target captures maximizes the total yield of ^{11}C and that the specific activity – the activity per unit volume – is highest for thinner targets since the total volume scales linearly with thickness for the disk and super-linearly for the full sphere. Finally, the yield of $2x10^6$ radioactive ^{11}C nuclei results from 10 mJ ($7.3x10^{10}$ MeV) of energetic protons per pulse, corresponding to 1% conversion efficiency based on laser energy.

The activity level that can be accomplished with 1 J pulses scales with the pulse repetition rate of the laser. Equation **4** implies 90% of saturated activity is reached after three half-lives corresponding to 60 minutes' irradiation time. Since one mCi activity requires 6×10^{10} radioactive atoms, this corresponds to 3×10^4 pulses, or a pulse rate of 8.3 Hz.

Conclusion:

Energetic protons formed in quasi-neutral plasma jets can be converted to ^{11}C radioactive atoms by irradiation of solid target materials. A prototypical case based on a BN target reveals the importance of target geometry and composition through the angular variation of proton energy distributions and the nature of the target materials' cross-sections. Using the GEANT4 transport code to describe the proton slowing down and the production of radioisotopes such as ^{11}C during the interaction of protons with the BN target.

- A planar boron nitride target 1.5 mm thick and subtending only .38 steradian solid angle is a suitable primary target;
- The marginal utility of building a secondary target with solid angle greater than about 0.38 sr is low since the most energetic ions are biased in the forward direction;
- Assuming 1J, 300fs laser pulses at ~1µm wavelength, 10 W average power and 10 Hz repetition rate with a 50µm thick H_2 target close to the critical density suffice to generate 1mCi saturated yields.
- These conditions can produce 1 mCi of ^{11}C within 20-60 minutes.
- Higher activities are feasible using higher pulse repetition rates or enhancing the conversion efficiency above the 1% level obtained under these prototypical conditions.

References

1) Consortium members include the European nuclear agency CERN, Fermi lab, the European Space Agency (ESA), the Stanford Linear Accelerator (SLAC) and others.
2) http://geant4.web.cern.ch/geant4/
3) S. Agostinelliae *et al.*, Geant4—a simulation toolkit, Nucl. Instr. and Meth. A, 506 (2003) 250–303
4) J. Allison *et al.*, Geant4 Developments and Applications, IEEE Trans. on Nucl. Sci., Vol. 53, No. 1, (2006)
5) http://geant4.cern.ch/support/datafiles_origin.shtml

Chapter 8: Scaling of Proton Divergence and Flux: Implications for Isotope Production

Positron Emission Tomography (PET) is a powerful diagnostic, neuroimaging technique whose implementation requires the production of positron emitting isotopes with extremely short lifetimes (2-120 minutes). Four positron-emitting radioisotopes that are extensively used are ^{11}C, ^{13}N, ^{15}O and ^{18}F. The first three of these have short lifetimes but they can be substituted directly into biomolecules without changing their chemical or pharmacokinetic properties. For example, substituting ^{11}C for ^{12}C does not alter the reaction time or the biological behavior of the molecule. ^{18}F is employed, particularly appended to a deoxy glucose substrate, to track metabolism because it is metabolically sequestered and the isotope half-life of 120 minutes is logistically convenient. However, there are no natural biomolecules that contain fluorine, so these ligands necessarily have different biochemistry than the carbon, nitrogen, or oxygen species.

The usefulness of a PET tracer is limited by the elapsed time from their generation to their use. PET radiotracers lose their potency (or specific activity) immediately after the isotope is generated, so they must be used within a few half-lives. The half-life of ^{11}C is 20 minutes, so its incorporation into a tracer molecule and injection into a patient must occur within about an hour after production of ^{11}C. The need for extensive infrastructure associated with the size and shielding requirements of conventional or superconducting cyclotrons, combined with short lifetimes of the PET isotopes, requires colocation of the diagnostic and research facilities with the cyclotron installation. This logistical constraint limits the development of a broad palette of short-lived (20 minutes) ^{11}C based radio-ligands that are critical to the development brain quantitative imaging and pharmacokinetics.

- Flexible point-of-use, on demand, single dose radio-ligand synthesis will enable:
- New modes of molecular- level diagnostic imaging
- Exploitation of PET systems not adjacent to cyclotron facilities
- Combinatorial screening for drug discovery, metabolic analysis and pharmacokinetics

The objective of the MicroPET Point-of-Care, on demand, single dose positron-emitting biomolecule synthesis program is the development of a tabletop, transportable unit that will overcome the hurdles of the current cyclotron based multi-dose technology for the development of short-lived PET radio-ligands. Essential elements of the MicroPET system include:

A compact turn-key laser with average power of a few hundred watts, pulse energies of a few joules, and pulse widths of a few hundred femtoseconds.

A hydrogen gas target (primary target), with a peak H_2 molecular density above $5x10^{20}$ cm^{-3} that, when fully ionized, will produce plasma density equal or higher than the critical density of .8 μm laser ($1.6x10^{21}$ cm^{-3}), with control of density profile and density gradients

A liquid or high pressure gas precursor target (secondary target) that, when irradiated by the multi-MeV protons in the quasi-neutral energetic plasma generated by the interaction of the laser with the primary target, will result in production of more than $5x10^{11}$ ^{11}C molecules

A microfluidic system capable of transforming a purifying an injectable reagent using the isotopic product of the precursor.

The objective of the current DARPA/BTO program is to quantify by experimental and theoretical analyses the performance and scaling characteristics of elements 1-3 above. The complete MicroPET system will use microfluidic systems (element 4 above) that exist and are maturing rapidly for diverse applications.

This chapter is organized in three sections:

1) Characteristics of the quasi-neutral plasma jet and secondary target necessary to produce useful molecular imaging probes.
2) Laser and primary target performance characteristics needed to obtain the quasi-neutral plasma jet to achieve the activity required for the ^{11}C labeled molecular probe.
3) Scaling of the ^{11}C yield vs laser and primary target characteristics.

^{11}C production rates and quasi-neutral plasma jet requirements

Work presented in the chapters 5 and 6 shows that use of a secondary target of liquid N_2 doped with 0.5% O_2 using the $^{14}N(p,\alpha)^{11}C$ reaction is an excellent candidate for the complete system in part due to simple and swift isolation of the $^{11}CO_2$ product.

Specific activity, the fraction of molecules that are radioactive, is the most critical property of the radiotracer. High specific activity minimizes the amount of tracer that is required and maximizes the signal to background ratios. Minimizing the total amount of tracer is crucial in biological measurements where larger doses can perturb the biochemical balance of the subject. For example, typical molecules labeled with ^{11}C have specific activities of about 10mCi/nmole (370 MBq/nmole). Only one in a thousand of these molecules are labeled by ^{11}C; the rest contain ^{12}C.

The activity, A, of radiotracers in decays per second (dps) is given by

$$A=\ln(2)N/\tau$$

Here N is the number of activated atoms and τ is the isotope's half-life in seconds. The named unit for one decay per second (dps) is the Becquerel (Bq). An alternative unit often used in Curie (Ci) = 3.7 $\times 10^{10}$ Bq. The number of ^{11}C atoms N required to reach an activity level A in mCi is given b

$$N=\frac{1}{\lambda}\frac{dN}{dt}=\frac{(A/mCi)\times 3.7\times 10^{7}\,dps}{\ln 2/1.2\times 10^{3}}=6.4\times 10^{10}(A/mCi)$$

Approximate estimates of the proton energy and flux required to achieve an activation intensity A, for example 1mCi that corresponds to the production of 6.4x1010 11C atoms, can be found by referring to Figs 1-3. Fig.1 gives the cross section of the $^{14}N(p,\alpha)^{11}C$ reaction as a function of energy. Only protons with energy exceeding 5 MeV will participate in the production of radioactive carbon. However, energies in the range of the maximum cross section of 8 MeV and 10-12 MeV will be sufficient.

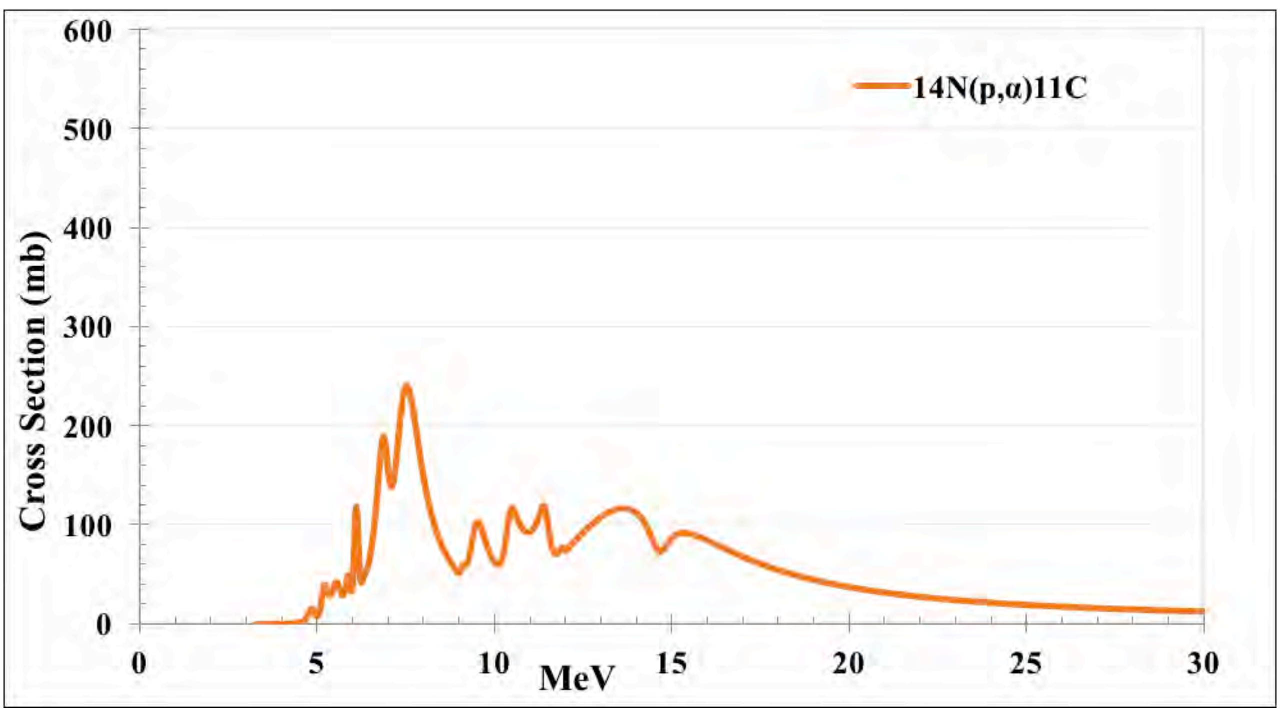

Figure 1: Cross section of $^{14}N(p,\alpha)^{11}C$ reaction as a function of proton energy

The efficiency with which proton flux is converted to ^{11}C activity is calculated with the GEANT4 code [1]. This code simulates the interaction of energetic particles with matter. It has been successfully applied to problems in high energy, nuclear, and accelerator physics, as well as medical and space science. Detailed descriptions of the algorithms and numerics can be found in Agostinelliae et al. [1] and Allison et al. [2]. GEANT4 is an open source software toolkit developed by a multinational collaboration (CERN, Fermilab, SLAC, KEK, ESA etc.) and is maintained by the international consortium members. The code provides a complete set of tools for building geometry, assigning materials, simulating events, tracking particle histories, and visualization of the results. It makes use of the "G4TENDL"[3] dataset that allows calculation of isotope production yield for incident protons with energy up to 200 MeV. We have calculated using these methods and plotted in Figure 2 the activation probability as a function of proton energy. The activation probability was computed by considering mono-energetic protons incident on ^{14}N thick secondary target. Although protons with energy above 8-10 MeV have slightly higher conversion efficiency, a proton distribution centered around 7.5-8 MeV will require 2.5-5x10^3 protons to create on atom of ^{11}C.

Another important characteristic of radioisotope production is the saturation yield as a function of the incident proton energy E, defined as:

$$\text{Saturation yield} = A_o/I(1-\exp[-t/\tau])$$

where Ao is the is the activity of ^{11}C at the End Of Bombardment (EOB); I is the number of incident protons of energy E per second; and t is the irradiation time. In other words, the maximum amount of radioisotope that can be produced represents a balance between production by proton current and decay by emission of radiation. The term $(1-\exp[-t/\tau])$ represents the growth of the radioisotope activity during an irradiation time t; it approaches unity as t increases beyond a few times τ. No matter what proton current is used there will be diminishing returns of ^{11}C after two hours, and 75% of the saturated activity is reached in 40 minutes. These considerations are important factors constraining energy per pulse and repetition rate of the MicroPET laser. An indication of the energetic proton flux required to achieve useful levels of saturated activity is shown in Figure 3. For example, 1011 protons per second (17 nA) with average energy of 7.5 MeV produces approximately 10 mCi of 11C.

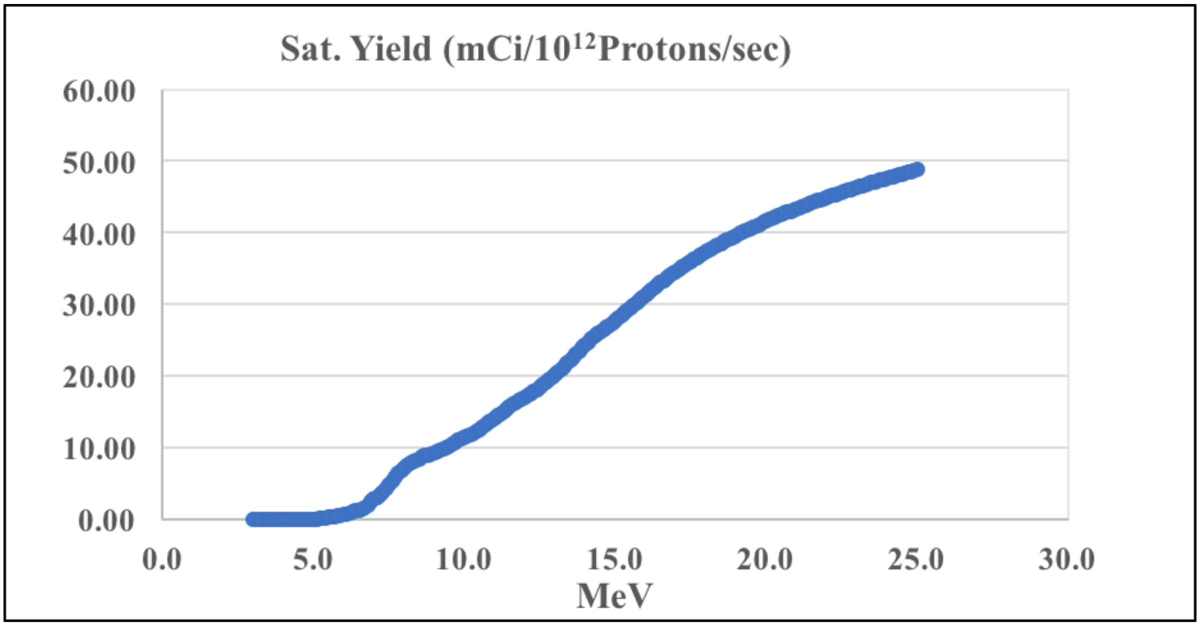

Figure 3: Saturation Yield of the $^{14}N(p,a)^{11}C$ reaction as a function of proton energy.

Laser and primary target characteristics that optimize the directed flux of energetic protons

Given the fundamental constraints imposed by radioisotope production and decay summarized above we consider next the roles played the laser and primary target characteristics needed to produce a plasma jet that meets the MicroPET objectives. We focus specifically on overall energy transfer from the laser pulse to ^{11}C atoms . What combination of laser and primary gas target parameters maximize the yield of ^{11}C atoms for fixed laser energy? The experimental work has all been conducted with Ti:Sapphire laser pulses whose wavelength is 0.8 μm. The energy per pulse, intensity profile, pulse duration and repetition rate are all important. The primary target is characterized by the ratio of the maximum number density to the laser critical density $n_{c\approx}10^{21}$ #/cm^3, the target length, target transverse width, and the density gradients at the entrance and exit planes of the laser pulse. Milestone Report # 4) focused surveyed physics aspects of a short pulse, high power laser interacting with gaseous target with ~100 μm dimensions. Important features different from those found in the literature for lasers impinging on solid targets were:

- A plasma waveguide follows the laser focus in the plasma target and guides the laser through the target;
- Large amplitude (over 5x10^3 Tesla) azimuthal, quasi-stationary, self-generated magnetic fields surround the wall of the plasma channel and the plasma-vacuum interfaces;
- Multi-MeV electrons are heated by the laser-plasma interaction in the waveguide. The relativistic electrons are confined by the self-generated field and guided towards the plasma-vacuum boundaries;

- The most important proton acceleration occurs by the expansion of the hot electron plasma at the plasma-vacuum boundaries. Although conceptually like Target-Normal Sheath Acceleration (TNSA), the expansion is modified by the effect of the magnetic field on the hot electrons at the plasma boundaries;
- Maximum proton acceleration occurs at the plasma-vacuum boundary with the highest electron temperature;
- Maximum proton acceleration at the front plasma-vacuum interface occurs when the laser energy deposition length L_H is comparable to the target length L;
- The energy deposition length L_H can be controlled by using a combination of focusing optics and plasma target profiles that focus the laser close to the middle of the target. Use of a slightly subcritical peak density results in pulse group velocity in the forward direction favoring hot electron generation close to the front boundary between the plasma and vacuum; and
- Filamentation can be inhibited by matching the numerical aperture of the input optics to the numerical aperture of the plasma waveguide, or by choosing the plasma target aspect ratio.

We refer the reader to Milestone report 4 for details of the laser-target interaction physics. The emphasis of the present report is on:

(i) Quantification of the performance and scaling of the essential elements of pulsed laser proton acceleration from H_2 jets that can be used in the engineering design of the MicroPET system; and

(ii) Comparison with the experimental results in the range < .5 J/pulse accessible by our current laser.

In this section, we study the maximum proton energy and average proton energy, proton distribution function, and conversion efficiency from laser power to energetic proton flux collimated in the forward direction within ±20° from laser as a function of energy per laser pulse. The study used two-dimensional simulations (see Milestone report #4). A list of the simulation parameters, ID numbers, and the key results are in Table I. Columns 2-4 list the laser energy per pulse, the pulse length, and the value of the vector potential α. Columns 5-7 list the length L, the transverse size D, and the ratio of the peak density n to the critical density n_c of the primary target. The results presented here all have $n/n_c=0.5$ as we have found higher values contribute to undesirable plasma filamentation. The laser wavelength is $\lambda=1\mu m$ corresponding to critical density $n_c=1.8x10^{21}$ #/cm^3 and the plasma target profile is super-Gaussian with n=6. Columns 8-10 list the parameters of the forward accelerated protons collected in a solid angle of 0.38 sr (+/- 20^o from the laser axis). Column 8 gives the average energy in this jet and column 9 shows the efficiency with which laser energy accelerates protons in the required direction. Column 10 summarizes the number of energetic protons contained in the collimated beam normalized to $5x10^9$ protons at an energy 1J per pulse.

The maximum proton energy, defined here as the 95th percentile of the proton distribution function, the average energy of the protons collimated in a 0.38 sr forward cone, and the laser-to-proton energy conversion efficiency are the most important merit functions. As these simulations use 'superparticles' to represent the physics some caution is necessary when interpreting the numerical results. Table I shows correct parametric scaling of the real values and are anchored to experimental data from solid target studies.

ID	**E_L J**	**T_L fs**	**a**	**L µm**	**D µm**	**n/n_c**	**<E> MeV**	**Efficiency**	**protons (*5*10^9)**
27A	.5	200	3.1	40	50	.5	2.01	0.22%	0.694
27B	1	200	4.4	40	50	.5	4.00	0.32%	1.000
27C	2	200	6.2	40	50	.5	6.85	0.35%	1.268
27D	3	200	7.6	40	50	.5	8.34	0.32%	1.426
29A	3	100	10.7	40	50	.5	6.69	0.27%	1.512
29B	3	50	15.2	40	50	.5	6.40	0.27%	1.560
29C	3	30	19.6	40	50	.5	7.23	0.33%	1.694
30A	3	200	7.6	50	50	.5	7.37	0.30%	1.522
30B	3	200	7.6	60	50	.5	7.53	0.31%	1.542
30C	3	200	7.6	70	50	.5	7.13	0.28%	1.476
28A	.125	200	1.6	40	50	.5	0.86	0.07%	0.121
28B	.25	200	2.2	40	50	.5	1.28	0.16%	0.378
28C	.375	200	2.7	40	50	.5	1.79	0.21%	0.540

Table I: Particle-in-cell parameters

Figure 4 shows the average energy of collimated protons versus energy per pulse for a common pulse length of 200 fs (RUNS 27, 28, 30). Laser pulses with energy below 1J will produce few protons with energy above the threshold required to produce ^{11}C. The blue markers at 3J per pulse in Fig.5 are results from RUN30, with target lengths L=50, 60 and 70 μm, while the red markers used in RUNS27 had L=40 μm. This scaling indicates the importance of adjusting the target thickness to the pulse duration to optimize acceleration of protons.

The collimated proton distribution functions associated with the simulation parameters used in Figure 4 are shown in Figures 5 and 6. These proton distributions will be used in the Section 4 to compute the ^{11}C atoms per pulse as a function of laser energy and target parameters.

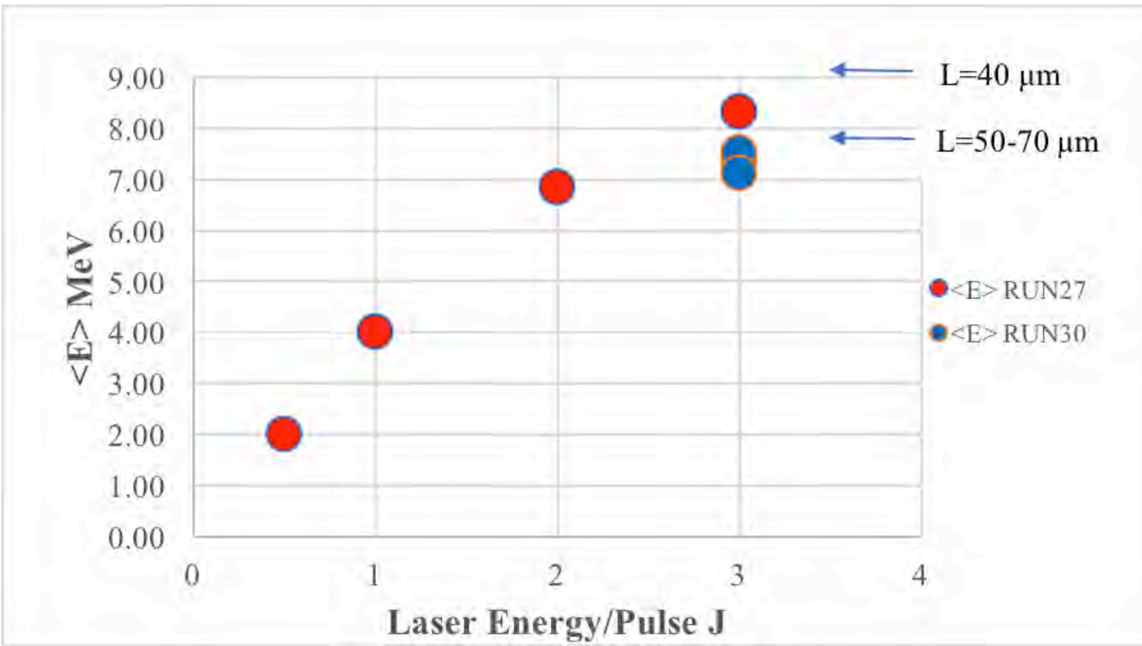

Figure 4: Average energy of the forward collimated (0.38 sr) energetic protons. Saturation begins above ~2J per pulse. Blue marks refer to average energy for target lengths longer than 40 μm used in RUN27, resulting in lower average energy.

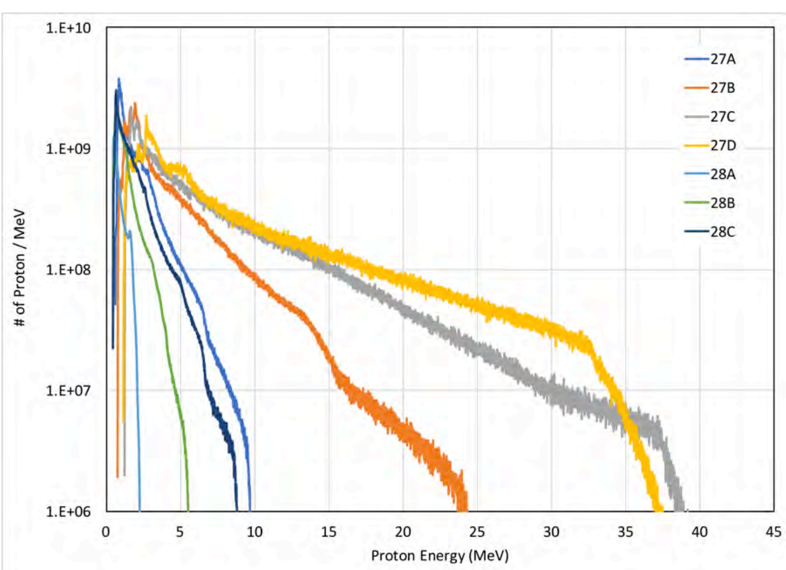

Figure 5: Forward collimated proton distribution functions normalized to 5x10⁹ protons for energy per pulse from .125 J to 3 J. Notice that only the last three have significant number of protons with energy more than 5MeV.

Figure 5 shows the collimated proton distribution functions for laser pulse energies from .125J to 3J as a function for primary target dimensions L=40 μm, D=50 μm. Laser pulse energies less than 1J yield too few protons with energy above 5 MeV that ultimately produce ^{11}C.

Figure 6 shows the forward collimated proton distribution functions for 3 J per pulse and T=200 fs for several primary target lengths L=40-70 μm and D=50 μm (RUNS 27D, 30A-C). The average proton energy for the thin primary target (L= 40 μm) is higher than the thicker targets despite the lack of high-energy tail in the resulting proton distributions. Furthermore, as shown in Section 4 below, the thin target is optimally matched to the ^{11}C activation per proton shown in Figure 2. This is because, as detailed in Milestone 4 report, the distance between the laser self-focusing location and the end of the primary target matches the laser energy deposition distance at L=40 μm.

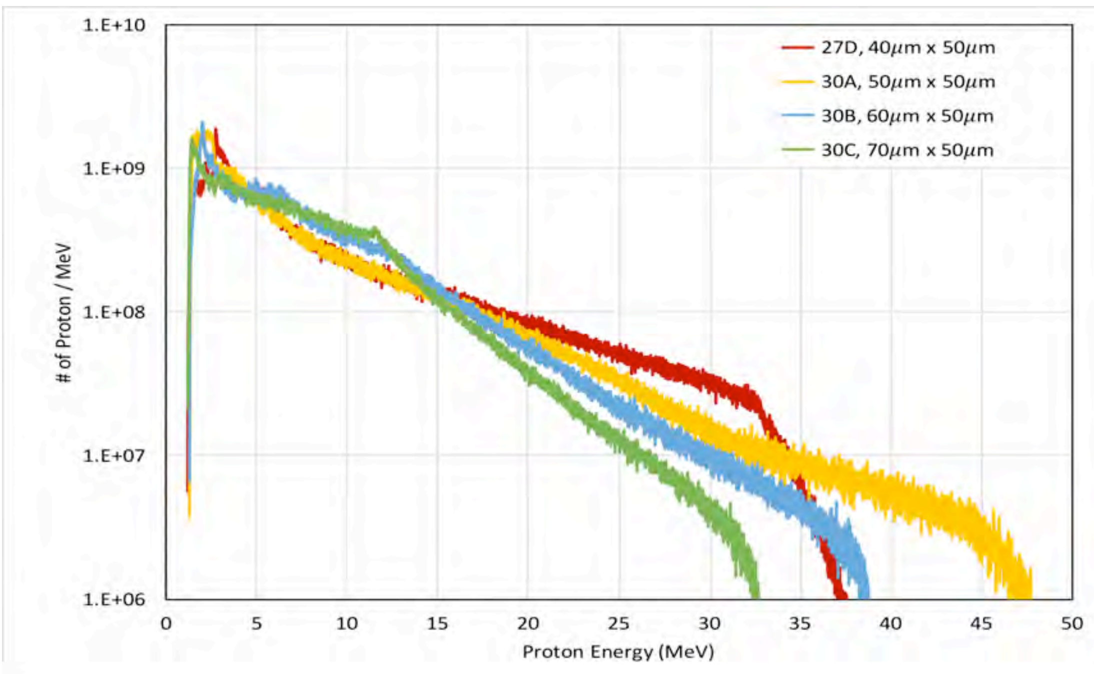

Figure 6: Forward collimated proton distribution functions for 3J energy per pulse, T = 200 fs but L= 40-70 μm.

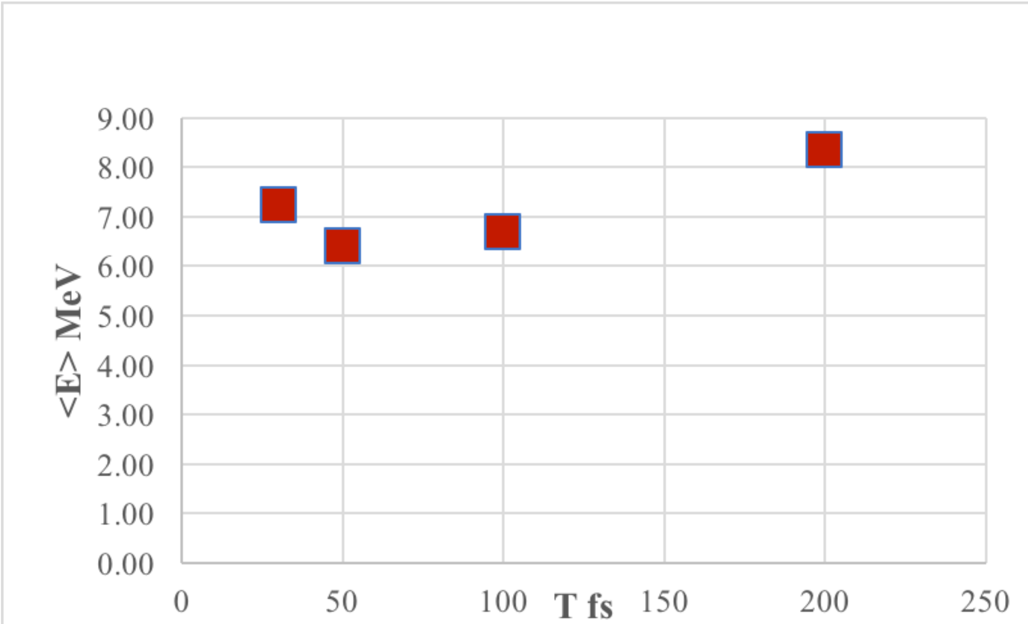

Figure 7: Average energy of forward collimated protons as a function of laser pulse length as a function of pulse length for at 3J per pulse.

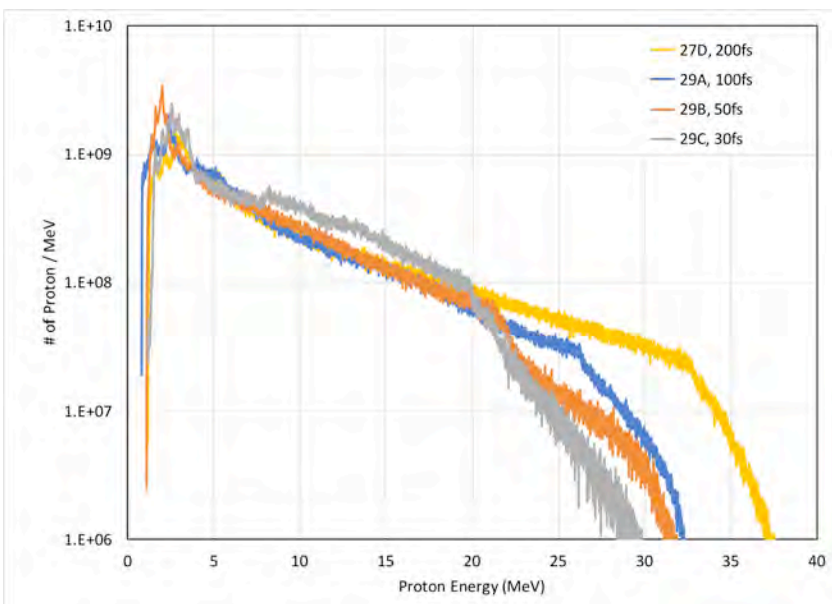

Figure 8: Forward collimated proton distribution function for 3J energy per pulse, L=40 mm, D=50 mm for pulse lengths 30, 50, 100 and 200 fs, corresponding to values of a=19.6, 15.2,107 and 7.6. Contrary to the conventional wisdom optimum distribution is obtained at 200 fs with a=7.6.

Figure 7 evaluates pulse length, or equivalently the vector potential α, for the case of 3J per laser pulse (Runs 27D and 29A-C). The highest average energy is obtained for the longest, 200 fs pulse. The corresponding collimated energetic proton distributions are shown in Figure 8, confirming the superior performance of the 200 fs pulse despite its having the lowest vector potential α. We attribute this effect to the two-step acceleration mechanism discussed in our previous report and illustrated in Figure 9. At the shortest, T=30 and 50 fs, pulse durations the proton distribution function is dominated by Target Normal Sheath Acceleration (TNSA) that scales with the value of the vector potential α. While this delivers energetic protons on a volume averaged basis it yields much smaller intensity collimated in the forward direction. Longer pulses, especially here at T=200 fs, enhance the directed flux. The predominance of the collimated protons is driven by a second mechanism operating on the TNSA accelerated protons. This mechanism combines the self-generated magnetic fields and ambipoplar electric fields, operates on timescales up to 900 fs, and forward-directed proton fluxes.

Figure 9: A comparison of the forward collimated energetic protons to the total number of energetic protons outside the target. Notice that the ratio of forward to total increases with the pulse length. Detailed analysis of the runs indicates that before t=.9 ps the number of collimated is relatively small but later in the run a significant number of the protons energized by the TNSA process enters the second acceleration mode controlled by the self-generated magnetic fields.

Figure 10 shows the effect of pulse energy on the average proton energy and the proportion of high-energy collimated protons, scaled to $5x10^9$ protons per second at 1J. The number of high energy collimated protons increases faster than the average energy for pulses up to ~2J, while the trend reverses at higher pulse energies. This impacts the design of the MicroPET system.

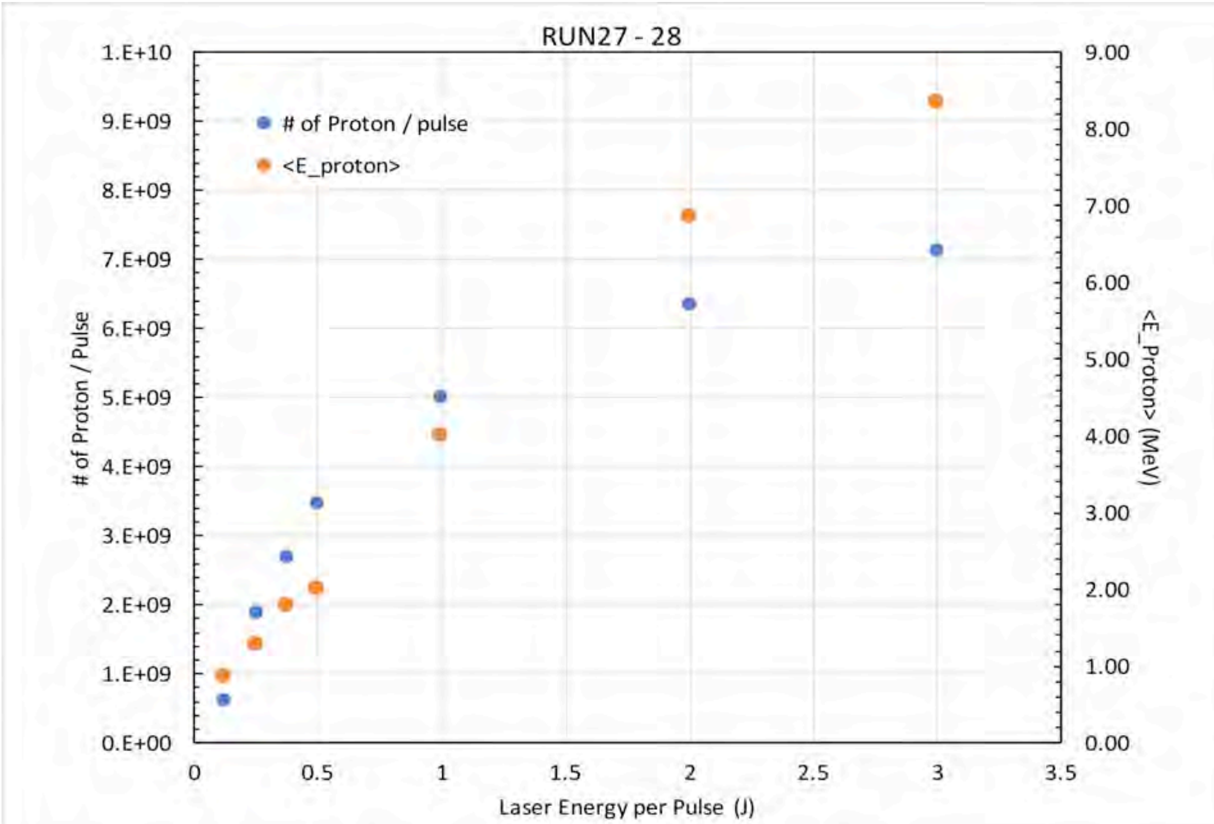

Figure 10: Average energy per proton and number of energetic proton collimated in the forward direction as a function of energy per pulse. The slope of the proton yield changes abruptly above ~1 J per pulse.

The useful flux for generating PET isotopes increases nonlinearly with both proton yield and average energy. The combined impact of pulse energy on these factors leads to a local maximum in the efficiency with which laser energy is converted to useful proton flux. This maximum occurs for the collimated proton flux at a pulse energy of ~2J, as shown in figure 11 below.

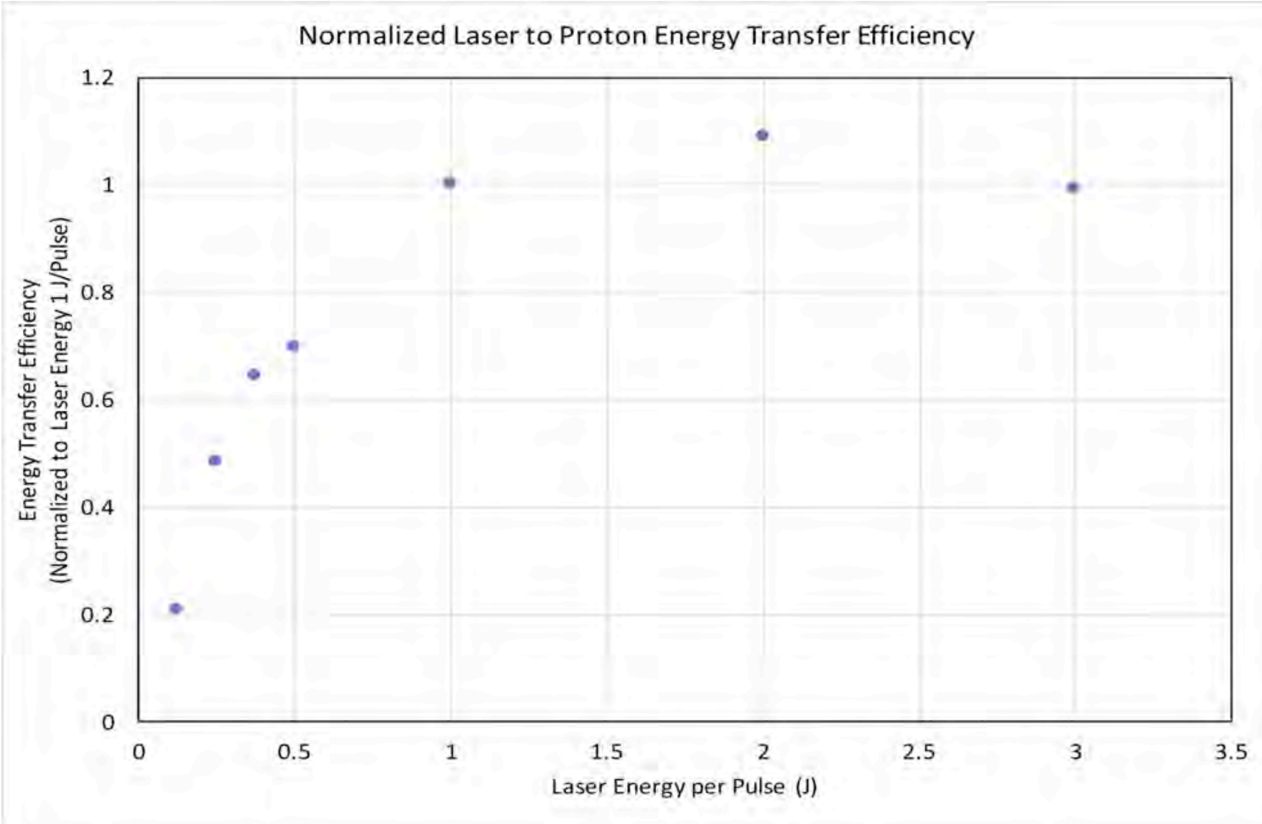

Figure 11: Relative laser-to-protons collimated forward efficiency as a function of energy per pulse, indicating optimal operation near 2J per pulse.

Summarizing, the laser-generated plasma jet requires matching the target thickness to the laser pulse energy and duration to drive the two component acceleration mechanism and efficiently generate a directed flux of useful protons.

Study of C11 conversion efficiency and input to system design

Combining the results of the previous sections leads to calculation of the ^{11}C yield per pulse. We use the GEANT4 code with the distribution functions for forward collimated protons shown in Figure 6 and 7. This procedure assumes that ^{14}N secondary target is thick, in other words, its longitudinal length degrades the energy of the irradiating flux to below the threshold for the nuclear reaction, in this case 5 MeV. As detailed in chapter 7, this corresponds to a less than 1 mm for a liquid N_2 target and below 1 cm for gaseous secondary target pressurized to 100 atmospheres. Figure 9 shows the yield per pulse as a function of the energy per pulse. Notice that the yield increases linearly with the value of the energy per pulse but saturates above 2J per pulse, indicating optimal efficiency at 2J per pulse. This is consistent with the insights described in section 3, Figure 11.

Additional scaling of ^{11}C yield at per 3J pulse with target thickness and laser pulse length are shown in Figures 13 and 14. These reflect the physical mechanisms described in connection with figures 7 and 6, respectively, and support the conclusion that a precise match between primary

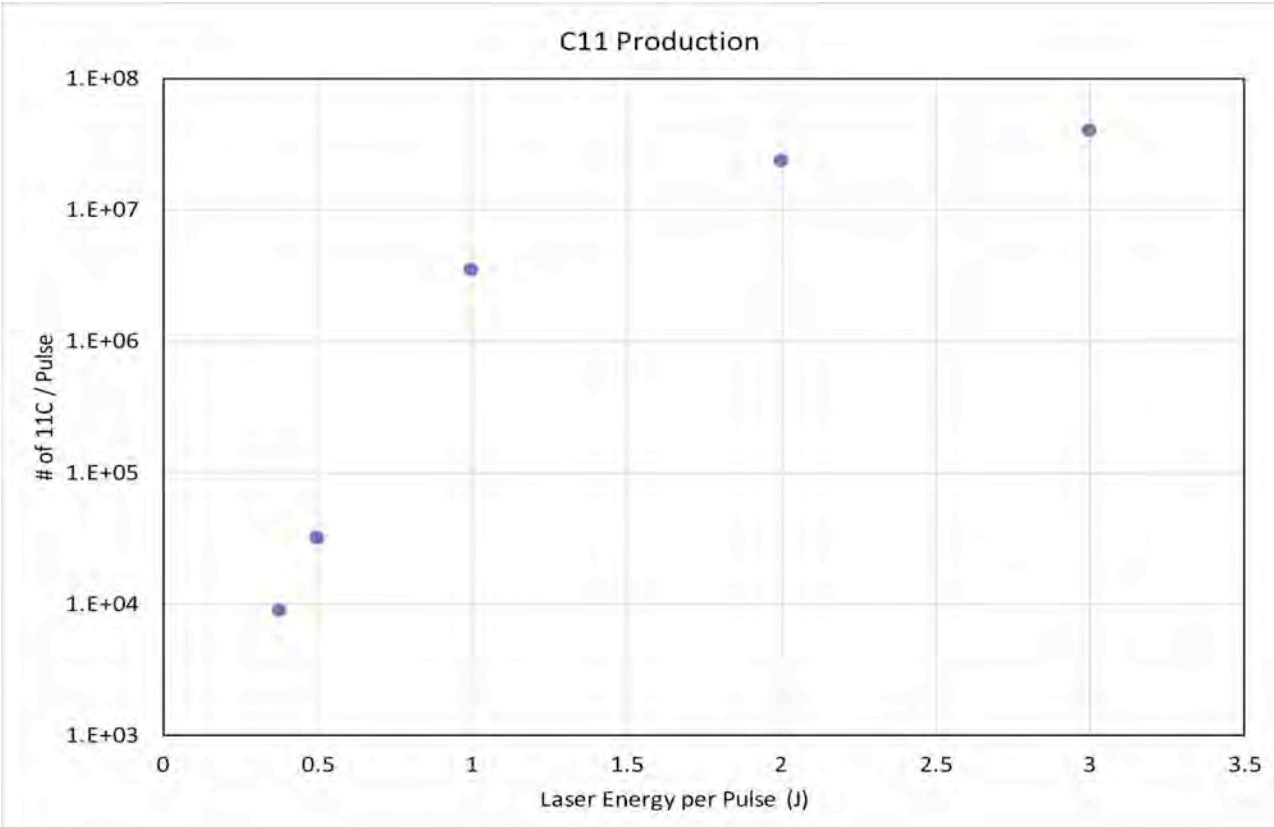

Figure 12: Scaling of C11 production yield with the energy per pulse. Notice similarity with the scaling of the average energy shown in Figure 4.

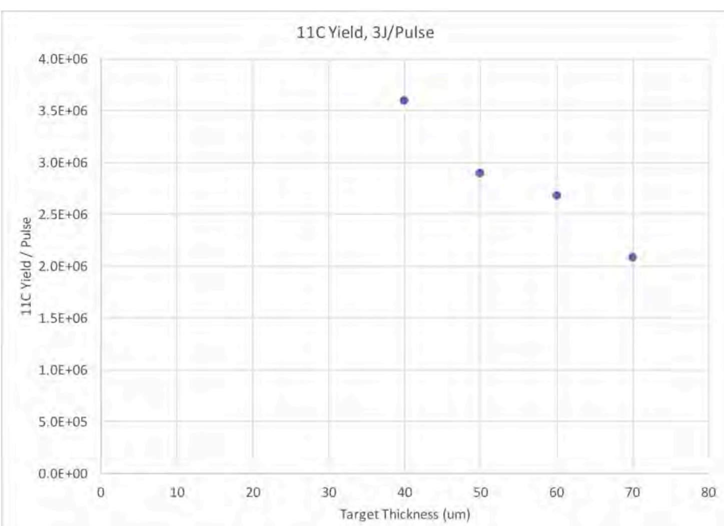

target conditions, laser pulse configuration, and secondary target geometry is important to the efficient production of radioisotopes from quasi neutral plasma jets.

Figure 13: Scaling of the C11 yield with primary target length for 3J per pulse, indicating optimal operation at 40μm, consistent with the results of Figure 4

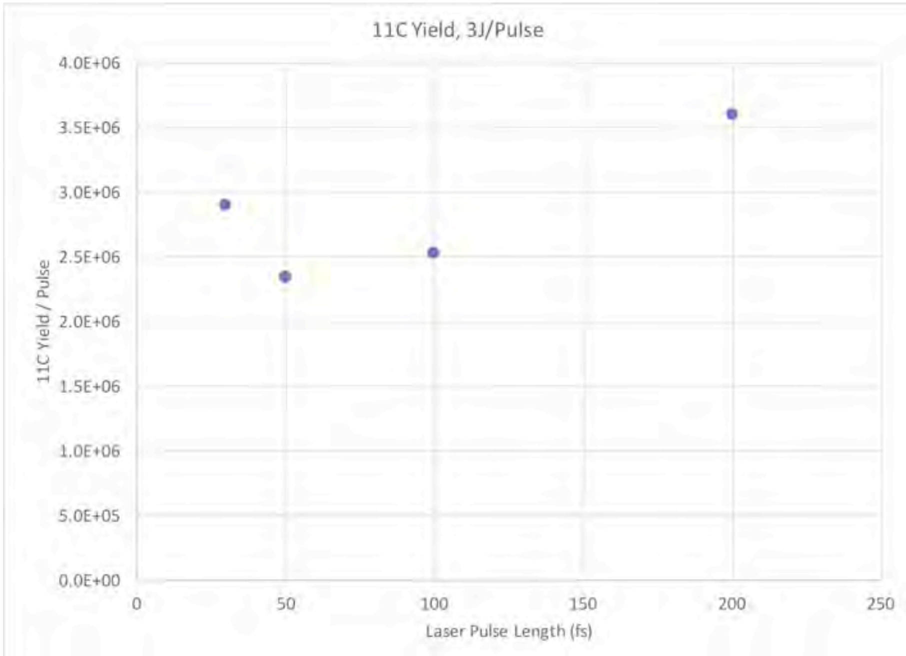

Figure 14: C11 yield vs pulse length for 3J per pulse.

Figure 15 explores the pulse rate and energy per pulse required to achieve specified activity after one hour of irradiation, corresponding to approximately three ^{11}C half-lives. This figure combines the essentially nonlinear dependence of useful yield on the physics of the plasma jet and secondary target on one hand and the competition between production and radiative loss.

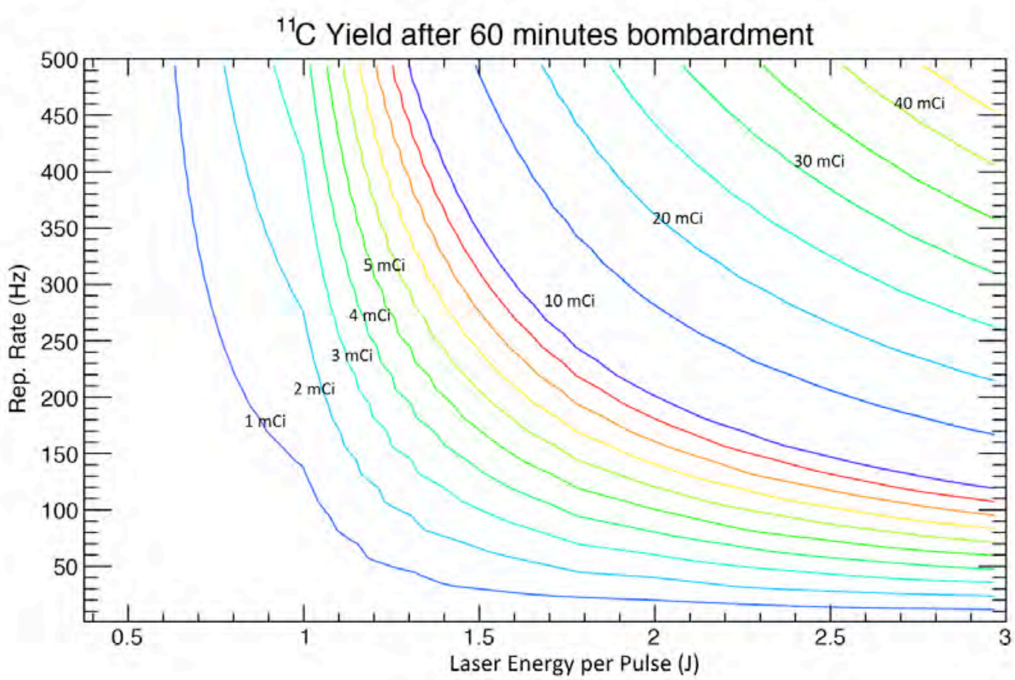

Figure 15: Isocontours of ^{11}C activity obtained in one hour of irradiation for various pulse rate and energy per pulse combinations. These can be used in designing strawman MicroPET operating systems.

The results discussed here are based primarily on two-dimensional particle-in-cell simulations. These are consistent with the mechanistic insights gleaned from fully 3-d simulations (Appendix) that are computationally very intensive and therefore infeasible for systematic parametric analyses.

This study of performance and scaling characteristics of the quasi neutral plasma jets has revealed that the available laser facility at UMD is not quite powerful enough to produce measureable amounts of ^{11}C. However, the understanding we have gleaned supports the prospect of successful demonstration and development with a slightly more powerful laser system.

References:

1) S. Agostinelliae *et al.*, Geant4—a simulation toolkit, Nucl. Instr. and Meth. A, 506 (2003) 250–303.
2) J. Allison *et al.*, Geant4 Developments and Applications, IEEE Trans. on Nucl. Sci., Vol. 53, No. 1, (2006)
3) http://geant4.cern.ch/support/datafiles_origin.shtml

Chapter 9: N_2/O_2 target design and interaction scaling report

Gas or Liquid N_2 with trace O_2?

The positron emitting isotope of carbon, ^{11}C, is conventionally produced by irradiating a N_2:O_2 gas mixture in a cell with a beam of high energy protons through a thin metal window. The absorption of an energetic proton by the stable ^{14}N isotope triggers a nuclear reaction that produces an alpha particle (^{4}He) and ^{11}C nucleus. The presence of trace (0.5-2%) oxygen captures this carbon atom as ^{11}CO and $^{11}CO_2$ which can then be trapped in a molecular sieve or by condensation on a cold finger.

Cyclotron ion beams spread within a cylindrical gas target through scattering and absorption, so conical rather than cylindrical target cells can maximize the specific activity of the resulting gas. The average current of cyclotron sources (tens of μA) and the low thermal conductivity of N_2 gas, even at the 20 bar pressures often employed, have inspired complex internal cell designs to control convective heat transfer to the walls, as shown in figure 1.

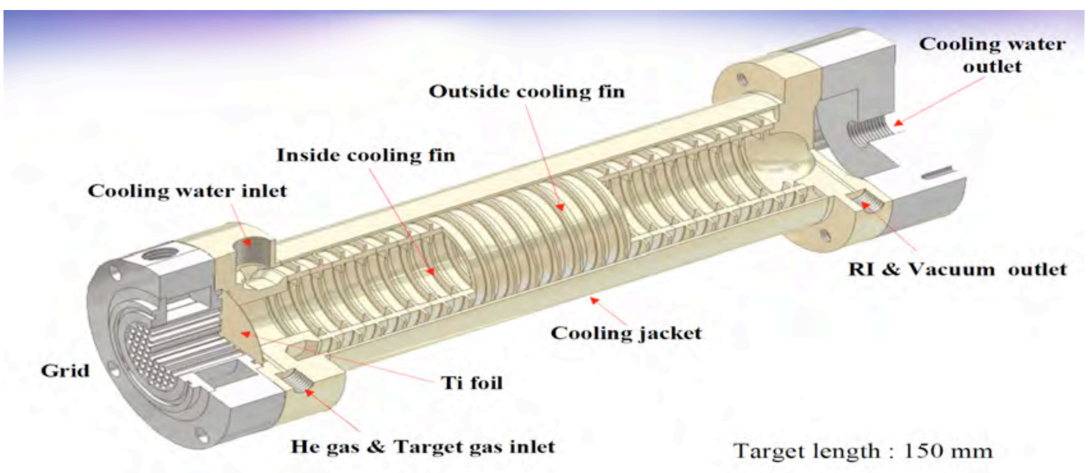

Figure 1: High pressure cell design for production of $^{11}CO_2$ from N_2:O_2 gas mixtures from a presentation by Hur.[1] The fins are devised to improve the surface area for convective heat transfer to the walls.

---

[1] Hur, Min Goo, The Carbon-11 Gas target Design with Cooling Fins at the Cavity for High Production Yield, Korea Atomic Energy Institute, 2010 at http://www.intds.org/TALKS-2010/Hur_C11-1.pdf. (copy appended)

The MicroPET approach generates pulses of protons with broad energy distributions that make more efficient use of the cross-sections for production of ^{11}C shown in figure 2.

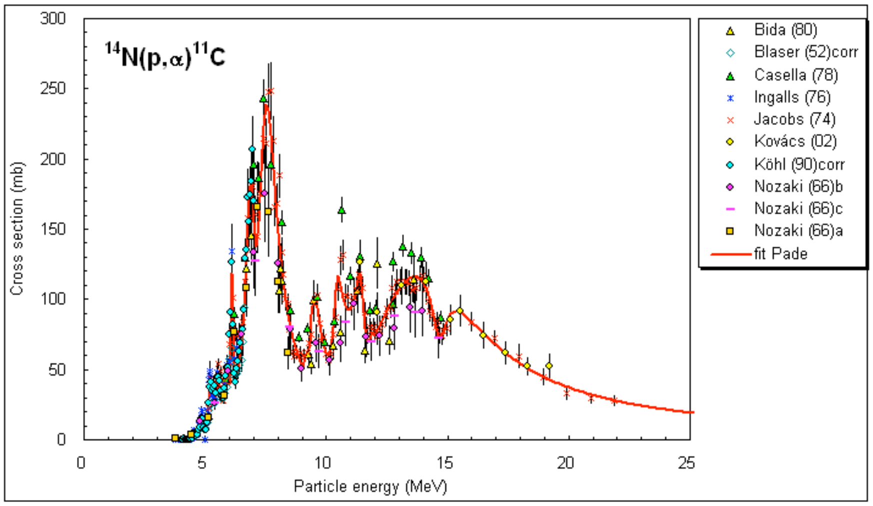

Figure 2: Recommended cross-section for production of ^{11}C from ^{14}N.[2]

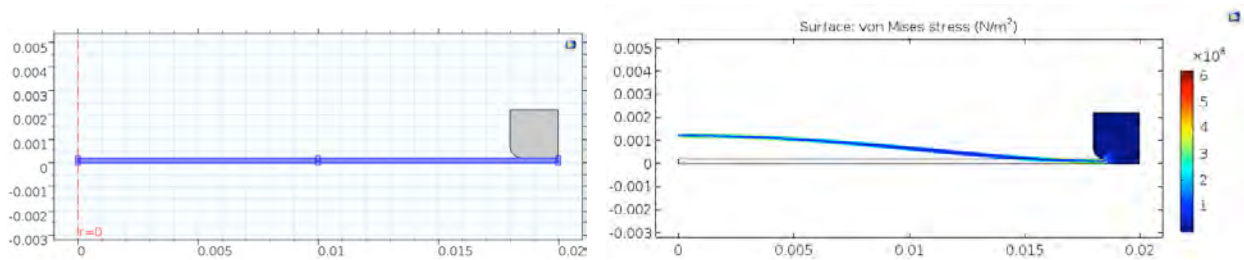

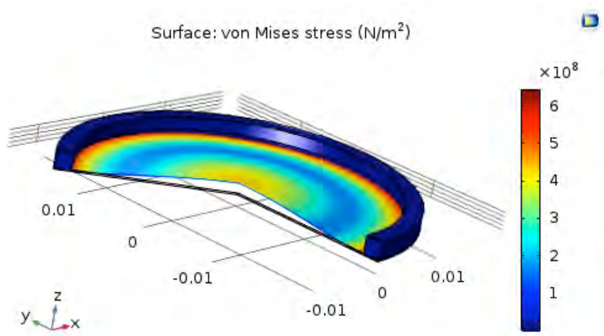

Figure 3: Cross-sectional view of the radially symmetric window configuration. (top left): Havar window 200μm thick and 4 cm diameter clamped by a filleted steel ring. (top right) Stress and strain of a cross-section in the cylindrically symmetric configuration at 10 MPa (100 bar) pressure. (left) Stress and strain on the window at 10 MPa. The yield strength of Havar is $2.3x10^9$Pa, so the design safety factor is 4 in this configuration.

As described in the companion milestone reports the distribution of ion energies and angular trajectories is substantially broader from the quasi-neutral plasma jet. We have therefore explored a target cell that has smaller axial extent and higher gas pressures to optimize the specific activity of the product. A window made of Havar (a

[2] N. Soppera, E. Dupont, M. Bossant, **JANIS Book of proton-induced cross-sections,** OECD NEA Data Bank, June 2012.

Co:Cr:Ni alloy) can withstand 100 atmospheres of pressure with minimal stress and strain, as can be seen in typical finite element results for a 0.2mm window 4cm in diameter in figure 3.

Figure 4 overlays the cross-section with a typical ion energy distribution into a solid angle of .038 sr from a 50 fs, 4×10^{19}W/cm^2 pulse hitting a target density of 2×10^{20} cm^{-3}. Monte Carlo scattering simulations show only modest shifts to this distribution on passing through 100 μm of Havar alloy.

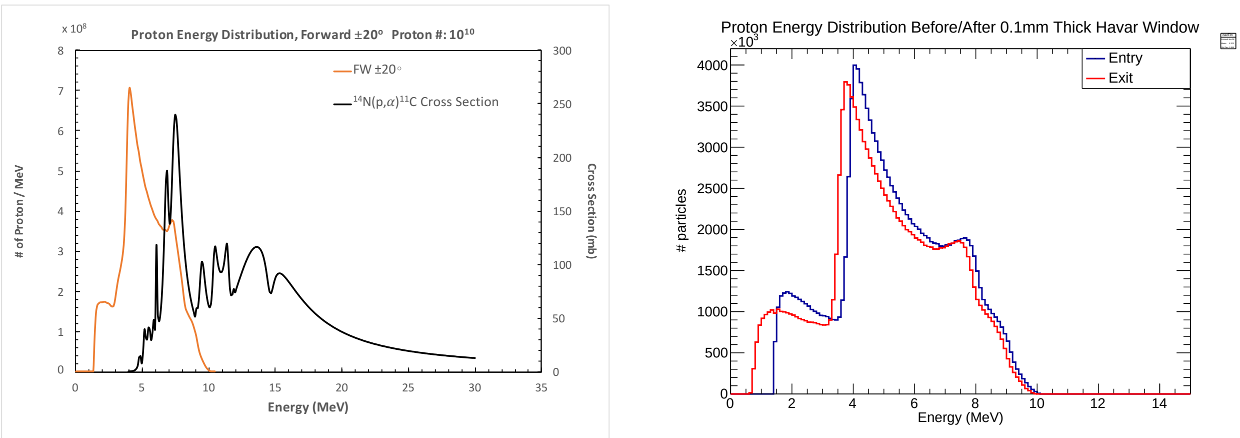

Figure 4: Proton energy distribution overlaid with the cross-section for ^{11}C production from ^{14}N (left) and its shifts on passing through 100μm of Havar alloy (right).

We next examine the rate of producing ^{11}C from the proton pulse whose energy distribution is shown in red, above, at 50 and 100 atmosphere pressure in figure 5. The volume required to efficiently convert protons to ^{11}C increases substantially as the target density drops from liquid to gas at 100 and then 50 atmospheres. Liquid nitrogen at 1 atmosphere pressure has density and thermal conductivity that are 7.5 times those of the gas at 100.

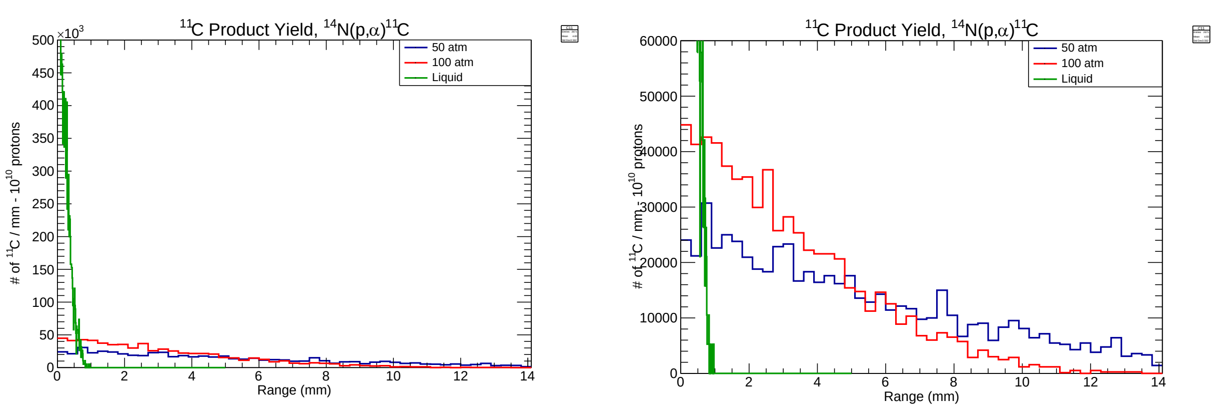

Figure 5: Range-dependent generation of ^{11}C for target gas at 50 and 100 atmospheres and a liquid nitrogen target (expanded view at right). Volumetric efficiency increases dramatically with target density.

The heat generated from by inelastic scattering of an incident quasi-neutral plasma jet (from the 50 fs pulse described above) in 100bar of nitrogen is shown in figure 6. The integral of this curve is about 3mJ per pulse, implying a heating rate of 30mW at 10 Hz, which in turn is enough energy to vaporize 150 mg of liquid nitrogen per second. This heating rate is easily matched by a thermoelectric cooler or thermal contact at the rear target surface with a bath of liquid nitrogen, making fins and elaborate high pressure target chambers unnecessary.

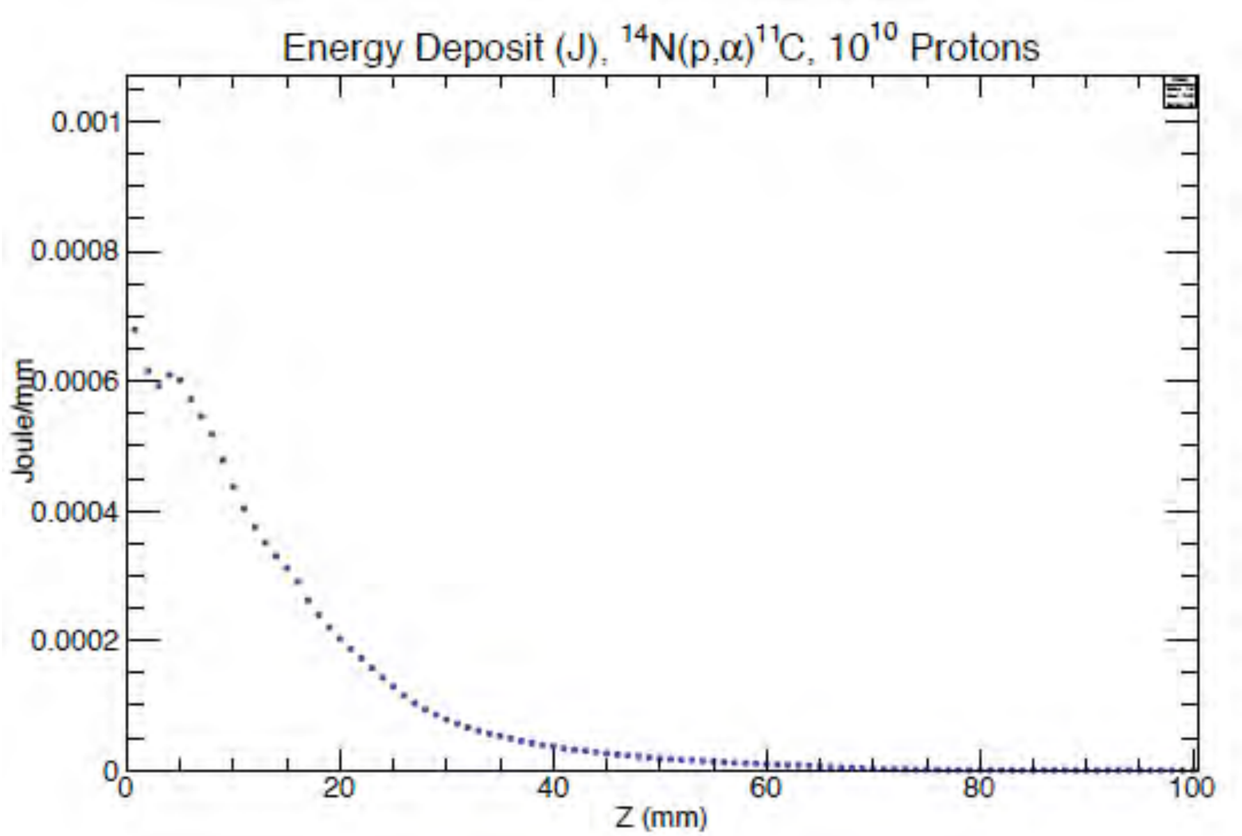

Figure 6: Energy deposition in 100 bar pressure N_2 gas from the quasi-neutral jet produced by the 50fs pulse described previously.

Target interaction scaling with plasma jet characteristics

Using the well-established cross-sections for generation of ^{11}C from protons we have explored the relationship between plasma jet parameters and isotope yield. Figure 6 shows a representative case where the 50 fs case described above is compared to a 300 fs, 2 x 10^{19}W/cm^2 pulse irradiates the same gas target. The total proton yield into .038 sr is about five times greater (5.5×10^9 versus 9.1×10^7) for this case, but the essential difference is the shift in the proton's energy distribution, which produces ten times the production rate per proton. The shifted distribution results from acceleration by a collapsing strong magnetic field that occurs only at longer pulse lengths. As seen graphically in figure 6, where the integral of the product of the cross-section and energy distribution yield these rates, the quasi-neutral plasma conditions can have a dramatic impact on the production efficiency of ^{11}C.

In other words, the scaling of the efficiency with which ^{11}C is produced in this configuration depends linearly on the integral of the product of the ion energy distribution and the proton capture cross section after accounting for window transmission effects.

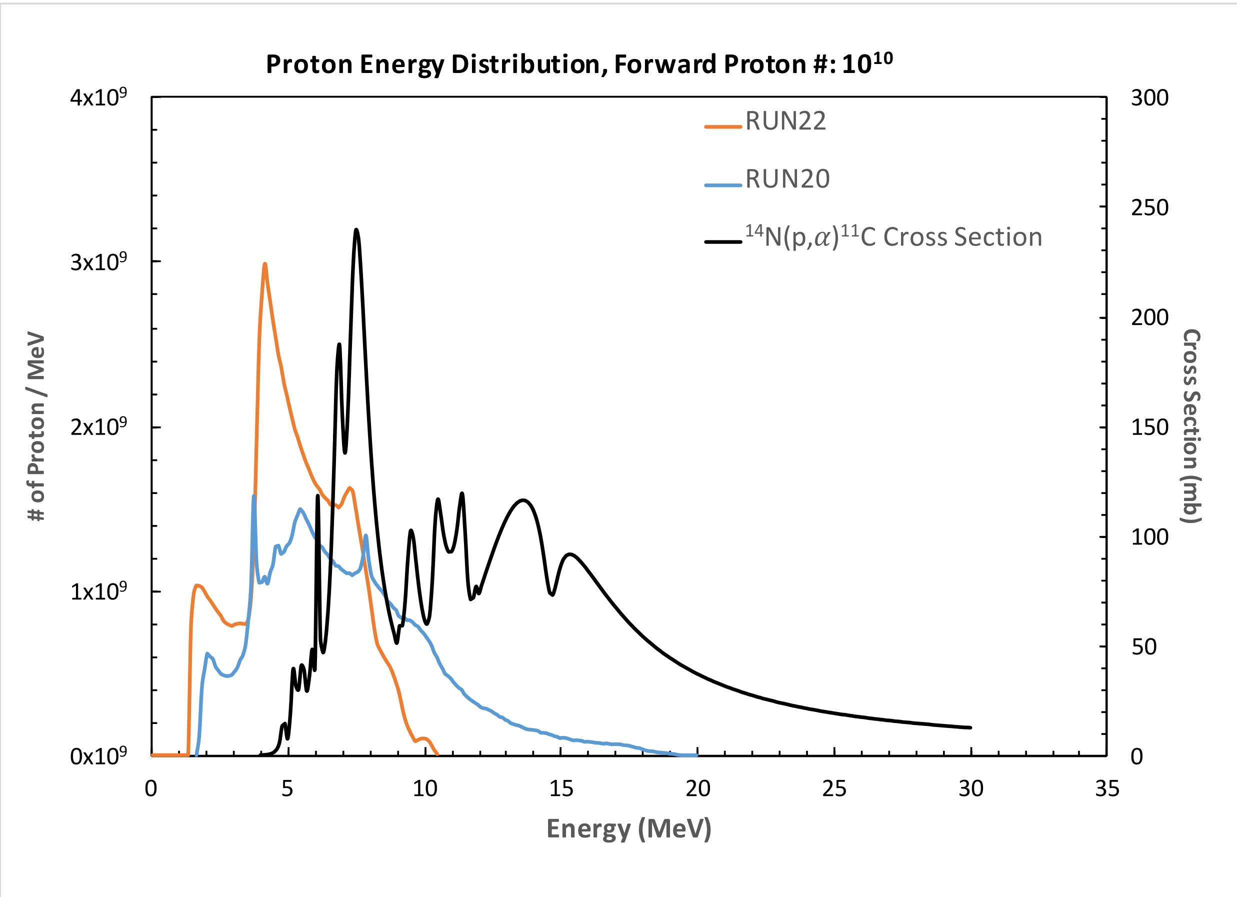

Figure 7: Ion energy distributions for a short pulse (RUN22: 50fs, $4x10^{19}W/cm^2$ and RUN20: 300fs, $2x10^{19}W/cm^2$) overlaid on the ^{11}C production cross-section. The rate of producing ^{11}C per proton is ten times larger for RUN20 than for RUN22.

Conclusion

The optimal configuration for a ^{11}C source is a cryogenic liquid N_2 disk with trace O_2 cooled by liquid nitrogen or a thermoelectric plate on the distal face and exposed to our quasi-neutral plasma jet through a 0.1-0.2mm thick Havar window. This configuration achieves excellent thermal control, conversion in a small total volume, and permits simple accumulation of the radiolabeled $^{11}CO_2$ in a frozen solid phase during exposure. The scaling of ^{11}C production with the fluxes from diverse quasi-neutral plasma jets is illustrated by showing an order of magnitude increase in efficiency when shifting from 50fs to 300fs optical pulses and accessing the collapsing magnetic field that is produced only in the latter case.

Appendices

1) A. J. Goers, Electron Acceleration by Femtosecond Laser Interaction with Micro-structured Plasmas, Dissertation, University of Maryland, College Park, 2015. PAGE 85-256
2) A.J. Goers, *et al.*, *Proton acceleration by multi-terawatt laser interaction with a near-critical density hydrogen jet,* Poster presented at the American Physical Society Advanced Accelerator Conference, Washington, D.C., July 2016. PAGE 257
3) A.J. Goers, *et al.*, *Proton acceleration by multi-TW interaction with a near-critical density hydrogen jet*, presentation at American Physical Society 16th Division of Plasma Physics meeting, San Jose, CA, November 2016. PAGE 258-273
4) G. Hine, unpublished notes on 3-D Particle-in-cell simulations of quasi neutral plasma jets., University of Maryland, College Park, December 2016 PAGE 274-282

ABSTRACT

Title of Document: ELECTRON ACCELERATION BY FEMTOSECOND LASER INTERACTION WITH MICRO-STRUCTURED PLASMAS

Andrew James Goers, Ph.D., 2015

Directed By: Professor Howard Milchberg
Department of Physics

Laser wakefield accelerators are promising alternatives to RF accelerator technology for compact sources of relativistic electrons. This dissertation presents three experiments using structured plasmas designed to advance the state of the art in laser based electron accelerators with the goal of reducing the energy of the drive laser pulse. First, guiding of relativistically intense femtosecond laser pulses in plasma waveguides is presented. Electron acceleration up to 120 MeV is observed from an ionization injected laser wakefield accelerator driven in a 1.5 mm long He-like nitrogen plasma waveguide. Second, progress toward a proof of concept demonstration of quasi-phase-matched direct laser acceleration (QPM-DLA) in a corrugated plasma waveguide is presented. In particular, guiding of a quasi-radially polarized femtosecond laser pulse, which provides the accelerating field in the QPM-DLA scheme, is demonstrated in a 1 cm long plasma channel. Finally, electron acceleration up to ~10 MeV is demonstrated using sub-terawatt drive laser pulses

interacting with a thin (~200 μm), high density (~10^{20} cm^{-3}) plasma. Electron acceleration in this experiment is observed with drive pulse energies as small as 10 mJ, opening the way for high repetition rate (~kHz) wakefield-accelerated electron beams with existing laser technology. A bright, coherent wave breaking "flash" is also observed and associated with the violent initial acceleration of the plasma electrons that are injected into the plasma wake. The flash bandwidth is consistent with half-cycle optical emission caused by the unipolar electron acceleration, and can radiate ~1% of the total drive laser pulse energy.

ELECTRON ACCELERATION BY FEMTOSECOND LASER INTERACTION WITH MICRO-STRUCTURED PLASMAS

By

Andrew James Goers

Dissertation submitted to the Faculty of the Graduate School of the University of Maryland, College Park, in partial fulfillment of the requirements for the degree of Doctor of Philosophy
2015

Advisory Committee:
Professor Howard Milchberg, Chair
Professor Phillip Sprangle
Professor Konstantinos D. Papadopoulos
Professor Ki-Yong Kim
Dr. Jared Wahlstrand

Dedication

For my darling wife, Chelsea.

Acknowledgements

I would like to thank Professor Howard Milchberg for the privilege of working and learning in his group over the past five plus years. Howard's drive and passion for physics is truly inspiring, and it is clear from working with him how much he wants his students to succeed. I truly appreciate the confidence and trust he has placed in my abilities as a scientist.

I would like to thank Yu-Hsin Chen and Brian Layer for working with me and getting me up to speed during my first year in the lab. I had the honor of sharing many late nights (sometimes into early mornings), frustrating days, and the joy of discovery and success with Sung Yoon, Jennifer Elle, and George Hine. Collaboration with you three has made graduate school rewarding beyond simple academic terms. Our next generation of graduate students Linus Feder, Bo Miao, Fatholah Salehi, and Daniel Woodberry have already proven to be creative and capable scientists. Howard's lab is definitely on a track to continued success with your talents, and I am happy to call you all friends. I would also like to thank the crew from Small Lab, Dr. Jared Wahlstrand, Sina Zahedpour, Eric Rosenthal, Nihal Jhajj, and Ilia Larkin for a fresh perspective over lunch or Town Hall breaks. I'm also grateful to the IREAP facilities and administrative staff for their assistance and support; in particular Nolan Ballew, Jay Pyle, and Bryan Quinn have always been happy to help when I've needed advice or assistance with mechanical projects.

Finally, I would not have been able to complete this endeavor without all the encouragement and support provided by my wife, Chelsea Goers, and my parents, Steven and Willona Goers. We did it. Woot!

Table of Contents

Dedication ii
Acknowledgements iii
Table of Contents iv
List of Figures 1
Chapter 1: Introduction 7
1.1 Motivation and outline of the dissertation 7
1.2 Laser wakefield acceleration 11
1.2.1 The ponderomotive force 12
1.2.2 Laser wakefields 14
1.2.3 Pulse propagation and self-modulation 19
1.2.4 Electron injection 22
1.2.5. Acceleration limits and dephasing 25
1.3 Quasi-phase-matched direct laser acceleration 27
Chapter 2: The UMD 25 TW Laser System 33
2.1 Overview of high peak power, femtosecond laser systems – Chirped Pulse Amplification and Ti:Sapphire lasers 33
2.2 UMD 25 TW Ti:Sapphire Laser Architecture 34
2.3 Spectral phase compensation using an acousto-optic modulator 40
2.3.1 Dispersion and higher order spectral phase in femtosecond laser pulses .. 40
2.3.2 Second harmonic FROG 43
2.3.3 Spectral phase compensation with an acousto-optic programmable dispersive filter 47
2.4 Laser pre-pulse characterization by third order autocorrelation 51
2.5 Laser wave front correction using an adaptive optics loop 55
2.5.1 Diffraction limited focusing, M^2, and Strehl ratio 55
2.5.2 Correction of laser phase front aberrations using closed loop adaptive optics 56
2.6 Measurement of spatiotemporal effects 61
2.7 Modelocked Nd:YAG Laser System 63
Chapter 3: Optical guiding at relativistic intensities in cluster-based plasma channels 65
3.1 Introduction to plasma channel guiding 65
3.1.1 Self guiding and relativistic self-focusing 66
3.1.2 Optical guiding in pre-formed plasma waveguides 68
3.2 Plasma waveguides generated in clustered gas targets 72
3.2.1 Advantages of using cluster based targets 72
3.2.2 Demonstration of efficient coupling into a cluster based plasma channel. 74
3.2.3 Measurement of nearly pure N^{5+} plasma waveguides 78
3.3 Guiding at relativistic intensities in pure N^{5+} plasma waveguides 80
3.4 Ionization injected wakefield acceleration in an N^{5+} waveguide 82
Chapter 4: Guiding of quasi-radially polarized modes in a plasma channel 90
4.1 Direct acceleration in a plasma slow wave structure 90
4.2 Generation of modulated waveguides for DLA 93

4.3 Generation and focusing of quasi-radially polarized beams 97
4.4 Guiding of a TEM_{01} mode in a plasma channel 103
Chapter 5: Characterization of a micrometer-scale cryogenically cooled gas jet for near critical density laser-plasma experiments 105
5.1 Introduction 105
5.2 High density valve design 106
5.3 Isentropic flow model 108
5.4 Experimental setup 112
5.5 Hydrogen jet density measurements 114
5.6 Cluster size and density characterization 118
5.6.1 Cluster formation in high pressure gas jets 118
5.6.2 Rayleigh scattering-based cluster measurement 119
5.7 Conclusion 123
Chapter 6: Multi-MeV electron acceleration by sub-terawatt laser pulses in high density plasma 125
6.1 Introduction 125
6.2 Experimental setup 126
6.3 Electron acceleration 129
6.4 Wave breaking radiation 132
6.5 Acceleration mechanism 137
6.6 Summary 138
Chapter 7: Summary and Future Work 140
7.1 Summary 140
7.2 Future Work 141
7.2.1 Plasma channel guiding experiments 141
7.2.2 Quasi-phase-matched direct laser acceleration 142
7.2.3 High density laser-plasma interaction experiments 143
Bibliography 145

List of Figures

Figure 1.1. Basic schematic of a laser wakefield accelerator. The high intensity laser pulse drives a charge density wave in a plasma traveling with a phase velocity near the speed of light. The high amplitude electrostatic field associated with the charge density wave can accelerate a co-propagating electron bunch to high energy. Image from ref [250]........ 8

Figure 1.2. The density variation averaged over the laser frequency time scale, $\delta nn0$, (dashed curve) and axial electric field, $EzE0$, (solid curve) of a plasma wave driven by a Gaussian laser pulse with RMS length $L = kp - 1$ and peak vector potential $a0 = 0.5$ (a) and $a0 = 2.0$ (b). The pulse is moving to the right centered at $kp\zeta = 0$ and the fluid quantities are found by numerically solving equation (1.16)-(1.18). Figure from ref [5]........ 18

Figure 1.3. Self-modulation of the pulse by the driven plasma wave can result in high amplitude waves. The laser pulse (red) initially drives a low amplitude plasma wave (blue). The plasma wave represents a longitudinally varying refractive index which, after sufficient propagation distance, can modulate the pulse amplitude on a scale of the plasma wavelength. The individual pulselets resonantly drive the plasma wave, resulting in a higher wave amplitude. The dashed line on the right shows the original pulse intensity envelope. 20

Figure 2.1. Block diagram of the 25 TW laser system used to perform the experiments in this dissertation........ 35

Figure 2.2. Spectrum of the laser pulse at various points in the amplification chain. Gain narrowing reduces the spectral bandwidth in the regenerative and multi-pass amplifiers to a final bandwidth of 26 nm, with the majority of the narrowing occurring in the regenerative amplifier. Gain shifting, again primarily in the regenerative amplifier, shifts the center wavelength from 790 nm in the oscillator to 808 nm after amplification........ 37

Figure 2.3. Amplified and expanded beam profile before (a) and after (b) implementing a vertical beam inversion after the second pass of the MPA. Lineouts along the x (c) and y (d) axes show a moderate improvement in the beam uniformity after the beam flip. 38

Figure 2.4. (a) Theoretical energy output per pass in the MPA pumped by two 9 mm diameter, 1.5 J frequency doubled Nd:YAG lasers. The seed pulse reaches gain saturation on the fourth pass. (b) Measured seed beam profile after the fourth and final pass through the MPA crystal. The pulse energy is 1.4 J........ 39

Figure 2.5. (a) A schematic of the single shot SHG FROG used for characterization of the pulse spectral amplitude and phase. The pulse is split using a thin pellicle beamsplitter and focused using a cylindrical lens into a BBO crystal. Focusing using a cylindrical lens allows the time delay, τ, to be mapped onto the geometrical dimension, x, perpendicular to the direction of focusing as illustrated in (b). The sum

frequency signal pulse is imaged to the entrance slit of an imaging spectrometer to form the complete SHG FROG spectrogram in a single shot. 44

Figure 2.6. SHG FROG measurement of a pulse exhibiting strong cubic spectral phase. The measured trace (a) and retrieved trace (b) closely match, with a FROG error of 0.006. Extracted spectral domain (c) and time domain (d) representations of the pulse electric field amplitude and phase show the effect of non-negligible third order spectral phase. 46

Figure 2.7. Measured (a) and retrieved (b) SHG FROG traces after spectral phase compensation by the Dazzler AOPDF. The retrieved spectral phase (c) is much flatter and the retrieved temporal intensity envelope (d) is nearly bandwidth limited with FWHM pulsewidth 39 fs. 49

Figure 2.8. The FWHM pulse duration measured by the SHG FROG as a function of GDD applied by the Dazzler along with a least squares fit to a hyperbola. 51

Figure 2.9. The third order nonlinearity in the high dynamic range autocorrelator makes pre- and post- pulses distinguishable. Overlap of the main pulse in the fundamental arm with the pre-pulse of the second harmonic arm ($\tau - 1$) gives a third harmonic signal equal to the square of the signal from overlapping the main pulse of the second harmonic arm with the pre-pulse of the fundamental arm. 52

Figure 2.10. Sample third order autocorrelation trace of the amplified pulse. Higher resolution scans are shown around areas with known pulse structure. 54

Figure 2.11. Schematic layout of an adaptive optics loop utilizing a reference arm for downstream aberration correction. First, a loop is closed with the SID4 behind the laser focus correcting the beam to a perfect diverging wave front. These mirror voltages are then used to obtain a reference wave front upstream of the final focusing optic. For daily operation, the loop is closed with the SID4 in this reference arm which corrects for aberrations in the full laser chain. 58

Figure 2.12. Measured laser wave front and focal spot before (a) and after (b) convergence of the adaptive optics loop. The phase measurements are in units of waves with $\boldsymbol{\lambda = 800nm}$. The wave front curvature and tilts have been removed for clarity. The spatial scale is the same in both focal spot images though the color scales are individually normalized. 60

Figure 2.13. Schematic drawing of the inverted field autocorrelator (IFA). A pulse with angular spatial chirp is sent through a modified Mach-Zehnder interferometer and interfered with a slight tilt in the direction perpendicular to the angular spatial chirp. Interference fringes will be visible on the CCD only in the region where the pulses overlap within a coherence length. 62

Figure 2.14. Inverted field autocorrelation traces before (a) and after (c) correction of a 0.5 μrad/nm angular chirp on a 39 fs pulse. The focal spot before (b) the correction is elliptical and becomes much more symmetric after improvement of the grating parallelism (d). 63

Figure 3.1. Experimental setup for making plasma waveguides in cluster jets. A 140 ps channel forming pulse is focused with an axicon lens over the elongated cluster jet.

A synchronized femtosecond pulse is focused onto the end of the plasma waveguide through a hole in the axicon. Plasma density is measured using femtosecond transverse interferometry, and guided modes are monitored by relay imaging the exit mode to a CCD camera. 74

Figure 3.2. Temporal evolution of a plasma waveguide formed from an Nd:YAG laser pulse (250 mJ, 140 ps) interacting with a nitrogen cluster jet. The cluster jet is cooled to a gas reservoir temperature of -170º C and held at 400 psi. The plasma density is initially peaked on axis, but hydrodynamic expansion of the hot plasma creates a density minimum on axis and a radially propagating shock wall. 75

Figure 3.3. Consecutive exit modes from a 1 cm long nitrogen plasma waveguide injected with a 50 mJ, 40 fs laser pulse focused to a 13 μm FWHM spot size and delayed by 450 ps with respect to the 250 mJ Nd:YAG channel forming pulse. Average measured energy throughput was 50% with a standard deviation of 11%. Maximum throughput reached 79%... 76

Figure 3.4. (a) Cluster jet nozzle with externally attached 100 μm thick sapphire skimmers. (b) 3D printed nozzle with integrated 400 μm thick skimmers. Both are shown in the same custom cryogenic cooling jacket. 77

Figure 3.5. Extracted phase shift profiles of a nitrogen plasma waveguide before and ~1 ps after guiding a femtosecond pulse. The waveguide alone (a) has a 250 μm density ramp. Injection of a 0.5 TW pulse (b) and a 2 TW pulse (c) show the presence of a small amount of residual monomer gas at the entrance to the plasma waveguide. The associated exit mode profiles still show a bright Gaussian spot on axis. The color scale is the same on all three phase images. 78

Figure 3.6. Phase shift profiles of the exit of a nitrogen plasma waveguide before (a) and ~1 ps after (b) guiding a 0.4 TW laser pulse. The difference between the two profiles (c) reveals additional ionization only outside the waveguide. Abel inverted density profiles before and after guiding a 10 TW pulse (d) also show additional ionization only outside the waveguide.. 79

Figure 3.7. Energy throughput and normalized intensity at the exit of a 1 cm nitrogen plasma waveguide with on axis density $5 \times 1018\ cm - 3$ as a function of incident laser power. The injected pulse is 40 fs FWHM with a spot size of 13 μm. Exit modes are shown for incident powers 0.1, 0.4, and 2 times the critical power for relativistic self-focusing... 81

Figure 3.8. Laser spectrum before and after it is guided through a 1 cm nitrogen plasma waveguide. Spectral broadening is observed with a redshifted tail indicative of coupling to plasma density perturbations. 82

Figure 3.9. Abel inverted electron density profiles produces by focusing the Nd:YAG channel forming pulse with an axicon lens (a) and an f/20 spherical lens (b). Lineouts along the dashed white line show a nearly parabolic density profile in the axicon case and a flat density profile in the lens focusing case. 83

Figure 3.10. (a) Optical spectra of the 10 TW pulse before (blue) and after interaction with a flat (black) and guiding (red) electron density profile, each with a peak on axis density of $1.4 \times 1019\ cm - 3$. A low intensity (0.4 TW) guided mode (b) shows a

Gaussian mode with 14 μm FWHM. High power (10 TW) exit modes from the channel profile (c) and flat density profile (d) show improved confinement by the plasma waveguide. 85

Figure 3.11. Electron beam profiles from the N^{5+} waveguide (a) and the N^{5+} flat density profile (b). A typical spectrum (c) shows acceleration with a peak at 60 MeV while the highest energy spectrum (d) is peaked near 120 MeV. 86

Figure 3.12. Charge density plots from Turbowave 2D PIC simulations after 1.4 mm propagation in a He-like nitrogen plasma waveguide (a) and a hydrogen plasma waveguide (b) with the same electron density profile. No beam injection is observed in the hydrogen channel case. The longitudinal (c) and transverse (d) phase space of the electrons ionized from N5+ to N6+ in the waveguide after 1.4 mm propagation show similar beam profile and energy as observed in experiments........................... 88

Figure 4.1. Experimental setup for creating modulated plasma waveguides using (a) a ring grating to modulate the focused intensity of the channel generating pulse and (b) wire obstructions for creating density modulations by periodically interrupting cluster flow. The general DLA scheme is also presented. 94

Figure 4.2. Abel inverted density profile of wire modulated plasmas as a function of probe delay. After ~1 ns delays a density minimum develops on axis providing a suitable density profile for optical guiding. Axial density modulations with a 220 μm period are generated by obstructing the cluster flow with 25 μm diameter tungsten wires. 95

Figure 4.3. Lineouts of phase profiles in a plasma generated over a cluster jet obstructed by a single wire as a function of cluster jet reservoir temperature. At high temperatures and low mean cluster sizes shock waves are clearly evident while only a ballistic shadow of the wire appears at low temperatures and large mean cluster sizes. 96

Figure 4.4. Concept of a segmented waveplate used for generating approximately radially polarized light. Slices of a $\lambda/2$ waveplate are arranged with slowly varying orientation of the birefringent crystal's slow axis. This causes a varying rotation of the laser polarization with the azimuthal angle.. 98

Figure 4.5. A pellicle beamsplitter cut in half with a razor blade was used to transform a linearly polarized Gaussian beam into an approximation of a Hermite-Gaussian TEM_{01} mode. The angle of the pellicle was tuned to apply a π phase shift on one half of the beam with respect to the other. 100

Figure 4.6. The focus of the half-pellicle beam (a) resembles a pure TEM_{01} Hermite-Gaussian mode (b). Lineouts along the maxima are compared in (c). 101

Figure 4.7. The Abel inverted density profile of the first 1.4 mm of an 11 mm nitrogen plasma waveguide (a) with a lineout shown in (b). A Gaussian input mode with an 11 μm spot size (c) is guided with approximately 60% energy throughput and the same spot size as the input mode (d)... 103

Figure 4.8. Series of guided modes at the exit of an 11 mm nitrogen plasma waveguide. The modes retain the two-lobe structure of the injected near-TEM_{01} mode with an energy throughput of ~30%. 104

Figure 5.1. Custom fabricated straight (a) and tapered (b) nozzles with ~100 μm throats. The gas jet is held in a custom cooling block (c) which can cool the jet to cryogenic temperatures. 107

Figure 5.2. Experimental setup for characterizing the high density gas jet (a). Density measurements were made using transverse interferometry. A raw interferogram (b) and Abel inverted density profile (c) are shown along with a raw image of Rayleigh scattering used to measure the cluster size and density in the jet. 113

Figure 5.3. Sample 2D hydrogen molecule density profile (a) with 1000 psi backing pressure and -160° C reservoir temperature and lineouts 70, 100, and 200 μm above the nozzle (b). The peak density as a function of height decays exponentially (c) and the FWHM increases linearly with height above the jet (d). 115

Figure 5.4. Nitrogen molecule density versus time delay at 200 μm above the 100 μm needle nozzle with the jet reservoir held at 800 psi and -110° C for 500 μs, 1000 μs, and 1500 μs open times. 116

Figure 5.5. Peak jet density 200 μm above the 100 μm needle nozzle as a function of valve backing pressure at a fixed reservoir temperature -160º C (113 K) (a) and as a function of reservoir temperature at a fixed backing pressure 1000psi (b). 117

Figure 5.6. Density as a function of height above the needle (solid) and tapered (dashed) nozzles with 50 (green), 100 (red), and 150 (blue) μm throat all at -160º C and 1000 psi 118

Figure 5.7. Average cluster density (a) and average cluster size (b) as a function of radial position at various heights above the 150 μm diameter nozzle orifice at jet backing pressure and temperature 1000 psi and -160° C... 122

Figure 5.8. Rayleigh scatter signal versus backing pressure (a) and cluster density (solid line) and size (dotted line) at a height ~1 mm above the 150 μm nozzle (b) with the jet reservoir held at -160° C. 123

Figure 6.1. Experimental setup. A horizontally polarized Ti:Sapphire laser pulse (10-50 mJ, 50 fs, λ=800 nm) interacts with a cryogenically-cooled, dense thin H2 gas jet (a), whose neutral and plasma density profiles are measured by 400 nm probe interferometry (b). A portion of the transmitted laser pulse is reflected by a pellicle (c) and measured by a spectrometer (d). The electron beam from the jet is apertured by a 1.7mm horizontal slit (e), enters a 0.13 T permanent magnet spectrometer, and is dispersed on an aluminum foil-shielded LANEX screen (f), which is imaged by a low noise CCD camera (not shown). (f) shows example quasi-monoenergetic and exponential spectra for a 40 mJ pulse at Ne=2×1020 cm-3. Shadowgraphic imaging of the laser interaction region above the needle orifice (g) (needle seen as a shadow at bottom) and imaging (g) and spectroscopy (h) of the wave breaking flash. The pump polarization could also be rotated to the vertical by a half wave plate. 127

Figure 6.2. Single shot electron beam images for energies > 1 MeV for a range of laser energies and peak profile electron densities. The colour palette was scaled up by 10× for the 10 mJ column. The onset laser power for detectable electron beam generation was ~3Pcr across our range of conditions. 129

Figure 6.3. **(a)** Accelerated electron spectra for peak jet electron density 4.2×10^{20} cm^{-3} for varying laser energy. The inset shows total charge >2 MeV as a function of laser energy. The range of effective temperatures of these exponential-like distributions is indicated. The horizontal black lines indicate the experimental uncertainty in the energy, determined by geometry-limited spectrometer resolution. The dashed curve is a 3D PIC simulation for 40 mJ pump which has been scaled by a factor 0.14 to line up with the experimental curve for 40 mJ. **(b)** Accelerated electron spectra at laser energy 40 mJ for varying peak electron density. The dashed curves are from 3D PIC simulations and were scaled by the factor 0.14. 130

Figure 6.4. Top panel: Side images of intense radiation flashes from wave breaking (10 shot averages). The horizontally polarized pump laser pulse propagates left to right. Image intensities are normalized to the maximum intensity within each column. The vertical dashed line is the centre of the gas jet, whose profile is shown in the lower left. The 40 mJ, 1.1×1020cm−3 image for vertical pump polarization (enhanced 10×), is dominated by 800 nm Thomson scattering on the left and the flash on the right. Bottom panel: Spectra (10 shot averages) of the flash for conditions enclosed by the dashed black box in the top panel. 133

Figure 6.5. A sample spectral interferogram between the broadband wave breaking flash and a compressed supercontinuum pulse generated in a Xe gas cell. Fringes are visible across the full 250 nm supercontinuum bandwidth, showing that the broadband flash is spectrally coherent. 136

Figure 6.6. 2D PIC simulations showing contributions of LWFA and DLA to electron energy gain for a fixed peak plasma density $N_e = 0.07N_{cr}$ for drive laser energies 15-100mJ. Each blue dot is a tracked electron. Regions above and to the left of the solid red line indicate DLA as the dominant form of acceleration, whereas regions below and to the right are dominated by LWFA. The dashed red diagonal marks zero net energy gain. LWFA dominates acceleration at low drive laser energies, transitioning to DLA at high drive laser energies...................................... 138

Chapter 1: Introduction

1.1 Motivation and outline of the dissertation

For nearly a century, particle accelerators have been tools of discovery in a wide variety of fields, enabling a number of advances in physics, chemistry, medicine, and biology. Modern RF electron accelerators use periodic, resonantly excited copper cavities phased such that a relativistic electron experiences a constant accelerating force over the length of the accelerator. Accelerating gradients in RF linear accelerators are limited to <100 MV/m by electrical breakdown at the walls of the copper cavities [1,2] with typical accelerating gradients operating near ~10 MV/m [1]. These copper cavities can be staged over long distances to reach GeV electron energies while keeping the RF field strength below the breakdown threshold. Smaller machines can supply few MeV electrons in relatively compact devices for applications such as materials processing or electron radiography [3]. The ~10 MV/m maximum accelerating gradient is what leads to the large footprint of high energy linear accelerators, and unless advancements in accelerator technology can yield higher gradients future TeV scale electron beams will require RF linacs stretching 10s of kilometers. Further, widespread application of lower energy (1-10 MeV) electron beams is limited by the size and expense of the electron injectors, RF sources, and cavity structures required for linear accelerators.

The application of high power lasers to particle acceleration has been studied as a way to reach much higher accelerating gradients with the aim of making much cheaper, more compact electron and ion accelerators [4–6]. With the advent of chirped pulse amplification [7,8] and the use of Ti:Sapphire as a gain medium [9,10],

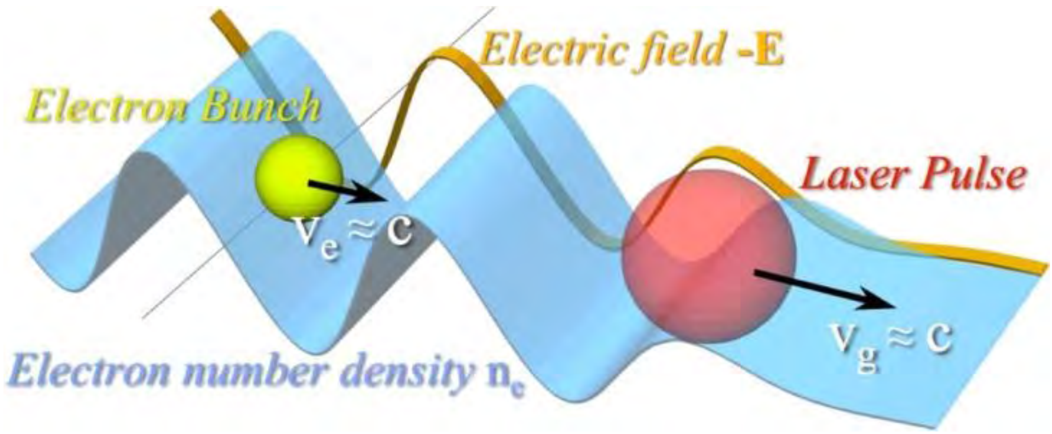

Figure 1.1. Basic schematic of a laser wakefield accelerator. The high intensity laser pulse drives a charge density wave in a plasma traveling with a phase velocity near the speed of light. The high amplitude electrostatic field associated with the charge density wave can accelerate a co-propagating electron bunch to high energy. Image from ref [250].

achievable laser intensities have risen dramatically in the last thirty years with reported peak intensities in excess of 10^{22} W/cm^2 [11]. Peak fields at the focus of femtosecond laser pulses routinely reach beyond 1 TV/m, and a number of schemes have been proposed for directly using them as drivers of next generation compact, high energy particle accelerators [12–16].

While the electric fields associated with femtosecond pulses are extremely strong they are, of course, oscillatory. As a result it is difficult for a particle to gain net energy directly from the laser pulse. In 1979, it was realized by Tajima and Dawson [17] that the plasma medium can act as a transformer between the fast oscillating laser electric fields and more slowly varying plasma fields. By far the most studied scheme for laser driven particle acceleration is the laser wakefield accelerator concept, which is illustrated in Fig. 1.1 [5,17,18]. In laser wakefield accelerators (LWFAs) the high intensity femtosecond laser pulse drives a nonlinear plasma wave. At typical densities in the range 10^{18}-10^{19} cm^{-3}, the plasma wave's electrostatic field can be ~100 GV/m, with the plasma wave traveling at the laser group velocity. This moving electrostatic structure can accelerate a properly phased electron beam to high energy.

Laser driven accelerators have a number of unique properties that make them very promising as next generation accelerators. First, the accelerating fields associated with laser driven accelerators like the LWFA are typically 10^3-10^4 times stronger than those of standard RF accelerators. This means that, in principle, the total footprint of a particle accelerator could be drastically reduced, especially when GeV or multi-GeV beams are desired. Next, laser based accelerators driven by femtosecond pulses generally produce femtosecond radiation bursts. For example, electron bunch durations in LWFAs are intrinsically much shorter than a plasma wavelength which, for typically used plasma densities ~10^{18}-10^{19} cm^{-3}, corresponds to periods ~10-100 fs. Further, the radiation source size is approximately the laser focal spot size which is typically ~10 μm. The small source size and ultrashort bunch duration enable ultrashort, ultra-bright x-ray sources derived from the high energy electron beams which can be used for high resolution imaging applications as well as ultrafast x-ray or relativistic particle based pump-probe experiments [19].

Currently, laser plasma accelerators are limited in many practical applications by the stability of the electron beam parameters and the repetition rate of available drive laser sources. While improvements on the control and stability of wakefield accelerators have been demonstrated in recent years [20–23], the vast majority of laser wakefield accelerator experiments use joule-class, low repetition rate (< 10 Hz) laser systems. Indeed, the petawatt laser systems required to drive GeV accelerators are only accessible at large facilities and stretch the idea of a "table-top" accelerator.

This dissertation describes experiments using structured gas targets to reduce the drive laser energy needed for production of relativistic electron beams. In the rest of this chapter a brief introduction to the physics of laser wakefield accelerators will be described followed by an introduction to quasi-phase-matched direct acceleration of electrons in a corrugated plasma waveguide [12]. Chapter 2 describes the 25 TW femtosecond laser system used to perform the experiments in this dissertation. Chapter 3 presents experiments on the generation and characterization of plasma waveguides for extending the laser-plasma interaction length at relativistic intensity. An experiment demonstrating the effectiveness of the plasma waveguide for stabilizing the production of wakefield accelerated relativistic electron beams is also described. A novel laser driven acceleration scheme, called quasi-phase-matched direct laser acceleration (QPM-DLA), is presented at the end of this chapter as well as in Chapter 4. Chapter 4 presents experimental progress towards the realization of the QPM-DLA concept including novel methods for producing modulated plasma waveguides and, for the first time, controlled guiding of quasi-radially polarized pulses in a plasma waveguide. Chapters 5 and 6 are related to the development of a seed source of relativistic electrons for use in the QPM-DLA proof-of-principle. Chapter 5 describes a thin ~100 μm scale high density hydrogen gas jet capable of reaching plasma densities above $10^{21}\ cm^{-3}$. Chapter 6 describes experiments using this gas jet where relativistic electron beam generation is demonstrated using sub-terawatt femtosecond laser pulses. Accompanying the electron acceleration is intense coherent radiation in the optical frequency range associated with wave breaking and injection of electrons into the accelerating phase of the plasma wave. Measurements of this broadband “flash” are consistent with half cycle, ~1 fs optical radiation associated with the unipolar acceleration of the electrons in the wakefield. The dissertation concludes with a discussion of future research directions.

1.2 Laser wakefield acceleration

Laser wakefield accelerators were first proposed in 1979 by Tajima and Dawson [17], well before the technology existed for generating laser intensities high enough to efficiently drive nonlinear plasma waves. With advances in laser technology, in particular the advent of the chirped pulse amplification technique [7,8], compact multi-terawatt laser systems became readily available, and laser based acceleration experiments were performed by a number of groups world-wide. The first laser wakefield experiments were operated with relatively long pulse lasers (~1 ps) in the self-modulated regime and demonstrated acceleration gradients in excess of 100 GV/m [24–27]. Electrons were accelerated to energies ~10 MeV with total beam charges >1 nC. However, in this regime the accelerated electrons had exponential energy distributions, with a very small fraction at high energy, and large beam divergences.

In 2004 three groups simultaneously achieved accelerated bunches of much lower divergence and energy spread by controlling the laser and plasma parameters so that only a single oscillation of the plasma wave was driven to wave breaking and the laser-plasma interaction length was shorter than a dephasing length [28–30]. The electron beams in these experiments were quasi-monoenergetic (~100 MeV with a few percent energy spread) with low divergence (~10 mrad). Since 2004 the reproducibility and control of these beams has been greatly improved [20,22,23].

Laser wakefield experiments have pushed toward ever higher single stage energy gains with the current world record of 4 GeV produced in a 9 cm long plasma waveguide driven by a 300 TW laser [31]. Many experiments and theoretical proposals are also looking towards methods for generating electron beams with smaller energy spreads and lower transverse emittances, particularly for demanding applications such as injection of x-ray free electron lasers [32–34].

As the stability, reproducibility, and control of wakefield accelerators has improved, these ultrashort relativistic electron beams have been applied to the study of high energy photon sources. Multi-keV x-rays are generated by relativistic electrons executing betatron oscillations about the plasma wave ion column [35–38]. Thomson and Compton scattering experiments have been performed in the linear and recently nonlinear regimes, producing MeV gamma rays [19,39–41]. Wakefield accelerated electrons impinging on high Z targets have even been studied as a positron source [42,43]. As the achievable peak intensity of ultrashort pulses reaches ever higher, wakefield accelerated electron beams coupled to high intensity (~10^{23} W/cm^2) lasers could potentially study interesting QED physics such as quantum radiation reaction forces [44].

1.2.1 The ponderomotive force

The laser wakefield accelerator concept relies on the radiation pressure of a high intensity laser to drive a plasma wave. The force on the plasma due to the laser radiation pressure is often described via the ponderomotive force which is commonly expressed in terms of the laser normalized vector potential, $\boldsymbol{a_0} = e\boldsymbol{A}/mc^2$, where $\boldsymbol{A}$ is the laser vector potential, e is the elementary charge, m is the electron mass, c is the speed of light, and the laser electric field is $\boldsymbol{E} = -\frac{1}{c}\partial \boldsymbol{A}/\partial t$. Relativistic corrections to the electron motion become important when $a_0 \approx 1$. The laser intensity can be related to a_0 in practical units through

$$a_0 \cong 8.5 \times 10^{-10}[\lambda(\mu m)]\sqrt{I_0(W/cm^2)}. \tag{1.1}$$

For a laser pulse centered at $\lambda = 0.8\,\mu m$, $a_0 \approx 1$ for pulse intensities $I_0 \approx 2 \times 10^{18}\,W/cm^2$ based on equation (1.1). These intensities are routinely reached by tightly focusing femtosecond laser pulses.

The relativistic ponderomotive force in the plasma can be derived by considering the fluid momentum equation

$$\frac{1}{c}\frac{d\boldsymbol{u}}{dt} = \frac{1}{c}\frac{\partial \boldsymbol{u}}{\partial t} + \left(\frac{\boldsymbol{u}}{\gamma}\cdot\boldsymbol{\nabla}\right)\boldsymbol{u} = \frac{1}{c}\frac{\partial \boldsymbol{a_0}}{\partial t} + \boldsymbol{\nabla}\phi - \frac{\boldsymbol{u}}{\gamma}\times\boldsymbol{\nabla}\times\boldsymbol{a_0} \tag{1.2}$$

where $\boldsymbol{u} = \gamma\boldsymbol{v}/c$ is the normalized fluid momentum, $\gamma = \sqrt{1+u^2}$ is the fluid Lorentz factor, $\boldsymbol{a_0}$ is the laser normalized vector potential, and $\phi = e\Phi/mc^2$ is the normalized scalar potential associated with charge separation in the plasma. Recognizing that

$$\left(\frac{\boldsymbol{u}}{\gamma}\cdot\boldsymbol{\nabla}\right)\boldsymbol{u} = \frac{1}{\gamma}\left[\frac{1}{2}\boldsymbol{\nabla}\boldsymbol{u}^2 - \boldsymbol{u}\times\boldsymbol{\nabla}\times\boldsymbol{u}\right]$$

and

$$\frac{1}{2\gamma}\boldsymbol{\nabla}\boldsymbol{u}^2 = \frac{1}{2\gamma}\nabla\gamma^2 = \nabla\gamma$$

equation (1.2) becomes

$$\frac{1}{c}\frac{\partial(\boldsymbol{u}-\boldsymbol{a_0})}{\partial t} = \boldsymbol{\nabla}(\phi-\gamma) + \frac{\boldsymbol{u}}{\gamma}\times\boldsymbol{\nabla}\times(\boldsymbol{u}-\boldsymbol{a_0}). \tag{1.3}$$

The generalized ponderomotive force, $\boldsymbol{F_p}$, arises from the $\boldsymbol{\nabla}\gamma$ term in equation (1.3) so that

$$\boldsymbol{F_p} = -mc^2\nabla\gamma = -\frac{mc^2}{\gamma}\nabla u^2/2. \tag{1.4}$$

This can be related back to the laser vector potential by noticing that $\boldsymbol{u}_\perp \approx \boldsymbol{a_0}$ from conservation of canonical momentum which is exact when the system is one dimensional, i.e. the spot size w_0 satisfies $w_0 \gg \lambda_p \gg \lambda$. In this limit $\boldsymbol{F_{p,z}} = -\frac{mc^2}{\gamma}\frac{\partial}{\partial z}a_0^2/2$. Experiments in this dissertation were performed with laser vector potentials $a_0 \geq 1$ and $w_0 \sim \lambda_p$, so the ponderomotive force is best described by equation (1.4).

The ponderomotive force is independent of the sign of the particle charge and will always act to expel charges from regions of high intensity. The ponderomotive force on the ions will be weaker than the ponderomotive force on the electrons by a ratio $\boldsymbol{F_e}/\boldsymbol{F_i} = m_e/m_i$ where m_e and m_i are the electron and ion masses. Since $m_e/m_i \sim 10^{-3}$ the ion motion is usually negligible compared to the electron motion, and the ions are normally considered to be stationary.

1.2.2 Laser wakefields

In the weakly relativistic regime ($a_0 \ll 1$) the form of the plasma wave driven by the laser ponderomotive force can be found analytically if it is assumed that the drive laser pulse is non-evolving [45]. While experiments in this dissertation were performed at intensities $a_0 \geq 1$, the weakly relativistic treatment shows very clearly that the laser ponderomotive force is responsible for driving plasma waves and can act as a transformer of high intensity laser fields to quasi-static longitudinal accelerating fields. It also shows that the plasma wave is most efficiently excited when the laser pulse duration $\tau_L \sim 2\pi/\omega_p$. These insights apply even in the relativistic regime. Here we assume a cold plasma and stationary ions. These assumptions are justified considering the temperature of a field ionized plasma (~10 eV) is typically much smaller than the electron ponderomotive energy in the laser field (~100 eV – 1 MeV) and the ion displacement due to the ponderomotive force is $(m_e/m_i)^2 \sim 10^{-6}$ times the electron displacement. In the cold fluid limit the plasma continuity equation, Lorentz force law, and Poisson equation can be used to solve for the wakefields

$$\frac{\partial}{\partial t}\frac{\delta n}{n_0} + \nabla \cdot \boldsymbol{v} = 0 \tag{1.5}$$

$$m\frac{\partial \boldsymbol{v}}{\partial t} = -e(\boldsymbol{E}_\perp + \frac{\boldsymbol{v}}{c} \times \boldsymbol{B}_\perp + \boldsymbol{E}_{\boldsymbol{z}}) \tag{1.6}$$

$$\nabla \cdot \boldsymbol{E} = 4\pi e \delta n \tag{1.7}$$

where δn is a perturbation about the static plasma electron density n_0, $\boldsymbol{v}$ is the plasma fluid velocity, m is the electron mass, e the elementary charge, $\boldsymbol{E}_\perp$ and $\boldsymbol{B}_\perp$ are the laser transverse fields, and $\boldsymbol{E}_{\boldsymbol{z}}$ is the longitudinal field associated with the plasma wave. The fluid velocity consists of fast and slowly varying components, $\boldsymbol{v} = \boldsymbol{v}_{\boldsymbol{f}} + \boldsymbol{v}_{\boldsymbol{s}}$. The slowly varying part of the fluid velocity responds to the ponderomotive force so that equation (1.6) becomes

$$m\frac{\partial \boldsymbol{v}_{\boldsymbol{s}}}{\partial t} = \boldsymbol{F}_{\boldsymbol{p}} - e\boldsymbol{E}_{\boldsymbol{z}} = -\frac{1}{4}mc^2\nabla a_0^2 - e\boldsymbol{E}_{\boldsymbol{z}}. \tag{1.8}$$

Taking the time derivative of (1.5) and the divergence of (1.8) gives

$$\frac{\partial^2}{\partial t^2}\frac{\delta n}{n_0} = -\frac{\partial}{\partial t}\boldsymbol{\nabla} \cdot \boldsymbol{v}_{\boldsymbol{s}} = \frac{1}{4}c^2\nabla^2 a_0^2 - \frac{e}{m}\nabla \cdot \boldsymbol{E}_{\boldsymbol{z}}. \tag{1.9}$$

Using Poisson's equation

$$\frac{e}{m}\nabla\cdot\boldsymbol{E}_{\boldsymbol{z}}=\frac{4\pi e^2}{m}\delta n=\frac{4\pi e^2 n_0}{m}\frac{\delta n}{n_0}=\omega_p^2\frac{\delta n}{n_0}. \tag{1.10}$$

where $\omega_p^2=4\pi n_0 e^2/m_e$ plasma frequency. Substituting (1.10) into (1.9) gives

$$\left(\frac{\partial^2}{\partial t^2}+\omega_p^2\right)\frac{\delta n}{n_0}=\frac{c^2}{4}\nabla^2 a_0^2. \tag{1.11}$$

Thus, oscillations in the plasma density are driven by the divergence of the ponderomotive force.

Equation (1.11) can be formally solved using the Green's function for the one-dimensional harmonic oscillator

$$\frac{\delta n}{n_0}=\frac{c^2}{4\omega_p}\int_{-\infty}^{t}dt'\sin\left[\omega_p(t-t')\right]\nabla^2 a^2(\boldsymbol{r},t'). \tag{1.12}$$

The longitudinal field is found from (1.12) using Poisson's equation to be

$$\boldsymbol{E}_{\boldsymbol{z}}=-\frac{\omega_p mc^2}{4e}\int_{-\infty}^{t}dt'\sin\left[\omega_p(t-t')\right]\nabla a^2(\boldsymbol{r},t'). \tag{1.13}$$

The full solution is then obtained by integrating over the temporal shape of the laser pulse. These solutions are valid in the weakly relativistic regime ($a^2\ll 1$) where the density perturbation is small ($\delta n/n_0\ll 1$) and the longitudinal field is well below the cold nonrelativistic wave breaking field $E_z\ll E_0=mc\omega_p/e$. The plasma wakefield propagates with a phase velocity v_p , which is approximately equal to the laser group velocity $v_g=c\sqrt{1-\omega_p^2/\omega^2}$. Further, the wakefield is most efficiently excited when the laser pulse duration $\tau_L\sim 2\pi/\omega_p$, and the transverse size of the plasma wave is approximately the laser spot size.

The plasma wake in the nonlinear regime ($a_0^2\geq 1$ and $E_z\geq E_0$) can be found in the one dimensional case [46–49] by making the quasi-static approximation so that the drive laser and plasma fluid variables are assumed to depend only on the light frame coordinate $\zeta = z - v_p t$, where $v_p \cong v_g$ is the plasma wave phase velocity which is approximately equal to the laser group velocity. Using conservation of canonical momentum ($\boldsymbol{u}_\perp = \boldsymbol{a}$) and transforming equation (1.2) to the ζ coordinate frame gives

$$\gamma - \phi - \beta_p u_z = 1 \tag{1.14}$$

where again $\boldsymbol{u} = \gamma \boldsymbol{v}/c$ is the normalized fluid momentum, $\gamma = \sqrt{1+u^2}$ is the fluid Lorentz factor, $\beta_p = v_p/c$, and ϕ is the normalized scalar potential [48,49]. From the continuity equation in ζ coordinates we have

$$(\beta_p - \beta_z)n = \beta_p n_0 \tag{1.15}$$

where $\beta_z = v_z/c = u_z/\gamma$ [48]. Equations (1.14) and (1.15) can be substituted into Poisson's equation for the normalized scalar potential to find

$$\frac{\partial^2 \phi}{\partial \zeta^2} = k_p^2 \gamma_p^2 \left\{ \beta_p \left[1 - \frac{\gamma_\perp^2}{\gamma_p^2 (1+\phi)^2} \right]^{-1/2} - 1 \right\} \tag{1.16}$$

where $\gamma_\perp^2 = 1 + u_\perp^2 = 1 + a^2$ and $\gamma_p^2 = \left(1 - \beta_p^2\right)^{-1}$ [48–50]. Equation (1.16) can be solved numerically given an initial laser pulse profile. The wake electric field can then be found from

$$E_z = -E_0\, \partial\phi/\partial\zeta \tag{1.17}$$

where $E_0 = mc\omega_p/e$ is the cold nonrelativistic wave breaking field. Once the scalar potential is found by solving equation (1.16), the other fluid quantities can be found from [5,50]

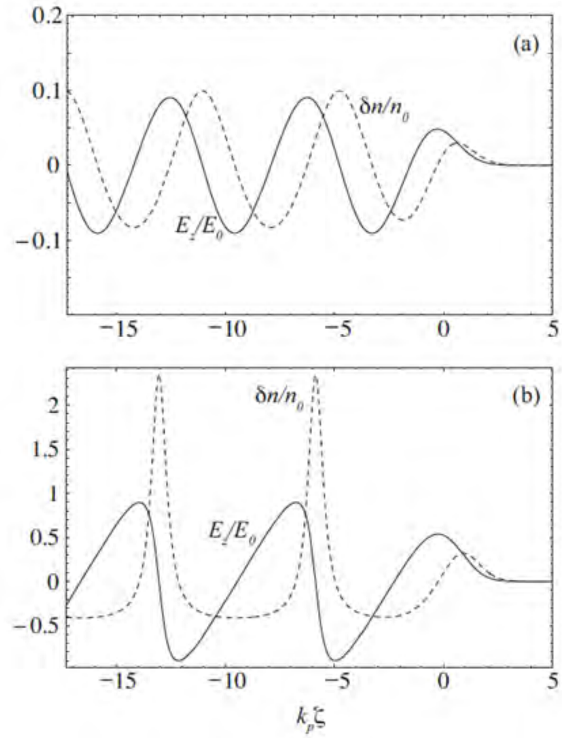

Figure 1.2. The density variation averaged over the laser frequency time scale, $\delta n/n_0$, (dashed curve) and axial electric field, E_z/E_0, (solid curve) of a plasma wave driven by a Gaussian laser pulse with RMS length $L = k_p^{-1}$ and peak vector potential $a_0 = 0.5$ (a) and $a_0 = 2.0$ (b). The pulse is moving to the right centered at $k_p\zeta = 0$ and the fluid quantities are found by numerically solving equation (1.16)-(1.18). Figure from ref [5].

$$n/n_0 = \gamma_p^2\beta_p\left[\left(1-\frac{\gamma_\perp^2}{\gamma_p^2(1+\phi)^2}\right)^{-1/2}-\beta_p\right] \tag{1.18}$$

$$u_z = \gamma_p^2(1+\phi)\left[\beta_p-\left(1-\frac{\gamma_\perp^2}{\gamma_p^2(1+\phi)^2}\right)^{1/2}\right] \tag{1.19}$$

$$\gamma = \gamma_p^2(1+\phi)\left[1-\beta_p\left(1-\frac{\gamma_\perp^2}{\gamma_p^2(1+\phi)^2}\right)^{1/2}\right]. \tag{1.20}$$

The result of solving equation (1.16)-(1.18) numerically for a Gaussian drive laser pulse of the form $a(\zeta) = a_0\exp(-\zeta^2/4L^2)\cos(k\zeta)$ with the RMS pulse length satisfying $k_pL = 1$ is shown in Fig. 1.2 for the cases $a_0 = 0.5$ and $a_0 = 2.0$ [5]. In the mildly relativistic case ($a_0 = 0.5$), the density perturbation and axial electric field are nearly sinusoidal with a period $\lambda_p = 2\pi/k_p$. In contrast, in the highly relativistic case ($a_0 = 2.0$), the wave steepens, the plasma period lengthens, and the axial electric field takes on a sawtooth shape.

In typical experimental conditions, the drive laser pulse undergoes significant evolution and effects such as relativistic self-focusing [51,52] make the problem highly three dimensional in nature. The experiments in this dissertation were performed in a highly nonlinear ($a_0 \geq 1$), multi-dimensional regime ($w_0 \sim \lambda_p$). Modelling of the experimental systems is, therefore, typically done using numerical simulations using either 3D fully relativistic fluid models [53,49]or kinetic simulations [54,55]. Particle in cell (PIC) simulations software, coupled with advances in high performance computing, have greatly improved the ability to model laser-driven wakefield acceleration, and more generally laser-plasma interactions.

1.2.3 Pulse propagation and self-modulation

As discussed above, the plasma wake is most efficiently driven by a laser pulse with temporal extent approximately equal to the plasma period. However, even if the drive pulse is much longer than the plasma period, large amplitude plasma waves can be excited through self-modulation of the laser by the plasma wave [25,51,53,56]. In this case the drive laser pulse longitudinally breaks up into a series of pulselets, each separated by the plasma wavelength. This can be qualitatively understood from the solution for the plasma density wave. Equation (1.12) shows that the plasma wave will be driven with a frequency ω_p and wavelength $\lambda_p = 2\pi c/\omega_p$. Therefore a laser pulse with longitudinal extent longer

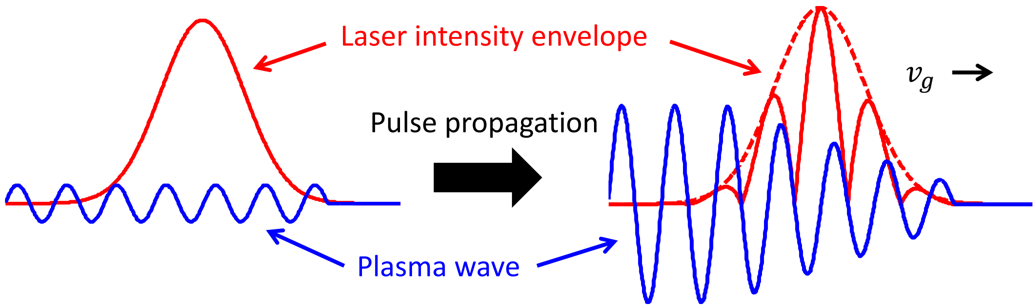

Figure 1.3. Self-modulation of the pulse by the driven plasma wave can result in high amplitude waves. The laser pulse (red) initially drives a low amplitude plasma wave (blue). The plasma wave represents a longitudinally varying refractive index which, after sufficient propagation distance, can modulate the pulse amplitude on a scale of the plasma wavelength. The individual pulselets resonantly drive the plasma wave, resulting in a higher wave amplitude. The dashed line on the right shows the original pulse intensity envelope.

than λ_p will experience alternating regions of low and high plasma density. The high density regions will defocus the laser pulse and the pulse can be focused into regions of low density. Furthermore, the pulse group velocity is higher in the low density plasma regions than in the high density regions, causing pulse compression on a scale of λ_p. These effects serve to modulate the pulse into a series of pulses, each of which resonantly drive the plasma wave, as illustrated in Fig. 1.3.

Laser wakefield acceleration in this "self-modulated" regime is important when working with relatively high density plasmas. For example, many early wakefield experiments were operated in the self-modulated regime when ultrashort (<100 fs) pulses were not available [25,27,56–58]. The experiments outlined in Chapter 6 of this dissertation demonstrate a laser wakefield accelerator driven by a 50 fs laser pulse interacting with plasma at densities $1 - 4 \times 10^{20} cm^{-3}$, with corresponding plasma periods in the range 11 fs – 5.7 fs. These experiments operate in the self-modulated wakefield accelerator regime. The time dependent refractive index associated with the axial plasma density modulations within the laser pulse lead to significant changes in the frequency spectrum of the drive laser pulse. Raman side bands are observed in the self-modulated regime, and the frequency spectrum of the pulse exiting the accelerator is useful as a diagnostic of the plasma wave amplitude [24,58,59].

Efficient acceleration of electron beams often requires the drive laser pulse to propagate at high intensity over many Rayleigh lengths. This can be achieved by implementing plasma guiding structures where the electron density follows a profile well-approximated as parabolic, $n(r) = n_0\left(1 + \frac{\Delta n}{n_0}\left(\frac{r}{w_{ch}}\right)^2\right)$, where $\Delta n = n(w_{ch}) - n(0) \geq \frac{1}{\pi r_e w_{ch}^2}$ is the depth of the plasma waveguide, r_e is the classical electron radius, and w_{ch} is the radius of the lowest order guided mode [60]. A nonrelativistic laser pulse experiences the refractive index profile $\eta(r)^2 = 1 - \frac{n(r)}{n_{cr}} = 1 - \frac{n_0}{n_{cr}}\left(1 + \frac{\Delta n}{n_0}\frac{r^2}{w_{ch}^2}\right)$, which is peaked on axis. This index profile admits bound Laguerre-Gaussian modes and matched guiding of a (nonrelativistic) laser pulse is achieved for a Gaussian beam of spot size w_{ch} [61].

At sufficiently high intensity, relativistic self-focusing [51,52] becomes important and can lead to nonlinear guiding in a uniform density plasma. In this case the plasma frequency is modified by the relativistic motion of the plasma electrons so that the refractive index becomes

$$\eta(r)^2 = 1 - \frac{\omega_p^2(r)}{\omega^2} = 1 - \frac{\omega_{p0}^2}{\gamma(r)\omega^2} \approx 1 - \frac{\omega_{p0}^2}{\omega^2} + \frac{\omega_{p0}^2}{\omega^2}\frac{a(r)^2}{4}$$

where ω_{p0} is the nonrelativistic plasma frequency. If the laser vector potential is peaked on axis, as is the case for lowest order laser modes, the refractive index is peaked on axis, and the pulse feels a focusing force [51,53]. Relativistic self-focusing is very similar to nonlinear self-focusing found in Kerr media, and will focus the pulse in the plasma until driven plasma waves stop the pulse collapse. A more complete description of pulse guiding and self-focusing is provided in Chapter 3 of this dissertation as well as in references [5,45,53].

1.2.4 Electron injection

While the driven plasma wave represents an accelerating structure, the plasma electrons oscillating in a plasma wave will not have sufficient initial velocity to be trapped and accelerated along with the wave. An electron will be trapped in the accelerating region of the wake only if it is injected with sufficient initial momentum such that the electron velocity is approximately the plasma wave phase velocity [62]. The Lorentz factor associated with the plasma wave phase velocity, v_p, is $\gamma_p = \left(1 - v_p^2/c^2\right)^{-1/2} \approx \omega/\omega_p = \sqrt{n_{cr}/n_e}$ where n_e is the ambient electron density. Note that the phase velocity is reduced for higher plasma densities, so the trapping threshold is substantially reduced in the high density acceleration experiments presented in Chapter 6.

Self-injection of background electrons into the wake can occur when the plasma wave amplitude is driven to the wave breaking limit [24,63,64]. In the 1D nonlinear regime, the maximum sustainable electric field amplitude, or wave breaking field, is given by $E_{WB} = \sqrt{2(\gamma_p - 1)}E_0$ where $E_0 = cm\omega_p/e$ is the cold nonrelativistic wave breaking field. At these field amplitudes, electron orbits can gain sufficient momentum from the plasma wave to be injected into the accelerating region. Field amplitudes up to the wave breaking limit can be reached by using very high $a_0$drive laser pulses (i.e. the blow-out regime) or in high density, self-modulated wakefield accelerators.

Two dimensional effects have been shown to lower the laser amplitude threshold for driving plasma waves to the wave breaking limit [65]. In this case, transverse variations in the plasma frequency across the laser pulse spot size cause curvature of the plasma wave phase fronts. These transverse variations can be caused by a channel structure where the density is higher off axis or by the relativistic dependence of the plasma frequency on the laser pulse amplitude. The curvature of the plasma wave phase fronts increases for wave periods farther behind the drive laser pulse until the regular wave structure is destroyed by self-intersection of the electron trajectories and transverse wave breaking. When the electron fluid displacement is of the same order as the wave curvature radius some fraction of the electrons can be injected and trapped in the accelerating region of the wake [65]. The complicated, highly nonlinear nature of transverse wave breaking normally necessitates numerical simulation for accurate prediction of the drive pulse amplitude required to achieve self-injection. PIC simulations of the high density experiments described in Chapter 6 show highly curved wake phase fronts and transverse injection of electrons, leading to the observed MeV electron beams.

Self-injection, while ostensibly the easiest method for achieving injection into the plasma wave, does not provide fine control of the injection phase or position within the accelerator. This can lead to fluctuation in the output beam energy spectrum and charge. As such, controlled injection of external bunches or background plasma electrons into the nonlinear plasma wake has received a significant amount of theoretical and experimental attention [20,34,66–68]. Multi-pulse techniques have been proposed as a means of controlling the injection phase and position. Successful experimental implementations demonstrated electron beams with tunable mean energy and few percent energy spread [20,69]. For example, controlled injection has been achieved by pre-acceleration of background electrons by the ponderomotive force of a tightly focused "injector" pulse [20,67].

Recently, ionization of high Z dopants within the laser produced plasma has become a preferred method for controlled injection [70–74]. In this scheme, the laser produced plasma is formed in a gas typically consisting of a large fraction of helium or hydrogen with a small fraction (< 10%) of a higher atomic number gas such as nitrogen or argon. The high Z dopant is not fully ionized in the leading edge of the wakefield drive pulse. The particular dopant is chosen such that ionization of the inner shell electrons occurs near the peak intensity of the drive pulse. These electrons are "born" within the wake and can become trapped in the wake potential and accelerated to high energy. While the ionization injection technique can lower the injection threshold and provide relatively low emittance beams [75], continuous injection of electrons into the wake leads to large electron beam energy spreads. Combining optical injection techniques with ionization injection has been proposed for generating ultra-low emittance, low energy spread electron beams [32,76].

1.2.5. Acceleration limits and dephasing

The energy gain from laser wakefield accelerators is fundamentally limited by the depletion of the drive laser pulse energy and the mismatch between the accelerated electron bunch velocity and the drive pulse group velocity. Laser diffraction is also a limiting factor on the length, and thereby single stage energy gain, of wakefield accelerators. However, as shown in Chapter 3, plasma waveguides and/or relativistic self-focusing can avoid this limitation. The dephasing length, L_d, can be estimated by considering an electron moving at $v_e \approx c$ across a quarter plasma wavelength (i.e. through the region of the wake with both a longitudinal accelerating field and radially focusing field) [17]. For a pulse traveling at group velocity v_g through a uniform plasma this gives

$$\frac{\lambda_p}{4} = (c - v_g)\frac{L_d}{c} = \left(1 - \sqrt{1 - \frac{\omega_p^2}{\omega^2}}\right) L_d \approx \frac{\omega_p^2}{2\omega^2} L_d \xrightarrow{yields} L_d = \lambda_p^3/2\lambda^2.$$

The dephasing length increases as the plasma density decreases and λ_p increases. Channel guiding can decrease the dephasing length appreciably because of the slower group velocity of the pulse in the channel compared to a transversely uniform plasma [77]. Overcoming the dephasing length in the mildly relativistic regime by tapered or modulated plasma waveguides has been proposed with the goal of reaching higher single stage energy gains [78,79].

The pulse depletion length, L_{dep}, in the linear regime can be estimated by comparing the wake energy to the laser pulse energy, $E_z^2 L_{dep} \cong E_L^2 c\tau_p$ where E_z is the wake electric field, E_L is the laser electric field, and $c\tau_p$ is the pulse length [47].

The wake electric field is found by solving equation (1.17) for a given pulse shape. Assuming a square pulse shape of duration $\lambda_p/2$ gives a depletion length of

$$L_{dep} \cong \frac{\lambda_p^3}{\lambda^2}\frac{2}{a_0^2} = L_d\frac{2}{a_0^2}.$$

In the mildly relativistic regime, it should be noted that $L_d \ll L_{dep}$. However, as the pulse amplitude increases the dephasing and depletion lengths become comparable.

Estimates of the maximum energy gain of an electron in a wakefield accelerator have been made through analytic and numerical studies. The energy gain in the mildly relativistic, dephasing length limited regime can be obtained through $\Delta W_{max} = e\langle E_z\rangle_{\lambda_p/4}L_d$ where the accelerating field is averaged over the plasma wave phase region with both accelerating and radially focusing fields. In this regime, Hubbard et al [77] obtain a maximum energy gain of

$$\frac{\Delta W_{max}}{m_e c^2} \sim \frac{a_0^2}{\sqrt{1+a_0^2/2}}\left(\frac{\lambda_p}{\lambda_0}\right)^2\left(1+\frac{2\lambda_p^2}{\pi^2 w_{ch}^2}\right)^{-1} \quad (1.21)$$

where the factor of $\left(1+\frac{2\lambda_p^2}{\pi^2 w_{ch}^2}\right)^{-1}$ arises from considering the correction to the dephasing length caused by the slower laser group velocity in a plasma waveguide with matched spot size w_{ch}compared to a uniform plasma. A phenomenological study of energy scaling in the highly nonlinear, 3D blow-out regime $(a_0 \gg 1)$ was performed by Lu et al. arriving at the scaling law

$$\frac{\Delta W_{max}}{m_e c^2} \cong \left(\frac{P}{m^2c^5/e^2}\right)^{\frac{1}{3}}\left(\frac{\lambda_p}{\lambda}\right)^{\frac{4}{3}}$$

where P is the drive laser power, λ_p the plasma wavelength, and λ the laser pulse wavelength [80]. This regime assumes a pulse length matched to the plasma wavelength and a peak power above the critical power for relativistic self-focusing.

These scaling laws suggest that higher single stage energy gains can be achieved by driving accelerators with lower plasma density. However, efficiently driving high amplitude plasma waves at low densities requires increasingly longer pulse durations $(c\tau \sim \lambda_p)$ and higher energy drive lasers are necessary to maintain the same a_0. Following this scaling, current state of the art high energy wakefield accelerators are driven by ~100 TW – 1 PW scale laser systems in low density (< 10^{18} cm^{-3}) plasmas with the goal of reaching ~10 GeV single stage energy gains [31]. Conversely, for applications where lower energy electron beams are suitable, the requirement for a high energy drive laser is greatly relaxed. As demonstrated in Chapter 6, this leads to 1 – 10 MeV electron beams accelerated by femtosecond laser pulses as low in energy as ~10 mJ.

1.3 Quasi-phase-matched direct laser acceleration

While laser wakefield acceleration has received the most theoretical and experimental attention from the laser-driven accelerator community, several other techniques have been proposed for achieving high gradient acceleration using intense lasers. Many of these schemes, such as the inverse Cherenkov accelerator [15,16,81], the semi-infinite vacuum accelerator [82], and the vacuum beat wave accelerator [83], suggest the direct use of the laser electric field or ponderomotive force as the accelerating field. These schemes can lead to low emittance, ultrashort electron bunches but tend to suffer from a modest acceleration gradient (< 40 MV/m) and an acceleration distance limited to approximately a Rayleigh length.

More recently, nano-structured dielectric materials injected with moderate intensity femtosecond laser pulses have shown promise as next generation high gradient accelerators "on a chip" [14]. The dielectric materials are fabricated to form a series of resonant cavities for optical wavelengths in direct analogy to the resonant cavity slow-wave structures used in standard RF linacs. Dielectric accelerators could potentially achieve ~1 GV/m accelerating fields when driven by high efficiency, high repetition rate fiber lasers with pulse energy ~ 1 μJ and pulse lengths ~1 ps. With continued development of nano-fabrication techniques and short pulse fiber laser technology, dielectric accelerators could offer a very efficient and compact platform for acceleration of relativistic electron beams.

Much of the work presented in this dissertation was performed in support of a proof of concept demonstration of another direct acceleration scheme, namely quasi-phase-matched direct laser acceleration (QPM-DLA) in an axially modulated plasma waveguide [12,84]. The QPM-DLA scheme requires three main components for operation: a modulated plasma waveguide, a radially polarized laser pulse, and a seed source of relativistic electrons. Chapter 3 demonstrates a method for generation of a plasma waveguide which is used in Chapter 4 to create modulated channels. Also in Chapter 4 generation and guiding of a quasi-radially polarized pulse, which acts as the accelerating field in the DLA scheme, is demonstrated. Finally, Chapters 5 and 6 describe the production of a potential seed source of relativistic electrons which could be used for a QPM-DLA proof of concept experiment.

The QPM-DLA technique proposes using an axially modulated plasma waveguide to guide femtosecond laser pulses with a longitudinal field component over many Rayleigh lengths. As shown in Chapter 4, higher order transverse modes supported by the corrugated plasma channel have a significant axial field component. The corrugated waveguide structure can be shown [12,84] to generate axial field harmonics propagating with a phase velocity given by

$$\frac{v_p}{c} = 1 + \frac{\overline{N}_{e,0}}{2N_{cr}} + \frac{4}{k_0^2 w_{ch}^2} - \frac{m k_{mod}}{k_0}$$

where $\overline{N}_{e,0}$ is the longitudinally averaged on axis electron density, N_{cr} is the plasma critical density associated with the drive laser frequency, $k_0 = 2\pi/\lambda_0$ is the laser wavenumber, w_{ch} is the matched spot size of the channel, $k_{mod} = 2\pi/d_{mod}$ is the wavenumber associated with the density modulation period d_{mod}, and m is an integer. For suitable choice of plasma density $\overline{N}_{e,0}$, channel modulation period d_{mod}, and mode number m, the phase velocity of the axial mode can be set such that $v_p \leq c$. The guided pulse phase velocity can, therefore, be set equal to the velocity of an externally injected relativistic electron bunch. If the injected pulse has a significant axial field component, for example a radially polarized TEM_{01}^* mode, then the electron will gain energy from the laser as the two co-propagate.

The attractiveness of the QPM-DLA technique stems from the essentially linear energy gain of the electron bunch with the laser field strength. A simple scaling law for the energy gain in the QPM- DLA process was developed by York *et al.* [12] by considering the maximum energy gain ΔE_{DLA} of a highly relativistic test electron accelerated in a modulated channel,

$$\frac{\Delta E_{DLA}}{m_e c^2} \sim 4\delta a_0 \left(\frac{\sigma_z}{w_{ch}}\right)\left(\frac{\lambda_p}{\lambda_0}\right)^2 \left(1 + \frac{2\lambda_p^2}{\pi^2 w_{ch}^2}\right)^{-2} \tag{1.22}$$

where $\delta = \frac{N_{e,max} - \bar{N}_{e,0}}{\bar{N}_{e,0}}$ is the modulation depth of the corrugated plasma waveguide, a_0 is the laser normalized vector potential, σ_z is the longitudinal extent of the laser pulse, λ_p is the plasma wavelength, and λ_0 is the laser wavelength. This can be compared to the scaling law for wakefield acceleration given above by equation (1.21). For typical experimental parameters $\lambda_0 = 800\ nm$, $w_{ch} = 15\ \mu m$, $a_0 = 0.25$, $\frac{\sigma_z}{c} = 300\ fs$ corresponding to a 1.9 TW laser power, $\bar{N}_{e,0} = 7 \times 10^{18} cm^{-3}$, $\delta = 0.9$, and a modulation period $d_{mod} = 349\ \mu m$, York *et al.* [12] calculate a peak energy gain of $\frac{\Delta E_{DLA}}{m_e c^2} \sim 1000$. This is comparable to the energy gain $\frac{\Delta E_{LWFA}}{m_e c^2} \sim 750$ calculated in [77] for a wakefield accelerator driven by a 7.16 TW laser in a suitable plasma channel. However, the linear dependence of ΔE_{DLA} on a_0 implies that even with peak powers ~10 GW typical of common CPA regenerative amplifiers, $\frac{\Delta E_{DLA}}{m_e c^2} \sim 50$. In this energy range, the highly nonlinear wakefield accelerator is generally unable to operate.

The initial velocity of the externally injected electron bunch is an important requirement for a successful proof of principle QPM-DLA experiment. For a fixed modulation period, d_{mod}, and fixed longitudinally averaged plasma density, $\bar{N}_{e,0}$, over the length of the accelerator, changes in the electron velocity due to acceleration by the laser field will cause it to dephase unless the electron is already sufficiently relativistic (and thus does not experience a significant change in velocity due to acceleration). This can be quantified by a trapping condition on the electron bunch which requires that the bunch Lorentz factor satisfy

$$\gamma_{th} \cong \left(\frac{k_m w_{ch}}{4\delta a_0}\right)\left(\frac{N_{cr}}{\overline{N}_{e,0}}\right)$$

where a_0 is the laser normalized vector potential $(a_0 \ll 1)$ [84,85]. In practice, this leads to a requirement for already highly relativistic electron beams. For example, for a modulation period $d_{mod} = 350\ \mu m$, modulation depth $\Gamma = 0.9$, laser spot size $w_{ch} = 12\ \mu m$, laser normalized amplitude $a_0 = 0.1$, laser critical density $N_{cr} = 1.7 \times 10^{21}\ cm^{-3}$ for an 800 nm Ti:Sapphire drive laser, and $\overline{N}_{e,0} = 1 \times 10^{19}\ cm^{-3}$ we find that $\gamma_{th} = 102$, so the injected electron beam must have an energy of at least ~50 MeV to experience linear energy gain in the modulated waveguide. Yoon et al. [85] showed that the required initial electron momentum can be drastically reduced by using a ramped plasma density or, equivalently, a ramped modulation period to phase match the interaction between the laser pulse and accelerating electron beam as the electron velocity increases. Indeed, PIC simulations performed by Yoon et al. demonstrated the feasibility of using density ramps to trap and accelerate electron bunches with initial energy as low as 5 MeV.

The seed electron source has proven to be a significant impediment to a proof of concept demonstration of the QPM-DLA technique. The seed source should be at least 5 MeV to satisfy the initial trapping threshold given suitable ramping of the plasma density or modulation period. For highest efficiency the bunch duration should be significantly shorter than the ~100 fs drive pulse duration. Further, femtosecond scale synchronization with the drive pulse is required, which implies an optically generated, or at least optically triggered, seed electron source. Finally, since potential high repetition rate operation is the hallmark of the QPM-DLA scheme, a seed source capable of high repetition rate is ideal. The standard wakefield accelerators described in Sec. 1.2 meet the first three requirements, but the >100 mJ laser systems used to drive these accelerators are not readily available at high repetition rates. The low divergence and energy spread available from wakefield accelerators is actually something of a drawback as an injector for the QPM-DLA scheme. This type of seed beam demands extremely precise alignment into the corrugated waveguide and precise matching of the modulation period to the accelerated beam energy, assuming the beam energy is not already high enough that a ramped modulation period is unnecessary.

The high density self-modulated wakefield accelerator presented in Chapter 6 of this dissertation is a good candidate as an ultra-short, femtosecond synchronized, high repetition rate injector for a QPM-DLA experiment. The experiments presented make use of the scaling laws for relativistic self-focusing and self-phase modulation to drive a high amplitude plasma wave with sub-terawatt, ~10 mJ laser pulses in a high density ($> 10^{20} cm^{-3}$) plasma. Wave breaking and self-injection lead to ~500 pC electron beams with exponential energy distributions reaching well above the required 5 MeV threshold in a moderately collimated beam with ~200 mrad divergence angle. Thus, between the plasma channel generation results presented in Chapter 3, the modulation techniques and quasi-radially polarized mode guiding presented in Chapter 4, and the high repetition rate seed source presented in Chapter 6, all the components necessary for a proof of principle QPM-DLA experiment have been demonstrated.

Chapter 2: The UMD 25 TW Laser System

2.1 Overview of high peak power, femtosecond laser systems – Chirped Pulse Amplification and Ti:Sapphire lasers

The field of intense laser-plasma interactions has been enabled by the rapid advancement and availability of multi-terawatt femtosecond laser systems [86,87]. Indeed, within the past decade a number of commercially available systems capable of reaching relativistic intensities have come to market, moving the tools required for studying relativistic optics from large facilities into university laboratories. The vast majority of these systems are based on Ti:Sapphire (Ti:Al_2O_3) gain media employing the chirped pulse amplification (CPA) technique [8,86,87]. Ti:Sapphire was developed in the mid-1980s as a solid state lasing medium and has become the gain medium of choice for nearly all multi-terawatt femtosecond laser systems primarily due to its extremely broad gain bandwidth which allows lasing between 670-1070 nm. Due to this broad bandwidth, Ti:Sapphire oscillators have been demonstrated to support pulses as short as two optical cycles [88,89], and commercial oscillators operating with pulse durations ~20 fs are now ubiquitous. Other optical and mechanical properties, such as a large stimulated emission cross section, large saturation fluence, and high thermal conductivity make Ti:Sapphire an excellent choice for use as a gain medium in laser amplifiers [9,90]. The fluorescence lifetime of Ti:Sapphire, however, is short, only 3.2 μs, which means pulsed laser systems are generally required as a pump with the absorption band peaking around 500 nm.

Peak powers in the multi-terawatt regime generally require multiple stages of amplification. Direct amplification of femtosecond pulses is severely limited by nonlinear phase accumulation, which can lead to severe beam distortion or self-focusing and laser crystal damage. The CPA technique [7,8] avoids these issues by first applying a large linear chirp to the ultrashort pulse prior to amplification, typically stretching the pulse by a factor of ~1000. The resulting pulse peak intensity is small enough to be amplified without risking damage to the amplifier rods. A pulse compressor then removes the linear chirp applied by the stretcher and any material dispersion in laser chain, ideally returning the amplified pulse to its original femtosecond-scale duration.

2.2 UMD 25 TW Ti:Sapphire Laser Architecture

All of the experiments in this dissertation were performed using a 25 TW Ti:Sapphire laser system delivering a maximum of 0.9 J on target with a full width at half maximum pulse duration as short as 39 fs. The system was designed as a 20 TW system by Coherent, Inc. It was subsequently upgraded to a 25 TW system using a more energetic pump laser, and incorporating a deformable mirror – wave front sensor loop for phase front control and a Fastlite Dazzler acousto-optic phase modulator for adaptive spectral phase control. The system architecture, depicted in Fig. 2.1, employs a standard CPA design. The output of a Coherent Micra femtosecond oscillator is stretched and amplified in a Coherent Legend regenerative amplifier followed by amplification in a four pass bowtie amplifier. After amplification the pulse is compressed back to 39 fs with a time-bandwidth product of $\Delta t_{FWHM}\Delta\nu_{FWHM} \cong 0.472$. A pulse with a Gaussian spectral amplitude will have a time bandwidth product of $\Delta t_{FWHM}\Delta\nu_{FWHM} \cong 0.441$, which for our 26 nm FWHM amplified bandwidth corresponds to a 36.5 fs FWHM pulse duration.

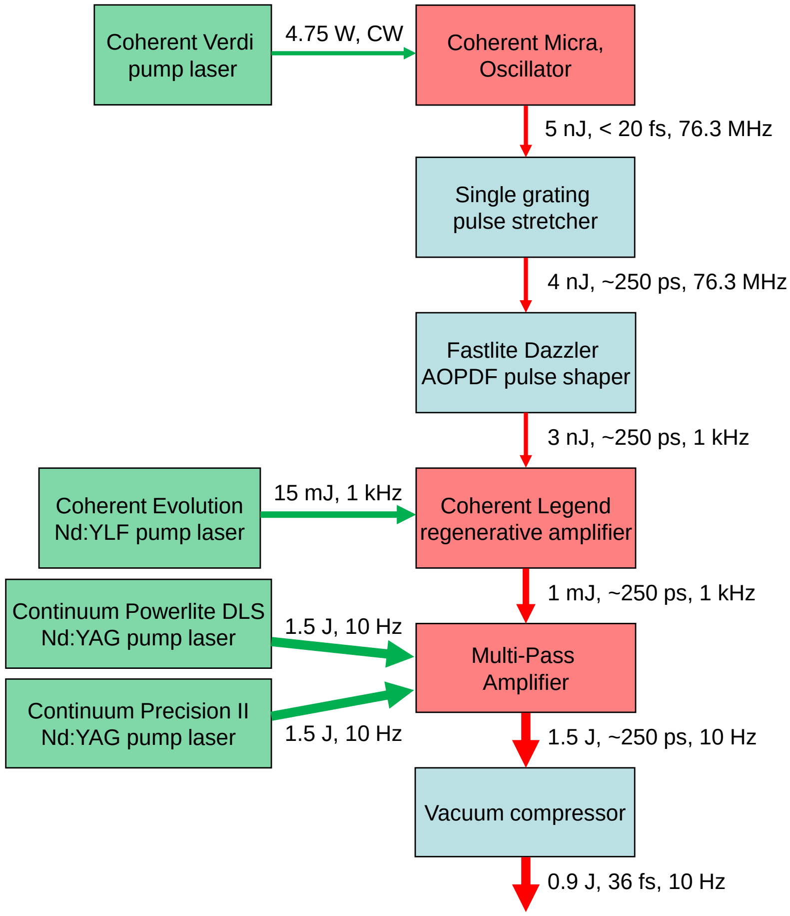

Figure 2.1. Block diagram of the 25 TW laser system used to perform the experiments in this dissertation.

The Coherent Micra is a Kerr lens modelocked femtosecond oscillator pumped by a 4.75W continuous wave Nd:YVO_4 laser (Coherent Verdi). It delivers <20 fs pulses with bandwidths ~80 nm centered at 790 nm. The Micra operates at a repetition rate of 76.3 MHz with output pulses synchronized to the oscillator of a home built ~140ps Nd:YAG laser system, described at the end of this chapter. Intra-cavity bandwidth tuning is achieved through a pair of Brewster prisms which compensate for the material dispersion within the cavity.

The ~5 nJ, < 20 fs pulses from the Micra are sent through a Faraday isolator to a single grating stretcher which adds positive group delay dispersion, stretching the pulse to ~250 ps. After the stretcher, the pulse passes through an acousto-optic phase modulator (Fastlite Dazzler) which is used to correct higher order spectral phase from the laser chain. The use of the Dazzler for pulse shaping will be discussed in detail below. After phase modulation the pulse is injected into a 1 kHz regenerative (regen) amplifier (Coherent Legend) pumped by a 15 W, Q-switched Nd:YLF laser (Coherent Evolution). Electro-optic Pockels cells enable controlled switching of the seed pulse into the regen cavity and switching out of the amplified pulse. The Pockels cells operate by applying a ~1 ns rise time high voltage pulse across a KD*P crystal. The electro-optic (Pockels) effect is an electric field-induced birefringence in the KD*P crystal. The voltage (electric field) and thickness of the KD*P are tuned for half wave rotation after double passing the crystal. High contrast polarizing optics within the regen cavity then trap the seed pulse only when its polarization has been rotated by the switch in Pockels cell. After a sufficient number of round trips within the cavity (approximately 24 in our system) the gain saturates and the switch out Pockels cell is fired, rotating the pulse polarization back to vertical and rejecting the amplified pulse out of the resonator. The pulse is amplified in the regen to ~800 μJ, providing a total gain of ~10^5 with a nanosecond pre-pulse contrast of ~1000:1.

The strong gain within the regenerative amplifier affects the spectral characteristics of the amplified pulse. The fluence of the k-th pass through the amplifier is given by

$$I_k = T I_S \ln\{e^{g_0(\omega)L}\left[e^{I_{k-1}/I_S} - 1\right] + 1\} \tag{2.1}$$

where T is the transmission in a single resonator round trip, $I_S$is the saturation fluence (1 J/cm^2 for Ti:Sapphire), and $g_0(\omega)$ is the frequency dependent small signal gain

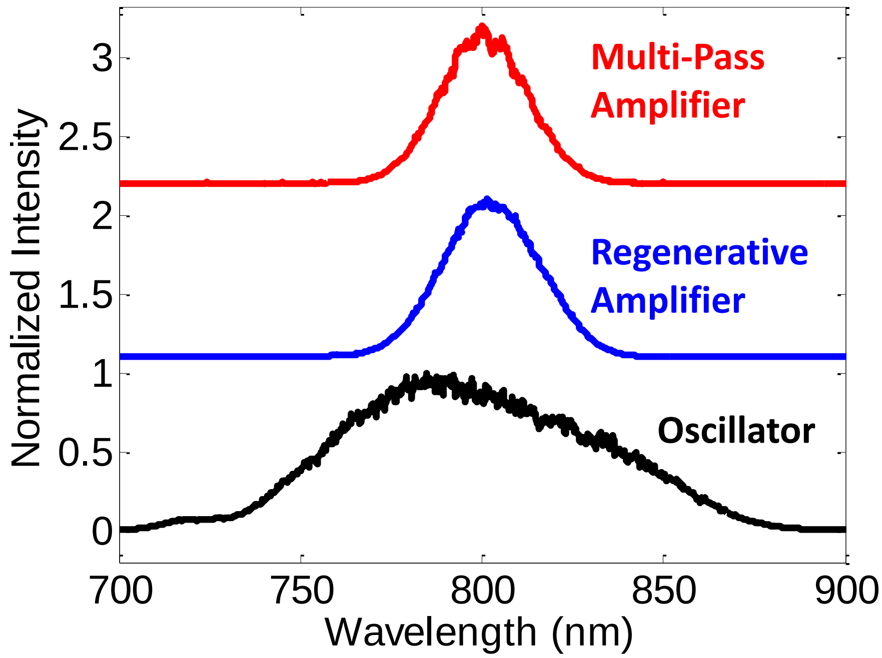

Figure 2.2. Spectrum of the laser pulse at various points in the amplification chain. Gain narrowing reduces the spectral bandwidth in the regenerative and multi-pass amplifiers to a final bandwidth of 26 nm, with the majority of the narrowing occurring in the regenerative amplifier. Gain shifting, again primarily in the regenerative amplifier, shifts the center wavelength from 790 nm in the oscillator to 808 nm after amplification.

coefficient [91]. The frequency dependence of the small signal gain coefficient leads to a large difference in the final amplification near the peak of the Ti:Sapphire gain curve compared to the wings [92–94]. This effect, known as gain narrowing, can lead to drastic reduction in the amplified pulse bandwidth. As evidenced by Fig. 2.2, gain narrowing reduces the pulse bandwidth from the ~80 nm FWHM oscillator bandwidth to 34 nm FWHM after the regenerative amplifier.

Second, gain saturation in the last few passes through the regenerative amplifier shifts the center of the pulse spectrum from an 800 nm center wavelength to ~808 nm. With a positive chirp on the seed pulse, the redder frequencies arrive at the amplifier rod before the bluer frequencies. At gain saturation this means the red frequencies experience a larger gain than the blue frequencies, thereby red-shifting

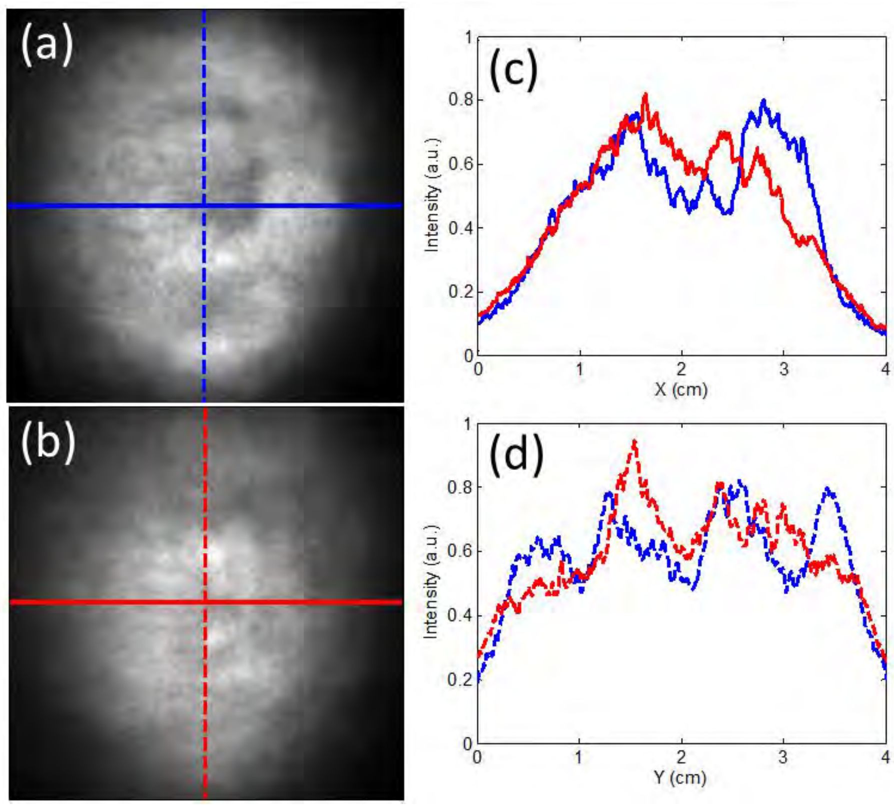

Figure 2.3. Amplified and expanded beam profile before (a) and after (b) implementing a vertical beam inversion after the second pass of the MPA. Lineouts along the x (c) and y (d) axes show a moderate improvement in the beam uniformity after the beam flip.

the entire pulse spectrum [93]. Gain narrowing in the regenerative amplifier is a particular issue in this system as it represents the main factor limiting the achievable pulse duration.

The pulse proceeds from the regenerative amplifier through an external Pockels cell into a bowtie configuration multipass amplifier (MPA). The external Pockels cell reduces the pulse repetition rate from 1 kHz to 10 Hz and improves the nanosecond pre-pulse contrast from the regen to better than 10^6:1. The Gaussian mode beam from the regenerative amplifier is then expanded to a 2.5 mm FWHM and executes four passes through the MPA's 1" diameter Ti:Sapphire rod. After the second pass, a periscope flips the beam vertically to average out any top-bottom spatial irregularities. The effect of the periscope addition to the MPA is shown in Fig. 2.3 which shows the amplified beam profile. The total energy before and after addition of the periscope was unchanged. The MPA's Ti:Sapphire rod is symmetrically end-pumped by two 10 Hz, Q-switched, frequency doubled Nd:YAG laser systems delivering 1.5 J each at λ=532 nm. The pump beams are relay imaged with a slight demagnification so that they have a 9 mm diameter top hat profile at the MPA rod. Gain in the MPA was simulated by iteratively solving equation (2.1) starting with the measured beam profile and energy from the regen output. The pulse energy after each pass, shown in Fig. 2.4(a), shows saturation on the last pass through the MPA with total output energy of 1.43 J and 47% extraction efficiency. The measured beam out of the MPA has a ~9 mm diameter top hat profile, shown in Fig. 2.4(b), and measured pulse energy of 1.4 J.

After amplification, the beam passes through a waveplate – thin film polarizer (TFP) combination which is used for laser pulse energy control during experiments.

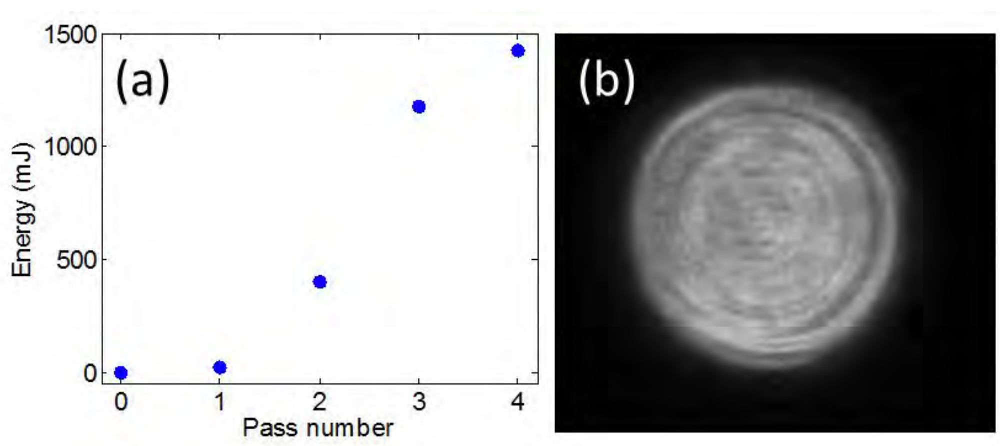

Figure 2.4. (a) Theoretical energy output per pass in the MPA pumped by two 9 mm diameter, 1.5 J frequency doubled Nd:YAG lasers. The seed pulse reaches gain saturation on the fourth pass. (b) Measured seed beam profile after the fourth and final pass through the MPA crystal. The pulse energy is 1.4 J.

The TFP, when used in transmission, has a fairly poor extinction ratio of only 9:1. However, the pulse compressor is polarization dependent and attenuates any vertically polarized component of the laser pulse with ~1% transmission. Before entering the pulse compressor, the amplified beam is expanded to a 4 cm diameter to reduce the total fluence on the compressor gratings below 100 mJ/cm^2, the rule-of-thumb maximum fluence for gold gratings [95]. Pulse compression is achieved using a Treacy-style grating compressor [96] housed in a vacuum chamber (the "vacuum compressor") with approximately 63% energy throughput. Maximum on-target energy of 900 mJ and pulse duration of 39 fs produces a maximum 25 TW peak power on target.

2.3 Spectral phase compensation using an acousto-optic modulator

2.3.1 Dispersion and higher order spectral phase in femtosecond laser pulses

An electric field component of a general laser pulse at a fixed point in space can be described in the time domain as

$$E_{laser}(t) = E_0(t)e^{-i\omega_0 t+\Phi(t)}$$

where $E_0(t) = \sqrt{I(t)}$ is the electric field amplitude, $I(t)$ is the laser intensity, ω_0 is the carrier frequency, and $\Phi(t)$ is the pulse temporal phase. Similarly, the spectral representation of the pulse, $\tilde{E}(\omega)$, can be written in terms of a complex spectral amplitude and phase as

$$\tilde{E}(\omega) = \tilde{\mathrm{E}}_0(\omega)e^{i\phi(\omega)}.$$

The time domain pulse representation is linked to its frequency domain counterpart through the Fourier transform pair

$$E(t) = \frac{1}{2\pi}\int_{-\infty}^{\infty} \tilde{E}(\omega) e^{-i\omega t} d\omega$$

$$\tilde{E}(\omega) = \int_{-\infty}^{\infty} E(t) e^{i\omega t} dt.$$

From this relationship we can see that complete characterization of the pulse can be achieved through measurement of the pulse amplitude and phase in either the time or frequency domain. The spectral phase $\phi(\omega)$ can be expanded in powers of $(\omega - \omega_0)$ as

$$\phi(\omega) = \phi_0 + (\omega - \omega_0)\phi_1 + \frac{(\omega - \omega_0)^2 \phi_2}{2} + \frac{(\omega - \omega_0)^3 \phi_3}{3!} \ldots$$

where $\phi_n = \frac{d^n \phi}{d\omega^n}$. The zero order term, ϕ_0, represents a constant phase offset of the carrier frequency with respect to the peak of the pulse envelope or some other reference time, and is thus called the "carrier-envelope" phase. The first order dispersion ϕ_1 represents a delay in the time domain. The second order dispersion, or group delay dispersion (GDD), describes a linear frequency chirp in the time domain. Higher order dispersions $(\phi_3, \phi_4, etc.)$ yield nonlinear frequency chirps and more complicated time domain pulse shape distortions. For an arbitrary spectral amplitude, $\tilde{E}(\omega)$, the shortest pulse duration in the time domain will occur when the spectral phase is linear, meaning that ϕ_2 and higher order dispersion terms in $\phi(\omega)$ all vanish. Therefore, in short pulse CPA systems careful attention must be paid to dispersion management along the amplifier chain.

In any CPA chain, the pulse picks up spectral phase from dispersive elements, such as the gratings in a pulse stretcher and compressor, as well as from material dispersion inside the laser chain. A pulse propagating through an optical medium of length L will distort in the time domain due to the dependence of the refractive index on wavelength where the accumulated higher order spectral phase is given by

$$\phi_2 = \frac{\lambda^3 L}{2\pi c^2}\frac{d^2 n}{d\lambda^2},$$

$$\phi_3 = -\frac{\lambda^4 L}{4\pi^2 c^3}\left(3\frac{d^2 n}{d\lambda^2} + \lambda\frac{d^3 n}{d\lambda^3}\right),$$

$$\phi_4 = \frac{\lambda^5 L}{8\pi^3 c^4}\left(12\frac{d^2 n}{d\lambda^2} + 8\lambda\frac{d^3 n}{d\lambda^3} + \lambda^2\frac{d^4 n}{d\lambda^4}\right).$$

Additionally, most grating stretchers and compressors will add higher order spectral phase due to optical aberrations [97,98]. The total spectral phase accumulated along the laser chain is then the sum of the spectral phase accumulated from the stretcher, material dispersion, and the compressor

$$\phi_{total}(\omega) = \phi_{stretcher}(\omega) + \phi_{material}(\omega) + \phi_{compressor}(\omega) \tag{2.2}$$

where

$$\phi_{material}(\omega) = \sum_{i=1}^{N} n_i(\omega)\frac{\omega}{c}L_i$$

is the spectral phase accumulated from each of the N components the pulse passes through. Like orders can be grouped in equation (2.2) so that

$$\phi_{2,total} = \phi_{2,stretcher} + \sum_{i=1}^{N}\frac{\lambda^3 L_i}{2\pi c^2}\frac{d^2 n_i}{d\lambda^2} + \phi_{2,compressor}$$

$$\phi_{3,total} = \phi_{3,stretcher} - \sum_{i=1}^{N}\frac{\lambda^4 L_i}{4\pi^2 c^3}\left(3\frac{d^2 n_i}{d\lambda^2} + \lambda\frac{d^3 n_i}{d\lambda^3}\right) + \phi_{3,compressor}$$

$$\phi_{4,total} = \phi_{4,stretcher} + \sum_{i=1}^{N} \frac{\lambda^5 L_i}{8\pi^3 c^4}\left(12\frac{d^2 n_i}{d\lambda^2} + 8\lambda\frac{d^3 n_i}{d\lambda^3} + \lambda^2\frac{d^4 n_i}{d\lambda^4}\right) + \phi_{4,compressor}.$$

A properly designed stretcher-compressor pair will ideally be able to satisfy $\phi_{2,total} = \phi_{3,total} = \phi_{4,total} = 0$ so as to achieve the shortest pulse possible.

In practice, it is difficult to fully compensate for material dispersion using simple grating based stretcher and compressor pairs. Fundamental to the CPA technique is the addition and compensation of quadratic spectral phase or chirp by the stretcher and compressor, and fine adjustments to the incidence angle in the compressor can partially compensate for cubic spectral phase. However, uncompensated third and fourth order spectral phase can cause significant pulse distortion in the time domain. This section describes the measurement and compensation of higher order spectral phase components in our laser chain using the frequency resolved optical gating (FROG) technique for pulse measurement and an acousto-optic programmable dispersive filter (AOPDF) for spectral phase compensation.

2.3.2 Second harmonic FROG

Modelling of ultrashort laser-plasma interaction experiments requires a complete diagnosis of the pulse shape in the time domain. A number of femtosecond pulse measurement techniques have been proposed and demonstrated with wide variation in accuracy and complexity [99–102]. Femtosecond scale characterization of the amplified pulse shape was performed using the second harmonic generation frequency resolved optical gate (SHG FROG) technique, based on the simplicity of

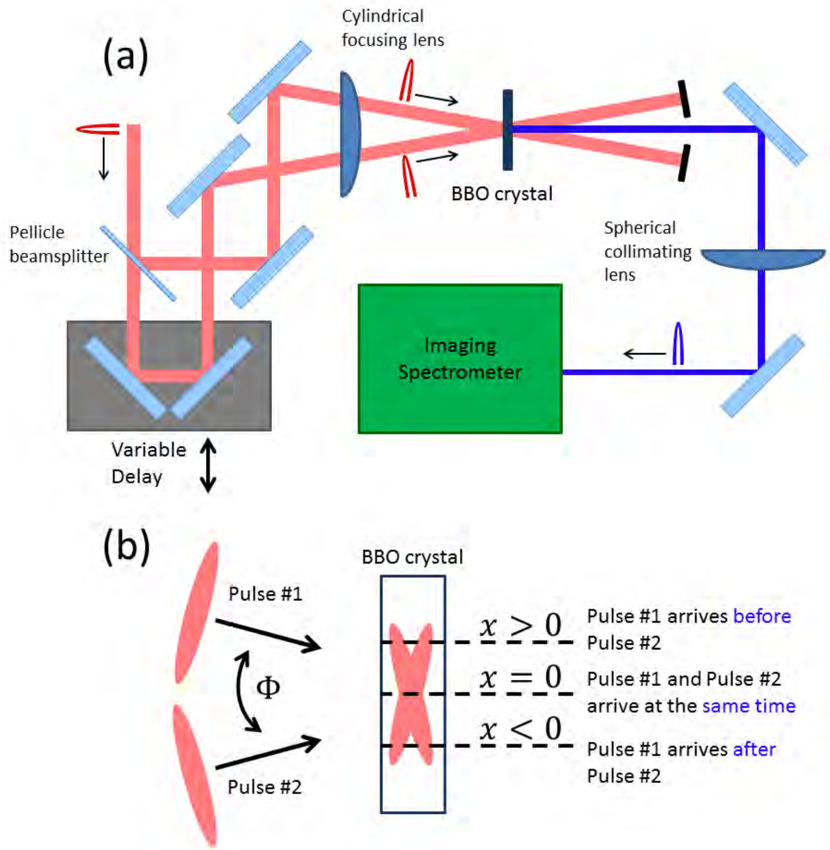

Figure 2.5. (a) A schematic of the single shot SHG FROG used for characterization of the pulse spectral amplitude and phase. The pulse is split using a thin pellicle beamsplitter and focused using a cylindrical lens into a BBO crystal. Focusing using a cylindrical lens allows the time delay, τ, to be mapped onto the geometrical dimension, x, perpendicular to the direction of focusing as illustrated in (b). The sum frequency signal pulse is imaged to the entrance slit of an imaging spectrometer to form the complete SHG FROG spectrogram in a single shot.

the measurement and the ability of the SHG FROG to fully reconstruct the ultrashort pulse in the time domain. The SHG FROG produces a time-frequency spectrogram by spectrally resolving an autocorrelation of the measured pulse. The FROG signal takes the form

$$I_{FROG}(\omega,\tau) = \left|\int_{-\infty}^{\infty} E(t-\tau)E(t+\tau)\exp(-i\omega t)\,dt\right|^2,$$

where $E(t)$ is the time dependent laser electric field and τ represents the delay between the pulse arrival times in the SHG crystal, as shown in Fig. 2.5, which is mapped onto a spatial dimension of the SHG signal by the crossing of the two beams in the BBO crystal. The delay, τ, is related to the crossing angle, Φ, and the transverse distance across the crystal, x, by $\tau = \frac{nx\sin(\Phi/2)}{c}$ where n is the crystal refractive index, c is the speed of light, and $x = 0$ at the location in the crystal where the two pulses arrive at the same time. The SHG signal is imaged from the crystal to the entrance slit of an imaging spectrometer which spectrally resolves the SHG signal at each delay point to form the full FROG spectrogram.

Reconstruction of the pulse amplitude and phase was performed using commercial reconstruction software [103] with measured spatial and spectral calibrations. The problem of retrieving pulse amplitude and phase from a FROG trace has been shown to be equivalent to the 2D phase retrieval problem frequently encountered in image processing [102], and the software implements the method of generalized projections to solve this reconstruction problem. The reconstruction accuracy can be quantified by the "FROG error" defined by

$$G = \sqrt{\frac{1}{N^2}\sum_{i,j=1}^{N}\left|I_{meas}(\omega_i, \tau_j) - \mu I_{ret}(\omega_i, \tau_j)\right|^2}$$

where $I_{meas}(\omega_i, \tau_j)$ is the measured FROG spectrogram, $I_{ret}(\omega_i, \tau_j)$ is the spectrogram retrieved by the algorithm, and μ is a normalizing constant that minimizes G [102]. This is effectively a measurement of the sum of squares error between the measured and retrieved FROG traces. A FROG error below 1% of the peak intensity of the FROG trace is generally considered as an acceptable reconstruction.

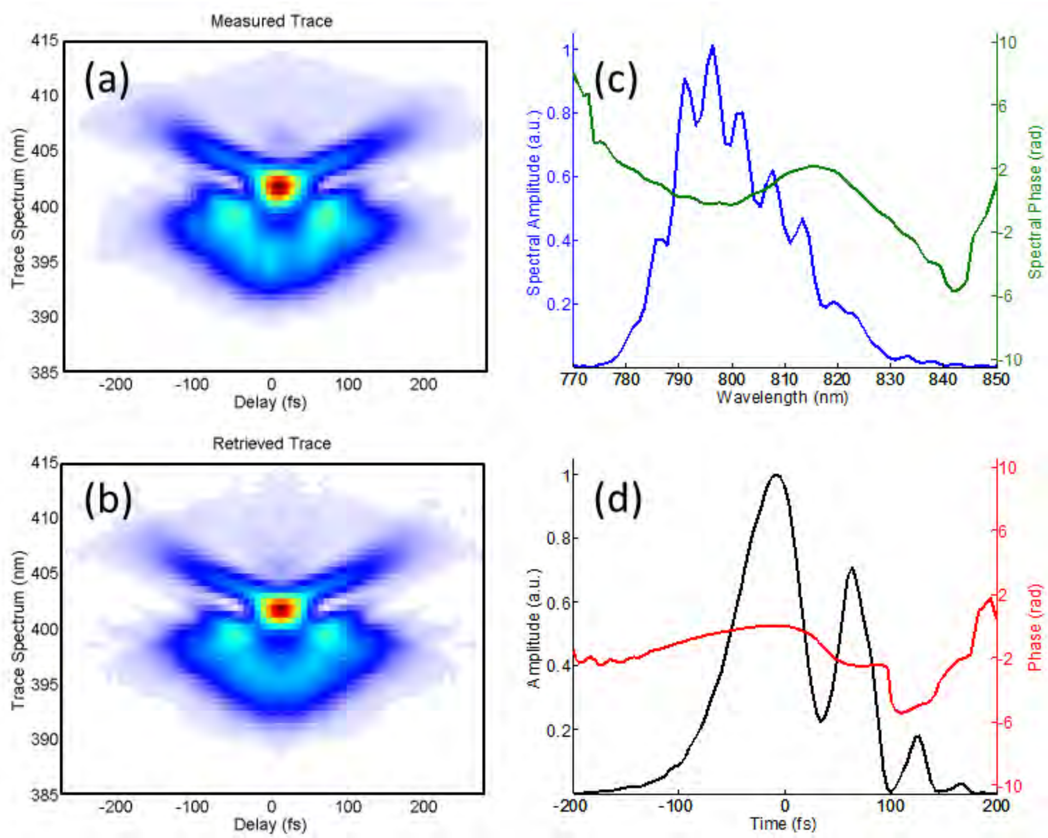

Figure 2.6. SHG FROG measurement of a pulse exhibiting strong cubic spectral phase. The measured trace (a) and retrieved trace (b) closely match, with a FROG error of 0.006. Extracted spectral domain (c) and time domain (d) representations of the pulse electric field amplitude and phase show the effect of non-negligible third order spectral phase.

A sample FROG trace is shown in Fig. 2.6(a) with the reconstructed FROG trace shown in Fig. 2.6(b). The frequency domain amplitude and phase corresponding to the reconstructed FROG trace are shown in Fig. 2.6(c), and the time domain pulse intensity and phase are shown in Fig. 2.6(d). The spectral phase of the measured pulse in Fig. 2.6 exhibits a strong cubic dependence which causes the multi-peaked structure seen in the time domain representation of the pulse. The SHG FROG geometry suffers from an ambiguity in the direction of time caused by the trace symmetry with respect to delay. Thus, the subsidiary peaks in the time domain reconstruction may have arrived either before or after the main peak.

The direction of time ambiguity can be resolved by adding a small amount of third order phase with a known sign with, for example, the acousto-optics programmable dispersive filter (AOPDF) described in the next section. Alternatively, an etalon can be inserted into the beam in advance of the SHG FROG. The etalon will generate a post pulse, so reconstruction of a FROG trace containing both pulses will fix the direction of increasing time.

2.3.3 Spectral phase compensation with an acousto-optic programmable dispersive filter

As mentioned above, higher order components of the pulse spectral phase, arising mainly from material dispersion, can be difficult to compensate and will distort an ultrashort pulse away from its bandwidth-limited duration. Figure 2.6(d) shows an example of our pulse with temporal "wings" caused mainly by uncompensated third order phase from the amplifier chain. Novel compressor designs have been used for complete compensation of the third and fourth order spectral phase along a full CPA laser chain without the use of adaptive pulse shaping [97,98]. However, these designs can be complicated and adaptive pulse shaping methods have shown great flexibility in compensating spectral phase in CPA systems without necessitating perfect stretcher-compressor matching [104–106]. These methods can also control spectral amplitude, allowing for mitigation of effects such as gain narrowing and gain shifting [106].

An acousto-optic programmable dispersive filter (AOPDF) was installed in the laser chain between the stretcher and regenerative amplifier. The AOPDF (Fastlite Dazzler [107]) is comprised of a programmable RF signal generator and a piezoelectric transducer attached to a bulk birefringent crystal. The RF pulse applied to the transducer generates a sound wave in the birefringent crystal counter-propagating to the incident optical pulse. If the RF pulse is of a single frequency, the incident optical pulse, polarized along the ordinary birefringence axis, undergoes Bragg scattering and couples to an extraordinary wave. The phase matching condition for Bragg scattering in the crystal is $\boldsymbol{k_2} \cong \boldsymbol{k_1} + \boldsymbol{q}$, where $\boldsymbol{k_1}$ is the incident optical wave vector, $\boldsymbol{k_2}$ is the scattered optical wave vector, and $\boldsymbol{q}$ is the acoustic wave vector. Further, the frequencies must satisfy the energy conservation relation $\omega_2 = \omega_1 + \Omega$. The Bragg condition is satisfied for only a narrow frequency band in the optical pulse, so in this configuration the RF pulse acts as a programmable optical filter where the optical frequency selection is controlled through the RF frequency of the acoustic wave. Since $\omega_1 \gg \Omega$ the optical frequency remains effectively unchanged, but the amplitude and phase at ω_1 of the extraordinary-coupled optical field *is* changed.

For pulse shaping in the AOPDF, a programmable, chirped RF pulse is used to satisfy the Bragg condition across a broad optical bandwidth within the birefringent crystal [106,108,109]. The variation in the instantaneous frequency of the RF pulse within the crystal controls the longitudinal position in which a selected optical frequency will be scattered from an ordinary into an extraordinary wave. This, in turn, controls the relative delay between frequency components in the optical pulse. Thus, the maximum time window over which the AOPDF can shape the optical pulse is given by the difference in optical transit times between the ordinary and extraordinary axes of the birefringent crystal. For our Dazzler this is an

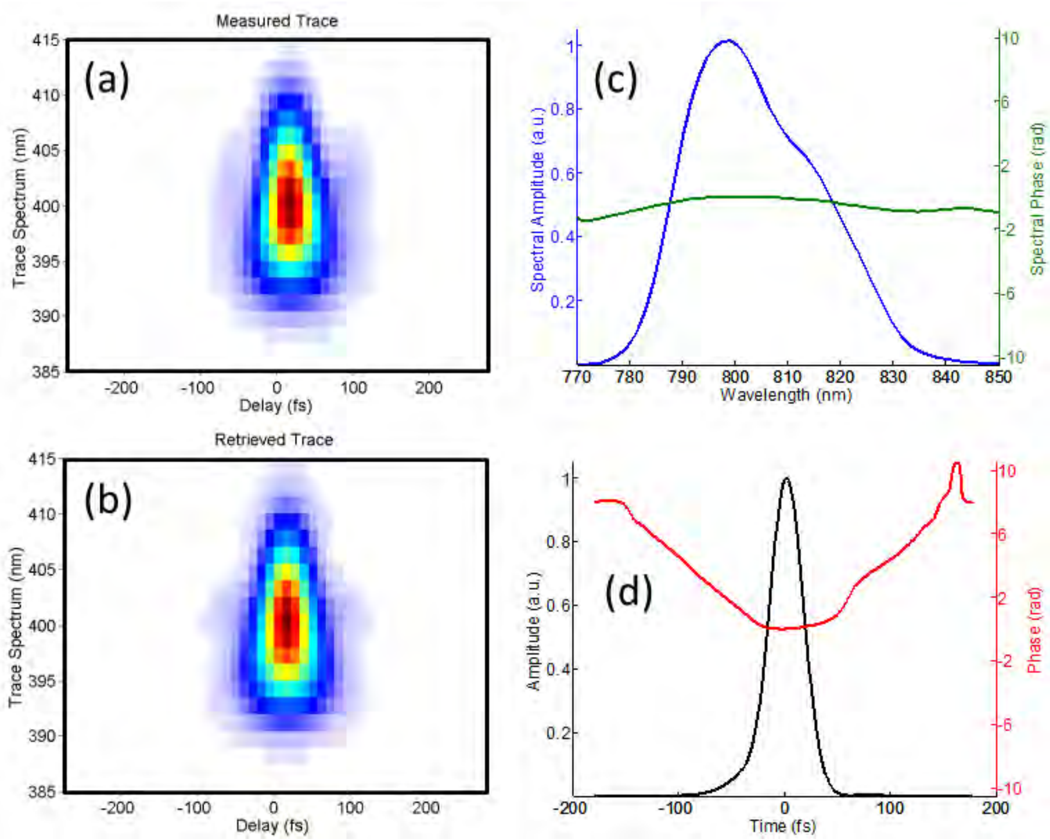

Figure 2.7. Measured (a) and retrieved (b) SHG FROG traces after spectral phase compensation by the Dazzler AOPDF. The retrieved spectral phase (c) is much flatter and the retrieved temporal intensity envelope (d) is nearly bandwidth limited with FWHM pulsewidth 39 fs.

approximately 8 ps time window. More precisely, the acousto-optic interaction leads to terms in the frequency domain wave equation of the form

$$S_2(\omega_2)\exp[i(k_2 z - \omega t)] \propto S_1(\omega_1)\exp[i(k_1 z - \omega_1 t)] \times S_{ac}(\Omega)\exp[i(\mathrm{qz} - \Omega\mathrm{t})]$$

where S_1 and S_2 are the incident and scattered complex spectral amplitudes for the optical waves and S_{ac} is the complex spectral amplitude for the acoustic wave [108]. Given the phase matching conditions this leads to $S_2(\omega_2) = S_1(\omega_1)\, S_{ac}(\Omega)$. In the time domain the scattered optical wave is a convolution of the incident optical wave with the acoustic wave. Therefore, given known input, $S_1(\omega_1)$, and a required output, $S_2(\omega_2)$, the required acoustic filtering function, $S_{ac}(\Omega)$ can be easily computed. With RF pulses in the ~50 MHz range with ~20 MHz bandwidths, pulse shaping over optical bandwidths >100 nm centered at 800 nm can be achieved, allowing for pulse shaping even in the few cycle regime [110].

The Fastlite Dazzler AOPDF installed between the stretcher and regen was used in conjunction with pulse measurements by an SHG FROG to compensate for higher order dispersion in the amplifier chain. For initial pulse measurements an RF waveform compensating for the material dispersion within the Dazzler crystal was used and the SHG FROG was placed after the vacuum compressor. The FROG trace and reconstructed pulse shown in Fig. 2.6 show temporal wings associated with uncompensated higher order phase, mainly 3rd order. The measured spectral phase was then fed back into the Dazzler software controlling the RF waveform in the AOPDF. This procedure was iterated until a flat spectral phase at the end of the amplifier was achieved, typically only requiring two or three iterations. Figure 2.7 shows a FROG trace and reconstructed pulse after phase optimization with the Dazzler. The wings are nearly eliminated, and the FWHM pulse duration is reduced to 39 fs. The Dazzler can also be used in experiments for fine control of the time-domain pulse shape. Figure 2.8 shows a plot of the FWHM pulse duration measured in the SHG FROG as a function of GDD applied by the Dazzler. The pulse duration has a hyperbolic dependence on the GDD as expected [101], and a least squares fit gives the minimum pulse duration as 38.7 fs.

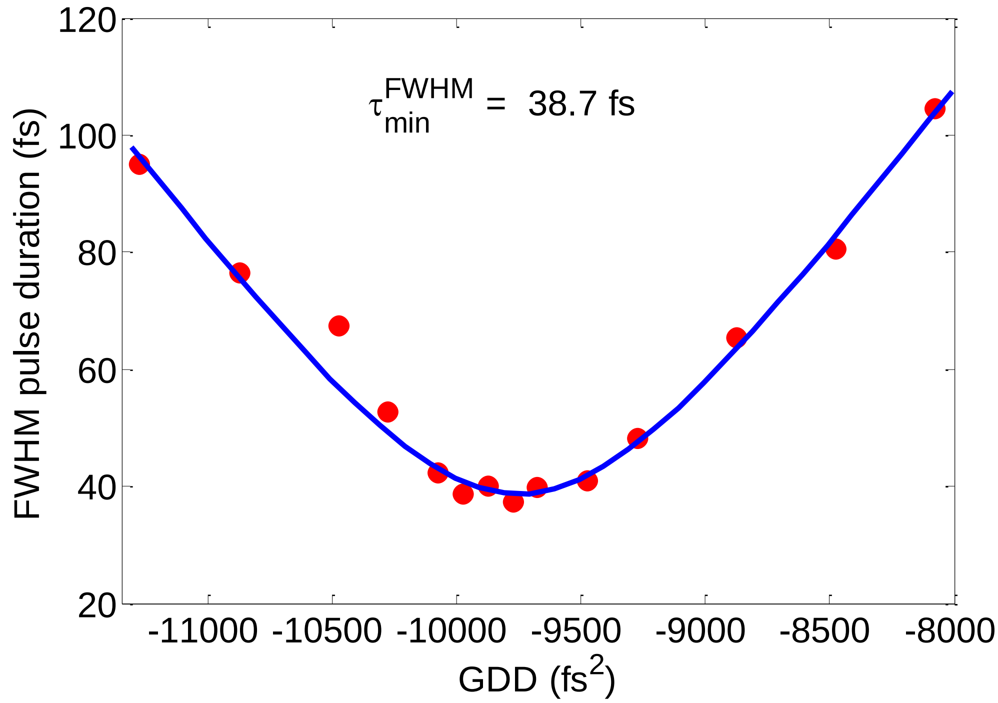

Figure 2.8. The FWHM pulse duration measured by the SHG FROG as a function of GDD applied by the Dazzler along with a least squares fit to a hyperbola.

2.4 Laser pre-pulse characterization by third order autocorrelation

With peak intensities of our 25 TW laser system exceeding 10^{19} W/cm^2, ionization of a target medium can occur well in advance of the main peak of the ultrashort laser pulse. For this reason the temporal structure of the laser pulse must be well-characterized over a wide temporal window and with a high dynamic range. Particularly in laser-solid or laser-cluster interactions, where collisional ionization can play an important role, knowledge of the picosecond and nanosecond 'pre-pulse' contrast is important to prevent unintended plasma generation prior to the main pulse arrival.

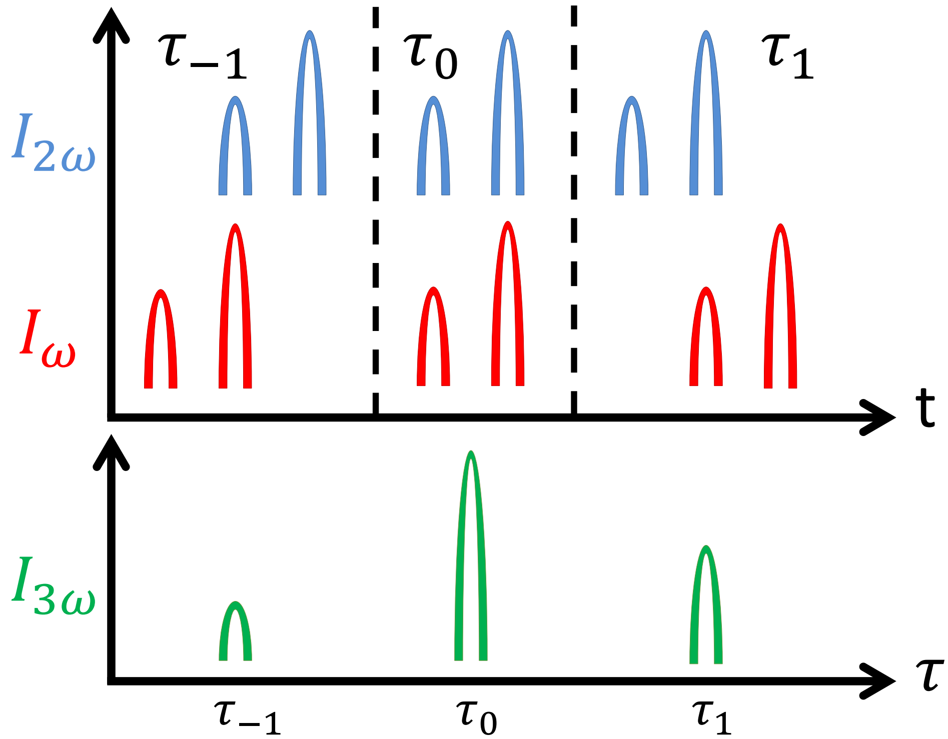

Figure 2.9. The third order nonlinearity in the high dynamic range autocorrelator makes pre- and post- pulses distinguishable. Overlap of the main pulse in the fundamental arm with the pre-pulse of the second harmonic arm (τ_{-1}) gives a third harmonic signal equal to the square of the signal from overlapping the main pulse of the second harmonic arm with the pre-pulse of the fundamental arm.

Pre-pulse and pulse pedestal measurements are made using a commercial third order scanning autocorrelator (Ultrafast Innovations [111]). For the autocorrelation measurement the beam is sent through a calibrated variable attenuator, then split into two arms, one of which is upconverted to the second harmonic while the other arm is sent through a variable delay line. The second harmonic and fundamental are then combined in a thin beta barium borate (BBO) crystal to generate a signal at the third harmonic of the femtosecond pulse. The signal is given by

$$I_{3\omega} = \int_{-\infty}^{\infty} I_\omega(t-\tau) I_{2\omega}(t)dt$$

and the delay, τ, between the fundamental and second harmonic is swept to map out the third order autocorrelation function over a ~650ps time range.

The use of a third order nonlinearity yields advantages for high contrast pulse measurements. First, the third harmonic signal is inherently background free since neither the fundamental or second harmonic arm can make a third harmonic photon alone. This is in contrast to second harmonic or polarization gating techniques where each arm can contribute background photons at the fundamental or second harmonic frequencies. Second, the use of a third order nonlinearity breaks the symmetry between positive and negative delays in the autocorrelation function, providing an unambiguous time direction. This enables distinguishing between pre-pulses and post-pulses. As the delay of the fundamental arm is scanned across the second harmonic arm, a pre-pulse will generate two peaks in the autocorrelation function, one at the delay where the pre-pulse in the fundamental arm overlaps with the main pulse in the second harmonic arm and one at the delay where the pre-pulse in the second harmonic arm overlaps with the main pulse in the fundamental arm. This is illustrated schematically in Fig. 2.9. The main pulse to pre-pulse contrast (i.e. the ratio of the main pulse to pre-pulse intensity) in the second harmonic beam will be equal to the main pulse to pre-pulse contrast of the fundamental arm squared due to the intensity dependence of the second harmonic signal. This means the third harmonic signal amplitude which comes from overlapping the main pulse in the fundamental arm with the pre-pulse in the second harmonic arm (τ_{-1} in Fig. 2.9) will be equal to the square of the third harmonic signal amplitude arising from an overlap of the main pulse in the second harmonic arm with a pre-pulse in the fundamental

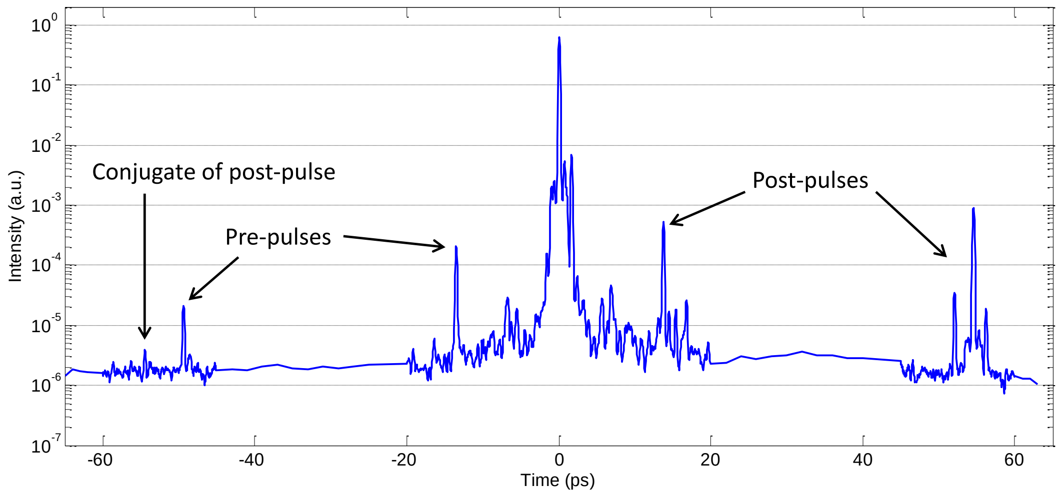

Figure 2.10. Sample third order autocorrelation trace of the amplified pulse. Higher resolution scans are shown around areas with known pulse structure.

arm ($\tau_1$in Fig 2.9). Therefore, to distinguish pre-pulses from post-pulses we look for peaks at exactly opposite delay in the autocorrelation trace. The larger of the two peaks represents the true position and contrast of the pre- or post-pulse.

Figure 2.10 shows an example third order autocorrelation trace of our 25 TW laser system. A number of features can be observed. First, the main pulse sits on a nanosecond scale pedestal at ~10^{-6} contrast (the measurement dynamic range is ~10^{9}). This is a common feature of CPA laser systems and arises from amplified spontaneous emission (ASE) within the power amplifiers. Next, a post pulse at 56 ps and a pre-pulse at 48 ps are observed at the 10^{-3} and 10^{-5} level, respectively, along with symmetric pre-and post-pulses at 13.5 ps with a contrast of 5×10^{-4}. Finally, the pulse sits on a ps-scale pedestal at the 10^{-3} level, which likely arises from a bandwidth mismatch on the many dielectric mirrors used through the system [112].

In experiments presented in Chapter 6 the laser was focused to ~10^{18} W/cm^2 into a high density hydrogen gas target. Since the intensity required for barrier suppression ionization in hydrogen is ~10^{14} W/cm^2 and the pulse exhibits prepulses at

13.5 ps and 2 ps with contrasts above 10^{-4}, care must be taken to understand the effects of preionization in these experiments. However, since typical hydrodynamic time scales in field-ionized plasmas are ~10-100ps, we do not expect significant hydrodynamic motion prior to the main pulse arrival.

2.5 Laser wave front correction using an adaptive optics loop

2.5.1 Diffraction limited focusing, M^2, and Strehl ratio

While high temporal contrast on the scale of 10^{-3} or better can be obtained in the leading edge of the ultrashort pulse, achieving high *spatial* contrast at the focus often tends to be much more difficult. The spot size to which a laser can be focused is intrinsically limited by diffraction. Under the paraxial approximation, the field profile at the focal plane of a lens or curved mirror represents the Fraunhofer diffraction pattern of the input field with a magnification dependent on the focal length of the lens. If we consider a Gaussian beam focusing with a convergence half angle θ, then the Gaussian transverse intensity profile at the focus will have a $1/_{e^2}$ radius $w_0 = \frac{\lambda}{\pi\theta}$. This is the smallest spot size achievable for a given focusing f-number ($f/\# = \frac{f}{D} \approx \frac{1}{2\theta}$)and such a spot is said to be diffraction limited [91].

Spatial intensity and phase aberrations on the focusing beam will cause non-optimal interference of the component waves contributing to the net field at the focal plane, causing focal spot distortion and reduced peak fluence. A common measure of beam focusability is the M^2 factor which is defined by $w_L = M^2 \frac{\lambda}{\pi\theta} = M^2 w_0$. Here

w_L is the measured radius at the beam waist which should be calculated through the second order moment of the intensity as

$$\frac{w_L^2}{2} = \frac{\int r^2 I(r) dA}{\int I(r) dA}.$$

A realistic, aberrated beam can therefore be described as M^2 times diffraction limited. A second measure of beam quality relevant to the focusing of high intensity lasers is the Strehl ratio. For small spatial aberrations the Strehl ratio is defined as the ratio of the peak intensity in the focal plane in the presence of phase front aberration to the peak intensity obtained if no phase aberration were present [86]. This measurement effectively distinguishes between focal spot degradation due to spatial phase errors from error caused by non-Gaussian intensity profiles by only referencing the measured peak intensity to the maximum achievable peak intensity with the measured intensity profile.

2.5.2 Correction of laser phase front aberrations using closed loop adaptive optics

Adaptive optics loops for correcting optical aberrations have been employed in high resolution astronomical telescopes for many years with the goal of removing wave front distortions caused by the Earth's atmosphere as well as those originating from the telescope itself [113]. The goal of the adaptive optics loop is to remove wave front distortions introduced in an imaging (or focusing) system by applying a compensating wave front distortion with an additional optical element. This compensating distortion is normally applied by a "deformable mirror" which can controllably change its shape in response to an electrical or mechanical force. In order to properly compensate the spatial phase aberrations and achieve diffraction limited imaging (focusing) the wave front must be measured using a wave front sensor of sufficient accuracy and resolution.

More recently, adaptive optics loops have been applied for correction and shaping of laser focal profiles [114–117]. There have been a number of techniques demonstrated for controlled shaping of a laser phase front profile, ranging from MEMS devices to liquid crystal spatial light modulators to more conventional piezoelectric deformable mirrors [118–120]. The large beam diameters and peak fluences of multi-terawatt to petawatt systems has necessitated use of piezoelectric and actuator driven deformable mirrors [11,86,114,115] .

Phase front measurement is achieved through either Shack-Hartmann wave front sensors or through shearing interferometry techniques [11,121,122]. Both of these techniques rely on the measurement of local phase gradients relative to a reference flat wave front. For example, the four-wave shearing interferometer (Phasics SID4) used for wave front measurement in our laser system measures the interference between different orders of a beam diffracted from a 2D grating placed in front of a CCD. The diffraction orders are slightly tilted on the CCD so that interference occurs between four slightly different parts of the incident beam. The intensity maxima in the interference pattern will move based on the incident phase gradient which can be recovered using Fourier image processing techniques. Finally, numerical integration of the recovered phase gradient yields the wave front of the beam.

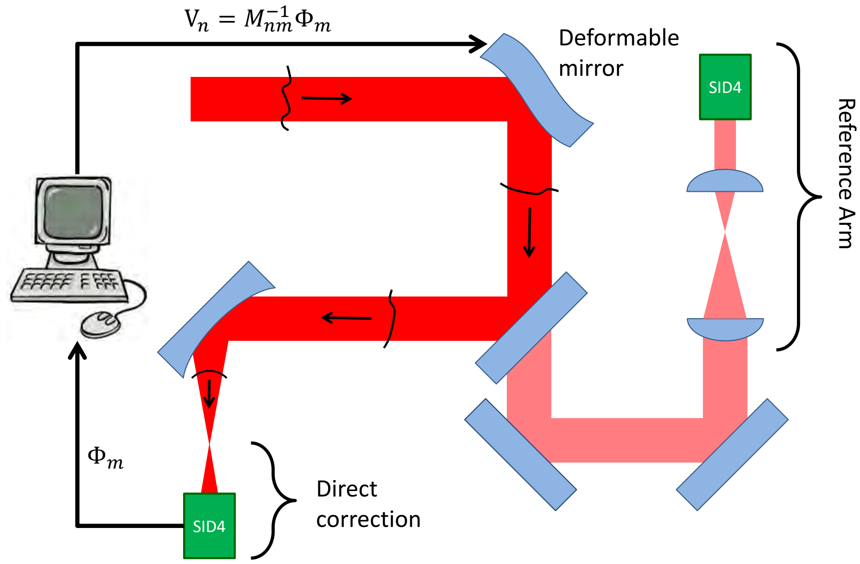

Figure 2.11. Schematic layout of an adaptive optics loop utilizing a reference arm for downstream aberration correction. First, a loop is closed with the SID4 behind the laser focus correcting the beam to a perfect diverging wave front. These mirror voltages are then used to obtain a reference wave front upstream of the final focusing optic. For daily operation, the loop is closed with the SID4 in this reference arm which corrects for aberrations in the full laser chain.

A closed loop adaptive optics system consisting of a bimorph deformable mirror for wave front control and a four-wave shearing interferometer for wave front measurement has been implemented on the 25 TW laser system. A schematic layout of the closed adaptive optics loop is shown in Fig. 2.11. The bimorph deformable mirror (NightN Ltd.) consists of 48 electrodes attached to two piezoelectric ceramic discs which are then glued to a thin, dielectric coated substrate. The wave front sensor is a Phasics SID4 four-wave lateral shearing interferometer operating with 160x120 measurement points. The plane of the deformable mirror is imaged to the wave front sensor so as to maintain a linear relationship between applied mirror voltages and measured wave front distortion. When this is the case, measuring the phase response of a voltage applied to each individual electrode on the deformable mirror provides a basis onto which an arbitrary wave front can be decomposed. This calibration procedure yields a transfer matrix, M_{mn}, such that the wave front distortion Φ_{m} is related to the vector of deformable mirror voltages, V_n, by $\Phi_m = M_{mn}V_n$. Since there are generally many more measurement points than mirror electrodes, M_{mn} is not a square matrix. However, a pseudo-inverse of the transfer matrix, M_{nm}^{-1}, can be found via singular value decomposition such that the required mirror voltages can be found from the desired phase front, Φ_{aim}, via $M_{nm}^{-1}\Phi_{aim} = V_{mirror}$. The loop is closed by measuring a distorted wave front, computing the phase difference between the measured phase and a flat or reference phase, then computing and applying the required mirror voltages to achieve the desired phase profile in the measurement plane. This process is iterated until it converges to the desired wave front profile.

In practice, the laser wave front is measured in two places to correct for the full optical path. First, the wave front sensor is placed in the diverging beam after the laser focus. A loop is closed, converging to a perfect spherical wave front with a beam divergence corresponding to the focusing geometry. The convergence to a perfect spherical wave front should give an ideal wave front near the focus, and a set of reference voltages are saved. Next, for daily operation the SID4 is placed in a secondary measurement arm looking at a small portion of the laser split from the main beam. The deformable mirror voltages corresponding to the perfect spherical wave front near the focus are applied and a reference interferogram is obtained in the measurement arm. For day to day operation the loop is then closed to the reference

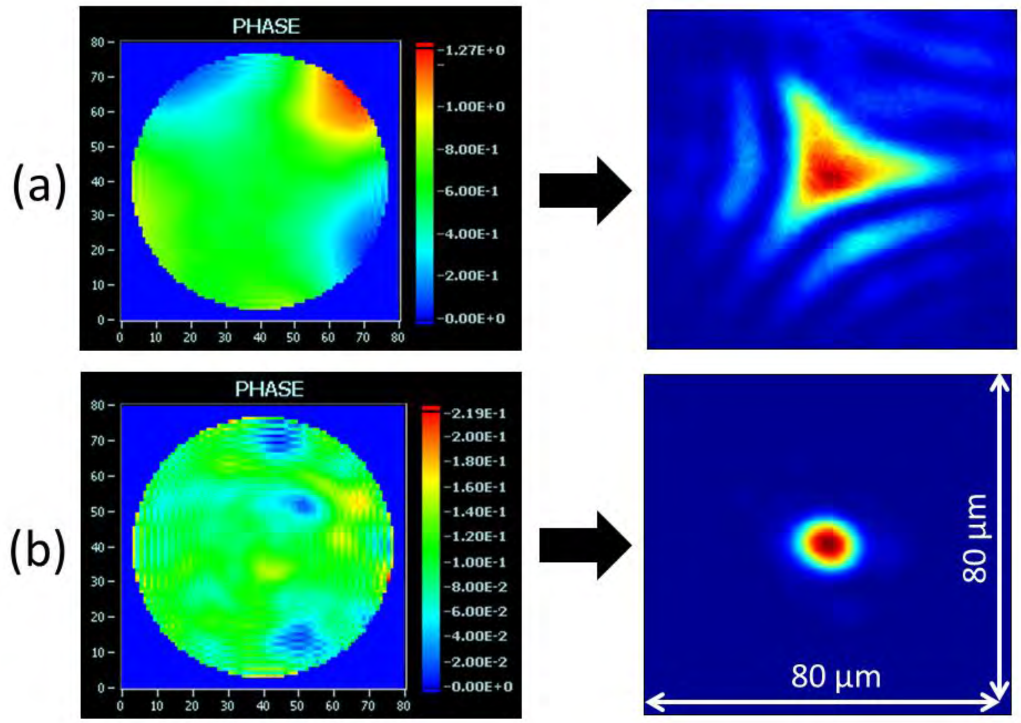

Figure 2.12. Measured laser wave front and focal spot before (a) and after (b) convergence of the adaptive optics loop. The phase measurements are in units of waves with $\boldsymbol{\lambda = 800nm}$. The wave front curvature and tilts have been removed for clarity. The spatial scale is the same in both focal spot images though the color scales are individually normalized.

phase front. The use of the reference interferogram effectively removes sensitivity to aberrations in the reference arm so long as they remain constant and allows for wave front correction downstream of the wave front measurement.

Figure 2.12 shows two pairs of phase fronts and corresponding laser focal spots before and after correction by the adaptive optics loop. The beam is focused using a poor optical quality f/9.5 off axis parabolic mirror, which has a surface accuracy worse than one wave peak to valley. The loop is able to correct the wave front error yielding a dramatic enhancement of the peak intensity at the focal spot. The beam Strehl ratio at the focus is 0.12 without correction and improves to 0.97 after convergence of the adaptive optics loop.

2.6 Measurement of spatiotemporal effects

A final class of measurement required to achieve peak energy density on target in an ultrashort laser experiment is the characterization and mitigation of spatiotemporal effects [123–126]. The main spatiotemporal aberrations present in CPA laser systems are angular chirp and transverse spatial chirp [124,126]. Angular spatial chirp occurs when the angle of the wave vector varies slightly as a function of frequency in the pulse. This leads to a tilt of the plane of peak laser intensity with respect to the beam propagation direction. A beam focused with angular spatial chirp will have a longer pulse duration near the beam waist, potentially causing a substantial reduction in the peak intensity [124,126]. Transverse spatial chirp occurs when the pulse's component frequencies travel in the same direction but are spatially separated across the beam diameter. This causes incomplete overlap of the beam frequencies in the focus, and therefore short pulse duration and high intensity exist in only a narrow region about the beam waist. Transverse spatial chirp has been proposed as a controlled way of avoiding nonlinear pulse propagation for laser surgery and laser machining applications [127–129].

For large beam diameters and short pulse durations (wide spectra), relevant levels of angular and transverse spatial chirp can be difficult to detect. In particular, angular chirp is known to arise in CPA systems from slight misalignments of the compressor diffraction gratings. A simple system proposed for the detection of angular chirp is the inverted field autocorrelator (IFA) [124]. The IFA is a simple Mach-Zehnder or Michelson interferometer in which one arm has an extra reflection which inverts the beam along one transverse dimension. A schematic representation

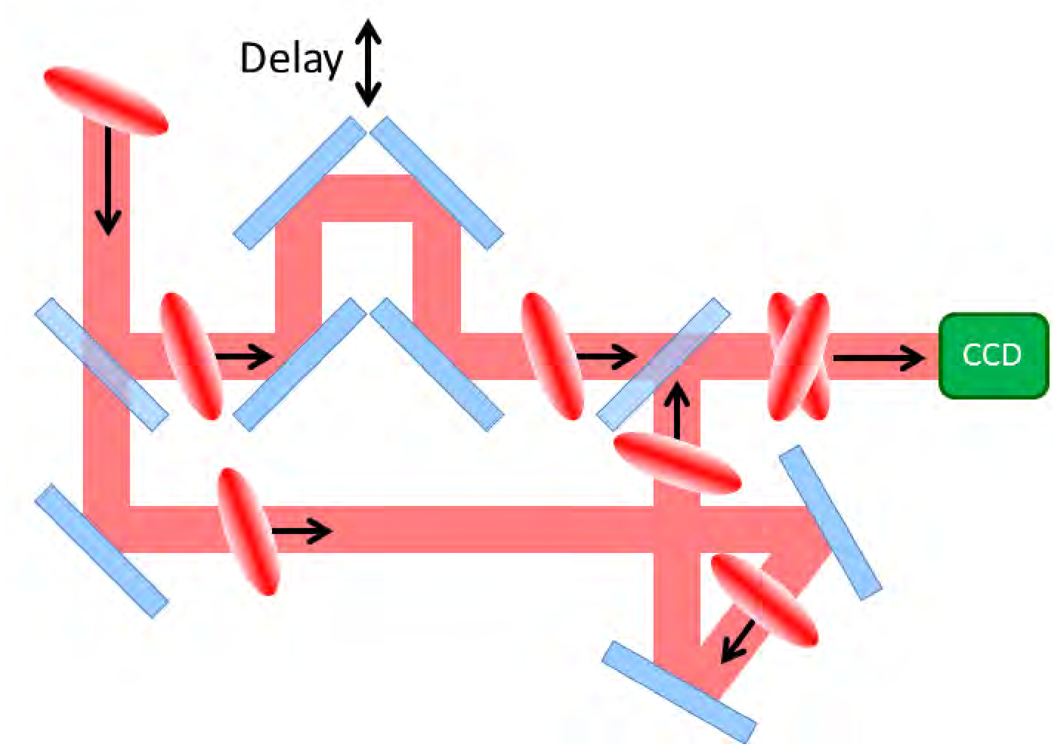

Figure 2.13. Schematic drawing of the inverted field autocorrelator (IFA). A pulse with angular spatial chirp is sent through a modified Mach-Zehnder interferometer and interfered with a slight tilt in the direction perpendicular to the angular spatial chirp. Interference fringes will be visible on the CCD only in the region where the pulses overlap within a coherence length.

of the IFA is shown in Fig. 2.13. The two arms of the IFA are interfered with a slight tilt in the direction perpendicular to the dimension with suspected pulse front tilt. If a beam passed through an IFA has pulse front tilt spanning a distance greater than approximately the coherence length of the pulse, interference fringes will not be observed across the full beam. Figure 2.14(a) shows an IFA trace of the amplified beam with 0.5 μrad/nm angular chirp, and figure 2.14(c) shows the IFA trace after a 4 arcminute correction to the rotation of the second compressor grating. The rotation of the compressor grating improves the parallelism of the gratings within the compressor and eliminates the angular chirp. The angular chirp also causes ellipticity in the focal spot of the focused beam due to the difference in wave vectors across the diameter of

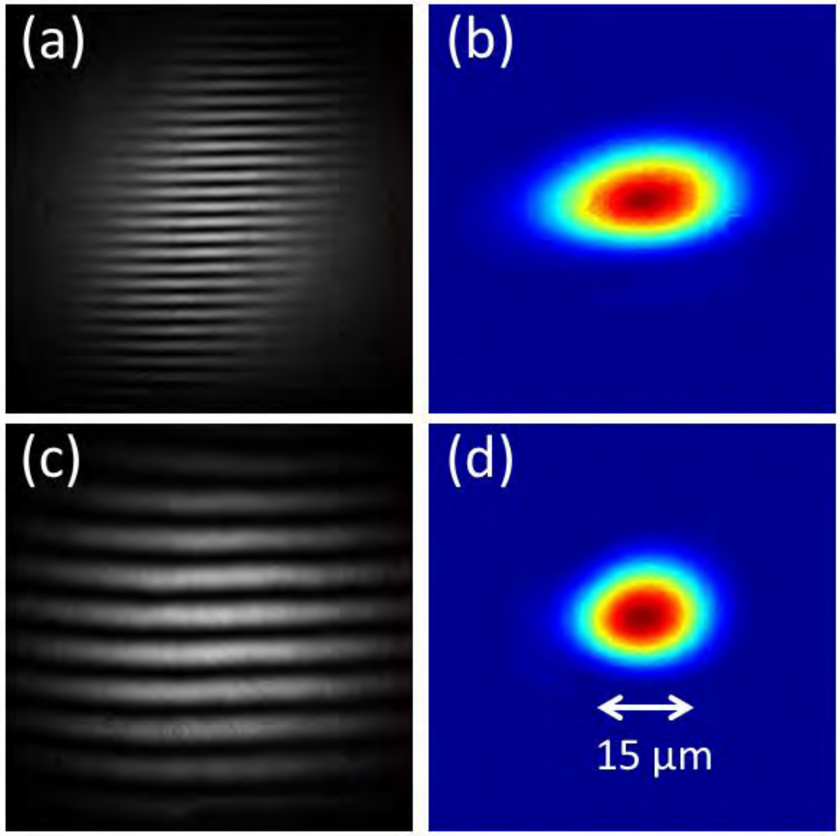

Figure 2.14. Inverted field autocorrelation traces before (a) and after (c) correction of a 0.5 μrad/nm angular chirp on a 39 fs pulse. The focal spot before (b) the correction is elliptical and becomes much more symmetric after improvement of the grating parallelism (d).

the focusing optic. Figure 2.14(b) shows the elliptical focal spot of a beam with angular chirp, and Fig. 2.14(d) shows the focal spot after correction of the grating parallelism.

2.7 Modelocked Nd:YAG Laser System

The output of the 25 TW laser system was synchronized with the output of a home built 140 ps, 800 mJ Nd:YAG laser system operating at 1064 nm with a 10 Hz repetition rate. The 38 MHz pulse train from the Nd:YAG oscillator (Time-Bandwidth Products GE-100) was synchronized to the 76 MHz Micra pulse train using a commercial synchronization system (Coherent Synchrolock). The Synchrolock used a feedback loop monitoring the two oscillator pulse trains and adjusted motorized stages within the Micra cavity to match the frequency of the Micra pulse train to twice the frequency of the GE-100 pulse train. The phase difference between the pulse trains was also controllable, so that amplified pulses from the two lasers could be timed to reliably arrive at a target synchronized to within < 10 ps. The Nd:YAG pulse was used as the channel forming pulse in the high intensity guiding experiments presented in Chapters 3 and 4, requiring synchronization of the Nd:YAG and Ti:Sapphire laser systems on a ~10 ps time scale for stable shot-to-shot guiding.

The modelocked oscillator for the Nd:YAG system outputs ~700 mW in a 38 MHz train of 140 ps pulses. The repetition rate of the oscillator output is reduced to 10 Hz by a Pockels cell and polarizing beam splitter combination and injected into a regenerative amplifier (RGA). The RGA is a self-filtering unstable resonator design and outputs ~10 mJ pulses at 10 Hz [130]. The second amplification stage in the Nd:YAG system is a two pass ring amplifier which boosts the pulse energy to ~100 mJ. A TFP-waveplate combination after the ring amplifier allows control of the total laser energy output. Following the TFP, the beam is sent through a vacuum spatial filter to eliminate strong diffraction rings caused by overfilling the ring amplifier rod. The diffraction rings must be removed by the vacuum spatial filter in order to prevent self-focusing and damage in the final, single-pass amplifier which boosts the pulse energy from 100 to 800 mJ. The details of the Nd:YAG laser design and operating principles can be found in previous work [131].

Chapter 3: Optical guiding at relativistic intensities in cluster-based plasma channels

3.1 Introduction to plasma channel guiding

Diffraction of focused pulses is a serious practical limitation to many applications of high intensity laser-matter interactions which require long interaction lengths at high intensity [5]. Such applications include laser wakefield acceleration of electrons [5,17] and the generation of coherent radiation in the x-ray [19], extreme ultraviolet [132–134], and THz range [135]. As outlined in Chapter 2, diffraction of a focused laser pulse in vacuum limits the region of peak intensity to scale lengths on the order of a Rayleigh length, $z_R = \pi w_0^2/\lambda$, where w_0 is the transverse $1/e^2$ focal spot size and λ is the laser wavelength. Without any sort of optical guiding this implies that longer interaction lengths (larger z_R) require larger spot sizes and therefore higher energy pulses to maintain the same peak intensity. This quickly becomes a practical limitation when relativistic intensities are desired over many centimeters.

The study of electromagnetic waves propagating in hollow conducting ducts, or waveguides, was first studied by Lord Rayleigh over a century ago [136], and the same basic principle of light confinement through structured index profiles has become an integral part of modern transport of electromagnetic radiation. For example, the graded or step index fiber optic cable is able to transport light up to many kilometer distances with sub-millimeter spot sizes. Optical waveguides offer one solution to the practical issue of maintaining ultrahigh peak intensities over long distances. The peak intensity of a multi-millijoule, focused femtosecond laser pulse, though, is well beyond the damage threshold of a standard material fiber. Indeed, material damage in solids sets in at intensities ~10^{12} W/cm^2 while focused femtosecond lasers can reach intensities well above 10^{18} W/cm^2. At these relativistic intensities, only plasma is immune to conventional material damage, so experimental and theoretical work has been undertaken to demonstrate and understand guiding of femtosecond laser pulses in plasmas.

3.1.1 Self guiding and relativistic self-focusing

Plasma nonlinearities such as ponderomotive charge displacement and relativistic corrections to the plasma refractive index can affect laser pulse propagation at high intensity. When a relativistic intensity pulse propagates through an initially uniform plasma, the plasma frequency is modified due to the mass increase that occurs near the peak velocity of the driven electrons as well as the density perturbation caused by the laser ponderomotive force (i.e. the plasma wave) so that

$$\omega_p^2(r) = \frac{4\pi N(r)e^2}{\gamma(r)m_e} = \frac{\omega_{p,0}^2}{\gamma(r)}\frac{N(r)}{N_0}$$

where N_0 is the ambient plasma electron density, e is the elementary charge, $\gamma(r) = \sqrt{1+\frac{a(r)^2}{2}}$ is the Lorentz factor assuming a linearly polarized laser, $a(r)$ is the pulse normalized vector potential which is a function of the radial coordinate r, m_e is the electron rest mass, and $\omega_{p,0}$ is the nonrelativistic plasma frequency [51,137]. The plasma refractive index in the limits $a_0 \ll 1$ and $\delta N(r) = N(r) - N_0 \ll N_0$ is then

$$\eta(r) = \sqrt{1 - \frac{\omega_{p,0}^2}{\gamma(r)\omega^2}\frac{N(r)}{N_0}} \approx 1 - \frac{\omega_p^2}{2\omega^2}\left(1 - \frac{a(r)^2}{4} + \frac{\delta N(r)}{N_0}\right)$$

where ω is the laser frequency and it is assumed that the plasma is sufficiently underdense ($\omega_p/\omega \ll 1$). The relativistic mass shift leads to a graded index profile with a maximum at the most intense part of the usually centrally peaked intensity profile. Like Kerr self-focusing in a neutral gas, a critical power for relativistic self-focusing can be derived as

$$P_{cr} = \frac{2ce^2}{r_e^2}\frac{\omega_p^2}{\omega^2} \approx 17\frac{\omega_p^2}{\omega^2} = 17\frac{N_{cr}}{N_e}GW$$

provided the pulse duration is much longer than the plasma period [46,52]. At powers above P_{cr}, relativistic self-focusing in the plasma proceeds until ponderomotive charge displacement reduces the electron density inside the regions of high intensity [53]. The self-focused pulse can then be trapped and guided in the driven high amplitude plasma wave, a process sometimes called ponderomotive channeling or ponderomotive charge displacement self-guiding.

Experimentally, relativistic self-focusing and ponderomotive channeling have been demonstrated by many groups in gas jets and static gas cells for distances up to a few tens of Rayleigh lengths [28,30,138,139]. Provided the laser power satisfies $P > P_{cr}$, ponderomotive channeling is arguably the simplest method for maintaining a relativistic interaction over many Rayleigh lengths as the confining index profile is automatic assuming an initial intensity profile peaked on axis. However, self-focusing at low densities, required for ~ GeV wakefield accelerators, requires increasingly high powers because $P_{cr} \propto N_e^{-1}$.

Further, Sprangle et al. showed that for pulses shorter than a plasma period relativistic self-focusing is much less effective because the ponderomotive charge displacement and relativistic contributions to the refractive index tend to cancel [46,53]. Considering the 1D longitudinal force balance equation between the laser ponderomotive force, $F_p = -\frac{1}{4}mc^2\nabla a_0^2$ (Eqn. (1.4) in the limit $a \ll 1$) and the space charge force due to the plasma wave yields

$$\nabla \cdot F_p = -\frac{1}{4}mc^2\nabla^2 a_0^2 = \nabla \cdot (-eE) = 4\pi e^2(N - N_0).$$

Rearranging this and using the (non-relativistic) formula for ω_p gives

$$\frac{1}{4}\nabla^2 a_0^2 \approx \frac{1}{4}\frac{\partial^2}{\partial z^2}a_0^2 = k_p^2\frac{\delta N}{N_0}$$

where $k_p = \omega_p/c$. If $\frac{\partial^2}{\partial z^2}a_0^2 \sim k_p^2 a_0^2$, which is true for pulses with longitudinal extent on the order of the plasma wavelength, then $a^2/4 \sim \delta N/N_0$ and the self focusing and ponderomotive displacement terms in the refractive index tend to cancel. Therefore, relativistic self-focusing is less effective for wakefield accelerators operating in the driven or resonant regime.

3.1.2 Optical guiding in pre-formed plasma waveguides

Guiding high intensity pulses can also be achieved through the use of pre-formed plasma waveguides [60]. As an example, consider a plasma with a parabolic density profile given by $N(r) = N_0 + \Delta N\ r^2/w_{ch}^2$ where $\Delta N = N(w_{ch}) - N(0) \geq \frac{1}{\pi r_e w_{ch}^2}$ is the depth of the plasma waveguide, r_e is the classical electron radius, and w_{ch} is the radius of the lowest order guided mode. In this case, the refractive index

$$\eta(r)^2 = 1 - \frac{N(r)}{N_{cr}} = 1 - \frac{N_0}{N_{cr}}\left(1 + \frac{\Delta N}{N_0}\frac{r^2}{w_{ch}^2}\right) \tag{3.1}$$

is peaked on axis. In the frequency domain the wave equation for an electromagnetic wave, $\tilde{E}(\omega)$, propagating through the plasma is

$$\left(\nabla^2 + \frac{\omega^2}{c^2}\eta(r)^2\right)\tilde{E} = \nabla\left(-\frac{1}{\eta(r)^2}\tilde{E}\cdot\nabla\eta(r)^2\right). \tag{3.2}$$

The right hand side of equation (3.2) can be neglected if $\Delta E/E \ll \Delta(\eta^2)/\eta^2$over the transverse size of the plasma channel [61]. In this limit the solutions to the wave equation are transversely polarized, or TEM, modes. For typical guided modes the field is well contained by the plasma waveguide so, $|\Delta E/E|{\sim}1$, while the typical maximum change in the refractive index over the same distance is $|\Delta\eta/\eta|{\sim}10^{-2}$ [61]. For higher order modes or spot sizes approaching the laser wavelength (i.e. non-paraxial beams), the polarization term cannot be neglected. Neglecting the polarization term and taking the ansatz solution to equation (3.2) of a wave propagating in the $+z$ direction, $E(x,y,z,t) = u(x,y)e^{i(\beta z-\omega t)}$, the wave equation reduces to

$$\left(\nabla_\perp^2 + \frac{\omega^2\eta(r)^2}{c^2} - \beta^2\right)u(x,y) = 0.$$

Substituting in equation (3.1) gives

$$\left(\nabla_\perp^2 + k_0^2\left(1 - \frac{N_0}{N_{cr}} - \frac{\Delta N}{N_{cr}}\frac{r^2}{w_{ch}^2}\right) - \beta^2\right)u(x,y) = 0\,.$$

Introducing the propagation wavenumber in the channel

$$\kappa^2 = k_0^2\left(1 - \frac{\beta^2}{k_0^2} - \frac{N(r)}{N_{cr}}\right) \tag{3.3}$$

the wave equation reduces to

$$(\nabla_\perp^2 + \kappa^2)u(x,y) = 0. \tag{3.4}$$

This admits strictly bound modes if κ^2 is strictly negative beyond some radius and leaky modes if $\kappa^2 < 0$ out to some radius after which $\kappa^2 > 0$ [61]. For the parabolic index case, there can only be bound modes since $n(r)^2 \to -\infty$ as $r \to \infty$. This is, of course, unphysical but can be used to good approximation if the plasma waveguide is much larger than the bound mode size. For the specific case of the parabolic index profile, an analytical solution to equations (3.3) and (3.4) can be found, and the transverse modes are Laguerre-Gaussian polynomials

$$u(r,\phi) = a_{pm} e^{-\frac{r^2}{w_{ch}^2}} \left(\frac{2r^2}{w_{ch}^2}\right) L_p^m \left(\frac{2r^2}{w_{ch}^2}\right) e^{im\phi}$$

with propagation wavenumber

$$\beta_{pm}^2 = k^2 - 4\pi r_e N_{e0} - \left(\frac{4}{w_{ch}^2}\right)(2p + m + 1).$$

At high intensities, the effects of relativistic self-focusing and plasma wave generation must also be taken into account so that the index profile is given by

$$\eta(r) = 1 - \frac{\omega_{p0}^2}{2\omega^2}\left(1 + \frac{\Delta N}{N_0}\frac{r^2}{w_{ch}^2} - \frac{a(r)^2}{4} + \frac{\delta N(r)}{N_0}\right).$$

Properly matched guiding, where the laser spot size remains constant over the full interaction length, taking into account all of these effects is complicated, but can be achieved to some extent by tailoring the pre-formed plasma profile to compensate nonlinear index modifications at high intensities [29,140].

Optical guiding in pre-formed plasma channels was first demonstrated through the hydrodynamic expansion of a plasma formed by focusing an intense pulse with an axicon lens into a high Z backfill gas [60]. The axicon focused ~100 ps pulse avalanche ionizes the backfill gas then heats the resulting plasma. The plasma expands at the ion sound speed and a shock wall forms, creating a nearly parabolic density profile out to the shock radius. Plasma waveguides formed in backfill gas suffer from poor coupling caused by ionization of the backfill by the high intensity pulse as it is injected into the waveguide [141,142]. Gas and cluster jet sources have been developed to avoid this drawback and will be described in the next section. The "ignitor-heater" method for generating plasma waveguides through hydrodynamic expansion in lower Z gases was demonstrated by separating the ionization and heating steps [143]. A femtosecond pulse ionizes the low Z gas and the resulting plasma is heated by a secondary ~100 ps pulse. The subsequent expansion again creates a nearly parabolic density profile near the plasma axis. The ignitor-heater technique was used to demonstrate optical guiding at relativistic intensities in a hydrogen plasma waveguide for the first time [144].

A second commonly used method for generating pre-formed plasma channels is through electrical discharge in a gas filled capillary [145,146]. Ablation of the capillary walls can create a plasma density profile with a minimum on axis [145], or cooling of the plasma discharge at the capillary walls can create a temperature gradient resulting in a nearly parabolic density profile [146]. Capillary discharge waveguides have the advantage of avoiding additional channel-forming lasers which must be timed to the ~10 ps level. Guiding in a capillary-based channel has been demonstrated over 9 cm, producing a current record 4.2 GeV wakefield accelerated electron beam [31]. In contrast, waveguides generated by the hydrodynamic expansion technique are normally limited to lengths of about an inch by the energy requirements of the channel-forming pulse. However, damage from ablation of the capillary walls leads to a relatively short capillary lifetime, and incompletely ionized impurities from the capillary walls can lead to ionization defocusing of an intense pulse within the channel. Measurement of the plasma transverse and longitudinal density profiles, easily performed using transverse probing techniques in gas jet based waveguides [147], is difficult for discharge-based waveguides because of the enclosed geometry of the capillary [148].

3.2 Plasma waveguides generated in clustered gas targets

3.2.1 Advantages of using cluster based targets

Three main drawbacks of the hydrodynamic expansion method can be mitigated by the use of clustered gas targets rather than a simple monomer gas jet or backfill [149,150]. First, the use of clusters can improve the laser absorption by as much as a factor of 10, leading to deeper channel formation with lower drive pulse energy [151]. Second, the use of clusters allows channel formation at much lower on axis density. Finally, gas jet and backfill waveguides generally suffer from tapering at the channel entrance and exit caused by non-uniform density gas or laser intensity profiles. In a highly clustered gas target the individual cluster motion is ballistic [152]. Therefore skimmers can be used to create sharp ~100 μm entrance and exit ramps to the channel.

Clusters are aggregates of van der Waals bonded atoms or molecules of typical diameter ~1-100 nm which form by condensation during the expansion and subsequent cooling of a high pressure gas ejected into vacuum [153]. In the experiments described in this chapter, multi-photon ionization on the leading edge of a 140 ps channel forming pulse, described in Chapter 2, creates an initial free electron population within the clusters. These free electrons, under influence of the strong laser field, collisionally ionize other atoms within the cluster leading to avalanche ionization of each individual cluster on a time scale < 1 ps [151,154]. The high density nano-plasmas expand and merge on a ~1-10 ps time scale much shorter than the 140 ps channel forming pulse. Thus, the clusters act to create plasma with a much higher initial free electron population compared to an unclustered gas at the same average density. This plasma is then heated by the bulk of the channel forming pulse and hydrodynamically expands to form a waveguide [149,150].

At low electron densities in an unclustered gas, efficient collisional breakdown requires high gas density, N_0, due to the initially exponential growth of the electron density $N_e(t) = N_{e0}\exp(SN_0t)$ where N_{e0} is the initial free electron density, N_0 is the gas density, and SN_0 is the collisional ionization rate. Waveguide formation in unclustered gases has been limited to minimum densities $\sim 10^{19}\ cm^{-3}$ by the exponential dependence of N_e on N_0. Further, the ionization generally occurs near the peak of the channel forming pulse so that only a fraction of the pulse energy is actually used to heat the plasma. This leads to absorption efficiencies of ~100 ps heating pulses of only up to ~10% in unclustered gas jets. In contrast, the ionization of the cluster jet occurs within each near solid density cluster early in the channel forming pulse, and the full pulse duration is used to heat the plasma, leading to absorption efficiencies up to 35%. A detailed description of long pulse absorption and waveguide formation in clustered gas targets can be found in [149,150].

3.2.2 Demonstration of efficient coupling into a cluster based plasma channel

Figure 3.1 shows an experimental setup for creating a plasma waveguide in an elongated cluster target. A ~140 ps Nd:YAG pulse is focused with an axicon lens over a 1 cm cluster jet. The channel forming pulse is synchronized with the 25 TW Ti:Sapphire femtosecond laser system to within < 10 ps. The Ti:Sapphire laser pulse is focused through a hole in the axicon onto the end of the ~100 μm diameter plasma. Guided mode profiles and energy throughputs are measured by imaging the guided Ti:Sapphire pulse onto a CCD camera. Electron density profiles are measured using

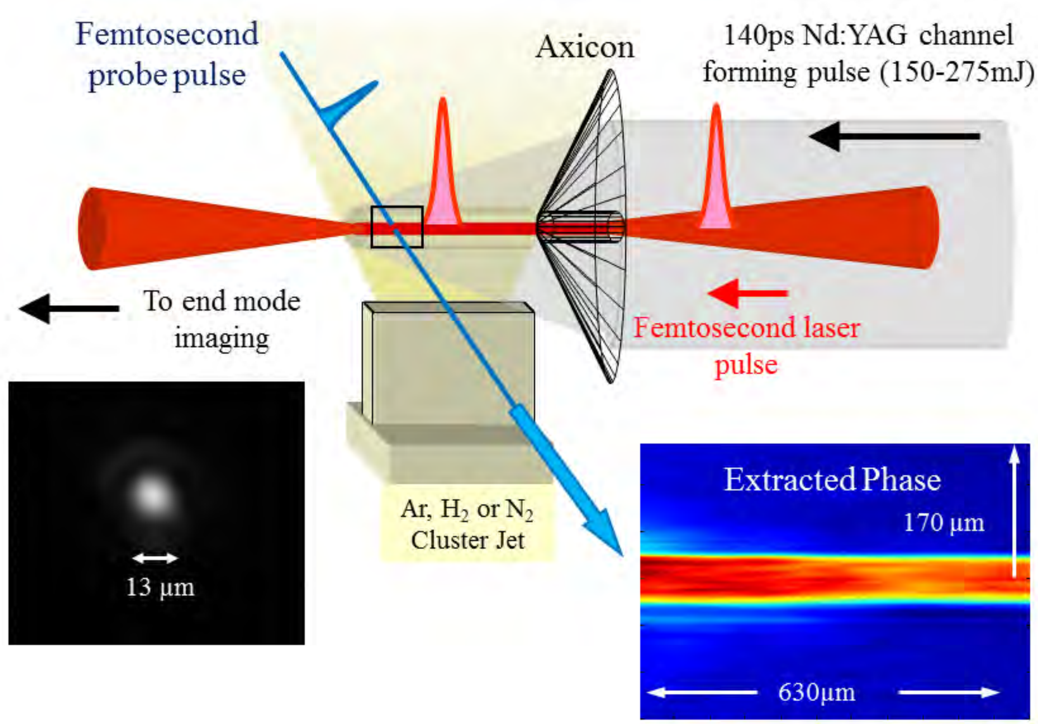

Figure 3.1. Experimental setup for making plasma waveguides in cluster jets. A 140 ps channel forming pulse is focused with an axicon lens over the elongated cluster jet. A synchronized femtosecond pulse is focused onto the end of the plasma waveguide through a hole in the axicon. Plasma density is measured using femtosecond transverse interferometry, and guided modes are monitored by relay imaging the exit mode to a CCD camera.

femtosecond transverse interferometry [147]. A portion of the Ti:Sapphire pulse is split from the main beam, frequency doubled, and directed transversely across the plasma. The plasma is imaged through a folded wave front interferometer onto a CCD camera. Phase extraction of the interferograms followed by Abel inversion allows extraction of the radial refractive index and plasma density within the field of view of the CCD assuming cylindrical symmetry [75,147].

Figure 3.2 shows the extracted radial density evolution of a plasma arising from the interaction of a 250 mJ Nd:YAG pulse with a nitrogen cluster jet. The initial density profile 100 ps after arrival of the channel forming pulse is peaked on

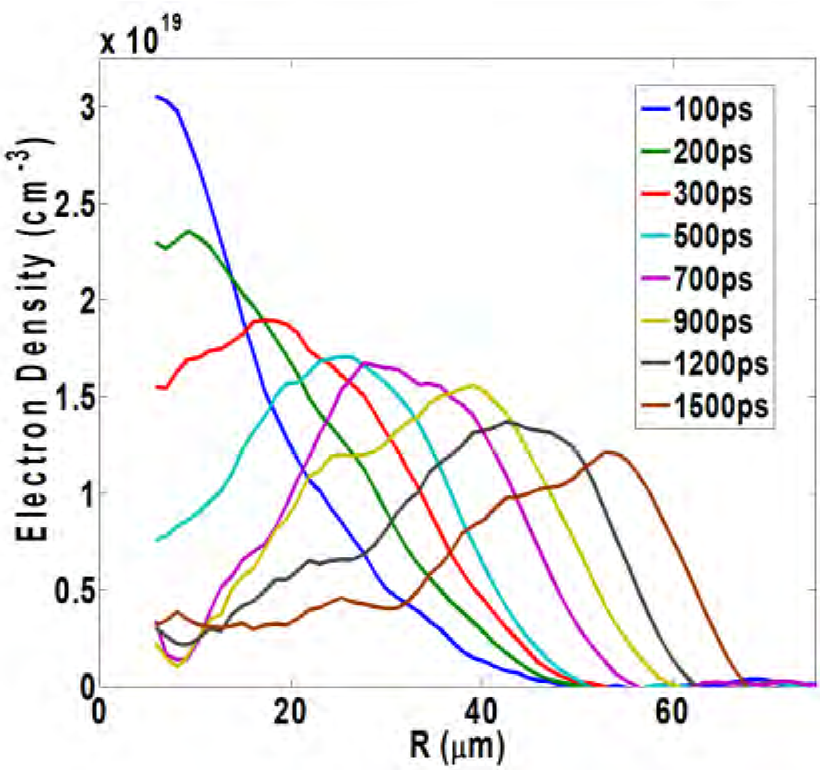

Figure 3.2. Temporal evolution of a plasma waveguide formed from an Nd:YAG laser pulse (250 mJ, 140 ps) interacting with a nitrogen cluster jet. The cluster jet is cooled to a gas reservoir temperature of -170º C and held at 400 psi. The plasma density is initially peaked on axis, but hydrodynamic expansion of the hot plasma creates a density minimum on axis and a radially propagating shock wall.

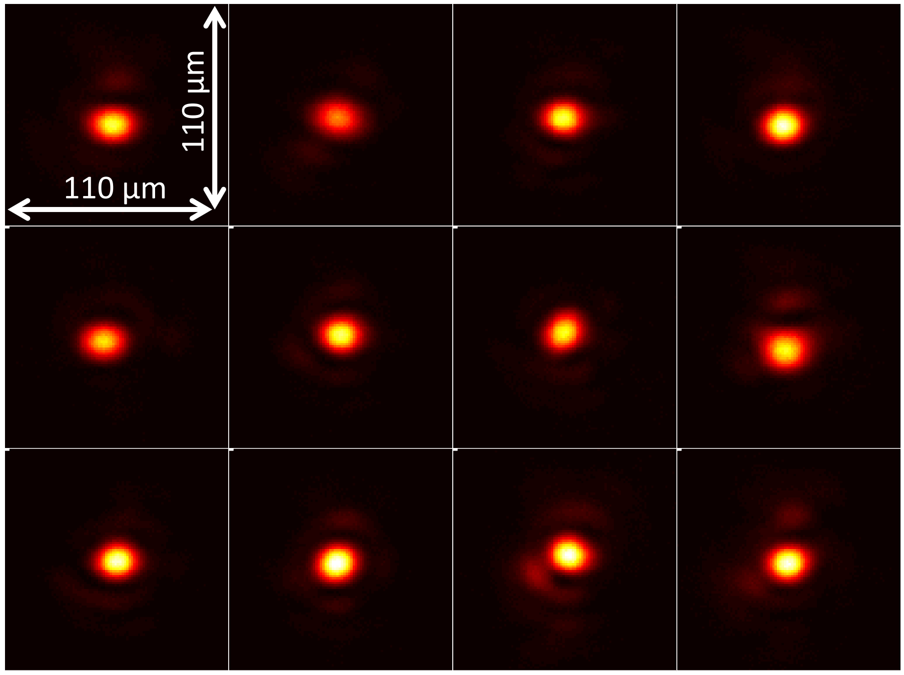

Figure 3.3. Consecutive exit modes from a 1 cm long nitrogen plasma waveguide injected with a 50 mJ, 40 fs laser pulse focused to a 13 µm FWHM spot size and delayed by 450 ps with respect to the 250 mJ Nd:YAG channel forming pulse. Average measured energy throughput was 50% with a standard deviation of 11%. Maximum throughput reached 79%..

axis. A deep density depression develops 500 ps later with a refractive index profile capable of guiding an injected laser pulse with 13 µm FWHM spot size. A sequence of twelve consecutive exit modes from the 1 cm long plasma waveguide is shown in Fig. 3.3, showing good mode stability. The injected 50 mJ, 40 fs laser pulse has a FWHM spot size of 13 µm and is guided with a maximum efficiency of 79% and average efficiency of 50%.

Efficient guiding of the injected femtosecond laser pulse first requires efficient coupling into the plasma waveguide. The coupling efficiency of laser pulses injected into waveguides generated in unclustered gas jet and backfill targets was limited by ~1 mm scale tapering of the electron density at the waveguide entrance. Ballistic flow of clusters in jets with a high cluster to monomer ratio has been shown

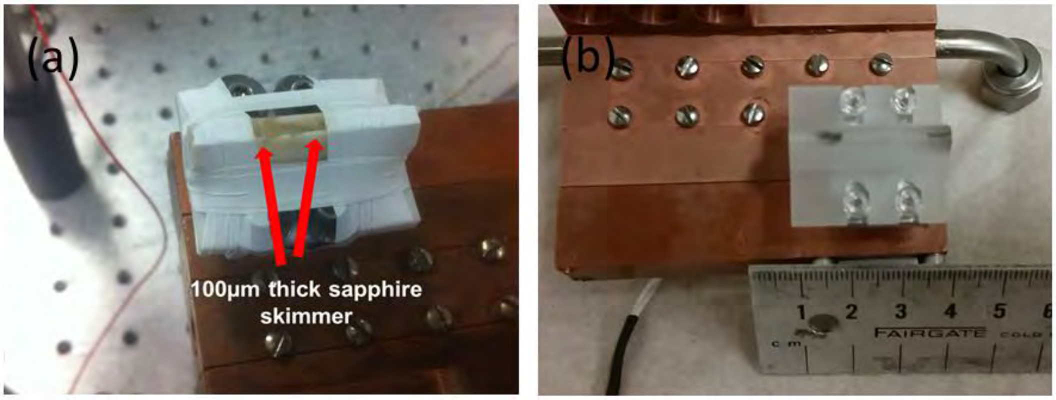

Figure 3.4. (a) Cluster jet nozzle with externally attached 100 µm thick sapphire skimmers. (b) 3D printed nozzle with integrated 400 µm thick skimmers. Both are shown in the same custom cryogenic cooling jacket.

to allow sculpting of gas density profiles on < 100 µm distance scales. Initially used for the purpose of creating modulated plasma waveguides [152,155], the same concept can be used to create sharp density transitions at the entrance and exit of the plasma waveguide. Images of two elongated cluster jet nozzles with thin skimmers at the entrance and exit are shown in Fig. 3.4. In Fig. 3.4(a) the 100 µm thick sapphire skimmers are externally attached to the elongated nozzle. Figure 3.4(b) shows a 3D printed polycarbonate nozzle with integrated ~400 µm thick skimmers.

Figure 3.5 demonstrates the sharp density transition from vacuum to the plasma channel created by the sapphire skimmers. The phase shift imparted on a probe beam by the entrance of a plasma waveguide formed in a nitrogen cluster jet is shown in Fig. 3.5(a). The waveguide entrance exhibits a density ramp of approximately 250 µm, significantly shorter than the >1 mm density gradients associated with unclustered jets. Figure 3.5(b) and 3.5(c) show the same channel ~1 ps after passage of a 0.5TW and 2 TW pulse, respectively, along with associated mode profiles at the exit of the 1 cm long waveguide. Though the channel entrance is sharp, there is still a small amount of unclustered, initially unionized gas at the

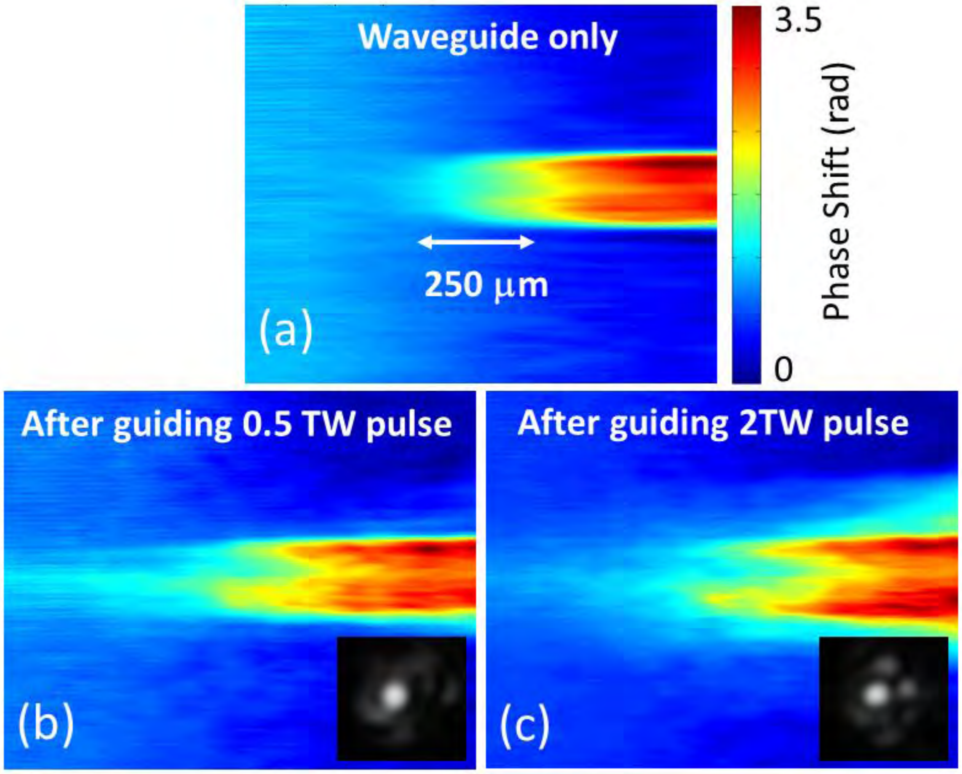

Figure 3.5. Extracted phase shift profiles of a nitrogen plasma waveguide before and ~1 ps after guiding a femtosecond pulse. The waveguide alone (a) has a 250 μm density ramp. Injection of a 0.5 TW pulse (b) and a 2 TW pulse (c) show the presence of a small amount of residual monomer gas at the entrance to the plasma waveguide. The associated exit mode profiles still show a bright Gaussian spot on axis. The color scale is the same on all three phase images.

channel entrance. For this particular channel Abel inversion of the phase profile in Fig 3.5(c) yields a plasma density in front of the waveguide of $2 \times 10^{18}\ cm^{-3}$. This density is clamped above approximately 1 TW (~10^{17} W/cm^2) in the injected pulse, consistent with ionization of the nitrogen monomers up to N^{5+}.

3.2.3 Measurement of nearly pure N^{5+} plasma waveguides

Collisional ionization within clusters has been shown to lead to higher ionization states than can be achieved through field ionization alone. Further, the ionization level tends to halt at closed shell ion configurations where there is a

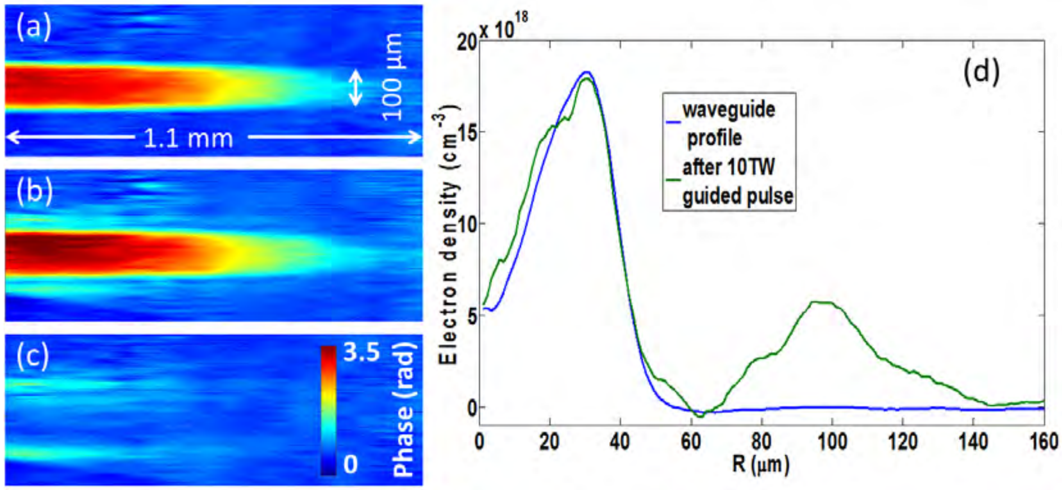

Figure 3.6. Phase shift profiles of the exit of a nitrogen plasma waveguide before (a) and ~1 ps after (b) guiding a 0.4 TW laser pulse. The difference between the two profiles (c) reveals additional ionization only outside the waveguide. Abel inverted density profiles before and after guiding a 10 TW pulse (d) also show additional ionization only outside the waveguide.

significant jump in ionization potential, for example He-like nitrogen or Ne-like argon [156,157]. This can be important for channel guiding experiments where ionization induced defocusing is meant to be avoided or in laser plasma accelerator experiments where the ionization injection scheme is employed [75].

The He-like ionization state of the nitrogen plasma waveguide was verified by guiding a 15 mJ, 40 fs (0.4 TW) Ti:sapphire laser pulse. The guide exit mode peak intensity was $10^{17}\ W/cm^2$, containing up to 80% of the injected pulse energy. Considering that the barrier suppression ionization threshold of Li-like N^{4+} (ionization potential 98 eV) ions is $\sim 10^{16} W/cm^2$, any Li-like nitrogen ions in the channel would be ionized by the guided pulse, resulting in an increase in electron density easily detectable by interferometry. Figure 3.6 shows probe phase profiles near the exit of the plasma waveguide, taken before (a) and ~1 ps after (b) guiding of the 0.4 TW pulse. Figure 3.6(c) is the difference between (a) and (b) and would reveal any extra ionization by the guided pulse. Further, Fig. 3.6(d) shows an Abel inverted density profile before and after guiding of a 10 TW pulse. It is seen that the only additional ionization occurs outside the waveguide, where uncoupled laser energy interacts with neutral clusters, verifying that the plasma channel interior is dominated by the N^{5+} species. As an added check on the ionization state, the measured nitrogen molecule densities were approximately 10 times less than the average plasma densities, indicating 5 times ionization of each nitrogen atom.

3.3 Guiding at relativistic intensities in pure N^{5+} plasma waveguides

As outlined in section 3.1, the guiding properties of a plasma channel can be significantly modified at relativistic intensities where nonlinear effects such as relativistic self-focusing and wake formation can modify the channel refractive index profile. Up to 12 TW pulses were injected into the ~1 cm pure N^{5+} plasma waveguides shown in Fig. 3.5 and Fig. 3.6, with an on axis plasma density of $5 \times 10^{18} cm^{-3}$ and (non-relativistic) matched spot size of 13 μm. The critical power for relativistic self-focusing at $\lambda = 800\, nm$ and $N_e = 5 \times 10^{18}\, cm^{-3}$ is approximately 6 TW, so we should expect to see an onset of self-focusing at these power levels. Figure 3.7 shows the energy throughput and normalized peak intensity at the exit plane of the channel shown in Fig. 3.6(d) ($N_0 = 5 \times 10^{18}\, cm^{-3}, w_{ch} = 13 \mu m$) as a function of injected laser power. Example guided mode profiles for three different laser powers are also shown. Each point on Fig. 3.7 is an average over 100 shots. At low powers we see excellent guided throughput with nearly 70% energy throughput in a single Gaussian mode. However, as the intensity is increased to

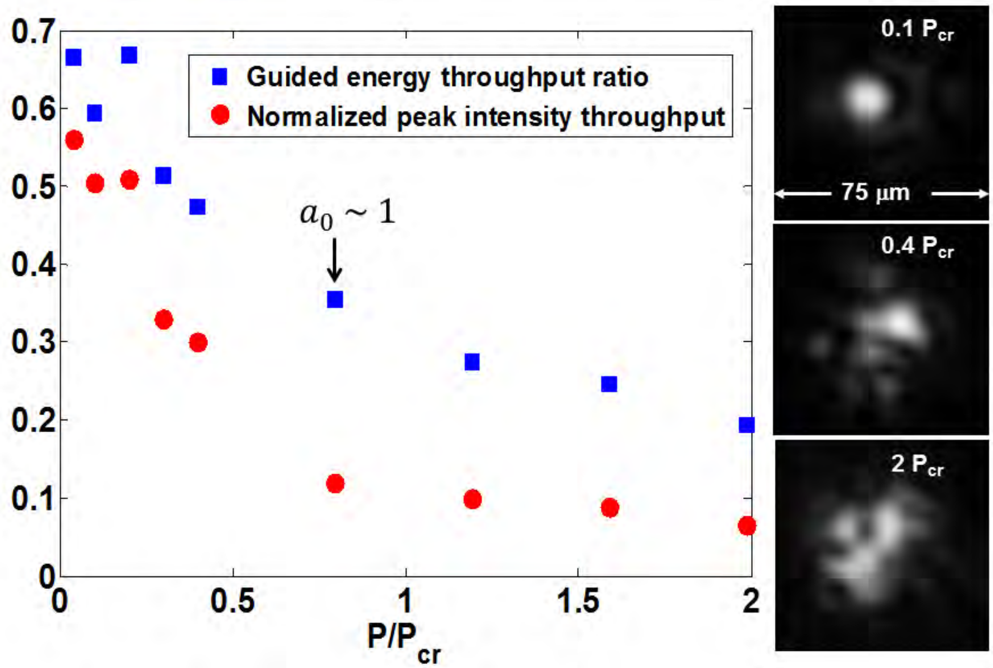

Figure 3.7. Energy throughput and normalized intensity at the exit of a 1 cm nitrogen plasma waveguide with on axis density $5 \times 10^{18}\ cm^{-3}$ as a function of incident laser power. The injected pulse is 40 fs FWHM with a spot size of 13 µm. Exit modes are shown for incident powers 0.1, 0.4, and 2 times the critical power for relativistic self-focusing.

approach $a_0 = 1$ and $P = P_{cr}$ the relative energy throughput decreases drastically, and the transverse profile at the channel exit is highly multi-mode.

Modification of the plasma refractive index by the relativistic laser pulse causes temporal as well as spatial modification of the pulse. Pulse self-compression and self-phase modulation in plasmas have been extensively studied both theoretically and experimentally. The symmetric red and blue shifting of a pulse in the driven wakefield regime has been suggested as a diagnostic for measuring the plasma wave amplitude in laser wakefield accelerators [158]. Measurements of the laser pulse spectrum at the exit of the nitrogen plasma waveguide were made to verify coupling of the pulse to plasma waves. Figure 3.8 shows the injected pulse spectrum and the spectrum at the exit of the plasma waveguide for 2.5 TW and 10 TW injected

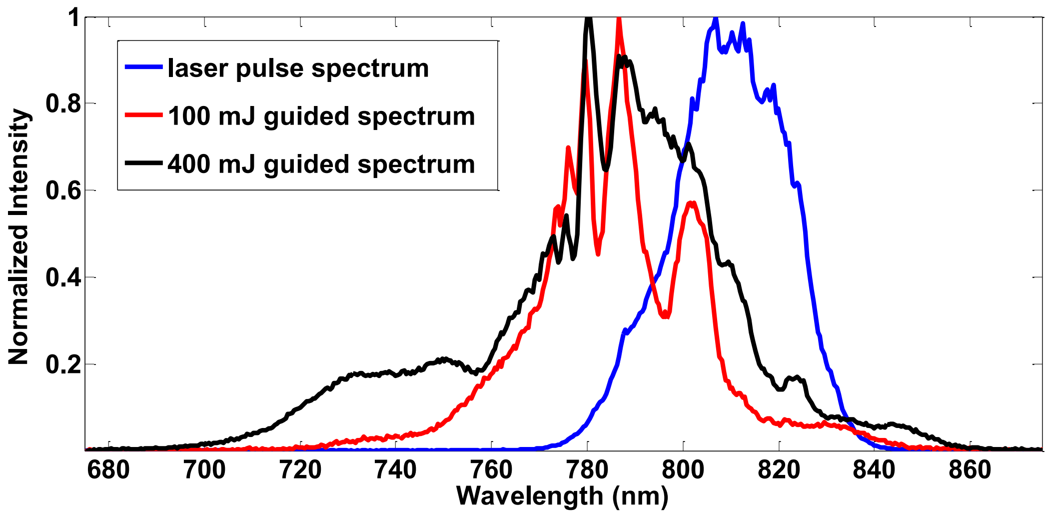

Figure 3.8. Laser spectrum before and after it is guided through a 1 cm nitrogen plasma waveguide. Spectral broadening is observed with a redshifted tail indicative of coupling to plasma density perturbations.

powers. The redshifted tail of the pulse at high intensity is indicative of coupling to plasma waves. Blue shifting of the pulse spectrum is likely caused by the ionization of the nitrogen monomers at the entrance to the waveguide.

3.4 Ionization injected wakefield acceleration in an N^{5+} waveguide

Along with extending the high intensity interaction length, the pure N^{5+} plasma waveguide provides an abundant source of electrons for injection into a wakefield accelerator. Recently, ionization injection of high Z dopants was proposed and demonstrated to increase electron beam charge and lower the intensity threshold for electron trapping [70–74,159,160]. In this scheme, inner shell electrons of a high Z dopant are ionized near the peak of the drive laser pulse and are trapped in the potential well of the plasma wave. In previous experiments, the high-Z dopant typically does not exceed ~10% of the total density due to laser pulse refraction by

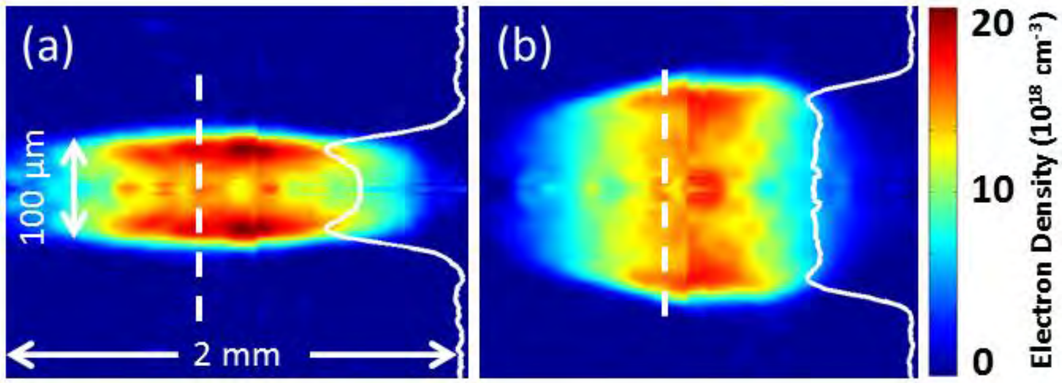

Figure 3.9. Abel inverted electron density profiles produces by focusing the Nd:YAG channel forming pulse with an axicon lens (a) and an f/20 spherical lens (b). Lineouts along the dashed white line show a nearly parabolic density profile in the axicon case and a flat density profile in the lens focusing case.

the additional plasma density created on axis [160]. We have demonstrated ionization injection-assisted wakefield acceleration in a pure He-like nitrogen (N^{5+}) plasma waveguide [75]. We have shown that use of a preformed plasma channel with a guiding structure stabilizes and narrows the accelerated electron beam compared to the use of a uniform transverse density profile [75].

The effect of the channel on electron beam generation was studied by focusing a Nd:YAG channel-forming pulse into a short, ~1.5 mm, nitrogen cluster jet. When the 200 mJ, 140 ps channel-forming pulse was focused with an axicon lens the resulting plasma expanded to form a plasma waveguide as shown in Fig. 3.9(a). When an f/20 lens was used to focus the Nd:YAG laser, a much broader plasma with a flat density profile was created as shown in Fig. 3.9(b). The target length of 1.5mm is approximately equal to the wakefield accelerator dephasing length associated with the measured on axis plasma density of 1.4×10^{19} cm^{-3} [80].

The wakefield drive pulse was an 800 nm, 40 fs Ti:sapphire laser pulse (see Chapter 2) focused by a f/9.5 off-axis parabolic mirror (OAP) and steered by an 800 nm mirror to a 15 μm FWHM spot with a peak normalized vector potential $a_0 = 1.2$. The drive pulse was synchronized with the plasma channel-forming pulse with less than 10 ps jitter and injected collinear to the plasma axis at an adjustable delay with respect to channel formation. For experiments with the plasma waveguide, the drive pulse was focused through a hole in the axicon, as shown in Fig. 3.1. For experiments with the flat plasma profile, the 1064 nm pulse was focused by a lens through an 800 nm turning mirror and onto the cluster target.

An image of this waveguide's low intensity exit mode, with spot size FWHM of 14 μm, is shown in Fig. 3.10(b), in agreement with the calculated mode for this index profile. The low intensity exit mode shows guiding over approximately 2.5 Rayleigh lengths. By tuning the gas jet backing pressure, the peak on-axis density for both cases was set to 1.4×10^{19} cm^{-3}. Both channels have long density ramps along the laser propagation axis which follow the neutral N_2 molecule density profile. Particle-in-cell (PIC) simulations presented later show that the density gradient at the end of the channel helps to trap the ionized inner-shell electrons by expanding the plasma bucket, as has been reported by other groups [34].

A 10TW drive laser pulse with a peak intensity of 3.3×10^{18} W/cm^2 (a_0 =1.2) at the focus was injected into both pre-formed plasma density profiles. Figure 3.10(a) shows optical spectra of the drive pulse after exiting the flat and waveguide profiles. The spectrum from the waveguide shows a significant red wing, consistent with pulse self-phase modulation over the guide length by a large amplitude plasma wave [158], while the spectrum from the flat profile is largely blue-shifted due to significant interaction of the drive pulse with unionized clusters outside the flat plasma profile.

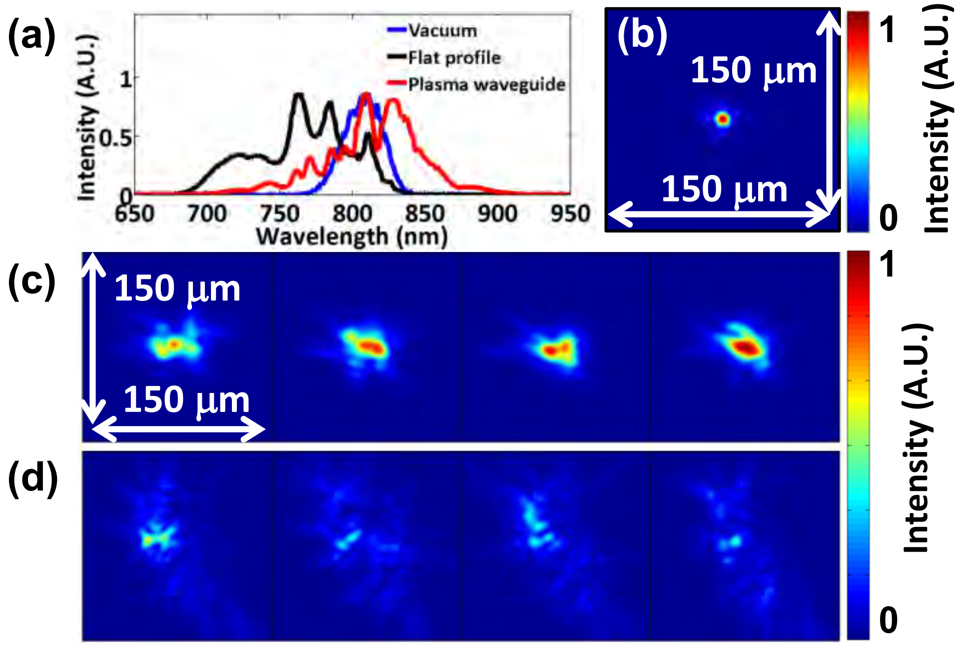

Figure 3.10. (a) Optical spectra of the 10 TW pulse before (blue) and after interaction with a flat (black) and guiding (red) electron density profile, each with a peak on axis density of $1.4 \times 10^{19}\, cm^{-3}$. A low intensity (0.4 TW) guided mode (b) shows a Gaussian mode with 14 μm FWHM. High power (10 TW) exit modes from the channel profile (c) and flat density profile (d) show improved confinement by the plasma waveguide.

Laser pulse exit mode images from the waveguide (Fig. 3.10(c)) show stable shot-to-shot confinement, although relativistic contributions to the waveguide index profile distort the mode compared to Fig. 3.10(b). By contrast, the beam from the flat profile (Fig. 3.10(d)) is not stable and shows a tight, relativistically self-focused spot that varies shot-to-shot along with significant unfocused energy outside of the flat plasma region. Interaction of the unfocused energy with unionized clusters explains the largely blue-shifted spectrum. This shows that even though the peak laser power satisfies P/P_{cr} >3 at the channel center, under our conditions the plasma waveguide is more effective than relativistic self-focusing in confining laser pulse energy to the propagation axis. This enables the guided pulse to drive a large amplitude plasma

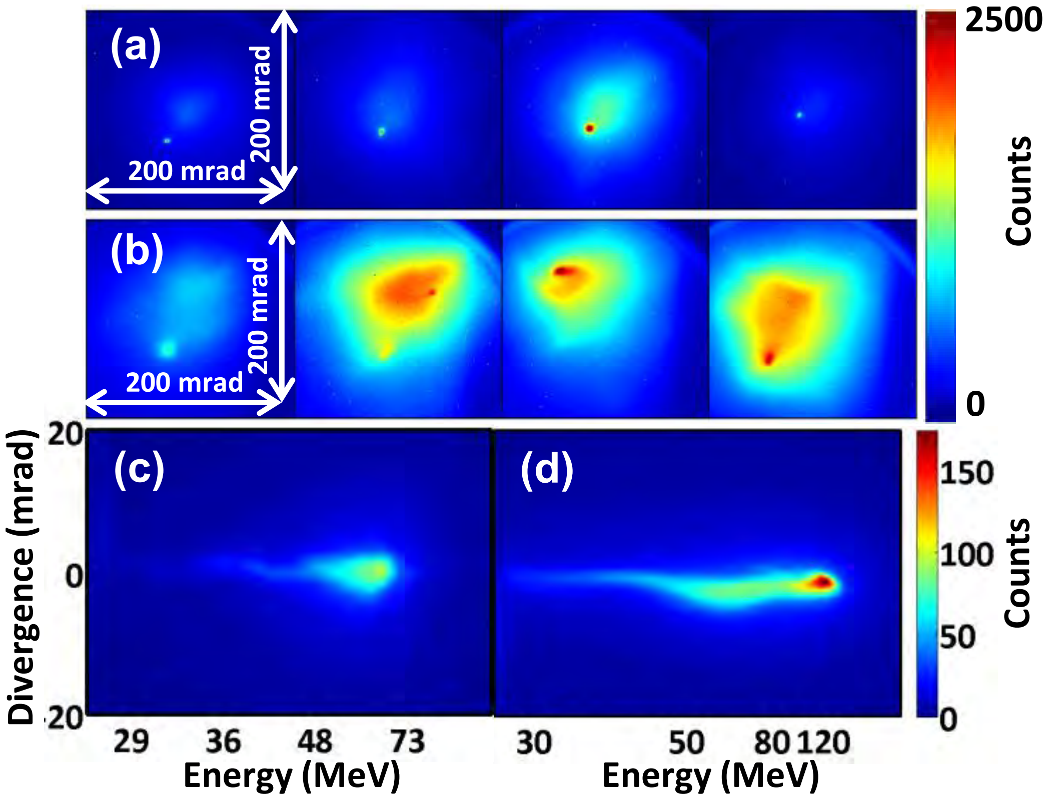

Figure 3.11. Electron beam profiles from the N^{5+} waveguide (a) and the N^{5+} flat density profile (b). A typical spectrum (c) shows acceleration with a peak at 60 MeV while the highest energy spectrum (d) is peaked near 120 MeV.

wave over a longer distance, resulting in the significant redshift missing in the flat plasma case.

The electron beam transverse profile and charge were measured using a Lanex fluorescing screen and published electron to photon conversion efficiencies [161,162]. The beam energy spectrum was measured using a 0.5 T magnetic spectrometer coupled to the same Lanex fluorescing screen. Figure 3.11 shows electron beam profiles from the waveguide plasma, (a), and from the flat waveguide, (b). The electron beam from the plasma waveguide is both more tightly collimated (2.8 mrad shot-averaged divergence vs. 6.6 mrad from the flat channel) and more stable (12 mrad standard deviation in beam pointing vs. 42 mrad). The charge in the tightly collimated, energetic electron beams of (a) is estimated to be approximately 5 pC based on prior calibration of the Lanex fluorescence [162] and estimated efficiency of the imaging system.

For the plasma waveguide, we observed a quasi-monoenergetic peak as large as 120 MeV (d), with average peak energy ~65 MeV (c), with a low energy tail extending down to 32 MeV. The low energy tail is commonly observed in ionization injection from continuous injection throughout the acceleration process [74,159,160]. For the flat channel, however, the electron energy could not be measured due to unstable beam pointing through the magnetic spectrometer.

To gain insight into the trapping and acceleration processes in the N^{5+} plasma waveguide 3D particle-in-cell simulations were performed using the code TurboWAVE [163], which includes a tunneling ionization model [164]. In order to assess the contribution of ionization injection from N^{5+} ions in the waveguide, simulations were performed for (*i*) a helium-like nitrogen plasma waveguide and (*ii*) a pre-ionized hydrogen channel with the same electron density profile as (*i*). A λ=800 nm, 40 fs, 3.3×10^{18} W/cm^2 peak intensity pulse, with a 14 μm FWHM beam waist was guided in both the N^{5+} and H^+ plasma waveguides. Corresponding to the measured waveguide profile of Fig. 3.9(a), each end of the simulated channel had an initial 700μm linear density ramp with on-axis densities rising from 8×10^{18} cm^{-3} to 1.4×10^{19} cm^{-3}, with a 100 μm plateau region in the middle. A short 50 μm ramp at either end brought the plasma density to vacuum. The total charge was neutralized by distributing either N^{5+} or H^+ ions within the channel.

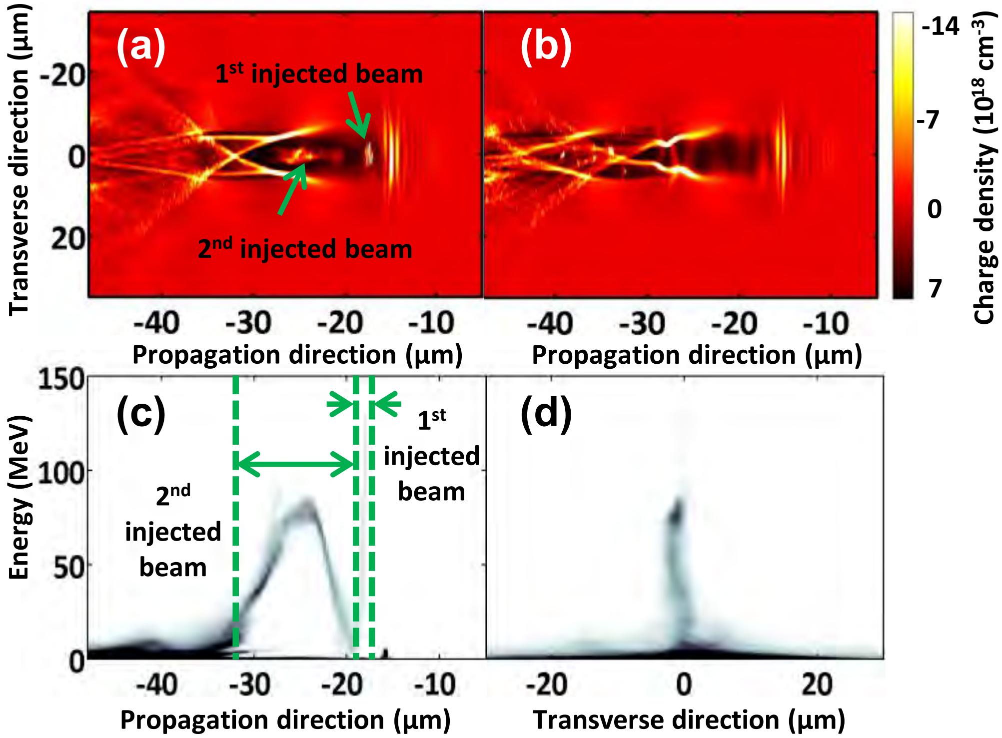

Figure 3.12. Charge density plots from Turbowave 2D PIC simulations after 1.4 mm propagation in a He-like nitrogen plasma waveguide (a) and a hydrogen plasma waveguide (b) with the same electron density profile. No beam injection is observed in the hydrogen channel case. The longitudinal (c) and transverse (d) phase space of the electrons ionized from N5+ to N6+ in the waveguide after 1.4 mm propagation show similar beam profile and energy as observed in experiments.

Electron beams similar to those observed experimentally, though with substantially higher charge, were produced from the simulated helium-like nitrogen plasma channel. A mono-energetic peak appears at 80MeV with a long low energy tail, as can be seen in the phase space plots Fig. 3.12(c) and 3.12(d). We can see the trapped electrons inside the bucket in Fig. 3.12(a), which shows a charge density plot near the end of the N^{5+} channel. In contrast, Fig. 3.12(b) shows that no significant trapping occurs in the hydrogen plasma channel.

Figures 3.12(a) and 3.12(c) also show that two spatially separated beams are trapped. The first beam has a lower charge (14pC) and a broad spectrum extending up to 150MeV, whereas the second beam contains much more charge (55pC) and the energy distribution has a quasi-monoenergetic peak at 80MeV. From the simulations, we observe that the second beam is trapped at the density down ramp, whereas the first beam is trapped starting from the entrance of the channel. Due to the significant difference in accelerated charge observed between the experiment and simulations, only the down ramp injected electrons are seen in the experimental electron spectra. The density down ramp traps significant charge in a short time by expanding the plasma bucket, giving rise to the quasi-monoenegertic peak. Even with the density down ramp, the plasma wave driven by the laser pulse was not strong enough to self-trap background plasma electrons without the help of ionization injection, and simulations showed that both beams are composed of K-shell electrons ionized near the peak of the drive laser pulse.

Chapter 4: Guiding of quasi-radially polarized modes in a plasma channel

4.1 Direct acceleration in a plasma slow wave structure

The vast majority of publications relating to laser driven plasma electron accelerators have focused on the laser wakefield (LWFA) technique described in the introduction to this dissertation. However, as outlined in that chapter, a major impediment to widespread application of these advanced accelerator concepts is the size, cost, and repetition rate of the drive lasers needed to create such an accelerator. Whereas the LWFA concept uses the large electrostatic fields associated with a laser driven nonlinear plasma wave, there have been a number of attempts to use the laser field itself, by far the largest electric field available in the lab, as an accelerating field [15,16,81,165,166]. There are three major impediments to using a laser electric field to accelerate charged particles. First, the laser field is oscillatory, so either the acceleration must be subcycle or the symmetry between the acceleration and deceleration phases must be broken. Second, the laser field is normally transverse to the laser propagation direction. This impediment can be overcome by using the strong longitudinal fields at the focus of a radially polarized pulse [15,167–169]. Acceleration of electron beams by tightly focused radially polarized beams in a background gas has been demonstrated, though at relatively small net energy transfer [15,165]. Finally, for high energy acceleration the high field intensity must be maintained over sufficient distances. This constraint is frequently limited by the

Rayleigh range of the focused beam but can be overcome through the use of guiding structures such as those presented in Chapter 3.

Recently a quasi-phase-matching DLA scheme has been proposed and studied both analytically and through particle-in-cell (PIC) simulations [12,84,85,170]. In this scheme the longitudinal field of a radially polarized femtosecond laser pulse is used as the accelerating field. The radially polarized pulse is injected along with a co-propagating relativistic electron beam into a plasma slow wave guiding structure. The slow wave structure is formed by applying axial density modulations to a plasma waveguide such as those described in Chapter 3.

In the limit that the laser frequency, ω_0, is much larger than the plasma frequency, $\omega_p = \sqrt{4\pi N_e e^2/m_e}$, the phase velocity of an electromagnetic wave propagating in an unmodulated plasma channel is given by

$$\frac{v_p}{c} = 1 + \frac{N_{e,0}}{2N_{cr}} + \frac{4}{k_0^2 w_{ch}^2}$$

where $N_{e,0}$ is the on axis electron density, N_{cr} is the laser critical density, w_{ch} is the matched spot size of the waveguide, and k_0 is the laser wavenumber [61]. It is evident that the phase velocity is strictly superluminal and, therefore, cannot be matched to the velocity of a co-propagating relativistic electron. However, in the presence of axial density modulations the phase velocity becomes

$$\frac{v_p}{c} = 1 + \frac{\bar{N}_{e,0}}{2N_{cr}} + \frac{4}{k_0^2 w_{ch}^2} - \frac{mk_{mod}}{k_0}$$

where now $\bar{N}_{e,0}$ is the longitudinally averaged on axis electron density, $k_{mod} = 2\pi/d_{mod}$ is the wavenumber associated with the density modulation period d_{mod}, and m is an integer [12,84]. The axial density modulations launch axial harmonics of the pulse which propagate at slower (for m>0) or faster (for m<0) phase velocity than the fundamental axial mode (m=0) through the waveguide. The m>0 waves are called "slow waves" in the RF and microwave literature and, through proper tuning of k_{mod}, can be made to propagate at or below the speed of light. The slow wave structure breaks the symmetry between accelerating and decelerating phases of the pulse as it interacts with the co-propagating electron beam, allowing a net energy transfer to the electrons over the length of the plasma waveguide. Similar to quasi-phase-matching in nonlinear optics [171,172], the electron periodically gains and loses energy as it propagates, with a net gain in each cycle resulting in a net energy gain over the full propagation path.

A simple scaling law for the energy gain in the quasi-phase-matched DLA process was developed by York *et al.* [12] by considering the maximum energy gain ΔE_{DLA} of a highly relativistic test electron accelerated in a modulated channel,

$$\frac{\Delta E_{DLA}}{m_e c^2} \sim 4\delta a_0 \left(\frac{\sigma_z}{w_{ch}}\right)\left(\frac{\lambda_p}{\lambda_0}\right)^2 \left(1 + \frac{2\lambda_p^2}{\pi^2 w_{ch}^2}\right)^{-2} \tag{4.1}$$

where δ is the modulation depth of the corrugated plasma waveguide, a_0 is the laser normalized vector potential, σ_z is the longitudinal extent of the laser pulse, λ_p is the plasma wavelength, and λ_0 is the laser wavelength [12]. Dephasing in the DLA process occurs when the accelerated electron outruns the laser pulse envelope. The DLA energy gain of equation (4.1) can be compared to that for LWFA,

$$\frac{\Delta E_{LWFA}}{m_e c^2} \sim \frac{a_0^2}{\sqrt{1 + a_0^2/2}}\left(\frac{\lambda_p}{\lambda_0}\right)^2 \left(1 + \frac{2\lambda_p^2}{\pi^2 w_{ch}^2}\right)^{-1} \tag{4.2}$$

as derived by Hubbard et al. in the mildly relativistic regime [77]. For typical experimental parameters $\lambda_0 = 800\,nm$, $w_{ch} = 15\,\mu m$, $a_0 = 0.25$, $\frac{\sigma_z}{c} = 300\,fs$ corresponding to a 1.9 TW laser power, $\bar{N}_{e,0} = 7\times10^{18} cm^{-3}$, $\delta = 0.9$, and a modulation period $d_{mod} = 349\,\mu m$, York *et al.* [12] calculate a peak energy gain of $\frac{\Delta E_{DLA}}{m_e c^2} \sim 1000$. This is comparable to the energy gain $\frac{\Delta E_{LWFA}}{m_e c^2} \sim 750$ calculated in [77] for a wakefield accelerator driven by a 7.16 TW laser in a suitable plasma channel. However, the linear dependence of the DLA energy gain with the laser field provides the strongest advantage of such a scheme. Even with peak powers ~10 GW typical of kHz regenerative amplifiers the DLA scheme can yield energy gains $\frac{\Delta E_{DLA}}{m_e c^2} \sim 50$ whereas highly nonlinear wakefield accelerators are generally unable to operate. This scaling argument shows that DLA is an intriguing technique for applications requiring moderate electron energies and high repetition rates in a compact and affordable package.

4.2 Generation of modulated waveguides for DLA

The first major hurdle for a proof of concept demonstration of DLA was the generation of a suitably micro-structured plasma waveguide to serve as the slow wave structure. This was first accomplished by Layer *et al*. using the hydrodynamic expansion method to form the plasma waveguide using a clustered gas target and an auxiliary ~100 ps pulse as outlined in Chapter 3 [173]. The axial modulations were achieved by imaging a diffractive “ring grating” to the axicon as shown in Fig. 4.1(a). Multiple diffraction orders from the ring grating interfering on axis created axial intensity modulations of the channel forming pulse. The axial intensity modulations

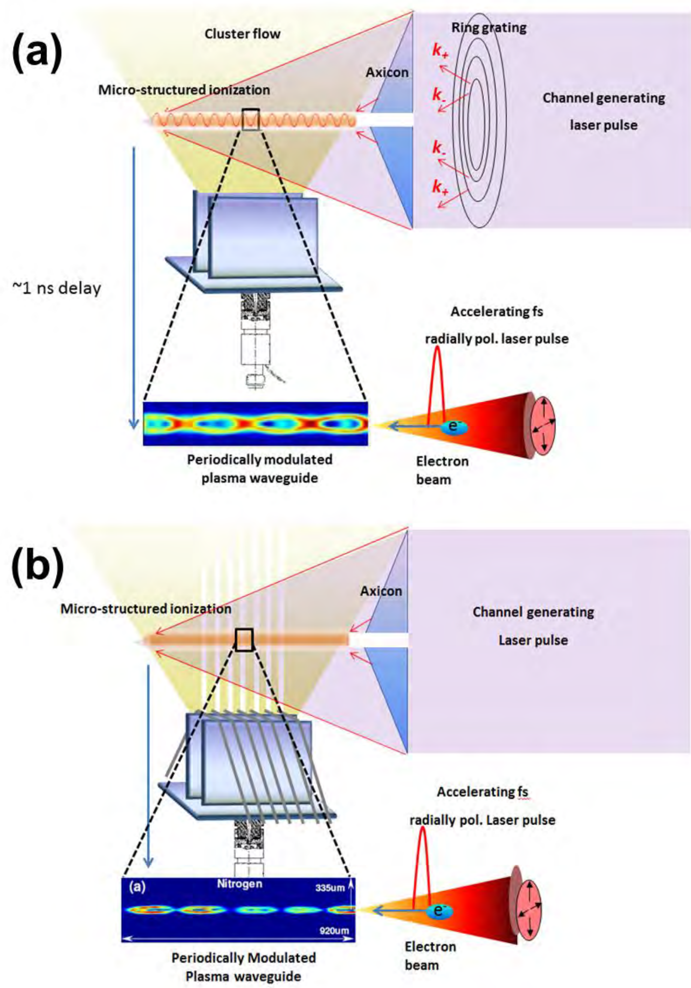

Figure 4.1. Experimental setup for creating modulated plasma waveguides using (a) a ring grating to modulate the focused intensity of the channel generating pulse and (b) wire obstructions for creating density modulations by periodically interrupting cluster flow. The general DLA scheme is also presented.

lead to a modulation of the ionization depth along the channel creating the necessary density modulations.

A simpler method, shown in Fig. 4.1(b), has been demonstrated for creating modulated channels in which the elongated cluster target is periodically obstructed using an array of thin wires [152,155,174]. The obstruction method has the advantage of providing large modulation depths, which may enhance the total energy gain in the accelerator [174]. Figure 4.2 shows the time evolution of a modulated

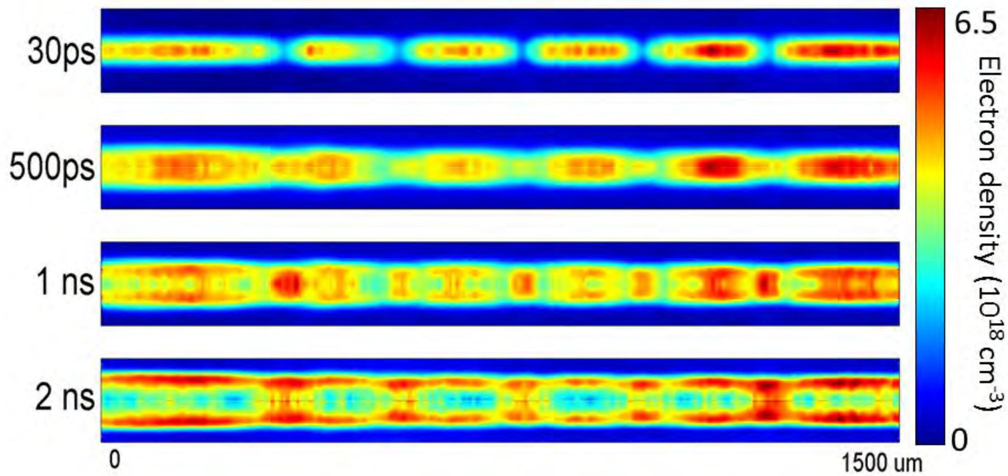

Figure 4.2. Abel inverted density profile of wire modulated plasmas as a function of probe delay. After ~1 ns delays a density minimum develops on axis providing a suitable density profile for optical guiding. Axial density modulations with a 220 μm period are generated by obstructing the cluster flow with 25 μm diameter tungsten wires.

channel created in a nitrogen cluster jet with a 200 μm period wire array. Using 25μm diameter tungsten wires, modulation periods as small as ~70 μm were possible without significant loss of density in the unobstructed regions between the wires. These small modulation periods can be important for ramping the quasi-phase-matching period to successfully accelerate lower energy electrons [170]. However, it was found that with such small wire spacings the cluster flow properties become important for maintaining a quality plasma channel [152]. If there is a significant monomer fraction to the supersonic flow past the wire obstructions , then shock waves form which can disassemble the clusters [174]. The effect of shocks is eliminated with increased cluster size accompanied by a reduced monomer component of the flow. When the cluster flow is ballistic (the mean free path for cluster collisions is much larger than the wire diameter) the shockwaves disappear and a clear shadow appears behind the wires. Figure 4.3 demonstrates the effect of

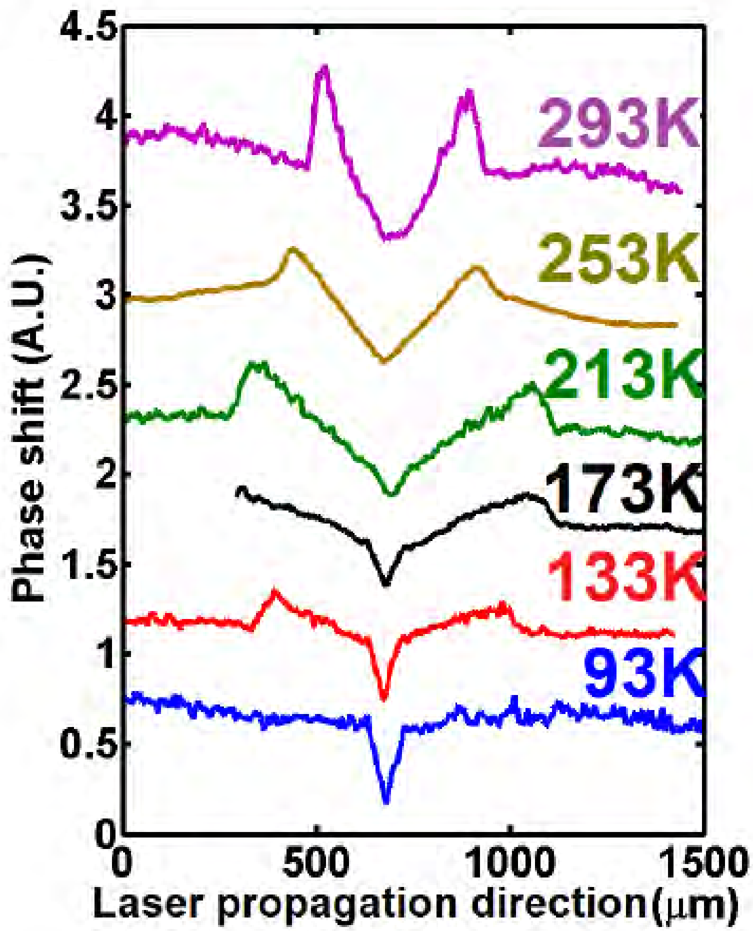

Figure 4.3. Lineouts of phase profiles in a plasma generated over a cluster jet obstructed by a single wire as a function of cluster jet reservoir temperature. At high temperatures and low mean cluster sizes shock waves are clearly evident while only a ballistic shadow of the wire appears at low temperatures and large mean cluster sizes.

jet reservoir temperature, and consequently cluster size, on shock formation behind a single wire in a nitrogen cluster jet.

Both the ring grating and wire modulation methods provide static modulation periods, and a new ring grating or wire array must be fabricated for each modulation period. For experimental optimization of the phase matching process a dynamic modulation period which can be controlled on the fly is preferred. This is particularly true in the case of period or density ramping, where the seed electron beam is of too low an initial velocity to be phase matched at a single period over the entire interaction length [85]. The use of a spatial light modulator to dynamically shape the intensity profile of the channel-forming pulse shows promise in providing dynamic modulation control [175]. This is the subject of ongoing work and could also provide fine control of channel profiles for improved coupling to plasma channels or controllable density dips which have been used as a diagnostic for laser wakefield accelerators [176,177].

4.3 Generation and focusing of quasi-radially polarized beams

Radially polarized laser beams (RPLBs), proposed as the drive field for the DLA scheme and other direct particle acceleration schemes, have found applications in a variety of fields including optical trapping [178,179], laser machining [180,181], and microscopy [182]. A RPLB is particularly interesting in all of these fields because, when focused with a high numerical aperture lens the (non-paraxial) RPLB can produce a dominant longitudinal field at its focal plane with a transverse extent smaller than the conventional diffraction limit for linearly polarized beams [182]. Due to this field structure, the RPLB has been described as a free space analog to TM modes found in RF and microwave waveguides [183,184]. In the paraxial limit, the fields of the RPLB can be derived by considering an axially polarized vector potential in the Lorentz gauge satisfying the Helmholtz equation [183]. The vector potential has standard Gaussian mode solutions the lowest of which is of the form

$$A_z = \frac{A_0}{k\tilde{q}(z)} \exp\left[ik\frac{x^2+y^2}{2\tilde{q}(z)} + ikz\right]$$

where $\tilde{q}(z) = z - iz_R$ is the complex Gaussian beam parameter and $k = \omega/c$ is the wavenumber. The electric and magnetic fields can then be calculated from simple relations $\vec{B} = \nabla \times \vec{A}$ and $\vec{E} = -\frac{ic}{k}\nabla \times B$ to be

$$B_\theta = \frac{-ikr}{\tilde{q}} A_z$$

$$E_r = cB_\theta$$

$$E_z = -\frac{2c}{\tilde{q}}\left(1 + \frac{ikr^2}{2\tilde{q}}\right) A_z.$$

Much effort has gone into the calculation of the longitudinal fields of RPLBs in nonparaxial and pulsed (non-monochromatic) limits in which case a significant fraction of the electromagnetic energy can be contained in the longitudinal field [13,182,184,185].

Methods have been demonstrated for generating RPLBs both inside and outside the laser cavity. Due to the complexity of maintaining radial symmetry inside of a laser cavity, which will normally be broken by polarizing or Brewster angle

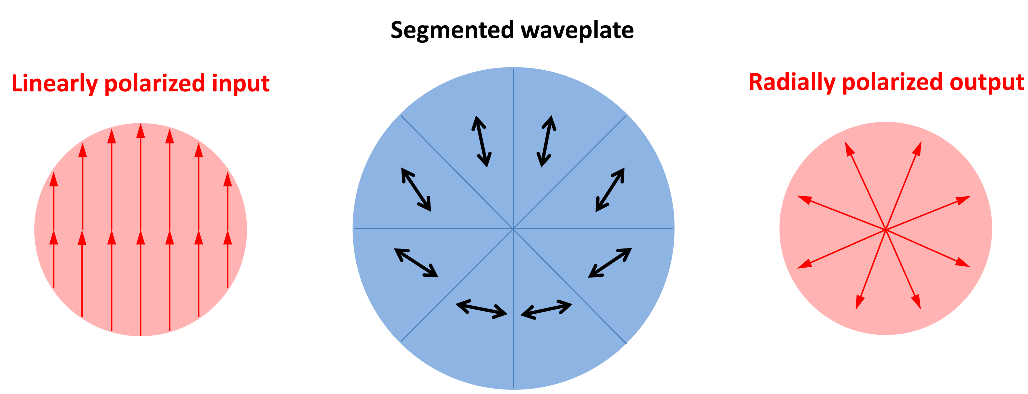

Figure 4.4. Concept of a segmented waveplate used for generating approximately radially polarized light. Slices of a $\lambda/2$ waveplate are arranged with slowly varying orientation of the birefringent crystal's slow axis. This causes a varying rotation of the laser polarization with the azimuthal angle

optics, extra-cavity radial polarizing schemes are of interest for generating a DLA drive pulse. The most commonly used method of generating radial polarization is the segmented waveplate [186,187]. This consists of a standard half wave plate which has been cut into various segments and rearranged such that the slow axis rotates around the optic as shown in Fig. 4.4. A linearly polarized beam passing through the segmented waveplate will experience a difference in polarization rotation around the azimuthal angle following the slow axis of the waveplate giving an approximately radially polarized beam. The degree of radial polarization (and cost of the waveplate) increases with an increasing number of segments. Recently, commercial radial polarizers based on liquid crystal spatial light modulators have become available which can give an excellent approximation to a purely radially polarized beam, but suffer from a relatively low damage threshold [188].

It has been shown that a RPLB can be constructed as a linear combination of linearly polarized Hermite-Gaussian TEM_{01} and TEM_{10} modes [90,189]. Therefore, we can consider the lowest order approximation to radial polarization to be a linearly polarized Hermite-Gaussian TEM_{01} mode. These modes can be produced by passing a linearly polarized beam through an appropriate (reflective or transmissive) step phase plate which applies a π phase shift across two halves of the beam. This was accomplished on our system by placing a 2 μm thick "half-pellicle" in the beam path. The half-pellicle is a standard optical pellicle in which half the film has been cut away with a razor blade. The angle of the pellicle was tuned to create a half wave difference in the optical path length across the beam as shown in Fig. 4.5(a). The measured intensity profile of the resulting beam at the focal plane is shown in Fig.

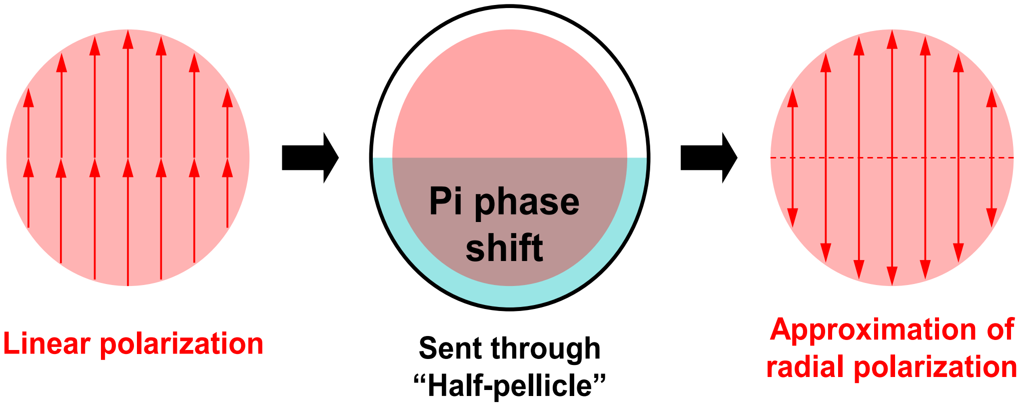

Figure 4.5. A pellicle beamsplitter cut in half with a razor blade was used to transform a linearly polarized Gaussian beam into an approximation of a Hermite-Gaussian TEM_{01} mode. The angle of the pellicle was tuned to apply a π phase shift on one half of the beam with respect to the other.

4.6(a). The focal plane of a pure TEM_{01} mode is shown in Fig. 4.6(b), and lineouts parallel to the polarization direction are plotted in Fig. 4.6(c). The overlap integral of the half-pellicle mode with a pure Hermite-Gaussian TEM_{01} mode is

$$\frac{P_{01}}{P_{HP}} = \frac{\int E_{HP} u_{01}^* dA}{\int |E_{HP}|^2 dA} = 0.85$$

where a flat phase profile is assumed so that $E_{HP} = \sqrt{I_{HP}}$.

The longitudinal field of a Hermite-Gaussian mode can be approximated in the paraxial limit by considering Gauss's law near the focal plane [81,182]. In the paraxial limit the electric field satisfies the Helmholtz equation

$$\frac{\partial}{\partial z} E = \frac{i}{2k} \nabla_{\perp}^2 E.$$

The Gaussian lowest order mode is given by

$$\boldsymbol{E}_{00}(x, y, z) = \boldsymbol{E}_0 \frac{w_0}{w(z)} \exp\left(-\frac{x^2 + y^2}{w(z)^2} + i \left[kz - \eta(z) + \frac{k(x^2 + y^2)}{2R(z)} \right] \right)$$

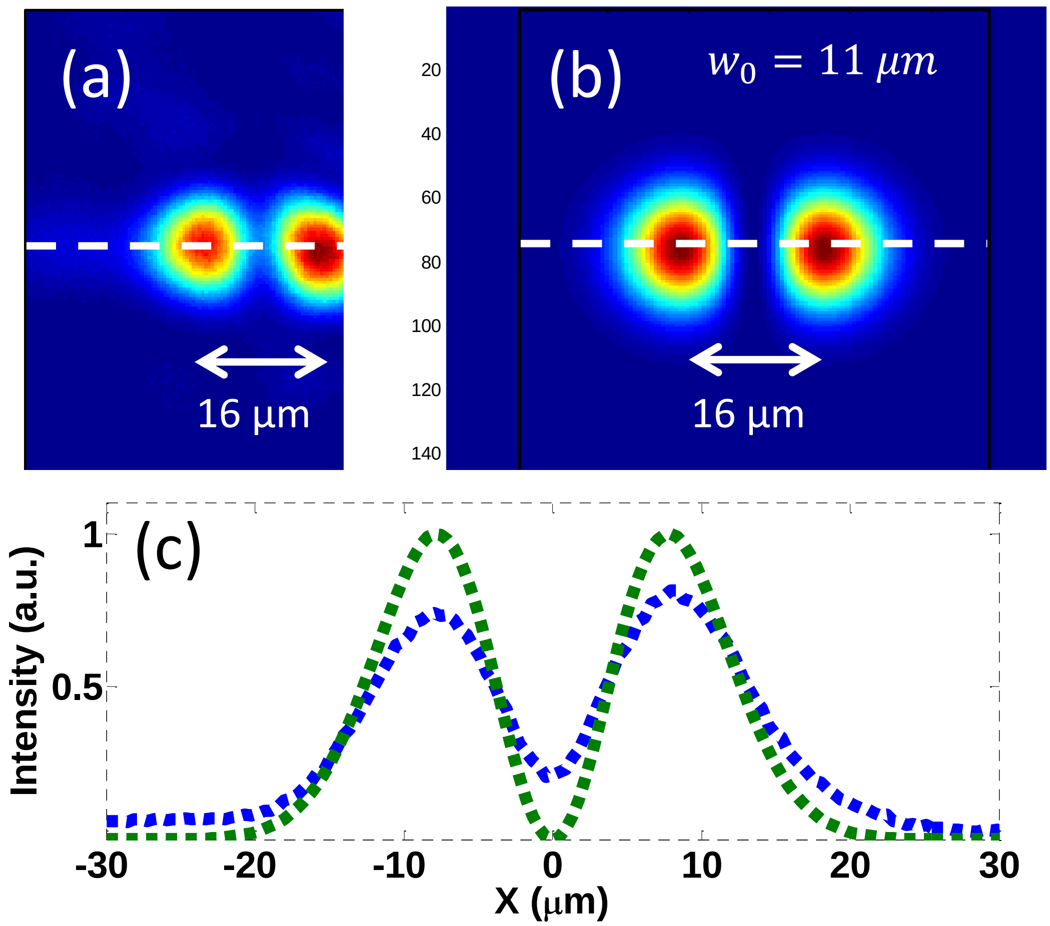

Figure 4.6. The focus of the half-pellicle beam (a) resembles a pure TEM_{01} Hermite-Gaussian mode (b). Lineouts along the maxima are compared in (c).

where $w(z) = w_0\sqrt{1 + z^2/z_R^2}$ is the beam spot size, $R(z) = z(1 + z_R^2/z^2)$ is the beam phase front curvature, $\eta(z) = \arctan(z/z_R)$ is the Guoy phase shift, and $z_R = kw_0^2/2$ is the Rayleigh length [91]. Higher order modes can be derived from the fundamental mode by the recursion relation

$$\boldsymbol{E}_{nm}^{HG}(x, y, z) = w_0^{n+m} \frac{\partial^n}{\partial x^n} \frac{\partial^m}{\partial y^m} \boldsymbol{E}_{00}(x, y, z)$$

which yields

$$\boldsymbol{E}_{01}^{HG}(x, y, z) = -\frac{2xw_0}{w(z)^2}\left(1 - \frac{ikw(z)^2}{2R(z)}\right) \boldsymbol{E}_{00}(x, y, z)$$

for the first higher order mode [190]. The paraxial approximation, by solving only the scalar wave equation, explicitly assumes $E_z = 0$ and all modes are TEM. However, using Gauss's law we can at least approximate the longitudinal field near the beam waist as

$$E_z(x, y, z = 0) = -\int \frac{\partial}{\partial x} E_x(x, y, z) dz,$$

where the beam is assumed linearly polarized in the x direction and we take $z = 0$ after the integration. For the E_{01}^{HG} mode this gives

$$E_z = -\frac{2i}{kw_0} E_0 \left[1 - \frac{2x^2}{w_0^2}\right] e^{-\frac{x^2+y^2}{w_0^2}}.$$

The longitudinal field is seen to be 90 degrees out of phase with the radial field and has a maximum on axis whereas the transverse field vanishes on axis with a maximum at $x = w_0/\sqrt{2}$. The ratio of longitudinal to transverse field maxima is found to be

$$\left|\frac{E_{max,z}}{E_{max,x}}\right| = \frac{\sqrt{2e}}{kw_0}.$$

For typical focusing parameters in our experiments, $kw_0 \sim 80$ so $\left|\frac{E_{max,z}}{E_{max,x}}\right| \sim 3\%$. As might be expected, this is exactly half the peak accelerating field calculated in the paraxial limit for a purely radially polarized beam with the same peak electric field [81]. If we instead compare the peak longitudinal field, $E_{z,max}^{01}$, of a TEM$_{01}$ mode to that of a purely radially polarized mode, $E_{z,max}^{r}$, with the same total *energy*, we find that $E_{z,max}^{01} = \frac{E_{z,max}^{r}}{\sqrt{2}} = 0.707 * E_{z,max}^{r}$.

4.4 Guiding of a TEM_{01} mode in a plasma channel

The approximately parabolic plasma channel described in Chapter 3 will support higher order modes, allowing matched guiding of the half-pellicle mode (near-TEM_{01} mode) with its associated axial field component [61]. The controlled guiding of higher order modes in a plasma channel has never before been demonstrated experimentally to the best of our knowledge. Plasma waveguides were generated by focusing a 250mJ, 140ps Nd:YAG laser pulse over an 11 mm nitrogen cluster jet. The clusters ionize and collisionally absorb the Nd:YAG pulse. The plasma expands at the ion acoustic speed and after approximately 700 ps forms a density minimum on axis with an index profile supporting guided modes. Figure 4.7 shows the Abel-inverted density profile of the first 1.4 mm of the 11 mm plasma as well as a transverse lineout showing the density minimum on axis and the approximately parabolic density profile between the shock walls. Figure 4.7(c) and

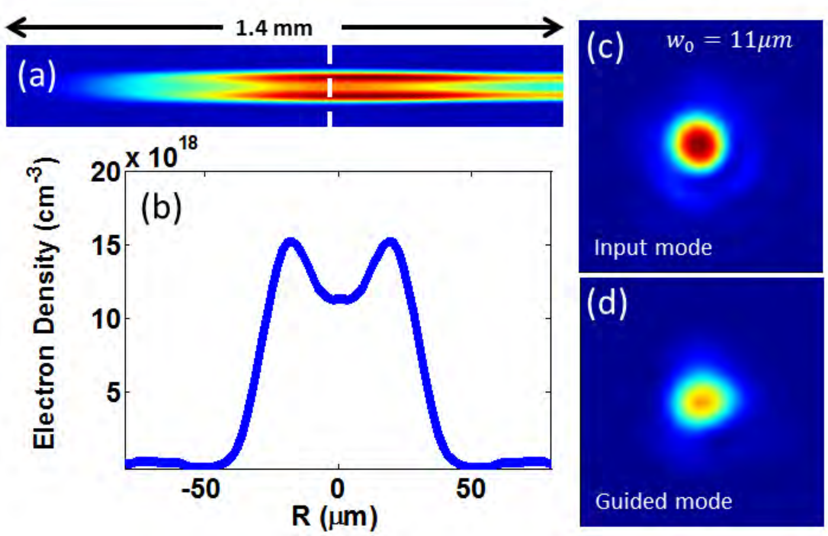

Figure 4.7. The Abel inverted density profile of the first 1.4 mm of an 11 mm nitrogen plasma waveguide (a) with a lineout shown in (b). A Gaussian input mode with an 11 μm spot size (c) is guided with approximately 60% energy throughput and the same spot size as the input mode (d).

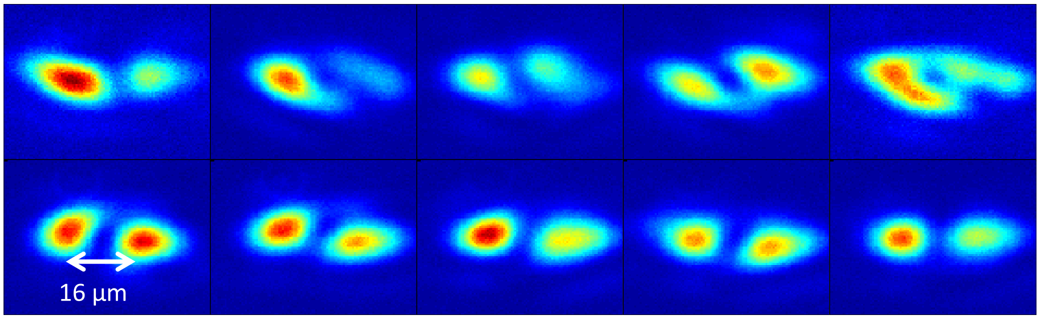

Figure 4.8. Series of guided modes at the exit of an 11 mm nitrogen plasma waveguide. The modes retain the two-lobe structure of the injected near-TEM_{01} mode with an energy throughput of ~30%.

4.7(d) show sample injected and guided Gaussian modes using the same spatial and color scales. The Gaussian input TEM_{00} mode (10 mJ, 40 fs) has a spot size of $w_0 = 11\ \mu m$. Guided throughput is approximately 60% over a distance of 20 Rayleigh lengths with an 11 µm spot size.

The half pellicle was inserted before the vacuum pulse compressor, and the beam was focused onto the entrance of the plasma waveguide with an injected focal spot profile shown in Fig. 4.6(a). The calculated w_0 of the approximate TEM_{01} mode was 11 µm, identical to the guided Gaussian mode in Fig. 4.7(d). Figure 4.8 shows a series of guided half-pellicle-injected modes from ten consecutive laser shots. The exit modes retain the TEM_{01} mode structure over the 11 mm propagation length with an average energy throughput of ~30%. While the energy throughput is somewhat low, the expected peak longitudinal field at the exit of the plasma waveguide is still an impressive ~100 MV/cm. Using the DLA relations for energy gain this gives a ~24 MV/cm accelerating gradient. This is well within detection limits for a proof of principle DLA demonstration with an input mode energy of 10 mJ and 30% energy throughput.

Chapter 5: Characterization of a micrometer-scale cryogenically cooled gas jet for near critical density laser-plasma experiments

5.1 Introduction

Gas jets have been employed as targets in high intensity laser-matter interaction studies for decades. Experiments utilizing gas jets span a wide variety of applications including electron and ion acceleration [27,29,191,192], high harmonic generation [193,194], x-ray lasers [133], and even generation of fusion neutrons [195]. The main draw of gas jets, as compared to solid targets or static gas fills, is the ability to create a well-controlled, automatically replenishing target that can be used at relatively high repetition rate without requiring target rasterization schemes. Fine control of the gas density and profile has been demonstrated by multiple groups through engineering of the valve design [196–198], nozzle geometry [199–202], and through external shaping of the resulting gas flow [152,155,203,204].

In experiments with these gas jets, the electron density has generally been limited to less than $\sim 10^{20}\ cm^{-3}$, with interaction lengths on the millimeter scale. This density precludes the study of the near critical plasma density regime with ultrashort Ti:Sapphire laser pulses ($N_{crit} \approx 1.7 \times 10^{21} cm^{-3}$). Two notable exceptions to this limitation are the schemes presented by Sylla et al. [197] and Kaganovich et al. [203] for achieving thin, high density plasmas suitable for the study of near critical phenomena. Sylla et al. achieved a critical density plasma by implementing a novel valve design which boosts the pressure above 4000 psi behind a ~400 μm nozzle. Kaganovich et al. generate a shockwave in a standard gas jet by ablating a metal plate with a nanosecond laser a controlled time before the main interacting pulse. The density of the gas in the thin shock can be many times higher than the ambient gas density, boosting the target density into the near critical regime.

Here, a simple method for generating thin, near critical density plasmas which avoids complicated pressure boosting schemes or secondary lasers is presented. The technique hinges on the use of a cryogenically cooled high pressure solenoid valve coupled to a variety of thin nozzles with diameters as small as 50 μm. Sonic nozzles are employed to maximize the peak molecule number density at the nozzle output for a given nozzle minimum diameter. The cryogenic cooling increases the molecule number density inside the reservoir for a fixed valve backing pressure which, in the isentropic limit, proportionally increases the number density at the orifice exit plane.

5.2 High density valve design

The valve used in the high density jet design is a solenoid valve held in a custom cooling jacket, shown in Fig. 5.1(c), which uses a combination of liquid nitrogen and electrically driven heating elements to control the valve reservoir temperature. The reservoir temperature can be controlled to within 1 degree Celsius between room temperature and ~ -160º C. A series of custom nozzles was fabricated which attach to the solenoid valve with two main designs. The first design, shown in Fig. 5.1(a), uses a straight ~1 cm long section of a thin needle which restricts the flow directly at the valve orifice. The second design, shown in Fig. 5.1(b), uses a precision tapered nozzle with 12 degree taper starting from ~2.5 mm diameter at the base. The minimum inner diameters, referred to as the nozzle throat, ranged from 50 μm to 150

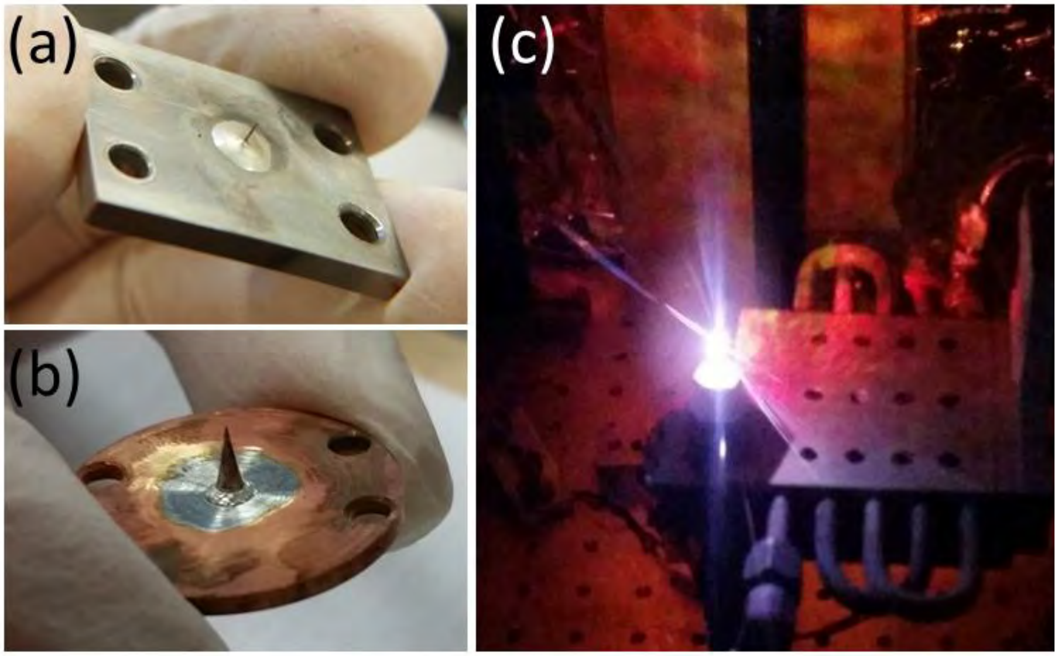

Figure 5.1. Custom fabricated straight (a) and tapered (b) nozzles with ~100 μm throats. The gas jet is held in a custom cooling block (c) which can cool the jet to cryogenic temperatures.

μm for both nozzle designs. In all nozzles, a "sonic" design was employed where the nozzle diameter at the exit plane was equal to the throat diameter. This is in contrast to supersonic nozzles employing a converging-diverging (de Laval) design to reach high Mach numbers [205].

Controlling the reservoir temperature and pressure along with the nozzle exit diameter allowed us to access peak molecular densities in the range 10^{19}-10^{21} cm^{-3}. The radial density profile of the gas flow was nearly Gaussian with full width at half maximum (FWHM) of 100-200 μm depending on the diameter of the nozzle exit orifice. Depending on the gas species used, when ionized this covers underdense through overdense plasma regimes for an 800 nm Ti:Sapphire laser ($N_{crit} \approx 1.7 \times 10^{21} cm^{-3}$).

5.3 Isentropic flow model

The flow of gas from the jet can be modelled as the steady, one-dimensional isentropic flow of an ideal gas into a low pressure reservoir [206]. The gas in the valve reservoir is held at a given stagnation (zero velocity) temperature, T_0, and pressure, P_0. Flow from the reservoir is forced through a narrow orifice by the pressure gradient between the reservoir and vacuum chamber which is held at a pressure, P_b. We seek to calculate the molecule density, n, at the exit of the nozzle as a function of the reservoir and nozzle parameters.

The steady flow assumption is validated by measurements of the gas density as a function of time presented in section 5.5 which show a fast rise in the gas density output followed by a plateau. The isentropic flow assumption requires that the flow be adiabatic and inviscid. We can validate the adiabatic nature of the flow by calculating the heat transfer from the nozzle to the gas as it transits the nozzle. The total heat transfer is given by $\Delta Q = -\kappa A \frac{dT}{dr} \Delta t$ where κ is the thermal conductivity of the gas ($\kappa \approx 0.069\, W/m/K$ for hydrogen at 100 K [207]), A is the gas contact area which is taken to be the inner wall of the nozzle ~3 mm^2, the temperature gradient dT/dr, taken across the diameter of the nozzle throat, is calculated using isentropic fluid equations presented below to be ~200 K/mm, and the transit time $\Delta t{\sim}10\mu s$ is estimated by assuming the gas flows at the sound speed ($c_s = \sqrt{\gamma\, k_B T_0/m} \approx 800\, m/s$) through the 1 cm long nozzle. With these parameters 0.5 μJ is transferred to the gas as it transits the nozzle. The change in temperature of the hydrogen gas through heat conduction is given by $\Delta T = Q/C_v$ where $C_v \approx 13 J/g/K$ is the specific heat capacity of hydrogen at constant volume. For the nozzle volume of 0.2

mm^3 and a hydrogen molecule density ~10^{21} cm^{-3} approximately 0.3 μmol of hydrogen is contained in the nozzle at a given time. Therefore the 0.5 μJ transferred to the gas as it transits the nozzle yields a temperature change ~0.1 K. This is much less than the temperature change in the gas due to expansion from the reservoir through the nozzle, which is ~10 K calculated from the isentropic flow relations given below with $M = 1$, so we may use the adiabatic approximation.

The effect of viscosity on the flow can be expressed through the dimensionless Reynold's number, $Re = \rho VD/\mu$, where ρ is the fluid mass density, V is the flow velocity, D is the nozzle diameter, and μ is the fluid dynamic viscosity. The Reynold's number represents the ratio of the inertial to viscous forces acting on the fluid, with high Reynold's numbers representing inertially dominated flow. We can estimate Re by considering a flow at the stagnation temperature and pressure within the jet reservoir moving through the needle nozzle at the sound speed. This will be shown below to give the correct order of magnitude for the Reynold's number under isentropic flow conditions. We consider the stagnation conditions $T_0 = -160C = 113\ K$, $P_0 = 1000\ psi = 7\ MPa$, $n_0 = 4.4 \times 10^{21} cm^{-3}$ and $c_s = \sqrt{\gamma k_B T/m} = 840\ m/s$. The dynamic viscosity of hydrogen can be approximated by Sutherland's formula for the viscosity of an ideal gas, $\mu = CT^{3/2}/(T + S)$ where C and S are empirically measured gas dependent constants [208]. For hydrogen, $C = 0.64$ and $S = 72$ [209] so at $T_0 = 113\ K$ the dynamic viscosity is $\mu = 4.2\ \mu Pa \cdot s$. Plugging these values in to the formula for Re with a tube diameter of 100 μm gives $Re \approx 3 \times 10^5$. The boundary layer thickness, δ_L, a distance L along the nozzle can be estimated as $\delta_L/L \sim 1/\sqrt{Re} = .002$. The needle aspect ratio is ~1/100, so the boundary layer thickess at the exit of the needle is estimated to be about 20% of the nozzle diameter. The boundary layers may reduce the overall flow rate somewhat, but the flow near the center of the nozzle may be approximated as isentropic.

In an ideal isentropic flow one can express the gas temperature, T, and pressure, P, in terms of the gas specific heat ratio, $\gamma = \frac{c_P}{c_V} > 1$ and the Mach number, $M = V/c_s$ where V is the fluid velocity and c_s the sounds speed via [210]

$$\frac{T_0}{T} = 1 + \frac{\gamma - 1}{2} M^2 \tag{5.1}$$

$$\frac{P_0}{P} = \left(1 + \frac{\gamma - 1}{2} M^2\right)^{\frac{\gamma}{\gamma-1}} \tag{5.2}$$

where P_0 and T_0 are the stagnation temperature and pressure (i.e. conditions where $M = 0$) . Equations (5.1) and (5.2) follow from the assumption that energy in the fluid is conserved so that the stagnation properties of the flow remain constant throughout the expansion. Further, since the flow is isentropic, $Pn^{-\gamma} = constant$, the gas density is given by

$$\frac{n_0}{n} = \left(1 + \frac{\gamma - 1}{2} M^2\right)^{\frac{1}{\gamma-1}}. \tag{5.3}$$

Equation (5.3) indicates the fluid density drops rapidly as the Mach number increases. Therefore, to reach the highest density possible at the nozzle exit, the Mach number should be minimized.

Equations (5.1)-(5.3) also lead to the definition of the fluid critical properties, defined as the fluid state corresponding to exactly sonic flow ($M = 1$) [210]. The critical properties, denoted with a *, can be written in terms of the stagnation properties as

$$\frac{T^*}{T_0} = \frac{2}{\gamma + 1},$$

$$\frac{P^*}{P_0} = \left(\frac{2}{\gamma + 1}\right)^{\frac{\gamma}{\gamma - 1}},$$

$$\frac{n^*}{n_0} = \left(\frac{2}{\gamma + 1}\right)^{\frac{1}{\gamma - 1}}.$$

Consider the steady gas flow from a region held at high pressure, P_0, to a region held at low pressure, $P_b < P_0$, as is the case for the high pressure jet flowing into the vacuum chamber. If $P_b < P^*$ then at some point between the (fixed) high and low pressure regions the flow will reach sonic velocity. For diatomic gases such as hydrogen, $\gamma = 1.4$ and $\frac{P^*}{P_0} = 0.528$. The ratio between the jet backing pressure and the vacuum chamber background pressure is ~10^{-5}, so the flow from the jet will reach at least the sound speed. Since the jet output density given by equation (5.3) is strictly decreasing as a function of M and we know the flow must reach at least the sound speed as it exits the nozzle, the achievable output density is maximized by a nozzle which has $M = 1$ at the exit plane, which is called a sonic nozzle. Sonic nozzles are achieved by using a converging or fixed nozzle cross section in contrast to supersonic nozzles which have a converging-diverging (de Laval) geometry [206].

The molecule density at the exit of the sonic nozzle is given by

$$n^* = n_0 \left(\frac{2}{\gamma + 1}\right)^{\frac{1}{\gamma - 1}} \cong 0.63 \times n_0 = 0.64 \times \frac{P_0}{k_b T_0} \tag{5.4}$$

where $\gamma = 1.4$ for a diatomic gas and the ideal gas equation of state are assumed. Equation (5.4) shows that increasing the gas density at the nozzle exit can be achieved by increasing the gas density in the nozzle reservoir. From the equation of state, increasing the reservoir density is achieved by increasing the nozzle backing pressure, P_0, or by decreasing the reservoir temperature, T_0. Cryogenic cooling of the reservoir temperature thus serves to increase the total jet output density proportional to T_0^{-1} where T_0 is given in Kelvin.

5.4 Experimental setup

The output density of the gas jet as a function of temperature, pressure, and nozzle geometry was characterized by transverse interferometry with a < 100 fs, 400 nm probe pulse derived from our 25 TW Ti:Sapphire laser system [141,211]. Figure 5.2 shows a diagram of the experimental setup. The phase shift due to the gas is extracted by shearing the 400 nm probe inside a folded wave front interferometer and extracting the phase shift through Fourier techniques [212]. The extracted 2D phase profile represents the phase shift, $\Delta\phi(x)$, accumulated by different chords through the gas profile and can be related to the radial gas density profile through the Abel transform

$$\eta(r) - 1 = -\frac{1}{k\pi}\int_r^{r_0}\left(\frac{d\Delta\phi(x)}{dx}\right)\frac{dx}{\sqrt{x^2 - r^2}} \tag{5.5}$$

and the relation

$$n(r) = \frac{\eta(r) - 1}{2\pi\alpha}.$$

Here $\eta(r)$ is the gas refractive index, $k = 2\pi/\lambda$ is the probe wavenumber, r is the radial coordinate, r_0 is a radius at which the gas density goes to zero, $n(r)$ is the gas number density, and α is the gas molecular polarizability. The integral transform of equation (5.5) can be solved numerically or, with a suitable phase shift profile

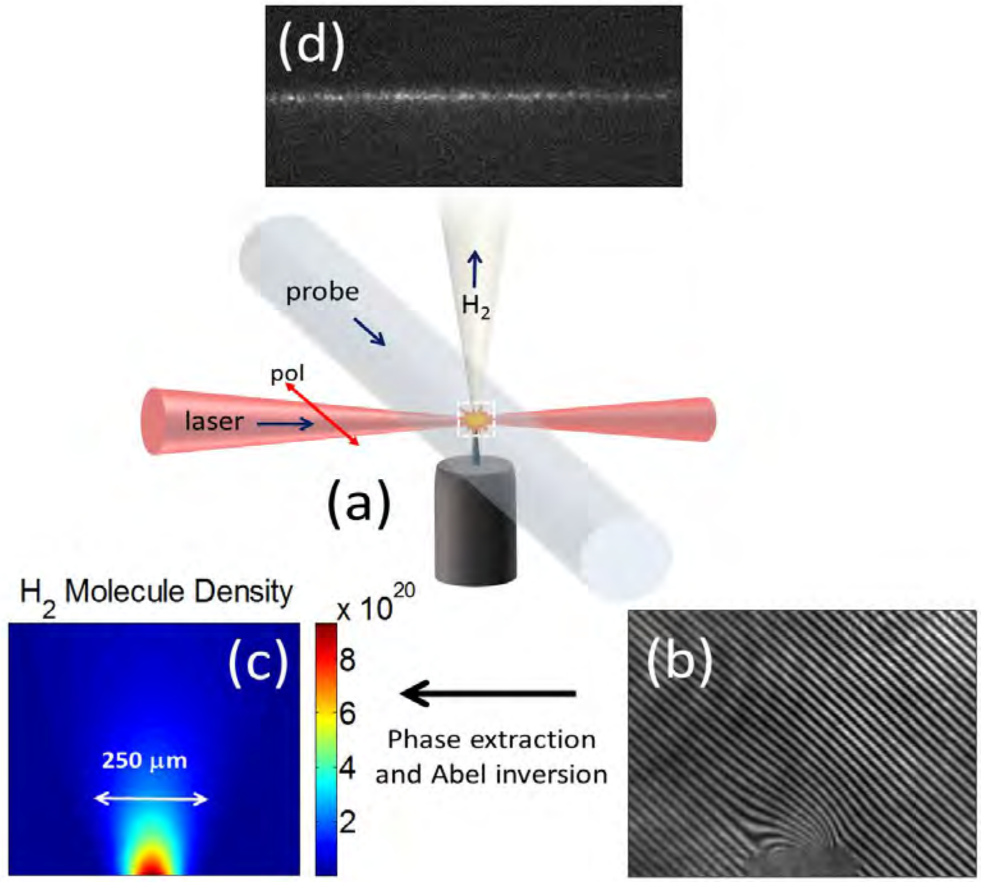

Figure 5.2. Experimental setup for characterizing the high density gas jet (a). Density measurements were made using transverse interferometry. A raw interferogram (b) and Abel inverted density profile (c) are shown along with a raw image of Rayleigh scattering used to measure the cluster size and density in the jet.

for $\Delta\phi(x)$, analytically. In all of our measurements $\Delta\phi(x)$ was fit very well by a Gaussian function at heights 50 μm or more above the nozzle orifice. Taking $\Delta\phi(x) = \Delta\phi_0 \exp\left(-\frac{x^2}{\sigma^2}\right)$ over the full axis, then the Abel inverted radial index profile is calculated from equation (5.5) to be

$$\eta(r) - 1 = \frac{1}{k}\frac{\Delta\phi_0}{\sqrt{\pi}\sigma}\exp\left(-\frac{r^2}{\sigma^2}\right).$$

A numerical Abel inversion routine based on the fast Fourier transform was also implemented [213]. Numerical Abel inversion generally agreed with the analytical

Abel inversion using the Gaussian fit to within ~10%. The insets in Fig. 5.2 show a sample raw interferogram (b), Abel inverted density profile (c), and a sample image of Rayleigh scattering (d) used to measure cluster size in the high density jet.

5.5 Hydrogen jet density measurements

Hydrogen gas is commonly used in laser plasma interaction experiments because of the ease with which it is fully ionized by the leading temporal edge of a suitably intense femtosecond laser pulse. Complete ionization mitigates ionization induced refraction of the main interacting pulse. However, since each hydrogen molecule can only contribute two electrons, high plasma densities have been very difficult to reach without the use of some higher Z dopant such as nitrogen or argon. Figure 5.3(a) shows a sample Abel inverted density profile of the hydrogen gas jet using a 100 μm needle nozzle, 1000 psi backing pressure, and -160º C reservoir temperature. The lineouts in Fig. 5.3(b) taken 70, 100, and 200 μm above the nozzle show a near-Gaussian radial density profile. The peak molecule density 70 μm above the nozzle is $9 \times 10^{20} cm^{-3}$ which, when fully ionized, gives a peak plasma density of $1.8 \times 10^{21} cm^{-3}$ or $1.03 * N_{crit}$ for $\lambda = 800\, nm$. Figure 5.3(c) shows the exponential decay of the peak gas density as a function of height above the 100 μm needle nozzle for a series of backing pressures. The decay length is approximately 67 μm independent of the valve backing pressure. The exponential decay of the peak density is driven by the gas expansion, and the profile FWHM increases linearly as a function of height above the nozzle, as shown in Fig. 5.3(d).

To minimize gas loading of the experimental chamber, the solenoid valve should have a fast rise time, reaching a stable output with minimal background gas

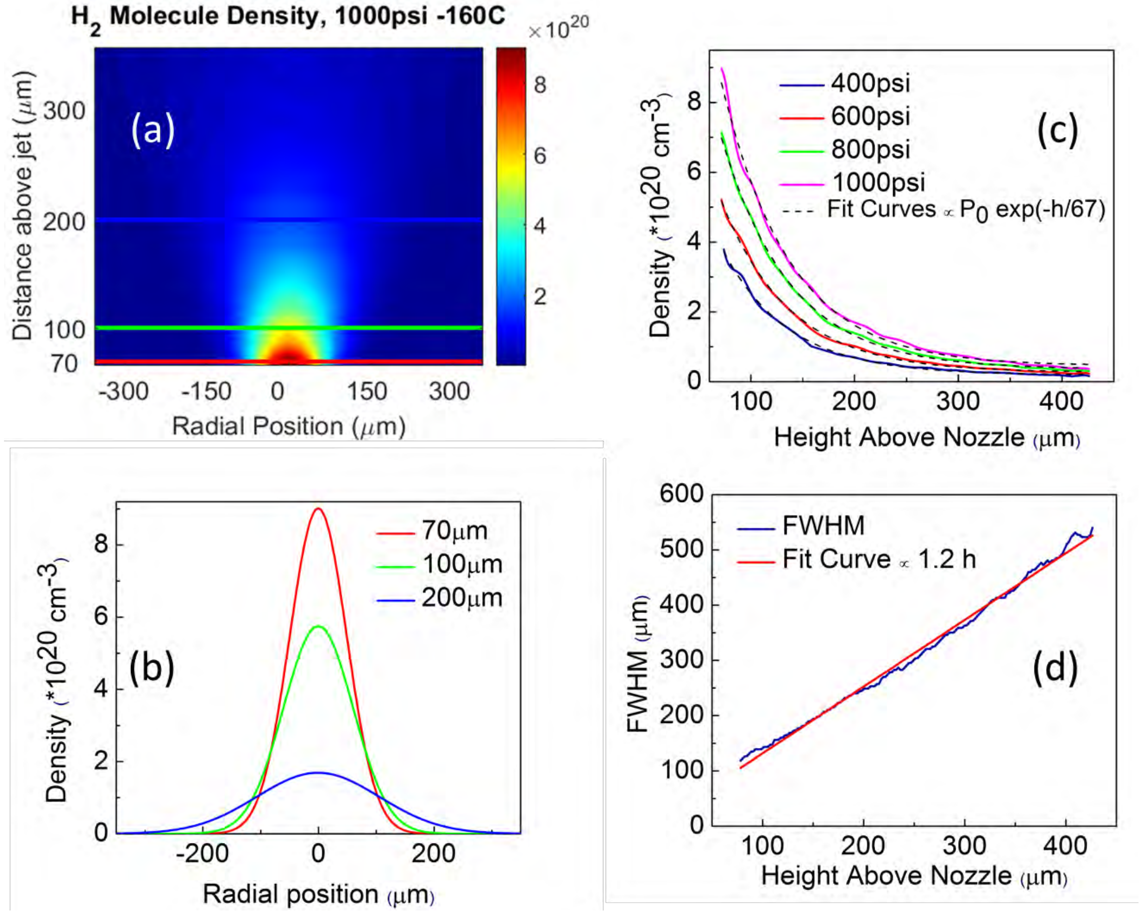

Figure 5.3. Sample 2D hydrogen molecule density profile (a) with 1000 psi backing pressure and -160° C reservoir temperature and lineouts 70, 100, and 200 μm above the nozzle (b). The peak density as a function of height decays exponentially (c) and the FWHM increases linearly with height above the jet (d).

filling the experimental chamber. Figure 5.4 shows the measured temporal evolution of the nitrogen gas output from a 100 μm needle nozzle with the jet reservoir held at 800 psi and -110º C for three different values of the valve opening time. Each point in Fig. 5.4 represents the maximum measured gas density at 200 μm above the needle nozzle. The 10%-90% rise time of the gas density is approximately 400 μs after which the measured output stabilizes for all three open times. The rise and fall times, measured as the time required for the gas density to go from 10%-90% of the peak value and vice versa, were found to be relatively independent of pressure,

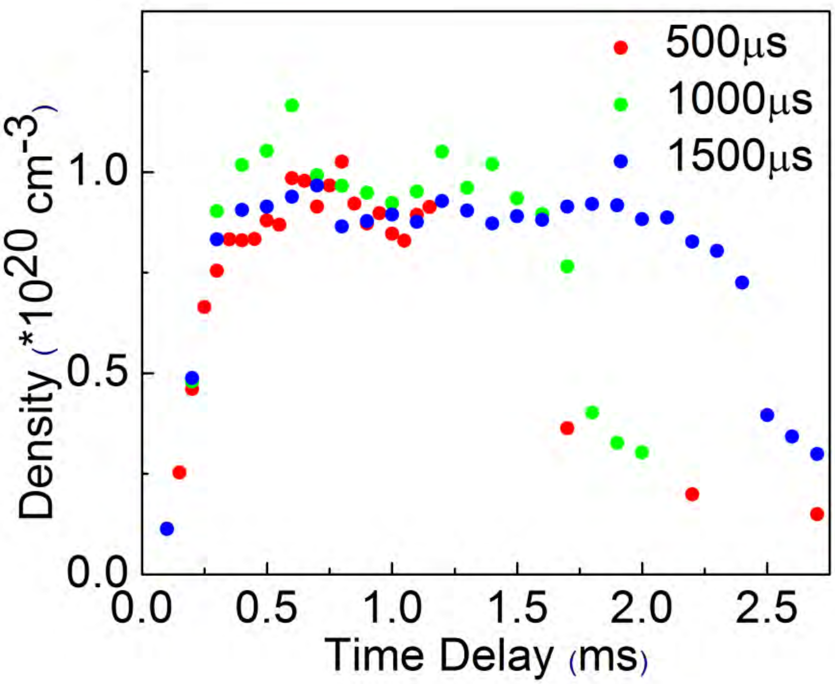

Figure 5.4. Nitrogen molecule density versus time delay at 200 μm above the 100 μm needle nozzle with the jet reservoir held at 800 psi and -110° C for 500 μs, 1000 μs, and 1500 μs open times.

temperature, and gas species, and a valve time of 700 μs was used for all of the results in this chapter unless otherwise specified.

The isentropic flow model discussed in section 5.3 predicts a linear dependence of the gas output density on backing pressure and an inverse dependence on the reservoir temperature. Figure 5.5(a) shows the peak density 200 μm above the 100 μm diameter needle nozzle as a function of backing pressure with a fixed temperature of -160º C. In agreement with the isentropic flow model, the measured density varies linearly with pressure. Figure 5.5(b) shows the dependence of the peak gas density at the same location for a fixed pressure of 1000 psi as a function of temperature. The peak density at -160º C is enhanced by a factor of ~2.4 compared to the peak density at room temperature, highlighting the effectiveness of cryogenic

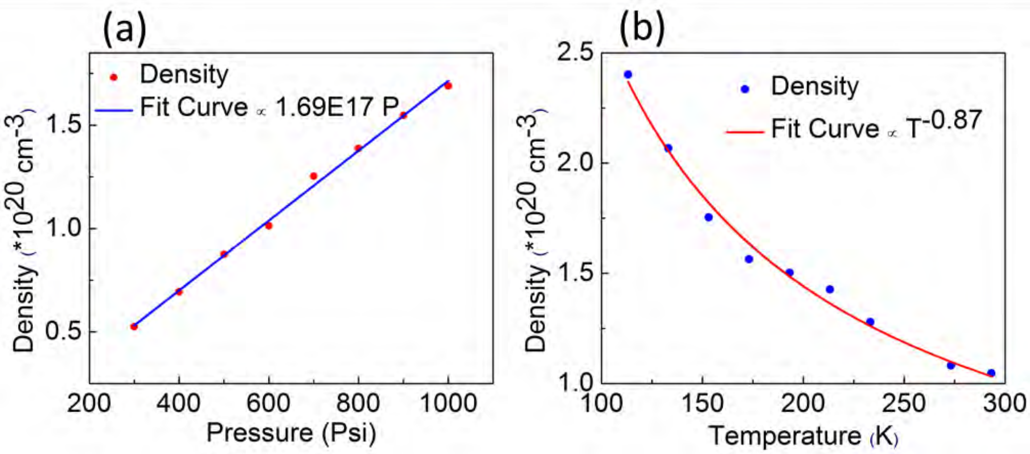

Figure 5.5. Peak jet density 200 μm above the 100 μm needle nozzle as a function of valve backing pressure at a fixed reservoir temperature -160º C (113 K) (a) and as a function of reservoir temperature at a fixed backing pressure 1000psi (b).

cooling for increasing gas jet density output. The measured density as a function of temperature is roughly proportional to ${T_0}^{-0.87}$. Departure from the $1/T_0$ dependence is possibly caused by viscous effects in the flow as the dynamic fluid viscosity, μ, is a function of the fluid temperature [208].

Finally, the density was measured for a series of nozzles with throat diameters of 50, 100, and 150 μm in both straight and tapered geometries. Viscous forces in the flow reduce the flow rate and thus the peak density at the nozzle exit for smaller diameter nozzles, consistent with the increased fraction of boundary layer flow discussed in section 5.3. Figure 5.6 shows the output density as a function of height for a fixed reservoir temperature and pressure of -160º C and 1000 psi for five nozzle designs. The density is almost equal for the same throat diameter in the tapered and straight nozzle geometry. However, the total output in both cases increases rapidly with increasing nozzle diameter.

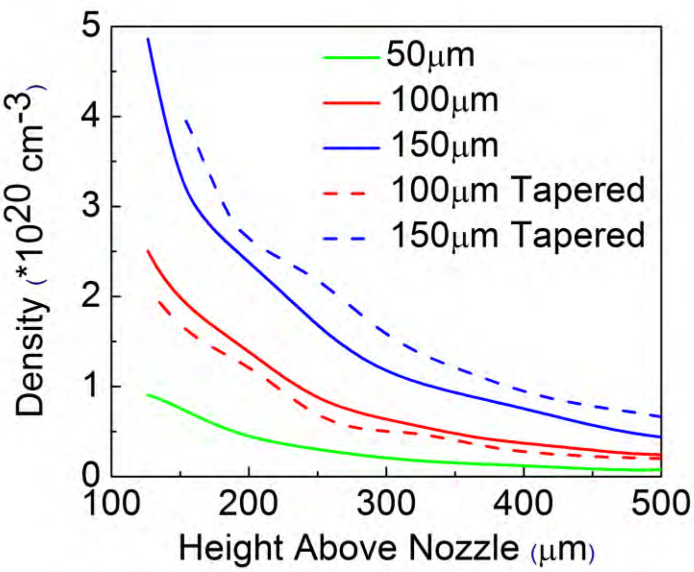

Figure 5.6. Density as a function of height above the needle (solid) and tapered (dashed) nozzles with 50 (green), 100 (red), and 150 (blue) μm throat all at -160º C and 1000 psi .

5.6 Cluster size and density characterization

5.6.1 Cluster formation in high pressure gas jets

In many experiments involving high pressure gas jets clustering of molecules can play an important role. Collisional ionization within the solid density clusters can greatly enhance ionization and increase laser-plasma coupling [149,214]. The laser cluster interaction has been demonstrated as a source of fast ions [191,215], electrons [216,217], x-rays [214,218], and even neutrons [195,219]. Ballistic cluster flows can also be used to make shaped plasma density profiles using obstructions smaller than the cluster mean free path [152].

The size and density of clusters formed in expanding gas jets has been empirically characterized by Hagena [153,220,221], who introduced the scaling parameter

$$\Gamma^* = \frac{kd^{0.85}P_0}{T_0^{2.29}}. \tag{5.6}$$

Here k is a gas dependent constant, d is the jet orifice diameter in μm, P_0 is the backing pressure in mbar, and T_0 is the jet stagnation temperature in Kelvin [220]. The value of k varies widely for different gases generally with larger values for more polarizable species. For example, $k = 1650$ for argon and $k = 180$ for hydrogen, while for helium $k = 3.85$ and there is negligible clustering [153,220].

Clustering starts to be observed for Γ^* in the range of $200 - 1000$ [221]. The average number of molecules in a cluster as a function of Γ^* was empirically characterized in the range $10^2 < \Gamma^* < 10^6$ and scales as $\langle n_c \rangle = 33\left(\frac{\Gamma^*}{1000}\right)^{2.35}$ [221–223]. The dependence of $\langle n_c \rangle$ on $\Gamma^{*2.35}$ shows that larger clusters nucleate at higher pressures and lower reservoir temperatures and from nozzles with larger diameters ($\langle n_c \rangle \propto \Gamma^{*2.35} \propto P_0^{2.35} T_0^{-5.38} d^{2.00}$).

5.6.2 Rayleigh scattering-based cluster measurement

The mean size and density of clusters in the high density gas jet can be estimated through an all optical technique combining transverse interferometry and collection of Rayleigh scattered light from the clusters. The technique, first demonstrated by Kim et al. [224], assumes complete clustering within the jet. The Rayleigh scattered energy into a collection lens by a laser propagating from point x to $x + \Delta x$ through a cluster jet is given by $\Delta E_{lens}(x) \approx E_{in} \bar{\sigma}_{lens}(x) N_c(x) \Delta x$ where E_{in} is the incident laser energy on the scattering volume, $\bar{\sigma}_{lens}$ is the cross section for scattering into the lens averaged over the cluster size distribution, and N_c is the average cluster density. For 90° scattering and cluster sizes much less than the laser wavelength $\sigma_{lens} = \pi k^4 |\gamma| (\alpha^2 - \alpha^4/4)$ where $k = 2\pi/\lambda$ is the laser wavenumber, $\gamma = a^3(\varepsilon - 1)(\varepsilon + 2)^{-1}$ is the cluster polarizability assuming a spherical cluster of radius a and dielectric constant ε, and α is the collection half angle of the imaging lens. Using this cross section in the equation for the scattered energy gives

$$\overline{a^6}\, N_c = \frac{1}{\pi k^4} \left| \frac{\varepsilon + 2}{\varepsilon - 1} \right|^2 \frac{\Delta E_{lens}}{E_{in} \Delta x} \left(\frac{1}{\alpha^2 - \alpha^4/4} \right) \tag{5.3}$$

where $\overline{a^6}$ is the average, over the cluster size distribution, of a^6. Transverse interferometry allows measurements of the real part of the refractive index $n_r(x) = 1 + 2\pi N_c \gamma_r$ where $\gamma_r = Re(\gamma)$. Rearranging gives

$$\overline{a^3}\, N_c = \frac{n_r(x) - 1}{2\pi} \left(\frac{\varepsilon + 2}{\varepsilon - 1} \right) \tag{5.4}$$

Combine equations (5.7) and (5.8) yields an effective cluster radius $a_{eff} \equiv \left(\overline{a^6}/\overline{a^3}\right)^{1/3}$ and number density $N_{c,eff} \equiv \overline{a^3} N_c / a_{eff}^3$ [211].

The above model, which assumes complete clustering, requires consideration of the effect of a non-zero monomer concentration on extracted measurements of a_{eff} and $N_{c,eff}$. If the jet contains a monomer fraction $\delta_m = N_m/(N_m + N_C \overline{n_c})$ where N_m is the monomer density and $\overline{n_c}$ is the number of atoms within the cluster averaged over the cluster size distribution within the jet, then the assumption of complete clustering causes an underestimation of a_{eff} by a factor $(1 - \delta_m)^{-1/3}$. The underestimation arises from the additional contribution of the monomers to the measured phase shift while contributing negligibly to the Rayleigh scattered signal. The cube root dependence greatly damps the effect of the uncertainty in δ_m since even an assumption of 95% monomers only increases the calculated a_{eff} by a factor of 2.7. Further, the effect of the cluster size distribution on a_{eff} can be calculated by comparing $a_{eff} \equiv \left(\overline{a^6}/\overline{a^3}\right)^{1/3}$ to $\bar{a}$ for various cluster size distributions, $f(a)$, where $\overline{a^n} = \int_0^\infty a^n f(n_c) dn_c$ and $a = r_{WS} n_c^{1/3}$ with r_{WS} the intra-cluster Wigner-Seitz radius. Using a log normal distribution for the number of molecules per cluster, we find that this method will tend to overestimate the cluster size. However, if the distribution is sufficiently narrow that the variance is within 40% of the mean, then the retrieved cluster size, a_{eff}, will be correct to within a factor of 2.

Rayleigh scattering is collected from the cluster jet by focusing a 25 mJ, ~10 ns cavity dumped beam from our Ti:Sapphire system into the thin jet at f/9.5. A calibrated imaging system collects the scattered signal in a plane perpendicular to the pump polarization and images the signal onto a CCD camera. The experimental setup and a raw image of the Rayleigh scattered light are shown in Fig. 5.2. The same transverse interferometry diagnostic described in section 5.2 was used to measure the clustered gas refractive index.

The hydrogen cluster size and density is found to vary as a function of the beam height above the nozzle orifice. Near the orifice, where the hydrogen molecule density is highest, no Rayleigh scattering was detected. A stronger Rayleigh scatter signal was observed farther from the nozzle, consistent with cooling-induced clustering as the gas expands into vacuum. Figure 5.7 shows the cluster size and density as a function of radial position at various heights above the 150 μm diameter tapered nozzle with a jet backing pressure of 1000 psi and reservoir temperature -160° C. The minimum average cluster radius measured for any conditions was

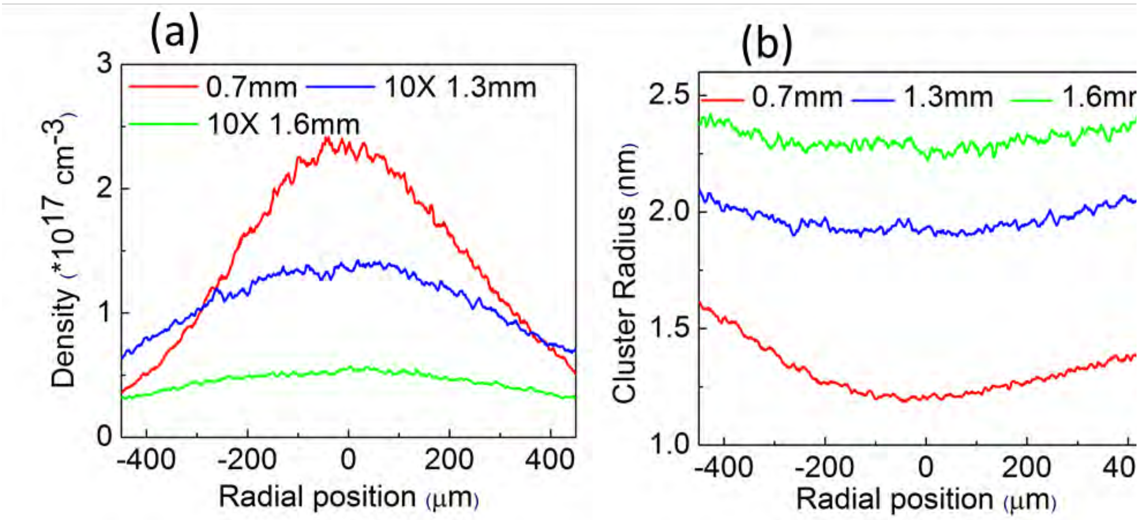

Figure 5.7. Average cluster density (a) and average cluster size (b) as a function of radial position at various heights above the 150 μm diameter nozzle orifice at jet backing pressure and temperature 1000 psi and -160° C.

approximately 0.5 nm limited by the photon collection efficiency of the Rayleigh scatter imaging system.

At positions greater than approximately 500 μm above the jet the cluster size is measurable and the dependence of clustering on jet backing pressure and reservoir temperature can be determined. The left panel of Fig.5.8 shows the nonlinear dependence of the spatially integrated Rayleigh scatter signal on jet backing pressure at a height ~1 mm above the 150 μm nozzle when the jet reservoir temperature is held at -160° C. The right panel of Fig. 5.8 shows the cluster size (dotted line) and density (solid line) at the same position as a function of backing pressure. The effective cluster radius dropped rapidly as the valve temperature was increased. The average cluster radius measured 1 mm above the 150 μm needle nozzle with 1050 psi backing pressure and -160° C was 1.8 nm. When the temperature was raised to -140° C the cluster radius dropped to 0.5 nm for the same backing pressure. Above -140° C the cluster size was too small to be measured by the Rayleigh scatter diagnostic.

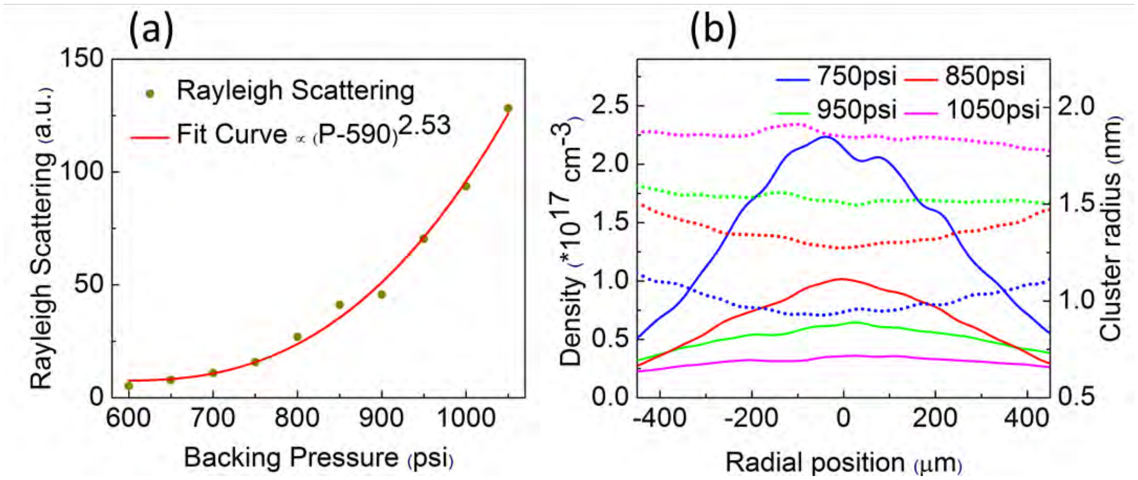

Figure 5.8. Rayleigh scatter signal versus backing pressure (a) and cluster density (solid line) and size (dotted line) at a height ~1 mm above the 150 μm nozzle (b) with the jet reservoir held at -160° C.

5.7 Conclusion

The development of thin, high density gas jet targets for near critical laser-plasma interaction experiments with Ti:Sapphire laser systems has thus far been limited to a few, rather complicated, efforts. In this chapter a jet design based on a cryogenically cooled pulsed solenoid valve with needle and tapered nozzles was described. The jet was shown to be capable of reaching hydrogen molecule densities as high as $9 \times 10^{20} cm^{-3}$ in a ~200 μm FWHM Gaussian density profile when the jet was backed with 1000 psi and cooled to -160° C. When fully ionized, this brings the peak plasma density above the (non-relativistic) critical density for Ti:Sapphire lasers, making this jet an interesting target for electron and ion acceleration experiments, as exemplified by the electron acceleration experiments performed using this jet presented in the next chapter.

Estimates of the output density scaling with the valve backing pressure and reservoir temperature were made by modelling the gas flow through the nozzle as steady and isentropic. Reaching the highest density output possible was found to require a sonic nozzle design with the output molecule density directly proportional to the molecule density within the valve reservoir. Through the equation of state this means the gas density at the nozzle exit scales as T_0^{-1} so that cryogenic cooling of the jet reservoir serves to increase the valve output density. Rayleigh scatter measurements showed that clustering of the high density gas occurs only ~500 μm and farther above the nozzle. Effective cluster radii ~1 nm were measured approximately 1 mm above the nozzle for the highest backing pressures and coldest reservoir temperatures. The cluster size measurements show that clustering is negligible in experiments operating near the nozzle exit plane where the gas density is highest.

Chapter 6: Multi-MeV electron acceleration by sub-terawatt laser pulses in high density plasma

6.1 Introduction

Laser-driven electron acceleration in plasmas has achieved many successes in recent years, including record acceleration up to 4 GeV in a low emittance quasi-monoenergetic bunch [31] and generation of high energy photons [38,41,225–227]. In these experiments, the driver laser pulse typically propagates in the 'bubble' or 'blow-out' regime [80,228] for a normalized peak vector potential $a_0 = eA_0/mc^2 \gg 1$. Plasma densities are deliberately kept low for resonant laser excitation and to avoid dephasing [80]. Essentially all of these experiments use 10 TW −1 PW laser drivers, with repetition rates ranging from 10 Hz to one shot per hour [229]. Even the electron acceleration experiments described in Chapter 3, where ionization injection and plasma channel guiding were leveraged to reduce the laser energy threshold for electron beam production, required multi-terawatt drive laser pulses to generate relativistic electron beams.

For many modest lab scale and portable applications, however, a compact, relatively inexpensive, high average current source of laser-accelerated relativistic electrons is sufficient and desirable. This chapter describes and experiment using the very dense and thin hydrogen gas jet characterized in Chapter 5, where the relativistic self-focusing threshold is exceeded even with ~10 mJ laser pulses and MeV-scale energy electron bunches are generated. This enables applications, such as ultrafast low dose medical radiography, which would benefit from a truly portable source of relativistic charged particle beams. The electron beams generated from interaction with the high density are also an interesting seed source for injection into secondary acceleration stages, such as the QPM-DLA scheme described in Chapter 4. Prior work has shown electron bunch generation of modest charge and acceleration (~10 fC/pulse, <150 keV) from a 1 kHz, ~10 mJ laser driving a thin (~100 μm), low density continuous flow argon or helium jet [230].

6.2 Experimental setup

Central to our experiment is the thin, high density pulsed hydrogen sonic gas jet described in Chapter 5, which reaches a maximum peak molecular density of 9×10^{20} cm^{-3}, and when fully ionized can exceed the plasma critical density, $N_{cr}=1.7\times10^{21}$ cm^{-3} at our laser wavelength of λ_0=800nm. The density profile is near-Gaussian, with a full width at half maximum (FWHM) in the range 150-250 μm, depending on the height of the optical axis above the jet orifice. Earlier versions of this jet were run in both pulsed [75] and continuous flow [231] for nitrogen and argon. High densities are achieved using a combination of high valve backing pressure and cryogenic cooling of the valve feed gas, which is forced through a 100μm diameter needle orifice. Cooling to −160º C enables a significant density increase for a given valve backing pressure.

Figure 6.1 shows the experimental setup. Pulses from a Ti:Sapphire laser (50 fs, 10-50 mJ) are focused into the gas jet (Fig 1a) at f/9.5 by a 15° off-axis parabolic mirror. Figure 6.1(b) shows neutral hydrogen profiles measured by interferometry. The wave front sensor and deformable mirror described in Chapter 2 are used to

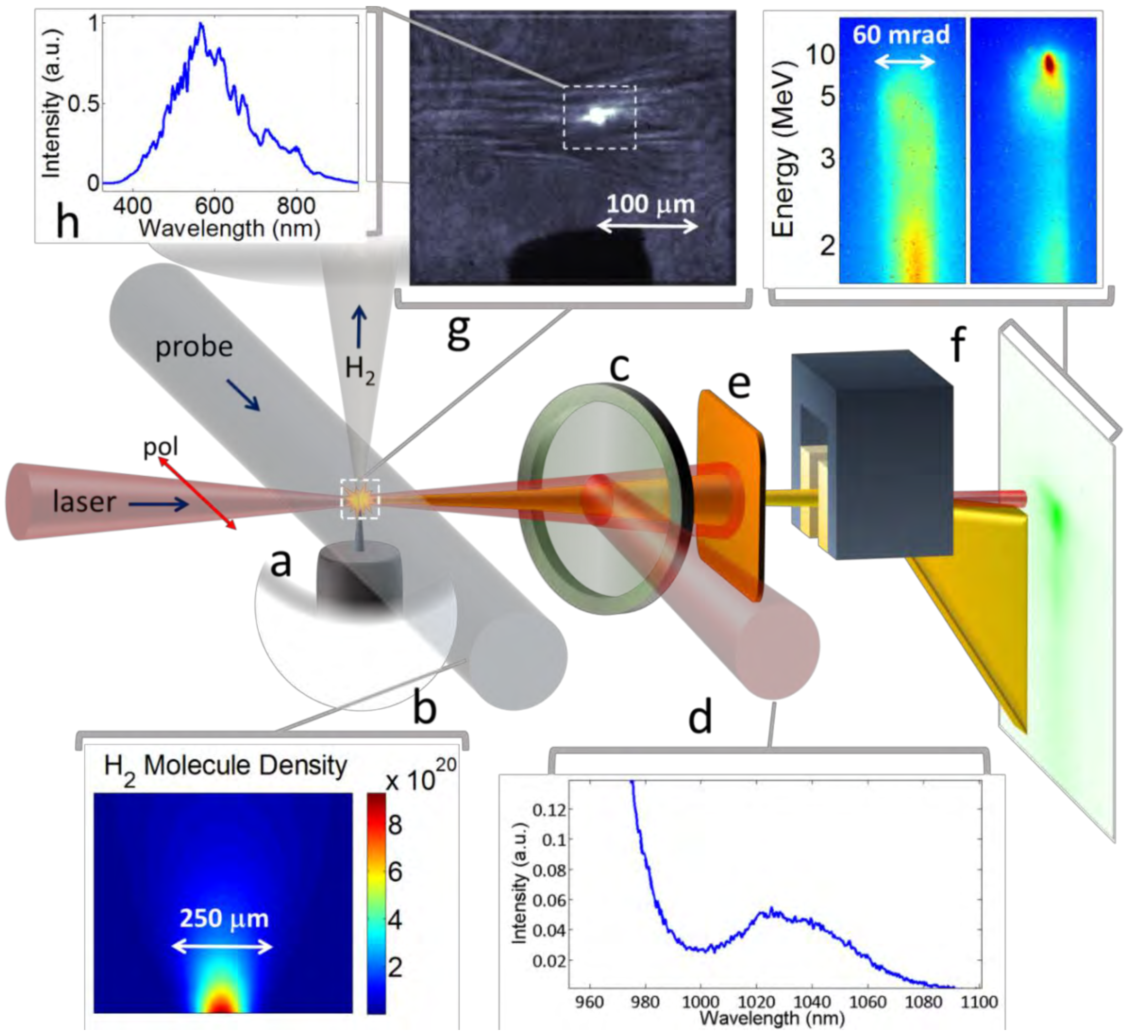

Figure 6.1. Experimental setup. A horizontally polarized Ti:Sapphire laser pulse (10-50 mJ, 50 fs, λ=800 nm) interacts with a cryogenically-cooled, dense thin H2 gas jet (a), whose neutral and plasma density profiles are measured by 400 nm probe interferometry (b). A portion of the transmitted laser pulse is reflected by a pellicle (c) and measured by a spectrometer (d). The electron beam from the jet is apertured by a 1.7mm horizontal slit (e), enters a 0.13 T permanent magnet spectrometer, and is dispersed on an aluminum foil-shielded LANEX screen (f), which is imaged by a low noise CCD camera (not shown). (f) shows example quasi-monoenergetic and exponential spectra for a 40 mJ pulse at Ne=2×1020 cm-3. Shadowgraphic imaging of the laser interaction region above the needle orifice (g) (needle seen as a shadow at bottom) and imaging (g) and spectroscopy (h) of the wave breaking flash. The pump polarization could also be rotated to the vertical by a half wave plate.

optimize the vacuum focal spot to w_{FWHM} =8.4 μm (1.2× the diffraction limit) containing 80% of the pulse energy, with a confocal parameter of 550 μm. For maximizing electron beam charge and energy, it was found that placing the focused beam waist at the center of the gas jet was optimal, without strong sensitivity to positioning. This is consistent with the laser confocal parameter being more than twice the jet width. We note that recent laser interaction experiments at near critical density [232,233] have used a complex pressure-boosted millimetre-scale gas jet [197].

The neutral jet density and plasma profiles were measured using a 400nm, 70fs probe pulse (Fig. 6.1(b), derived from the main pulse), which was directed perpendicularly through the gas jet to a folded wave front interferometer. Forward- and side-directed optical spectra were collected by fibre-coupled spectrometers, with the forward spectra directed out of the path of the pump laser and electron beam by a pellicle (Fig. 6.1(c)). Shadowgraphic images using the 400 nm probe and images of bright broadband wave breaking radiation flashes were collected using achromatic optics.

Relativistic electron spectra in the energy range 2−15 MeV were measured using a 0.13 T permanent magnet spectrometer 25 cm downstream of the gas jet (Fig. 6.1(f)). A copper plate with a 1.7 mm × 12 mm slit aperture in front of the magnet entrance (Fig. 6.1(e)) provided energy resolution while allowing measurement of beam divergence in 1D. Electron spectra were dispersed along a LANEX scintillating screen, shielded against exposure to the laser by 100 μm thick aluminum foil, and imaged using a low noise CCD camera. Full electron beam profiles were collected by the LANEX screen by translating the dispersing magnets and slit aperture out of the way. Estimates of the accelerated charge were made by calibrating the imaging system and using published LANEX conversion efficiencies [161,162].

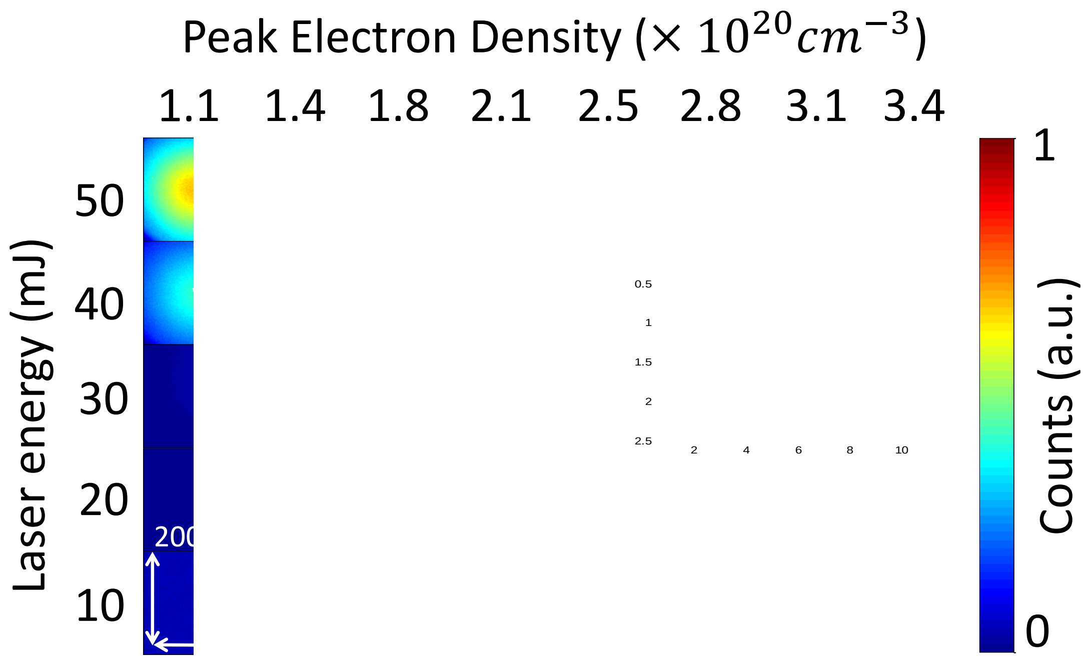

Figure 6.2. Single shot electron beam images for energies > 1 MeV for a range of laser energies and peak profile electron densities. The colour palette was scaled up by 10× for the 10 mJ column. The onset laser power for detectable electron beam generation was ~3Pcr across our range of conditions.

6.3 Electron acceleration

The high density of our target has the immediate effect of enabling relativistic self-focusing of low energy laser pulses and generation of a nonlinear plasma wake. Furthermore, the reduced laser group velocity (and therefore plasma wave phase velocity) at high density drops the threshold for electron injection. Figure 6.2 shows > 1 MeV electron beam generation for pulse energies in the range 10-50 mJ, or 0.2–1.0 TW, as a function of peak plasma density. Beam divergence is $\lesssim$ 200 mrad. The results are consistent with the inverse density scaling of the relativistic self-focusing critical power, $P_{cr} = 17.4(N_{cr}/N_e)$ GW [234,235], and the laser power threshold for appearance of a relativistic electron beam is $\sim 3P_{cr}$ across our range of conditions.

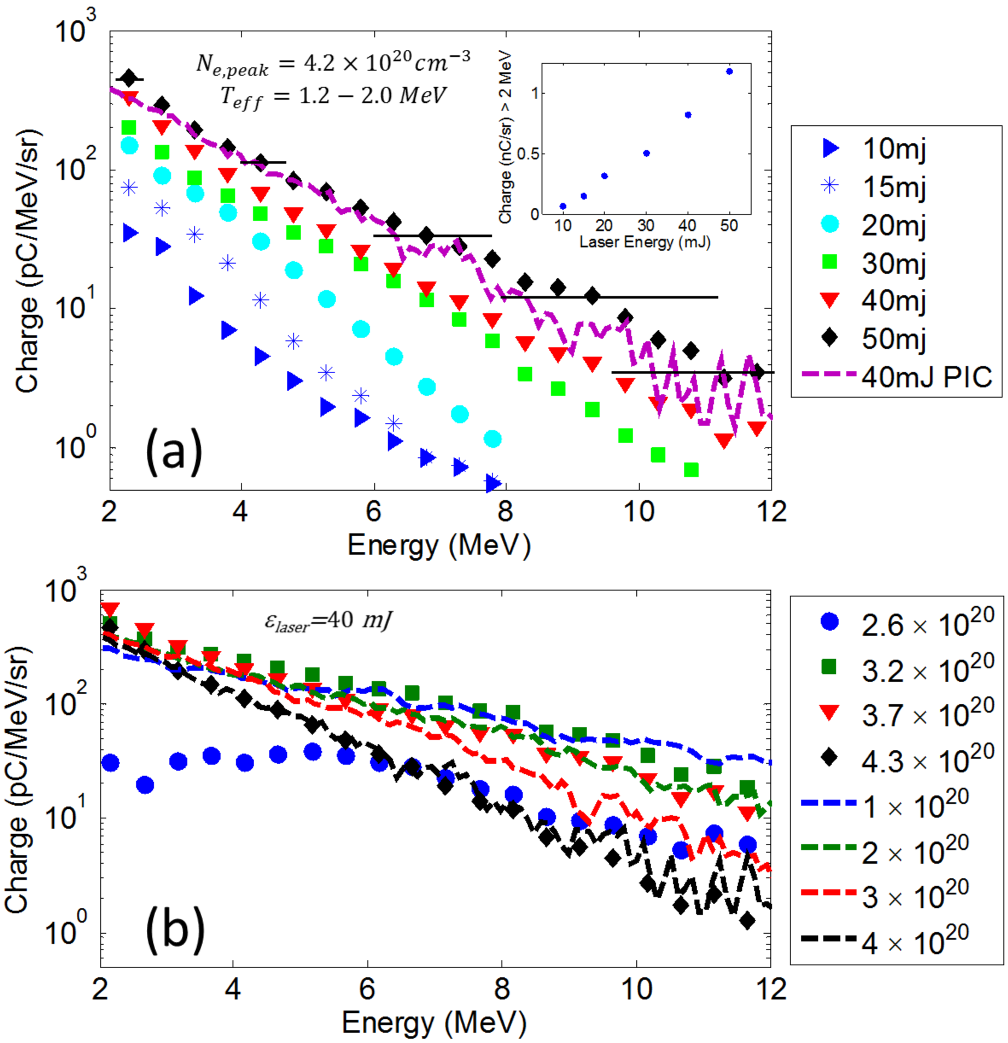

Figure 6.3. **(a)** Accelerated electron spectra for peak jet electron density 4.2×10^{20} cm^{-3} for varying laser energy. The inset shows total charge >2 MeV as a function of laser energy. The range of effective temperatures of these exponential-like distributions is indicated. The horizontal black lines indicate the experimental uncertainty in the energy, determined by geometry-limited spectrometer resolution. The dashed curve is a 3D PIC simulation for 40 mJ pump which has been scaled by a factor 0.14 to line up with the experimental curve for 40 mJ. **(b)** Accelerated electron spectra at laser energy 40 mJ for varying peak electron density. The dashed curves are from 3D PIC simulations and were scaled by the factor 0.14.

Electron energy spectra in the range 2−12 MeV are shown in Fig 6.3(a) for laser pulse energy 10-50 mJ and peak electron density N_e=4.2×10^{20} cm^{-3}, with the inset showing total accelerated charge > 2 MeV up to ~1.2 nC/sr for 50 mJ laser pulses. An electron spectrum simulated from a TurboWAVE 3D particle in cell (PIC) simulation [163] for the 40 mJ case is overlaid on the plot. Electron spectra as a function of peak density for fixed pulse energy of 40 mJ are shown in Fig. 6.3(b) along with results from the 3D PIC simulations. We note that for approximately 20% of shots near the self-focusing onset at each pressure, we observed quasi-monoenergetic peaks ranging from 3 MeV (~25 fC for 10 mJ) to 10 MeV (~1.4 pC for 50 mJ, see Fig. 6.1(f) with ~10 mrad beam divergence. Both the spectra and the beam spot positions are highly variable and are the subject of ongoing work.

Another consequence of the high density gas target interaction is that the pump pulse envelope is multiple plasma periods long. Over our experimental density range of $N_e = 1 - 4\times10^{20}$ cm^{-3}, the plasma period is $2\pi/\omega_0$~ 11fs–5.7 fs, placing our 50 fs pump pulse in the self-modulated laser wakefield acceleration (SM-LWFA) regime. Evidence of SM-LWFA is seen in the moderately collimated electron beams of Fig. 6.2 and the exponential electron spectra of Fig. 6.3, reflecting acceleration from strongly curved plasma wave buckets and electron injection into a range of accelerating phases. This is consistent with prior SM-LWFA experiments [24,56,236], except that here our dense hydrogen jet enables production of MeV spectra with laser pulses well below 1 TW. Further confirmation of self-modulation is seen in the spectrum of Raman forward scattered Stokes radiation shown in Fig. 6.1(d), for the case of laser energy 50 mJ (vacuum $a_0 \sim 0.8$) and peak density N_e =1.8×10^{20} cm^{-3}. The strong broadband red-shifted Raman peak located at $\lambda_s = 2\pi c/\omega_s$ ~ 1030 nm enables the estimate of self-focused a_{sf} ~ 2.7, using the measured electron density profile and $\omega_s = \omega - \omega_p/\sqrt{\gamma}$, where ω is the laser frequency and $\gamma = \left(1 + a_{sf}^2/2\right)^{1/2}$ is the relativistic factor. This estimate is in good agreement with the peak a_{sf} in our 3D PIC simulations.

6.4 Wave breaking radiation

In order for electrons to be accelerated, they must first be injected into the wakefield. Our 3D simulations show transverse wave breaking [65] of the strongly curved plasma wave fronts [237] behind the laser pulse, which injects electrons from a wide spread of initial trajectories into a range of phases of the plasma wave. Wave breaking is accompanied by a broadband radiation flash emitted by electrons accelerated from rest to near the speed of light in a small fraction of a plasma wavelength. Figure 6.1(g) shows a magnified single shot image of the sideways-collected flash superimposed on a shadowgram image of the relativistically self-focused filament. Figure 6.4 shows 10-shot average images of the flash for varying plasma peak density and laser energy collected along the pump polarization direction. Such radiation has been observed in prior work, although at a much lower energy and yield (~0.1 nJ for a 500 mJ pump pulse) [238]. Here, neutral density filters were employed to prevent the side-imaged flash intensity from saturating our CCD. We measure flash energies of ~15 μJ into f/2.6 collection optics for the 40 mJ, N_e $=3.4\times10^{20}$ cm^{-3} panel in Fig. 6.4, giving ~1.5 mJ or >3% of the laser energy if the emission is into 4π sr.

The axial location, total energy, and spectrum of the horizontally polarized component of the flash are independent of pump polarization, so the flashes do not originate from pump scattering. When the flash is collected perpendicular to the

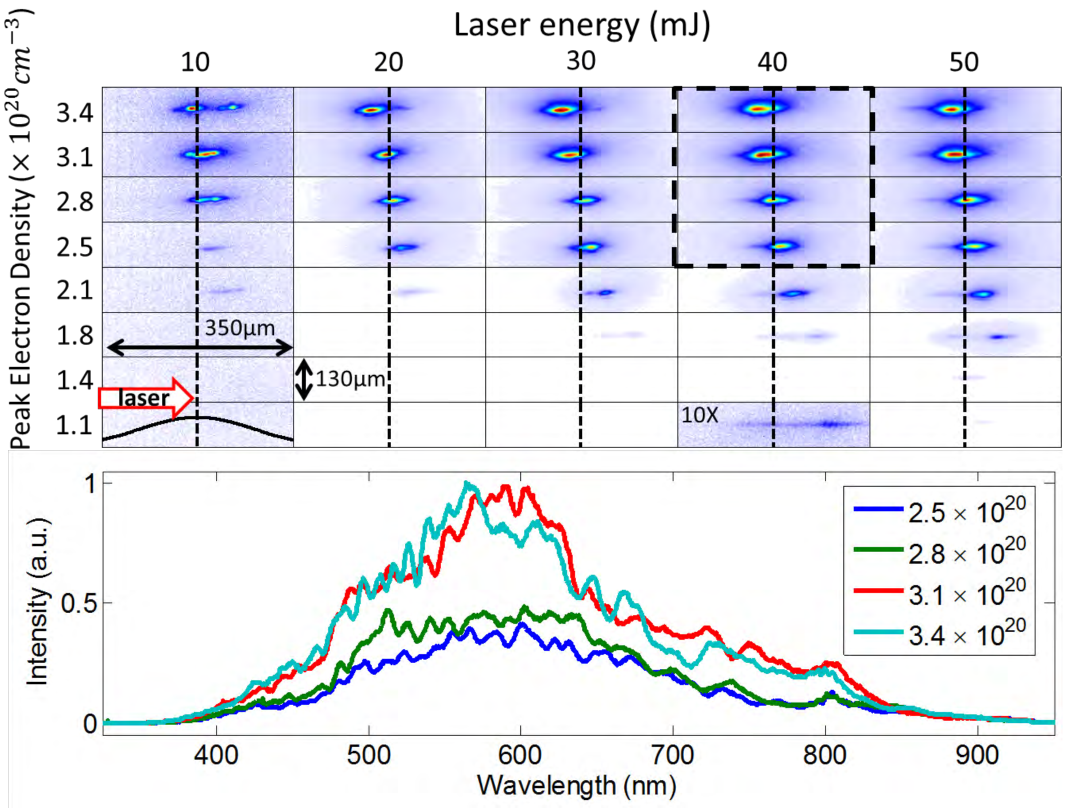

Figure 6.4. Top panel: Side images of intense radiation flashes from wave breaking (10 shot averages). The horizontally polarized pump laser pulse propagates left to right. Image intensities are normalized to the maximum intensity within each column. The vertical dashed line is the centre of the gas jet, whose profile is shown in the lower left. The 40 mJ, 1.1×1020cm−3 image for vertical pump polarization (enhanced 10×), is dominated by 800 nm Thomson scattering on the left and the flash on the right. Bottom panel: Spectra (10 shot averages) of the flash for conditions enclosed by the dashed black box in the top panel.

pump polarization, the vertically polarized component has a small contribution at 800nm, attributed to Thomson scattering, on top of the broadband flash spectrum. Broadband flash spectra (10 shot averages, with no filtering of the pump), peaking at λ_{rad}~550-600nm with bandwidth ~400nm, are shown at the bottom of Fig. 6.4 for pump energy 40 mJ and a range of densities. The figure panels show that the flash occurs on the hydrogen density profile up-ramp for higher densities and laser energies and on the down-ramp for lower densities and laser energies, as also borne out by our

3D simulations. This is explained by the earlier onset of relativistic self-focusing for higher density or laser energy, which is followed closely by self-modulation and wave breaking.

The huge increase in radiation flash energy compared to earlier experiments [238] stems from its coherent emission by electron bunches wave breaking over a spatial scale much smaller than the radiation wavelength and the consequent damping of these bunches by this radiation. As a rough estimate of this effect using 1D approximations, the near-wave breaking crest width Δx_{crest} of the nonlinear plasma wave is given by $\Delta x_{crest}/\lambda_p \sim \frac{1}{\pi}\left(\omega/\omega_p\right)^{3/4}(\Delta p_0/2mc)^{3/4}$ [239], where Δp_0 is the electron initial momentum spread. For N_e=3×10^{20} cm^{-3} and $\Delta p_0/mc \sim 0.06$ (from an initial spread ~ $(\Delta p_0)^2/2m$ < 1 keV from residual electron heating after ionization [240]) we get $\Delta x_{crest}/\lambda_p \sim 0.04$, or $\Delta x_{crest} \sim 0.12\lambda_{rad}$, significantly shorter than the peak radiated wavelength, ensuring coherent emission. The wave breaking electrons radiate as they execute curved orbits into the wake bucket just ahead of the crest, with emission power $P \sim n^2\left(\frac{2e^2}{3m^2c^3}\gamma^2\left|\frac{d\boldsymbol{p}}{dt}\right|^2\right)$ [241] and total radiated energy $\epsilon_{rad} \sim P\Delta t \sim P\Delta x_{crest}\,\gamma^{-1}/c$, where n is the number of accelerating electrons from the crest, $d\boldsymbol{p}/dt$ is the force on an electron, and Δt is the sub-femtosecond time for acceleration off the crest (accounting for Lorentz contraction), or equivalently, the crest lifetime. Taking $n \sim N_e\lambda_p^3$, $\gamma = \gamma_p = \omega/\omega_p$, and $|d\boldsymbol{p}/dt| \sim eE_{wb}$, where $E_{wb} = \sqrt{2}\left(m\omega_p c/e\right)\left(\gamma_p - 1\right)^{1/2}$ is the 1D wave breaking field [65], gives a total radiated energy of $\epsilon_{rad} \sim 2$ mJ, which is of the correct order of magnitude.

The strong curving of injected electron orbits by the ion column allows an estimate of the flash spectrum range using the synchrotron radiation critical frequency $\omega_{rad} \sim \omega_c \sim 3c\gamma^3/2\rho$ [241], where ρ is the orbit radius of curvature, which we take as $\rho \sim \lambda_p$, assuming trapping within a single plasma wave bucket. This gives $\lambda_c \sim 4\pi/3\,(N_e/N_{cr})\lambda_0 \sim 400 - 700\,nm$ for the density range shown in Fig. 6.4, reasonably overlapping the measured spectra. The synchrotron spectrum bandwidth is estimated as $(\Delta\lambda/\lambda)_{rad} \sim (\omega_{rad}\Delta t)^{-1} \sim 1$, in accord with the ~1 fs bandwidth in Fig. 6.4 characteristic of half-cycle optical emission, which is consistent with the violent unidirectional electron acceleration upon wave breaking. We note that half-cycle wave breaking radiation at high γ has been proposed as an attosecond x-ray source [242].

To probe its temporal duration and coherence, the flash was interfered in the frequency domain with a supercontinuum pulse, well-characterized in amplitude and phase generated in a Xe gas cell [243,244]. The supercontinuum pulse was compressed in a grism compressor [245], sent through a variable delay line, and directed across the gas jet perpendicular to the pump pulse. The flash and supercontinuum were both collected by an f/4 imaging system and imaged to the entrance slit of an imaging spectrometer at 5X magnification. The entrance slit, oriented perpendicular to the pump laser propagation direction, was used to spatially isolate single flashes. A sample spectral interferogram of the flash and compressed supercontinuum pulse is shown in Fig. 6.5. Fringes across the full supercontinuum bandwidth (~250 nm) were observed with high visibility, suggesting that the flash is coherent across its full bandwidth.

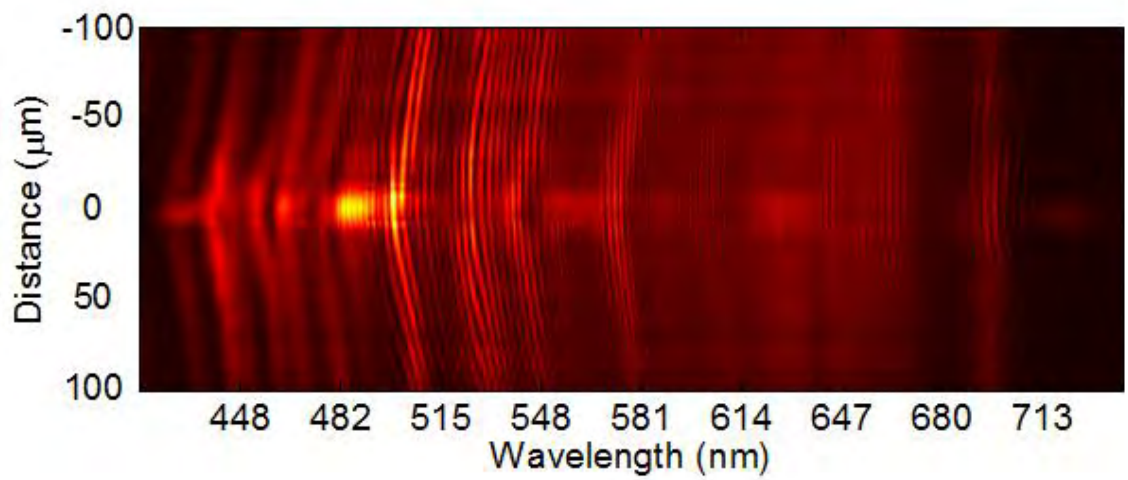

Figure 6.5. A sample spectral interferogram between the broadband wave breaking flash and a compressed supercontinuum pulse generated in a Xe gas cell. Fringes are visible across the full 250 nm supercontinuum bandwidth, showing that the broadband flash is spectrally coherent.

Measurement of the flash spectral phase was performed by chirping the supercontinuum pulse and using the stationary phase point method to determine the relative spectral phase between the flash and supercontinuum pulse [246,247]. In the stationary phase point method, a long, chirped pulse is interfered with a much shorter pulse in an imaging spectrometer, and a null in the total spectral phase occurs at the frequency where the arrival time of the two pulses is equal. The total spectral phase can be constructed by changing the delay of the chirped pulse with respect to the short pulse and recording the position of the null. If the spectral phase of the chirped pulse is already well known, then the spectral phase of the short pulse, in this case the flash, can be reconstructed. The extracted flash spectral phase from this technique was consistent with the flash being a nearly transform-limited pulse of ~1 fs duration. However, the uncertainty in the measurement of the supercontinuum spectral phase precludes a definitive measurement of the flash temporal pulse shape at this time. Definitive measurement of the flash pulse duration is the subject of ongoing research.

6.5 Acceleration mechanism

A question that has arisen in prior experiments and simulations of acceleration at higher plasma densities [27,248,249] is the relative contributions of laser wakefield acceleration (LWFA) and direct laser acceleration (DLA). The contribution of the plasma wave to electron energy gain (in units of mc^2) is $W_z = -\frac{e}{mc^2}\int E_z v_z dt$, where the integral is over the full electron trajectory and E_z and v_z are the longitudinal plasma wakefield and electron velocity. The DLA contribution, $W_\perp = -\frac{e}{mc^2}\int \boldsymbol{E}_\perp \cdot \boldsymbol{v}_\perp dt$, arises as near light-speed electrons, axially co-propagating with the laser field $\boldsymbol{E}_\perp$, oscillate with a $\boldsymbol{v}_\perp$component about the ion column axis at the betatron frequency $\omega_\beta = \omega_p/\sqrt{2\gamma}$ or its harmonics, in resonance with the field [248]. In our experiment, the jet location-dependence of electron injection determines the relative contributions of DLA and LWFA to the net energy gain. Early wave breaking injection on the density profile up-ramp occurs when the plasma wavelength is decreasing and more wake buckets lie under the laser pulse envelope, exposing injected electrons to DLA. On the down-ramp, the plasma wavelength is increasing and fewer buckets lie under the laser field envelope, so that injected electrons are less exposed to the laser field. The flash images of Fig. 6.4 are a map of injection locations through the jet, and therefore they spatially map the relative balance of DLA and LWFA, predicting that DLA dominates at high density /high laser energy and LWFA dominates at low density /low laser energy. This transition from LWFA to DLA is corroborated by 2D PIC simulations. Figure 6.6 shows the contributions for a subset of tracked particles accelerated to energies above 1 MeV. For a fixed peak density $N_e = 0.07N_{cr}$, the

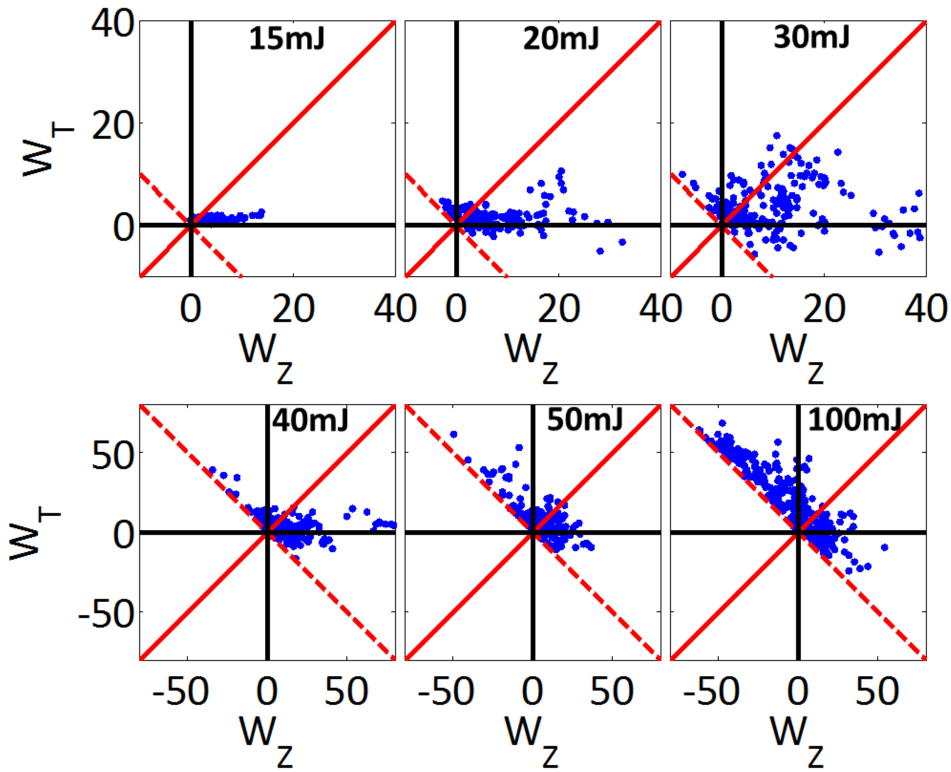

Figure 6.6. 2D PIC simulations showing contributions of LWFA and DLA to electron energy gain for a fixed peak plasma density N_e = $0.07N_{cr}$ for drive laser energies 15-100mJ. Each blue dot is a tracked electron. Regions above and to the left of the solid red line indicate DLA as the dominant form of acceleration, whereas regions below and to the right are dominated by LWFA. The dashed red diagonal marks zero net energy gain. LWFA dominates acceleration at low drive laser energies, transitioning to DLA at high drive laser energies.

figure panels show clearly that acceleration with low laser energies is dominated by LWFA, transitioning to DLA at energies above ~50 mJ.

6.6 Summary

In summary, we have demonstrated electron acceleration to the 10 MeV scale with laser pulses well below 1 terawatt, using a thin, high density hydrogen gas jet, with efficiency of laser energy to MeV electrons of a few percent. The high plasma density reduces the thresholds for relativistic self-focusing, nonlinear plasma wave generation, and electron injection. The reduced spatial scales associated with high density yields intense coherent wave breaking radiation, whose ~1 fs bandwidth is consistent with half-cycle optical emission upon violent unidirectional electron acceleration from rest to nearly the speed of light over a subwavelength distance. The flash is of sufficient intensity to self-damp the injected bunch, with the result that wave breaking radiation and acceleration are comparable energy channels. These results open the way to applications of relativistic electron beams with truly compact and portable high repetition rate laser systems.

Chapter 7: Summary and Future Work

7.1 Summary

The purpose of experiments in this dissertation was to advance the state of the art in laser driven electron accelerators, particularly with the goal of reducing the demand on the drive laser energy necessary for acceleration. Plasmas with transverse and longitudinal structure on the sub-millimeter scale were used to accomplish this goal. In Chapter 3, experiments were presented that studied guiding and electron acceleration in plasma waveguides produced by hydrodynamic motion of a hot plasma formed in a clustered gas jet. Guiding of low intensity pulses at efficiencies up to 80% with ~14 μm spot sizes was demonstrated over ~1 cm long channels. At higher intensities ($P > P_{cr}$) the energy throughput and mode quality deteriorated due to relativistic effects within the channel, and plasma wave generation was inferred from spectral measurements of the guided beam. The guiding structure was then shown to stabilize the pointing of wakefield accelerated electron beams produced in ~1.5 mm long N^{5+} channels. Particle-in-cell simulations were performed confirming that injection into wakes driven in He-like nitrogen plasma channels was due to tunnel-ionization of inner-shell electrons near the peak of the drive laser pulse.

Quasi-phase-matched direct acceleration (QPM-DLA) of electrons in a corrugated plasma channel was described in Chapter 4. A simple method for making a femtosecond laser pulse with a longitudinal field component capable of driving the QPM-DLA scheme was presented. Further, guiding of the higher order Hermite-

Gaussian mode in a plasma channel, vital for a proof of principle QPM-DLA scheme, was demonstrated over lengths up to 11 mm.

The QPM-DLA technique can accelerate electrons with a high gradient using a low energy, high repetition rate drive laser. However, the scheme requires a source of relativistic seed electrons. The seed source has been the limiting constraint to a proof of concept QPM-DLA experiment. Chapter 6 presented an experiment in which a high energy (>5 MeV) and high charge (~100 pC) electron beam was generated from the interaction of a sub-terawatt laser pulse with a high density (>10^{20} cm^{-3}) plasma. The electron beams observed in this experiment, interesting in their own right for electron radiography or bremsstrahlung x-ray generation experiments, could be an excellent seed source for a QPM-DLA proof of concept. The high density jet, characterized in Chapter 5, was capable of reaching the critical density for our Ti:Sapphire laser ($N_{cr} \approx 1.7 \times 10^{21} cm^{-3}$) while still maintaining a thin (~200 μm) density profile. The electron acceleration results made use of relativistic self-focusing and self-modulation of the < 50 mJ, 50 fs laser pulse to drive a plasma wave in the thin jet to the point of wave breaking. Coherent radiation of the electrons as they were accelerated from rest to nearly the speed of light was detected as a bright, extremely broadband “flash” radiating ~1% of the drive laser energy.

7.2 Future Work

7.2.1 Plasma channel guiding experiments

The wakefield accelerator presented in Chapter 3 was demonstrated at relatively high density ($\sim 1.4 \times 10^{19} cm^{-3}$) over a relatively short interaction length

(~1.5 mm). Scaling laws presented in Chapter 1 of the maximum electron energy available from wakefield accelerators suggest that higher energy electron beams can be produced in longer, lower density plasmas because of the increased dephasing length at lower density. While guiding was demonstrated at relativistic intensity in ~1 cm channels, no experiments as yet have been performed looking for high energy electron beams in these experiments. However, 2D TurboWave PIC simulations suggest that ionization injection and subsequent acceleration in a channel with a density profile similar to that presented in Fig. 3.6 can accelerate electrons up to ~0.5 GeV using a drive pulse of only ~6 TW peak power.

7.2.2 Quasi-phase-matched direct laser acceleration

Many of the experiments presented in this dissertation were performed in advance of a proof of concept demonstration of the QPM-DLA technique [12]. The three components necessary for this demonstration, a modulated waveguide, radially polarized drive pulse, and electron seed source, have all been demonstrated in this dissertation. Modulated plasma waveguide generation and guiding of quasi-radially polarized laser pulses were shown in Chapter 4. Modulation techniques outlined in Chapter 4 involving ring gratings [173] or wire modulated cluster jets [152,155], however, produce static modulation profiles. Real time optimization of the QPM-DLA process would benefit from a dynamic modulation technique. The use of a spatial light modulator to shape the intensity profile of the channel-forming pulse can produce computer controlled axial modulations, allowing dynamic control of the modulation depth and period during an experiment.

A proof of concept QPM-DLA experiment will require the radially polarized pulse, modulated waveguide, and seed source to be produced and diagnosed concurrently. While this presents no major technical hurdles, the geometry and diagnostics necessary to adequately diagnose each component of the experiment should be carefully considered. Use of the electron beams presented in Chapter 6 as a seed source must be carefully considered so that estimates can be made of the expected accelerated charge which is necessary for proper detector design. For instance, the relatively large divergence of the beams presented in Chapter 6 could be a problem given the small acceptance angle of a ~1 cm long, ~100 μm diameter plasma waveguide. If the electron beam divergence requires a small separation between the electron beam seed source and the modulated plasma waveguide, injection of the radially polarized pulse into the modulated channel could be geometrically difficult.

7.2.3 High density laser-plasma interaction experiments

The gas jet characterized in Chapter 5 and the experiments performed in Chapter 6 open up a number of interesting avenues for further research. First, the low drive pulse energy (~10 mJ) used to generate the multi-MeV electron beams suggests extension of the technique to kHz repetition rate laser systems. A higher repetition rate pulsed jet or, more likely, a continuous flow high density target will be necessary for experiments using a kHz drive laser. If kHz operation can be achieved, ultrafast high-repetition rate radiography or MeV electron diffraction experiments could be performed driven by a relatively compact laser system. Further reduction of the required pulse energy for electron injection, possibly to the few mJ range, may also be achieved through ionization injection. Electron beams were only observed at power levels $\sim 3P_{cr}$ because the plasma wave amplitude needed to reach the wave breaking threshold for electron injection into the wakefield. As demonstrated by experiments in Chapter 3, ionization injection can reduce the required drive laser power for electron acceleration.

In addition to the prospects of a high repetition rate MeV electron source, the experiments in Chapter 6 open the way to further experimentation with the physics of laser-plasma interaction at near critical densities. The bright wave breaking radiation flashes observed from the high density laser-plasma interaction were shown to be coherent through spectral interferometry experiments. However, error bars on the extracted flash spectral phase precluded the precise determination of the flash pulse duration. The mechanism suggested for the coherent flash emission, namely the violent unipolar acceleration of electrons at wave breaking, suggests that the flash is actually generated as a half-cycle optical pulse. Further experiments are currently being performed in an attempt to more precisely measure the flash pulse duration. Simulations of the interaction of a tightly focused, multi-TW pulse with our high density jet also suggest that ions within the plasma can be accelerated to high energy under certain conditions. Proton acceleration to multi-MeV energies at relatively high repetition rates ($\geq 10\,Hz$) from a gas jet target could open the way to applications such as on-demand production of short half-life radioisotopes used in nuclear medicine.

Bibliography

[1] T. P. Wangler, *RF Linear Accelerators*, 2nd ed (Wiley-VHC, 2008).

[2] A. Grudiev, S. Calatroni, and W. Wuensch, Phys. Rev. Spec. Top. - Accel. Beams **12**, 102001 (2009).

[3] R. W. Hamme and M. E. Hamme, *Industrial Accelerators an Their Applications* (World Scientrific, 2012).

[4] V. Malka, J. Faure, Y. A. Gauduel, E. Lefebvre, A. Rousse, and K. T. Phuoc, Nat. Phys. **4**, 447 (2008).

[5] E. Esarey, C. B. Schroeder, and W. P. Leemans, Rev. Mod. Phys. **81**, 1229 (2009).

[6] H. Daido, M. Nishiuchi, and A. S. Pirozhkov, Rep. Prog. Phys. **75**, 056401 (2012).

[7] P. Maine, D. Strickland, P. Bado, M. Pessot, and G. Mourou, IEEE J. Quantum Electron. **24**, 398 (1988).

[8] D. Strickland and G. Mourou, Opt. Commun. **55**, 447 (1985).

[9] W. R. Rapoport and C. P. Khattak, Appl. Opt. **27**, 2677 (1988).

[10] K. Wall and A. Sanchez, Lincoln Lab. J. **3**, 447 (1990).

[11] S. W. Bahk, P. Rousseau, T. A. Planchon, V. Chvykov, G. Kalintchenko, A. Maksimchuk, G. A. Mourou, and V. Yanovsky, Opt. Lett. **29**, 2837 (2004).

[12] A. York, H. Milchberg, J. Palastro, and T. Antonsen, Phys. Rev. Lett. **100**, 195001 (2008).

[13] C. Varin, S. Payeur, V. Marceau, S. Fourmaux, A. April, B. Schmidt, P.-L. Fortin, N. Thiré, T. Brabec, F. Légaré, J.-C. Kieffer, and M. Piché, Appl. Sci. **3**, 70 (2013).

[14] R. J. England, R. J. Noble, K. Bane, D. Dowell, C. Ng, J. E. Spencer, S. Tantawi, Z. Wu, R. L. Byer, E. Peralta, K. Soong, C.-M. Chang, B. Montazeri, S. J. Wolf, B. Cowan, J. Dawson, W. Gai, P. Hommelhoff, Y.-C. Huang, C. Jing, C. McGuinness, R. B. Palmer, B. Naranjo, J. Rosenzweig, G. Travish, A. Mizrahi, L. Schachter, C. Sears, G. R. Werner, and R. B. Yoder, Rev. Mod. Phys. **86**, 1337 (2014).

[15] W. D. Kimura, G. H. Kim, R. D. Romea, L. C. Steinhauer, I. V. Pogorelsky, K. P. Kusche, R. C. Fernow, X. Wang, and Y. Liu, Phys. Rev. Lett. **74**, 546 (1995).

[16] B. Hafizi, E. Esarey, and P. Sprangle, Phys. Rev. E **55**, 3539 (1997).

[17] T. Tajima and J. Dawson, Phys. Rev. Lett. **43**, 267 (1979).

[18] P. Sprangle, E. Esarey, A. Ting, and G. Joyce, Appl. Phys. Lett. **53**, 2146 (1988).

[19] S. Corde, K. Ta Phuoc, G. Lambert, R. Fitour, V. Malka, A. Rousse, A. Beck, and E. Lefebvre, Rev. Mod. Phys. **85**, 1 (2013).

[20] J. Faure, C. Rechatin, A. Norlin, A. Lifschitz, Y. Glinec, and V. Malka, Nature **444**, 737 (2006).

[21] A. J. Gonsalves, K. Nakamura, C. Lin, D. Panasenko, S. Shiraishi, T. Sokollik, C. Benedetti, C. B. Schroeder, C. G. R. Geddes, J. van Tilborg, J. Osterhoff, E. Esarey, C. Toth, and W. P. Leemans, Nat. Phys. **7**, 862 (2011).

[22] B. S. Rao, A. Moorti, R. Rathore, J. A. Chakera, P. A. Naik, and P. D. Gupta, Phys. Rev. Spec. Top. - Accel. Beams **17**, 011301 (2014).

[23] J. Osterhoff, A. Popp, Z. Major, B. Marx, T. P. Rowlands-Rees, M. Fuchs, M. Geissler, R. Hörlein, B. Hidding, S. Becker, E. A. Peralta, U. Schramm, F. Grüner, D. Habs, F. Krausz, S. M. Hooker, and S. Karsch, Phys. Rev. Lett. **101**, 085002 (2008).

[24] A. Modena, Z. Najmudin, A. E. Dangor, C. E. Clayton, K. A. Marsh, C. Joshi, V. Malka, C. B. Darrow, C. Danson, D. Neely, and F. N. Walsh, Nature **377**,

606 (1995).

[25] K. Nakajima, D. Fisher, T. Kawakubo, H. Nakanishi, A. Ogata, Y. Kato, Y. Kitagawa, R. Kodama, K. Mima, H. Shiraga, K. Suzuki, K. Yamakawa, T. Zhang, Y. Sakawa, T. Shoji, Y. Nishida, N. Yugami, M. Downer, and T. Tajima, Phys. Rev. Lett. **74**, 4428 (1995).

[26] A. Ting, C. I. Moore, K. Krushelnick, C. Manka, E. Esarey, P. Sprangle, R. Hubbard, H. R. Burris, R. Fischer, and M. Baine, Phys. Plasmas **4**, 1889 (1997).

[27] C. Gahn, G. Tsakiris, A. Pukhov, J. Meyer-ter-Vehn, G. Pretzler, P. Thirolf, D. Habs, and K. Witte, Phys. Rev. Lett. **83**, 4772 (1999).

[28] J. Faure, Y. Glinec, A. Pukhov, S. Kiselev, S. Gordienko, E. Lefebvre, J.-P. Rousseau, F. Burgy, and V. Malka, Nature **431**, 541 (2004).

[29] C. G. R. Geddes, C. Toth, J. van Tilborg, E. Esarey, C. B. Schroeder, D. Bruhwiler, C. Nieter, J. Cary, and W. P. Leemans, Nature **431**, 538 (2004).

[30] S. P. D. Mangles, C. D. Murphy, Z. Najmudin, A. G. R. Thomas, J. L. Collier, A. E. Dangor, E. J. Divall, P. S. Foster, J. G. Gallacher, C. J. Hooker, D. A. Jaroszynski, A. J. Langley, W. B. Mori, P. A. Norreys, F. S. Tsung, R. Viskup, B. R. Walton, and K. Krushelnick, Nature **431**, 535 (2004).

[31] W. P. Leemans, A. J. Gonsalves, H.-S. Mao, K. Nakamura, C. Benedetti, C. B. Schroeder, C. Tóth, J. Daniels, D. E. Mittelberger, S. S. Bulanov, J.-L. Vay, C. G. R. Geddes, and E. Esarey, Phys. Rev. Lett. **113**, 245002 (2014).

[32] X. L. Xu, Y. P. Wu, C. J. Zhang, F. Li, Y. Wan, J. F. Hua, C.-H. Pai, W. Lu, P. Yu, C. Joshi, and W. B. Mori, Phys. Rev. Spec. Top. - Accel. Beams **17**, 061301 (2014).

[33] C. B. Schroeder, E. Esarey, C. Benedetti, and W. P. Leemans, Phys. Plasmas **20**, 080701 (2013).

[34] C. G. R. Geddes, K. Nakamura, G. R. Plateau, C. Toth, E. Cormier-Michel, E. Esarey, C. B. Schroeder, J. R. Cary, and W. P. Leemans, Phys. Rev. Lett. **100**, 215004 (2008).

[35] A. Rousse, K. Ta Phuoc, R. Shah, A. Pukhov, E. Lefebvre, V. Malka, S. Kiselev, F. Burgy, J. P. Rousseau, D. Umstadter, and D. Hulin, Phys. Rev. Lett. **93**, 135005 (2004).

[36] K. T. Phuoc, S. Corde, R. Shah, F. Albert, R. Fitour, J.-P. Rousseau, F. Burgy, B. Mercier, and A. Rousse, Phys. Rev. Lett. **97**, 225002 (2006).

[37] S. Kneip, S. R. Nagel, C. Bellei, N. Bourgeois, A. E. Dangor, A. Gopal, R. Heathcote, S. P. D. Mangles, J. R. Marquès, A. Maksimchuk, P. M. Nilson, K. T. Phuoc, S. Reed, M. Tzoufras, F. S. Tsung, L. Willingale, W. B. Mori, A. Rousse, K. Krushelnick, and Z. Najmudin, Phys. Rev. Lett. **100**, 105006 (2008).

[38] H.-P. Schlenvoigt, K. Haupt, A. Debus, F. Budde, O. Jäckel, S. Pfotenhauer, H. Schwoerer, E. Rohwer, J. G. Gallacher, E. Brunetti, R. P. Shanks, S. M. Wiggins, and D. A. Jaroszynski, Nat. Phys. **4**, 130 (2008).

[39] G. Sarri, D. J. Corvan, W. Schumaker, J. M. Cole, A. Di Piazza, H. Ahmed, C. Harvey, C. H. Keitel, K. Krushelnick, S. P. D. Mangles, Z. Najmudin, D. Symes, A. G. R. Thomas, M. Yeung, Z. Zhao, and M. Zepf, Phys. Rev. Lett. **113**, 224801 (2014).

[40] K. Khrennikov, J. Wenz, A. Buck, J. Xu, M. Heigoldt, L. Veisz, and S. Karsch, Phys. Rev. Lett. **114**, 1 (2015).

[41] S. Kneip, C. McGuffey, J. L. Martins, S. F. Martins, C. Bellei, V. Chvykov, F. Dollar, R. Fonseca, C. Huntington, G. Kalintchenko, A. Maksimchuk, S. P. D. Mangles, T. Matsuoka, S. R. Nagel, C. A. J. Palmer, J. Schreiber, K. Ta Phuoc, A. G. R. Thomas, V. Yanovsky, L. O. Silva, K. Krushelnick, and Z. Najmudin, Nat. Phys. **6**, 980 (2010).

[42] G. J. Williams, B. B. Pollock, F. Albert, J. Park, and H. Chen, Phys. Plasmas **22**, 093115 (2015).

[43] G. Sarri, W. Schumaker, A. Di Piazza, M. Vargas, B. Dromey, M. E. Dieckmann, V. Chvykov, A. Maksimchuk, V. Yanovsky, Z. H. He, B. X. Hou, J. A. Nees, A. G. R. Thomas, C. H. Keitel, M. Zepf, and K. Krushelnick, Phys. Rev. Lett. **110**, 255002 (2013).

[44] A. Di Piazza, C. Müller, K. Z. Hatsagortsyan, and C. H. Keitel, Rev. Mod. Phys. **84**, 1177 (2012).

[45] E. Esarey, P. Sprangle, J. Krall, and A. Ting, IEEE Trans. Plasma Sci. **24**, (1996).

[46] P. Sprangle, E. Esarey, and A. Ting, Phys. Rev. Lett. **64**, 2011 (1990).

[47] A. Ting, E. Esarey, and P. Sprangle, Phys. Fluids B Plasma Phys. **2**, 1390 (1990).

[48] P. Sprangle, E. Esarey, and A. Ting, Phys. Rev. A **41**, 4463 (1990).

[49] E. Esarey, P. Sprangle, J. Krall, A. Ting, and G. Joyce, Phys. Fluids B Plasma Phys. **5**, 2690 (1993).

[50] D. Teychenné, G. Bonnaud, and J. Bobin, Phys. Rev. E **48**, 3248 (1993).

[51] C. E. Max, J. Aronst, and A. B. Langdon, Phys. Rev. Lett. **33**, 209 (1974).

[52] P. Sprangle, C.-M. Tang, and E. Esarey, IEEE Trans. Plasma Sci. **15**, 145 (1987).

[53] P. Sprangle, E. Esarey, J. Krall, and G. Joyce, Phys. Rev. Lett. **69**, 2200 (1992).

[54] C. K. Birdsall and A. B. Langdon, *Plasma Physics via Computer Simulation* (Taylor & Francis Group, 2005).

[55] J. P. Verboncoeur, Plasma Phys. Control. Fusion **47**, A231 (2005).

[56] C. Moore, A. Ting, K. Krushelnick, E. Esarey, R. Hubbard, B. Hafizi, H. Burris, C. Manka, and P. Sprangle, Phys. Rev. Lett. **79**, 3909 (1997).

[57] S. Le Blanc, M. Downer, R. Wagner, S.-Y. Chen, A. Maksimchuk, G. Mourou, and D. Umstadter, Phys. Rev. Lett. **77**, 5381 (1996).

[58] R. Wagner, S.-Y. Chen, A. Maksimchuk, and D. Umstadter, Phys. Rev. Lett. **78**, 3125 (1997).

[59] A. Ting, K. Krushelnick, C. Moore, H. Burris, E. Esarey, J. Krall, and P. Sprangle, Phys. Rev. Lett. **77**, 5377 (1996).

[60] C. G. Durfee and H. M. Milchberg, Phys. Rev. Lett. **71**, 2409 (1993).

[61] T. Clark and H. Milchberg, Phys. Rev. E **61**, 1954 (2000).

[62] C. B. Schroeder, E. Esarey, B. A. Shadwick, and W. P. Leemans, Phys. Plasmas **13**, 033103 (2006).

[63] D. Gordon, K. C. Tzeng, C. E. Clayton, A. E. Dangor, V. Malka, K. A. Marsh, A. Modena, W. B. Mori, P. Muggli, Z. Najmudin, D. Neely, C. Danson, and C. Joshi, Phys. Rev. Lett. **80**, 2133 (1998).

[64] S. Bulanov, N. Naumova, F. Pegoraro, and J. Sakai, Phys. Rev. E **58**, R5257 (1998).

[65] S. V. Bulanov, F. Pegoraro, A. M. Pukhov, and A. S. Sakharov, Phys. Rev. Lett. **78**, 4205 (1997).

[66] E. Esarey, R. F. Hubbard, W. P. Leemans, A. Ting, and P. Sprangle, Phys. Rev. Lett. **79**, 2682 (1997).

[67] D. Umstadter, J. Kim, and E. Dodd, Phys. Rev. Lett. **76**, 2073 (1996).

[68] G. Golovin, S. Chen, N. D. Powers, C. Liu, S. Banerjee, J. Zhang, M. Zeng, Z. Sheng, and D. Umstadter, Phys. Rev. Spec. Top. - Accel. Beams **18**, 011301 (2015).

[69] M. Chen, E. Esarey, C. G. R. Geddes, E. Cormier-Michel, C. B. Schroeder, S. S. Bulanov, C. Benedetti, L. L. Yu, S. Rykovanov, D. L. Bruhwiler, and W. P. Leemans, Phys. Rev. Spec. Top. - Accel. Beams **17**, 051303 (2014).

[70] A. Pak, K. A. Marsh, S. F. Martins, W. Lu, W. B. Mori, and C. Joshi, Phys. Rev. Lett. **104**, 025003 (2010).

[71] E. Oz, S. Deng, T. Katsouleas, P. Muggli, C. D. Barnes, I. Blumenfeld, F. J. Decker, P. Emma, M. J. Hogan, R. Ischebeck, R. H. Iverson, N. Kirby, P. Krejcik, C. O'Connell, R. H. Siemann, D. Walz, D. Auerbach, C. E. Clayton, C. Huang, D. K. Johnson, C. Joshi, W. Lu, K. A. Marsh, W. B. Mori, and M. Zhou, Phys. Rev. Lett. **98**, 084801 (2007).

[72] T. P. Rowlands-Rees, C. Kamperidis, S. Kneip, A. J. Gonsalves, S. P. D. Mangles, J. G. Gallacher, E. Brunetti, T. Ibbotson, C. D. Murphy, P. S. Foster, M. J. V. Streeter, F. Budde, P. A. Norreys, D. A. Jaroszynski, K. Krushelnick, Z. Najmudin, and S. M. Hooker, Phys. Rev. Lett. **100**, 105005 (2008).

[73] C. McGuffey, A. G. R. Thomas, W. Schumaker, T. Matsuoka, V. Chvykov, F. J. Dollar, G. Kalintchenko, V. Yanovsky, A. Maksimchuk, K. Krushelnick, V. Y. Bychenkov, I. V. Glazyrin, and A. V. Karpeev, Phys. Rev. Lett. **104**, 025004 (2010).

[74] Y.-C. Ho, T.-S. Hung, C.-P. Yen, S.-Y. Chen, H.-H. Chu, J.-Y. Lin, J. Wang, and M.-C. Chou, Phys. Plasmas **18**, 063102 (2011).

[75] A. J. Goers, S. J. Yoon, J. A. Elle, G. A. Hine, and H. M. Milchberg, Appl. Phys. Lett. **104**, 214105 (2014).

[76] N. Bourgeois, J. Cowley, and S. M. Hooker, Phys. Rev. Lett. **111**, 155004 (2013).

[77] R. R. Hubbard, P. Sprangle, and B. Hafizi, IEEE Trans. Plasma Sci. **28**, 1159 (2000).

[78] P. Sprangle, B. Hafizi, J. Penano, R. F. Hubbard, A. Ting, A. Zigler, and T. M. Antonsen, Phys. Rev. Lett. **85**, 5110 (2000).

[79] S. J. Yoon, J. P. Palastro, and H. M. Milchberg, Phys. Rev. Lett. **112**, 134803 (2014).

[80] W. Lu, M. Tzoufras, C. Joshi, F. S. Tsung, W. B. Mori, J. Vieira, R. A. Fonseca, and L. O. Silva, Phys. Rev. Spec. Top. - Accel. Beams **10**, 061301 (2007).

[81] P. Serafim, P. Sprangle, and B. Hafizi, IEEE Trans. Plasma Sci. **28**, 1155 (2000).

[82] T. Plettner, R. L. Byer, E. Colby, B. Cowan, C. M. S. Sears, J. E. Spencer, and R. H. Siemann, Phys. Rev. Lett. **95**, 134801 (2005).

[83] E. Esarey, P. Sprangle, and J. Krall, Phys. Rev. E **52**, 5443 (1995).

[84] J. P. Palastro, T. M. Antonsen, S. Morshed, A. G. York, and H. M. Milchberg, Phys. Rev. E **77**, 036405 (2008).

[85] S. Yoon, J. Palastro, D. Gordon, T. Antonsen, and H. Milchberg, Phys. Rev. Spec. Top. - Accel. Beams **15**, 081305 (2012).

[86] G. Mourou, T. Tajima, and S. Bulanov, Rev. Mod. Phys. **78**, 309 (2006).

[87] S. Backus, C. G. Durfee, M. M. Murnane, and H. C. Kapteyn, Rev. Sci. Instrum. **69**, 1207 (1998).

[88] U. Morgner, F. X. Kärtner, S. H. Cho, Y. Chen, H. A. Haus, J. G. Fujimoto, E. P. Ippen, V. Scheuer, G. Angelow, and T. Tschudi, Opt. Lett. **24**, 411 (1999).

[89] D. H. Sutter, G. Steinmeyer, L. Gallmann, N. Matuschek, F. Morier-Genoud, U. Keller, V. Scheuer, G. Angelow, and T. Tschudi, Opt. Lett. **24**, 631 (1999).

[90] W. Koechner, *Solid State Laser Engineering*, 6th ed. (Springer-Verlag New York, 2006).

[91] A. Siegman, *Lasers* (University Science Books, 1986).

[92] J. Zhou, C.-P. Huang, M. M. Murnane, and H. C. Kapteyn, Opt. Lett. **20**, 64 (1995).

[93] C. Le Blanc, P. Curley, and F. Salin, Opt. Commun. **131**, 391 (1996).

[94] C. P. Barty, C. L. Gordon, and B. E. Lemoff, Opt. Lett. **19**, 1442 (1994).

[95] P. Poole, S. Trendafilov, G. Shvets, D. Smith, and E. Chowdhury, Opt. Express **21**, 26341 (2013).

[96] E. Treacy, IEEE J. Quantum Electron. **5**, 454 (1969).

[97] B. E. Lemoff and C. P. Barty, Opt. Lett. **18**, 1651 (1993).

[98] S. Kane and J. Squier, J. Opt. Soc. Am. B **14**, 1237 (1997).

[99] R. Trebino and D. J. Kane, J. Opt. Soc. Am. A **10**, 1101 (1993).

[100] C. Iaconis and I. A. Walmsley, Opt. Lett. **23**, 792 (1998).

[101] C. Rulliere, *Femtosecond Laser Pulses: Principles and Experiments*, 2nd ed. (Springer, 2005).

[102] R. Trebino, *Frequency-Resolved Optical Gating* (Kluwer Academic Publishers, 2000).

[103] Femtosoft QuickFROG, www.femtosoft.com

[104] A. M. Weiner, Opt. Commun. **284**, 3669 (2011).

[105] A. M. Weiner, Rev. Sci. Instrum. **71**, 1929 (2000).

[106] F. Verluise, V. Laude, Z. Cheng, C. Spielmann, and P. Tournois, Opt. Lett. **25**, 575 (2000).

[107] www.fastlite.com

[108] P. Tournois, Opt. Commun. **140**, 245 (1997).

[109] D. Kaplan and P. Tournois, J. Phys. IV **12**, 69 (2002).

[110] J. Seres, A. Müller, E. Seres, K. O'Keeffe, M. Lenner, R. F. Herzog, D. Kaplan, C. Spielmann, and F. Krausz, Opt. Lett. **28**, 1832 (2003).

[111] www.ultrafast-innovations.com

[112] D. Kaganovich, J. R. Peñano, M. H. Helle, D. F. Gordon, B. Hafizi, and A. Ting, Opt. Lett. **38**, 3635 (2013).

[113] M. Hart, Appl. Opt. **49**, D17 (2010).

[114] R. Zhi-Jun, L. Xiao-Yan, M.-B. Lie, C.-Q. Xia, X.-M. Lu, R.-X. Li, and Z.-Z. Xu, Chinese Phys. Lett. **26**, 124203 (2009).

[115] F. Canova, A. Flacco, L. Canova, R. Clady, J.-P. Chambaret, F. Ple, M. Pittman, T. A. Planchon, M. Silva, R. Benocci, G. Lucchini, D. Batani, E. Lavergne, G. Dovillaire, and X. Levecq, Laser Part. Beams **25**, 649 (2007).

[116] S.-W. Bahk, P. Rousseau, T. A. Planchon, V. Chvykov, G. Kalintchenko, A. Maksimchuk, G. A. Mourou, and V. Yanovsky, Appl. Phys. B **80**, 823 (2005).

[117] Z.-H. He, B. Hou, V. Lebailly, J. A. Nees, K. Krushelnick, and A. G. R. Thomas, Nat. Commun. **6**, 7156 (2015).

[118] T. Bifano, Nat. Photonics **5**, 21 (2011).

[119] S. Serati and J. Stockley, Proc. SPIE **5894**, 58940K (2005).

[120] E. Steinhaus and S. G. Lipson, J. Opt. Soc. Am. **69**, 478 (1979).

[121] J.-C. Chanteloup, Appl. Opt. **44**, 1559 (2005).

[122] J. Primot and L. Sogno, J. Opt. Soc. Am. A **12**, 2679 (1995).

[123] K. Osvay, A. P. Kovács, G. Kurdi, Z. Heiner, M. Divall, J. Klebniczki, and I. E. Ferincz, Opt. Commun. **248**, 201 (2005).

[124] G. Pretzler, A. Kasper, and K. J. Witte, Appl. Phys. B Lasers Opt. **70**, 1 (2000).

[125] M. Trentelman, I. N. Ross, and C. N. Danson, Appl. Opt. **36**, 8567 (1997).

[126] C. Fiorini, C. Sauteret, C. Rouyer, N. Blanchot, S. Seznec, and A. Migus, IEEE J. Quantum Electron. **30**, 1662 (1994).

[127] R. Kammel, R. Ackermann, J. Thomas, J. Götte, S. Skupin, A. Tünnermann, and S. Nolte, Light Sci. Appl. **3**, e169 (2014).

[128] D. N. Vitek, D. E. Adams, A. Johnson, P. S. Tsai, S. Backus, C. G. Durfee, D. Kleinfeld, and J. A. Squier, Opt. Express **18**, 18086 (2010).

[129] E. Block, M. Greco, D. Vitek, O. Masihzadeh, D. A. Ammar, M. Y. Kahook, N. Mandava, C. Durfee, and J. Squier, Biomed. Opt. Express **4**, 831 (2013).

[130] P. G. Gobbi and G. C. Reali, Opt. Commun. **52**, 195 (1984).

[131] Thomas Clark, *Hydrodynamical and Optical Properties of the Plasma Waveguide*. PhD thesis, University of Maryland, College Park, 1998.

[132] H. Milchberg and T. Clark, Phys. Plasmas **3**, 2149 (1996).

[133] A. Depresseux, E. Oliva, J. Gautier, F. Tissandier, G. Lambert, B. Vodungbo, J.-P. Goddet, A. Tafzi, J. Nejdl, M. Kozlova, G. Maynard, H. T. Kim, K. T. Phuoc, A. Rousse, P. Zeitoun, and S. Sebban, Phys. Rev. Lett. **115**, 083901 (2015).

[134] H. Milchberg, C. Durfee, and J. Lynch, JOSA B **12**, 731 (1995).

[135] T. M. Antonsen, J. Palastro, and H. M. Milchberg, Phys. Plasmas **14**, 033107 (2007).

[136] Lord Rayleigh, Philos. Mag. **43**, 125 (1897).

[137] A. G. Litvak, Sov. Phys. JETP **30**, 344 (1970).

[138] K. Krushelnick, A. Ting, C. Moore, H. Burris, E. Esarey, P. Sprangle, and M. Baine, Phys. Rev. Lett. **78**, 4047 (1997).

[139] P. Monot, T. Auguste, P. Gibbon, F. Jakober, G. Mainfray, A. Dulieu, M. Louis-Jacquet, G. Malka, and J. Miquel, Phys. Rev. Lett. **74**, 2953 (1995).

[140] W. P. Leemans, B. Nagler, A. J. Gonsalves, C. Tóth, K. Nakamura, C. G. R. Geddes, E. Esarey, C. B. Schroeder, and S. M. Hooker, Nat. Phys. **2**, 696 (2006).

[141] S. P. Nikitin, T. M. Antonsen, T. R. Clark, Y. Li, and H. M. Milchberg, Opt. Lett. **22**, 1787 (1997).

[142] S. Nikitin, I. Alexeev, J. Fan, and H. Milchberg, Phys. Rev. E **59**, R3839 (1999).

[143] P. Volfbeyn, E. Esarey, and W. P. Leemans, Phys. Plasmas **6**, 2269 (1999).

[144] C. Geddes, C. Toth, J. van Tilborg, E. Esarey, C. Schroeder, J. Cary, and W. Leemans, Phys. Rev. Lett. **95**, 145002 (2005).

[145] A. Zigler, Y. Ehrlich, C. Cohen, J. Krall, and P. Sprangle, J. Opt. Soc. Am. B **13**, 68 (1996).

[146] D. Spence and S. Hooker, Phys. Rev. E **63**, 015401 (2000).

[147] T. R. Clark and H. M. Milchberg, Phys. Rev. Lett. **78**, 2373 (1997).

[148] A. J. Gonsalves, T. P. Rowlands-Rees, B. H. P. Broks, J. J. A. M. van der Mullen, and S. M. Hooker, Phys. Rev. Lett. **98**, 025002 (2007).

[149] H. M. Milchberg, K. Y. Kim, V. Kumarappan, B. D. Layer, and H. Sheng, Philos. Trans. A. Math. Phys. Eng. Sci. **364**, 647 (2006).

[150] H. Sheng, K. Y. Kim, V. Kumarappan, B. D. Layer, and H. M. Milchberg, Phys. Rev. E **72**, 036411 (2005).

[151] H. M. Milchberg, K. Y. Kim, V. Kumarappan, B. D. Layer, and H. Sheng, Philos. Trans. A. Math. Phys. Eng. Sci. **364**, 647 (2006).

[152] S. J. Yoon, A. J. Goers, G. A. Hine, J. D. Magill, J. A. Elle, Y.-H. Chen, and H. M. Milchberg, Opt. Express **21**, 15878 (2013).

[153] O. Hagena, Surf. Sci. **106**, 101 (1981).

[154] H. Milchberg, S. McNaught, and E. Parra, Phys. Rev. E **64**, 056402 (2001).

[155] B. D. Layer, A. G. York, S. Varma, Y.-H. Chen, and H. M. Milchberg, Opt. Express **17**, 4263 (2009).

[156] T. Ditmire, T. Donnelly, A. Rubenchik, R. Falcone, and M. Perry, Phys. Rev. A **53**, 3379 (1996).

[157] E. Parra, I. Alexeev, J. Fan, K. Kim, S. McNaught, and H. Milchberg, Phys. Rev. E **62**, R5931 (2000).

[158] S. Shiraishi, C. Benedetti, A. J. Gonsalves, K. Nakamura, B. H. Shaw, T. Sokollik, J. van Tilborg, C. G. R. Geddes, C. B. Schroeder, C. Tóth, E. Es rey, and W. P. Leemans, Phys. Plasmas **20**, 063103 (2013).

[159] M. Z. Mo, A. Ali, S. Fourmaux, P. Lassonde, J. C. Kieffer, and R. Fedosejevs, Appl. Phys. Lett. **100**, 074101 (2012).

[160] M. Z. Mo, A. Ali, S. Fourmaux, P. Lassonde, J. C. Kieffer, and R. Fedosejevs, Appl. Phys. Lett. **102**, 134102 (2013).

[161] Y. Glinec, J. Faure, A. Guemnie-Tafo, V. Malka, H. Monard, J. P. Larbre, V. De Waele, J. L. Marignier, and M. Mostafavi, Rev. Sci. Instrum. **77**, 103301 (2006).

[162] A. Buck, K. Zeil, A. Popp, K. Schmid, A. Jochmann, S. D. Kraft, B. Hidding, T. Kudyakov, C. M. S. Sears, L. Veisz, S. Karsch, J. Pawelke, R. Sauerbrey, T. Cowan, F. Krausz, and U. Schramm, Rev. Sci. Instrum. **81**, 033301 (2010).

[163] D. F. Gordon, IEEE Trans. Plasma Sci. **35**, 1486 (2007).

[164] M. V. Ammosov, N. B. Delone, and V. P. Krainov, Sov. Physi. JETP **64**, 1191 (1986).

[165] S. Payeur, S. Fourmaux, B. E. Schmidt, J. P. MacLean, C. Tchervenkov, F. Légaré, M. Piché, and J. C. Kieffer, Appl. Phys. Lett. **101**, 041105 (2012).

[166] Y. I. Salamin, Z. Harman, and C. H. Keitel, Phys. Rev. Lett. **100**, 155004 (2008).

[167] Y. Liu, D. Cline, and P. He, Nucl. Instruments Methods Phys. Res. Sect. A Accel. Spectrometers, Detect. Assoc. Equip. **424**, 296 (1999).

[168] P.-L. Fortin, M. Piché, and C. Varin, J. Phys. B At. Mol. Opt. Phys. **43**, 025401 (2009).

[169] L. J. Wong and F. X. Kärtner, Opt. Express **18**, 25035 (2010).

[170] Sung Jun Yoon, *Quasi-Phasematched Acceleration of Electrons in a Density Modulated Plasma Waveguide*. PhD thesis, University of Maryland, College Park, 2014.

[171] M. Yamada, N. Nada, M. Saitoh, and K. Watanabe, Appl. Phys. Lett. **62**, 435 (1993).

[172] G. Khanarian, R. A. Norwood, D. Haas, B. Feuer, and D. Karim, Appl. Phys. Lett. **57**, 977 (1990).

[173] B. Layer, A. York, T. Antonsen, S. Varma, Y.-H. Chen, Y. Leng, and H. Milchberg, Phys. Rev. Lett. **99**, 035001 (2007).

[174] B. D. Layer, J. P. Palastro, A. G. York, T. M. Antonsen, and H. M. Milchberg, New J. Phys. **12**, 095011 (2010).

[175] G. Hine, A. Goers, S. Yoon, J. Elle, and H. Milchberg, CLEO 2014 JW2A.87 (2014).

[176] P. Brijesh, C. Thaury, K. T. Phuoc, S. Corde, G. Lambert, V. Malka, S. P. D. Mangles, M. Bloom, and S. Kneip, Phys. Plasmas **19**, 063104 (2012).

[177] M.-W. Lin, Y.-M. Chen, C.-H. Pai, C.-C. Kuo, K.-H. Lee, J. Wang, S.-Y. Chen, and J.-Y. Lin, Phys. Plasmas **13**, 110701 (2006).

[178] T. Kuga, Y. Torii, N. Shiokawa, T. Hirano, Y. Shimizu, and H. Sasada, Phys. Rev. Lett. **78**, 4713 (1997).

[179] S. Sato, Y. Harada, and Y. Waseda, Opt. Lett. **19**, 1807 (1994).

[180] M. Meier, V. Romano, and T. Feurer, Appl. Phys. A **86**, 329 (2007).

[181] A. V Nesterov and V. G. Niziev, J. Phys. D. Appl. Phys. **33**, 1817 (2000).

[182] B. Hecht and L. Novotny, *Principles of Nano-Optics*, 2nd ed. (Cambridge University Press, 2012).

[183] L. W. Davis and G. Patsakos, Opt. Lett. **6**, 22 (1981).

[184] A. April, Opt. Lett. **33**, 1563 (2008).

[185] Y. I. Salamin, New J. Phys. **8**, 133 (2006).

[186] S. Quabis, R. Dorn, and G. Leuchs, Appl. Phys. B Lasers Opt. **81**, 597 (2005).

[187] G. Machavariani, Y. Lumer, I. Moshe, A. Meir, and S. Jackel, Opt. Lett. **32**, 1468 (2007).

[188] M. Stalder and M. Schadt, Opt. Lett. **21**, 1948 (1996).

[189] S. C. Tidwell, D. H. Ford, and W. D. Kimura, Appl. Opt. **29**, 2234 (1990).

[190] E. Zauderer, J. Opt. Soc. Am. A **3**, 465 (1986).

[191] Y. Fukuda, A. Y. Faenov, M. Tampo, T. A. Pikuz, T. Nakamura, M. Kando, Y. Hayashi, A. Yogo, H. Sakaki, T. Kameshima, A. S. Pirozhkov, K. Ogura, M. Mori, T. Z. Esirkepov, J. Koga, A. S. Boldarev, V. A. Gasilov, A. I.

Magunov, T. Yamauchi, R. Kodama, P. R. Bolton, Y. Kato, T. Tajima, H. Daido, and S. V. Bulanov, Phys. Rev. Lett. **103**, 165002 (2009).

[192] A. Lifschitz, F. Sylla, S. Kahaly, A. Flacco, M. Veltcheva, G. Sanchez-Arriaga, E. Lefebvre, and V. Malka, New J. Phys. **16**, 033031 (2014).

[193] A. Willner, F. Tavella, M. Yeung, T. Dzelzainis, C. Kamperidis, M. Bakarezos, D. Adams, M. Schulz, R. Riedel, M. Hoffmann, W. Hu, J. Rossbach, M. Drescher, N. Papadogiannis, M. Tatarakis, B. Dromey, and M. Zepf, Phys. Rev. Lett. **107**, 175002 (2011).

[194] C. Altucci, C. Beneduce, R. Bruzzese, C. De Lisio, G. S. Sorrentino, T. Starczewski, and F. Vigilante, J. Phys. D. Appl. Phys. **29**, 68 (1999).

[195] T. Ditmire, J. Zweiback, V. P. Yanovsky, T. E. Cowan, and G. Hays, Nature **398**, 489 (1999).

[196] M. Krishnan, K. W. Elliott, C. G. R. Geddes, R. A. van Mourik, W. P. Leemans, H. Murphy, and M. Clover, Phys. Rev. Spec. Top. - Accel. Beams **14**, 033502 (2011).

[197] F. Sylla, M. Veltcheva, S. Kahaly, A. Flacco, and V. Malka, Rev. Sci. Instrum. **83**, 033507 (2012).

[198] E. Parra, S. J. McNaught, and H. M. Milchberg, Rev. Sci. Instrum. **73**, 468 (2002).

[199] S. Semushin and V. Malka, Rev. Sci. Instrum. **72**, 2961 (2001).

[200] R. Azambuja, M. Eloy, G. Figueira, and D. Neely, J. Phys. D. Appl. Phys. **32**, L35 (1999).

[201] A. Murakami, J. Miyazawa, H. Tsuchiya, T. Murase, N. Ashikawa, T. Morisaki, R. Sakamoto, and H. Yamada, J. Plasma Fusion Res. **9**, 79 (2010).

[202] J. Fan, T. R. Clark, and H. M. Milchberg, Appl. Phys. Lett. **73**, 3064 (1998).

[203] D. Kaganovich, M. H. Helle, D. F. Gordon, and A. Ting, Phys. Plasmas **18**,

120701 (2011).

[204] A. Buck, J. Wenz, J. Xu, K. Khrennikov, K. Schmid, M. Heigoldt, J. M. Mikhailova, M. Geissler, B. Shen, F. Krausz, S. Karsch, and L. Veisz, Phys. Rev. Lett. **110**, 185006 (2013).

[205] K. Schmid and L. Veisz, Rev. Sci. Instrum. **83**, 053304 (2012).

[206] P. M. Gerhart, R. J. Gross, and J. I. Hochstein, *Fundamentals of Fluid Mechanics* (Addison-Wesley, 1992).

[207] Available online from U.S. Department of Energy Hydrogen Analysis Resource Center. www.hydrogen.pnl.gov/hydrogen-data/

[208] B. R. Munson, D. F. Young, and T. H. Okiishi, *Fundamentals of Fluid Mechanics*, 2nd ed. (John Wiley & Sons, Inc., 1997).

[209] Crane Company, *Flow of Fluide through Valves, Fittings, and Pipe*, (1988).

[210] P. H. Oosthuizen and W. E. Carscallen, *Compressible Fluid Flow* (McGraw-Hill, 1997).

[211] K. Y. Kim, V. Kumarappan, and H. M. Milchberg, Appl. Phys. Lett. **83**, 3210 (2003).

[212] M. Takeda, H. Ina, and S. Kobayashi, J. Opt. Soc. Am. **72**, 156 (1982).

[213] M. Kalal and K. A. Nugent, Appl. Opt. **27**, 1956 (1988).

[214] T. Ditmire, T. Donnelly, R. Falcone, and M. Perry, Phys. Rev. Lett. **75**, 3122 (1995).

[215] Y. Fukuda, H. Sakaki, M. Kanasaki, A. Yogo, S. Jinno, M. Tampo, A. Y. Faenov, T. A. Pikuz, Y. Hayashi, M. Kando, A. S. Pirozhkov, T. Shimomura, H. Kiriyama, S. Kurashima, T. Kamiya, K. Oda, T. Yamauchi, K. Kondo, and S. V. Bulanov, Radiat. Meas. **50**, 92 (2013).

[216] L. M. Chen, J. J. Park, K. H. Hong, J. L. Kim, J. Zhang, and C. H. Nam, Phys. Rev. E - Stat. Nonlinear, Soft Matter Phys. **66**, 17 (2002).

[217] Y. Shao, T. Ditmire, J. Tisch, E. Springate, J. Marangos, and M. Hutchinson, Phys. Rev. Lett. **77**, 3343 (1996).

[218] T. Caillaud, F. Blasco, F. Dorchies, Y. Glinec, C. Stenz, and J. Stevefelt, Nucl. Instruments Methods Phys. Res. Sect. B Beam Interact. with Mater. Atoms **205**, 329 (2003).

[219] T. Ditmire, J. Zweiback, V. P. Yanovsky, T. E. Cowan, G. Hays, and K. B. Wharton, Phys. Plasmas **7**, 1993 (2000).

[220] O. F. Hagena, J. Chem. Phys. **56**, 1793 (1972).

[221] O. F. Hagena, Rev. Sci. Instrum. **63**, 2374 (1992).

[222] H. Lu, G. Ni, R. Li, and Z. Xu, J. Chem. Phys. **132**, 124303 (2010).

[223] O. G. Danylchenko, S. I. Kovalenko, and V. N. Samovarov, Tech. Phys. Lett. **34**, 1037 (2008).

[224] K. Y. Kim, V. Kumarappan, and H. M. Milchberg, Appl. Phys. Lett. **83**, 3210 (2003).

[225] S. Cipiccia, M. R. Islam, B. Ersfeld, R. P. Shanks, E. Brunetti, G. Vieux, X. Yang, R. C. Issac, S. M. Wiggins, G. H. Welsh, M.-P. Anania, D. Maneuski, R. Montgomery, G. Smith, M. Hoek, D. J. Hamilton, N. R. C. Lemos, D. Symes, P. P. Rajeev, V. O. Shea, J. M. Dias, and D. A. Jaroszynski, Nat. Phys. **7**, 867 (2011).

[226] H. Schwoerer, B. Liesfeld, H.-P. Schlenvoigt, K.-U. Amthor, and R. Sauerbrey, Phys. Rev. Lett. **96**, 014802 (2006).

[227] S. Chen, N. D. Powers, I. Ghebregziabher, C. M. Maharjan, C. Liu, G. Golovin, S. Banerjee, J. Zhang, N. Cunningham, A. Moorti, S. Clarke, S. Pozzi, and D. P. Umstadter, Phys. Rev. Lett. **110**, 155003 (2013).

[228] A. Pukhov and J. Meyer-ter-Vehn, Appl. Phys. B Lasers Opt. **74**, 355 (2002).

[229] E. W. Gaul, M. Martinez, J. Blakeney, A. Jochmann, M. Ringuette, D. Hammond, T. Borger, R. Escamilla, S. Douglas, W. Henderson, G. Dyer, A. Erlandson, R. Cross, J. Caird, C. Ebbers, and T. Ditmire, Appl. Opt. **49**, 1676 (2010).

[230] Z. H. He, B. Hou, J. A. Nees, J. H. Easter, J. Faure, K. Krushelnick, and A. G. R. Thomas, New J. Phys. **15**, 053016 (2013).

[231] D. G. Jang, Y. S. You, H. M. Milchberg, H. Suk, and K. Y. Kim, Appl. Phys. Lett. **105**, 021906 (2014).

[232] F. Sylla, A. Flacco, S. Kahaly, M. Veltcheva, A. Lifschitz, G. Sanchez-Arriaga, E. Lefebvre, and V. Malka, Phys. Rev. Lett. **108**, 115003 (2012).

[233] F. Sylla, A. Flacco, S. Kahaly, M. Veltcheva, A. Lifschitz, V. Malka, E. D'Humières, I. Andriyash, and V. Tikhonchuk, Phys. Rev. Lett. **110**, 085001 (2013).

[234] G.-Z. Sun, E. Ott, Y. C. Lee, and P. Guzdar, Phys. Fluids **30**, 526 (1987).

[235] G. Schmidt and W. Horton, Phys. Fluids **30**, 526 (1987).

[236] D. Umstadter, S.-Y. Chen, A. Maksimchuk, G. Mourou, and R. Wagner, Science **273**, 472 (1996).

[237] S. V. Bulanov, F. Pegoraro, and A. Pukhov, Phys. Rev. Lett. **74**, 710 (1995).

[238] A. G. R. Thomas, S. P. D. Mangles, Z. Najmudin, M. C. Kaluza, C. D. Murphy, and K. Krushelnick, Phys. Rev. Lett. **98**, 054802 (2007).

[239] S. V. Bulanov, T. Z. Esirkepov, M. Kando, J. K. Koga, A. S. Pirozhkov, T. Nakamura, S. S. Bulanov, C. B. Schroeder, E. Esarey, F. Califano, and F. Pegoraro, Phys. Plasmas **19**, 113102 (2012).

[240] B. M. Penetrante and J. N. Bardsley, Phys. Rev. A **43**, 3100 (1991).

[241] J. D. Jackson, *Classical Electrodynamics*, 3rd ed. (Wiley, New York, 2001).

[242] F. Y. Li, Z. M. Sheng, M. Chen, L. L. Yu, J. Meyer-ter-Vehn, W. B. Mori, and J. Zhang, Phys. Rev. E **90**, 043104 (2014).

[243] Y.-H. Chen, S. Varma, I. Alexeev, and H. Milchberg, Opt. Express **15**, 7458 (2007).

[244] K. Y. Kim, I. Alexeev, and H. M. Milchberg, Appl. Phys. Lett. **81**, 4124 (2002).

[245] N. Forget, V. Crozatier, and P. Tournois, Appl. Phys. B Lasers Opt. **109**, 121 (2012).

[246] A. P. Kovács, K. Osvay, G. Kurdi, M. Görbe, J. Klebniczki, and Z. Bor, Appl. Phys. B Lasers Opt. **80**, 165 (2005).

[247] C. Sainz, P. Jourdain, R. Escalona, and J. Calatroni, Opt. Commun. **111**, 632 (1994).

[248] A. Pukhov, Z.-M. Sheng, and J. Meyer-ter-Vehn, Phys. Plasmas **6**, 2847 (1999).

[249] J. L. Shaw, F. S. Tsung, N. Vafaei-Najafabadi, K. A. Marsh, N. Lemos, W. B. Mori, and C. Joshi, Plasma Phys. Control. Fusion **56**, 084006 (2014).

[250] F. Albert, A. G. R. Thomas, S. P. D. Mangles, S. Banerjee, S. Corde, A. Flacco, M. Litos, D. Neely, J. Vieira, Z. Najmudin, R. Bingham, C. Joshi, and T. Katsouleas, Plasma Phys. Control. Fusion **56**, 084015 (2014).

Proton acceleration by multi-terawatt laser interaction with a near-critical density hydrogen jet

A. J. Goers[1], L. Feder[1], J. Murray[1], G. A. Hine[1], F. Salehi[1], D. Woodbury[1],
J.J. Su[1], D. Papadopoulos[1], A. Zigler[2], P. D. Haaland[3], and H. M. Milchberg[1]
[1]Institute for Research in Electronics and Applied Physics, University of Maryland, College Park, MD 20742
[2]Hebrew University of Jerusalem, Jerusalem, Israel 91904
[3]MicroPET, Inc. San Francisco, CA 94111

APPENDIX 2

Introduction

Laser-plasma ion accelerators have been studied extensively for nearly 20 years with potential applications ranging from radiography of high density plasmas to generation of nuclear isotopes to hadron therapy of cancers [1]. The majority of laser-plasma ion acceleration experiments study the interaction of picosecond to femtosecond pulses with thin foils ranging from ~10 μm down to ~10 nm thick [1]. While these experiments have been successful in demonstrating high energy ion acceleration these extremely fragile foils represent a major technical hurdle for providing ion beams with average currents comparable to current conventional RF accelerators since the target must be replaced after each shot.

High power laser interaction with thin, near critical density plasmas has also been proposed as a means of efficient acceleration of MeV protons via the "magnetic vortex acceleration" mechanism [2]. In this regime the ponderomotive force of a tightly focused laser pulse drives a relativistic electron current which generates a strong quasi-static azimuthal magnetic field. At the target rear this magnetic field expands and displaces plasma electrons, leading to a quasi-static electric field that can focus and accelerate plasma ions.

Recent advances in development of thin, high density gas jets have led to laser acceleration of electrons with few mJ laser systems from near critical density plasmas [3]. Here we show progress toward leveraging this same near critical density jet for acceleration of ions by a ~10 TW laser system operating at 10 Hz.

Application to radioisotope production

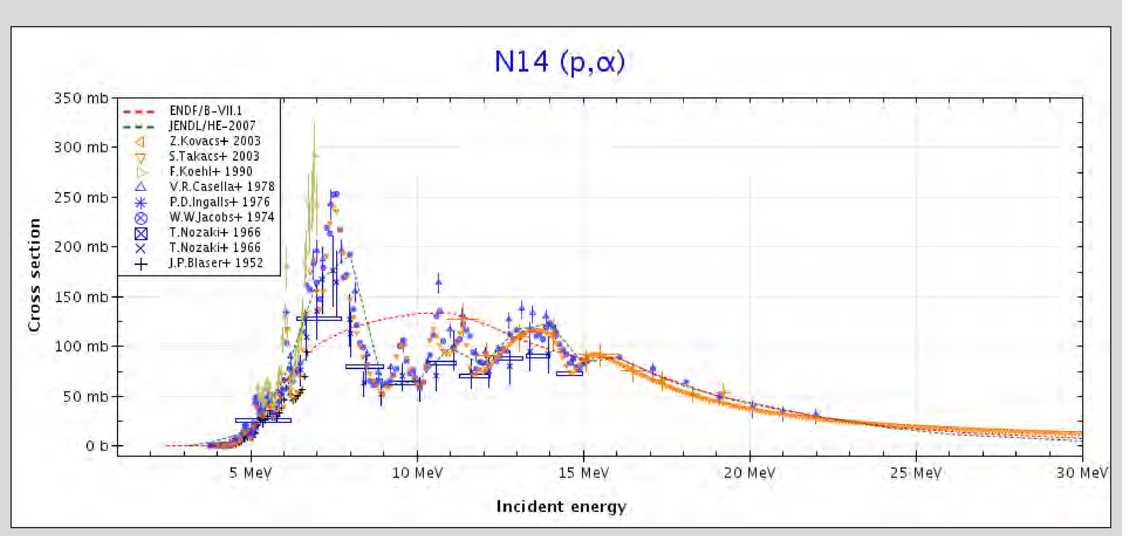

- Positron emission tomography is a high resolution medical imaging technique exploiting radioisotopes, such as C[11] ($\tau_{1/2} = 20\ min$) and F[18] ($\tau_{1/2} = 109\ min$)
- Laser accelerated proton beams have been considered for PET isotope generation, focusing on the TNSA mechanism [4]. These studies concluded that ~1 J class, ~1 kW average power femtosecond laser systems are required for medically relevant doses (~1 mCi).
- Ion acceleration in gas jet targets can potentially provide higher average current sources than solid targets by enabling high repetition rate operation

Simulations of magnetic vortex acceleration in underdense plasma

To gain insight into the magnetic vortex acceleration mechanism, 2D PIC simulations (EPOCH) were run examining the interaction of a 1.5 J, 300 fs laser pulse ($\lambda = 1\ \mu m,\ a_0 = 3.8$) with a thin, critical density plasma target.

The laser pulse first self-focuses, forming an ion channel and transferring energy to fast electrons.

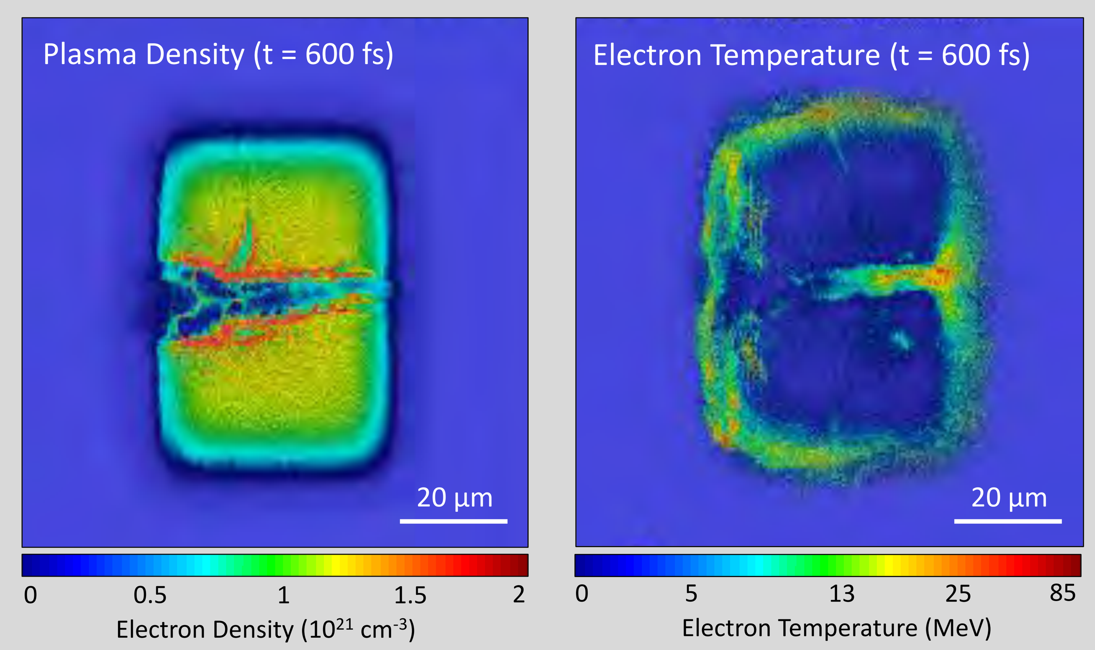

The fast electron current generates a ~ 5 kT azimuthal magnetic field which expands near the back side of the target. Charge separation driven by magnetic pressure creates a quasi-static electric field which can accelerate and focus protons.

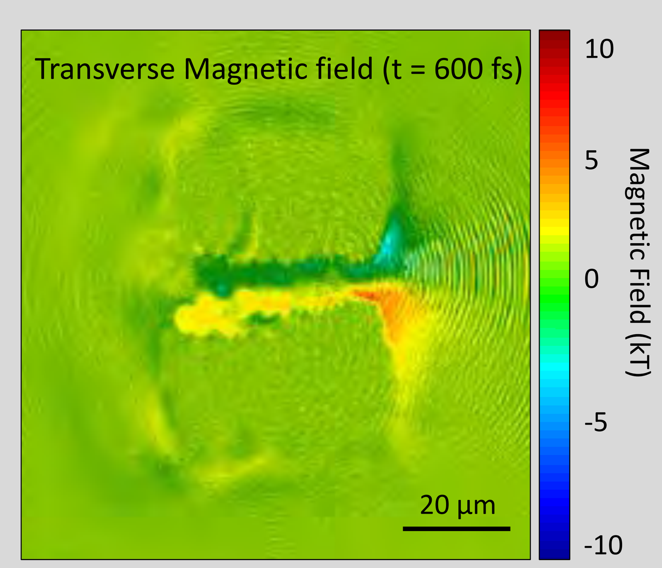

The quasi-static electric field at the back side of the target accelerates protons on a ~1 ps time scale, leading to maximum energies beyond 10 MeV. Total energy transfer from laser to protons with >5 MeV kinetic energy ~5%.

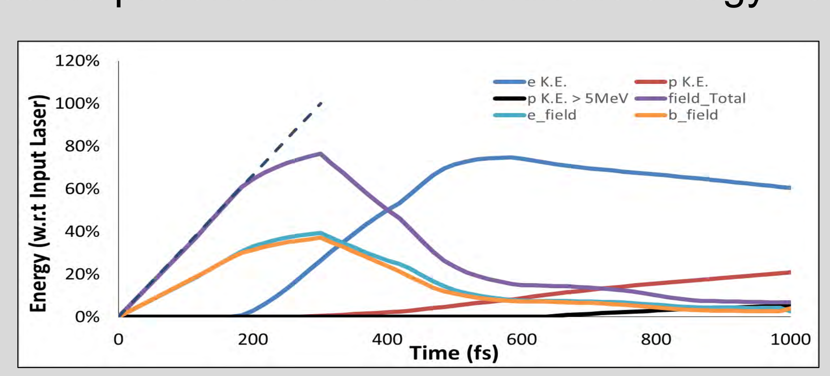

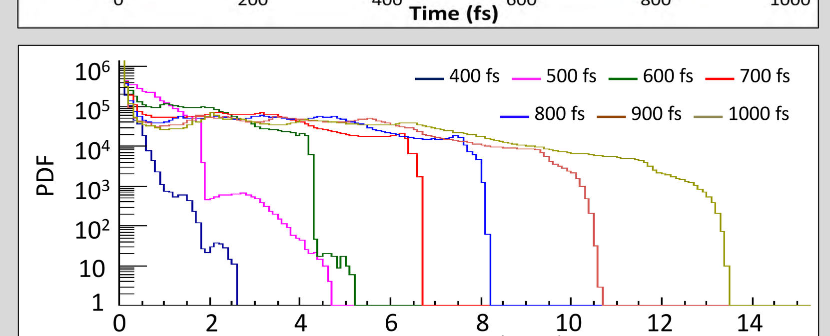

High density gas jet development

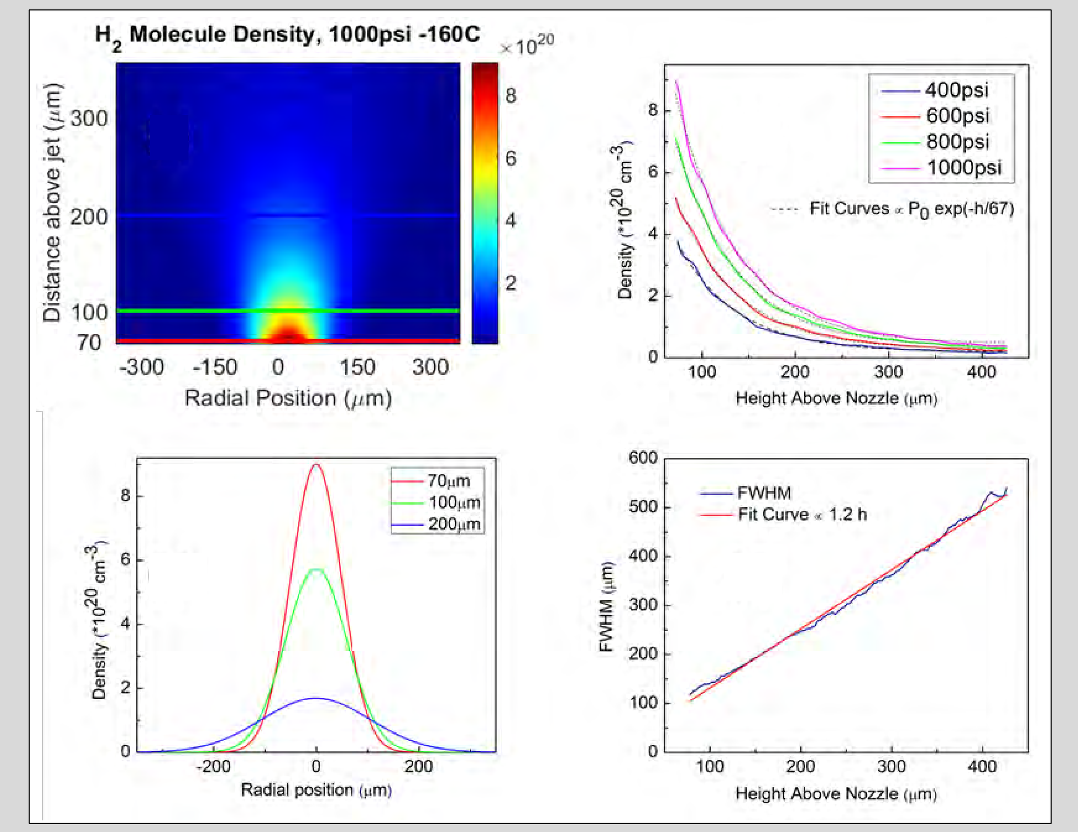

- Recently we have developed high density gas jets utilizing micro-nozzles with 50-150 micron inner diameters [3]
- Cryogenic cooling of the nozzles increases gas output approximately as 1/T

Experiment design and diagnostics

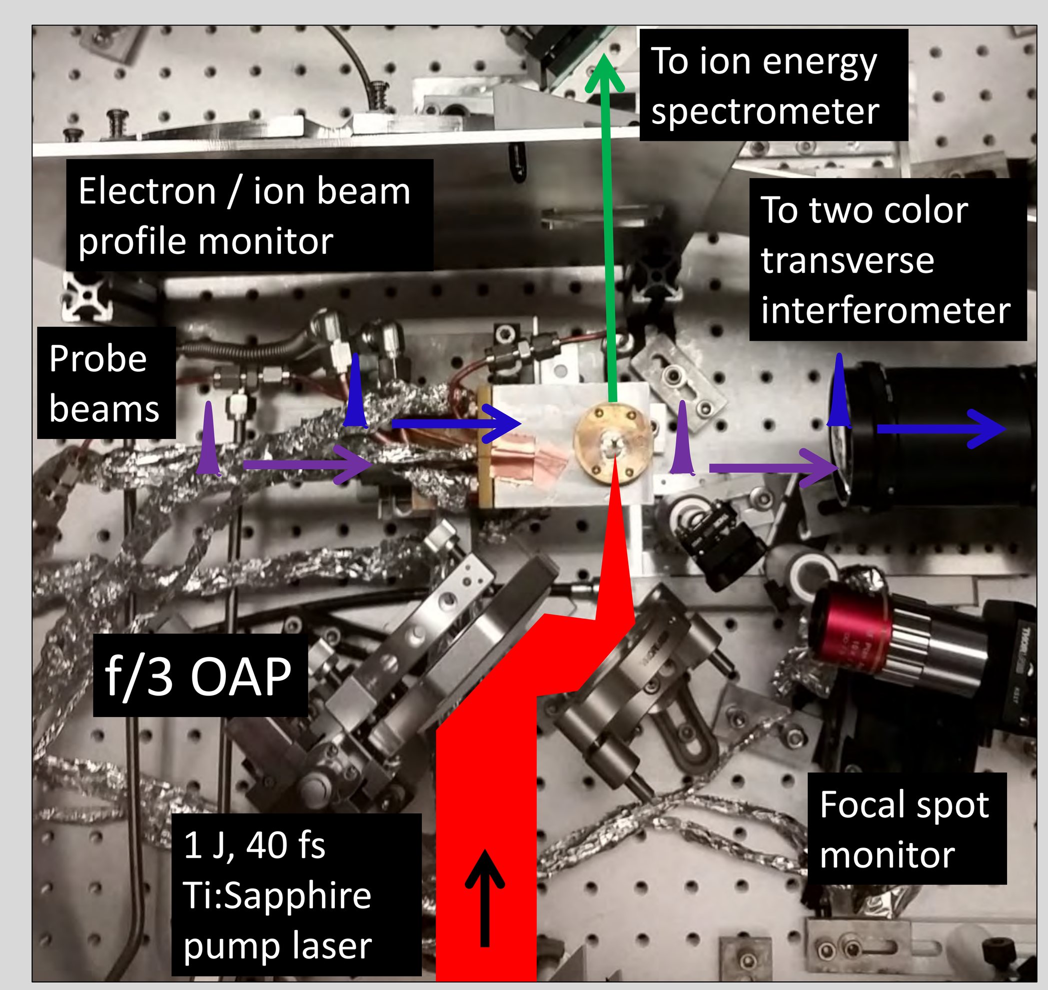

- The main drive pulse for the experiment is a 25 TW (1 J, 40 fs) Ti:Sapphire (λ=805 nm) laser system at UMD focused by an f/3 OAP
- Online focal spot imaging allows optimization with an adaptive optics loop, allowing diffraction limited focal spot size of 3 μm FWHM and a peak intensity >10[20] W/cm[2]

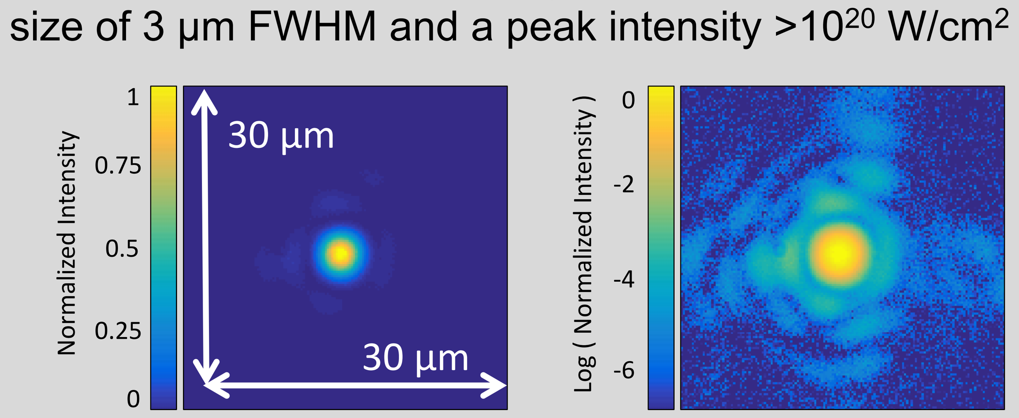

Experimental design and diagnostics

- Collinear THG yields co-propagating, femtosecond probe pulses at 400 nm and 266 nm, with pulse separation controlled by placing glass before the interaction and absolute delay controlled by an optical delay line

$$\Delta\tau = L * \left(\frac{1}{v_{g,2\omega}} - \frac{1}{v_{g,3\omega}}\right) \qquad v_g = c * \left(n - \lambda_0 \frac{dn}{d\lambda_0}\right)^{-1}$$

Fused silica:

$$\frac{v_g}{c}(400nm) = 0.661,\ \frac{v_g}{c}(266nm) = 0.619,\ L = 12.7\ mm \rightarrow \Delta\tau = 4.28\ ps$$

- 400 nm probe can be used to extract gas density and check for plasma generated by laser pre-pulses

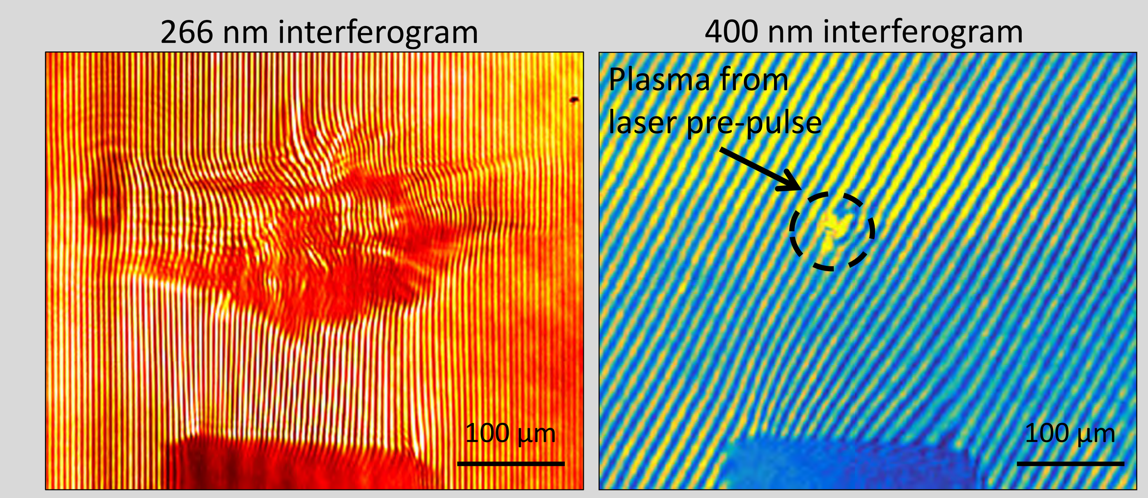

- Using CR39 for proton beam profile measurements and a permanent magnet spectrometer for energy measurement

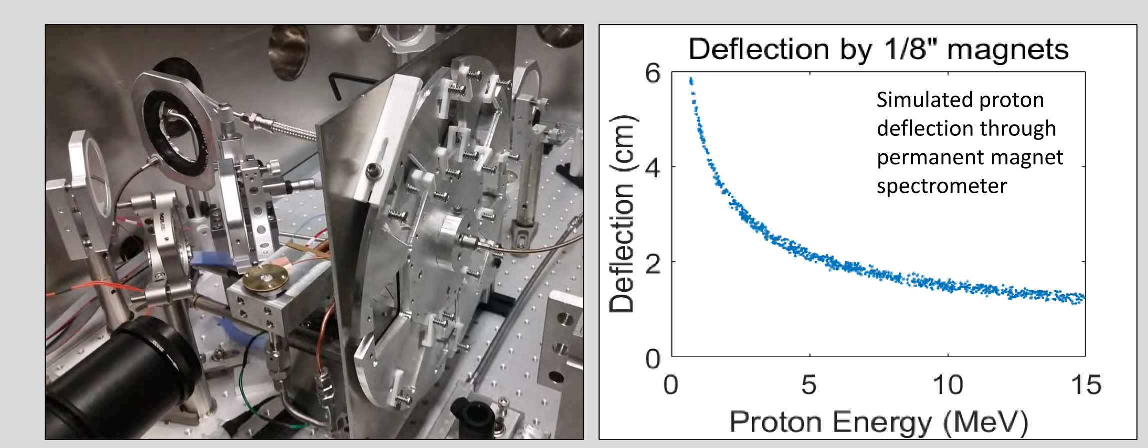

Conclusion

- Laser accelerated proton beams driven in near critical density plasmas may have application to generating medically relevant radioisotopes
- 2D PIC simulations demonstrate acceleration of protons to >10 MeV by quasi-static fields at the rear of the target.
- Experiments utilizing a thin, near critical density gas jet are underway to verify scaling of proton flux and peak energy as a function of laser and plasma parameters.

Citations and Acknowledgements

[1] A. Macchi, M. Borghesi, M. Passoni, Rev. Mod. Phys. **85**, 751 (2013). H. Daido, M. Michiuchi, and A. Pirozhkov, Rep. Prog. Phys. **75**, 056401 (2012).
[2] A. V. Kuznetsov et al. Plasm. Phys. Rep. **27**, 211 (2001). S. V. Bulanov et al. Plasm. Phys. Rep. **31**, 369 (2005). Yogo et al. Phys. Rev. E **77**, 016401 (2008). Nakamura et al. Phys. Rev. Lett. **105**, 135002 (2010).
[3] A.J. Goers et al. Phys. Rev. Lett. **115**, 194802 (2015).
[4] M. I. K. Santala et al. App. Phys. Lett. **78**, 19 (2001). I. Spencer et al. Nucl. Instrum. Methods B **183**, 449 (2001). S. Fritzler et al. App. Phys. Lett. **83**, 3039 (2003). K. W. D. Ledingham et al. J. Phys. D: Appl. Phys. **37**, 2341 (2004). E. Lefebvre et al. J. App. Phys. **100**, 113308 (2006).

This research was funded by the National Science Foundation, US Dept. of Energy (grant DESC0015516) and the Defense Advanced Research Projects Agency (DARPA) under Contract Number W911-NF-15-C-0217, issued by the Army Research Office. The views, opinions, and/or findings expressed are those of the author(s) and should not be interpreted as representing the official views or policies of the Department of Defense or the U.S. Government.

APPENDIX 3

UNIVERSITY OF MARYLAND AT COLLEGE PARK
INSTITUTE FOR RESEARCH IN ELECTRONICS AND APPLIED PHYSICS

Proton acceleration by multi-TW interaction with a near-critical density hydrogen jet

Andy Goers, George Hine, Linus Feder, Fatholah Salehi, Bo Miao, Daniel Woodbury, and Howard Milchberg

Laser plasma ion acceleration for PET isotopes

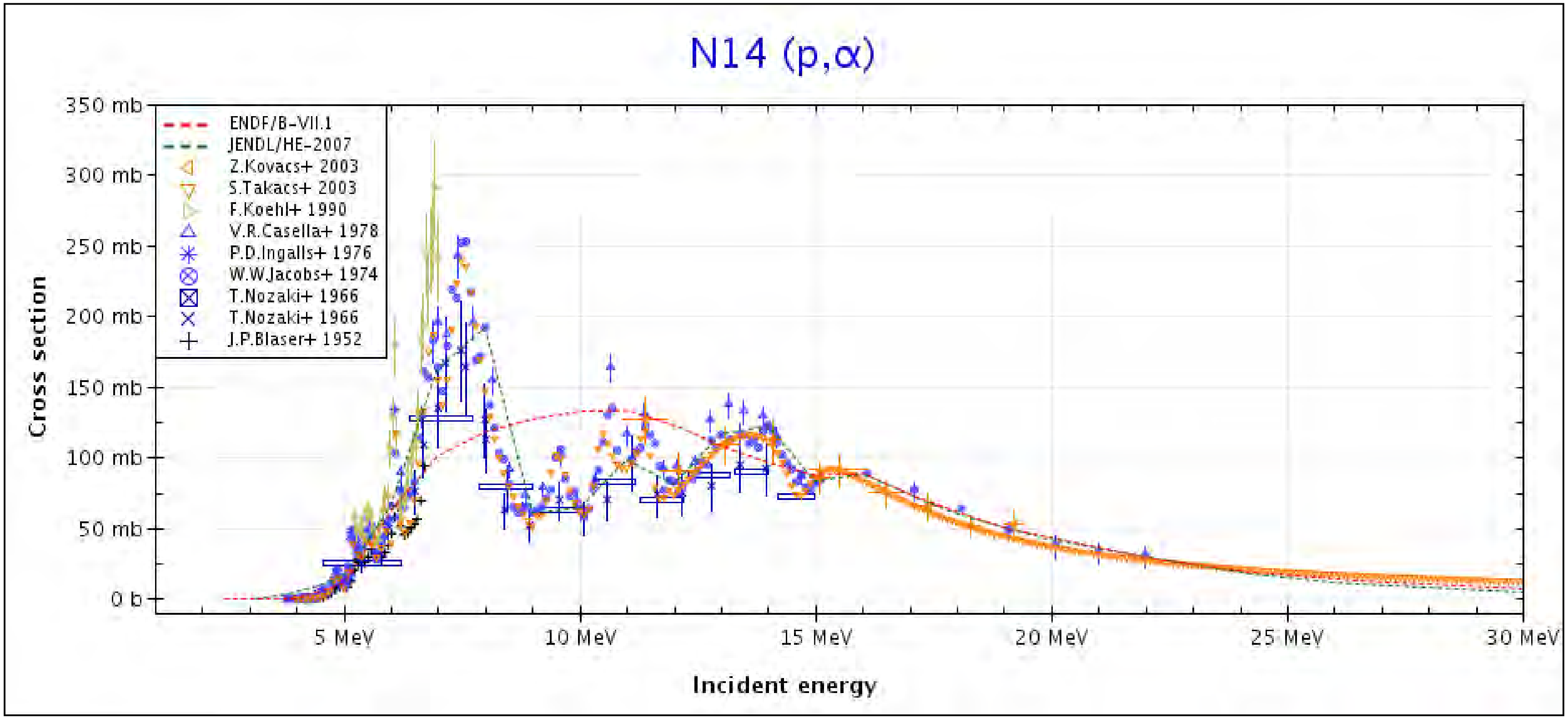

- Positron emission tomography (PET) exploits radioisotopes such as C^{11} ($\tau_{1/2} = 20\ min$) and F^{18} ($\tau_{1/2} = 109\ min$) for medical imaging
- A laser driven ion source delivering > 5 MeV protons with high average flux could be a viable PET isotope source

Laser plasma ion acceleration for PET isotopes

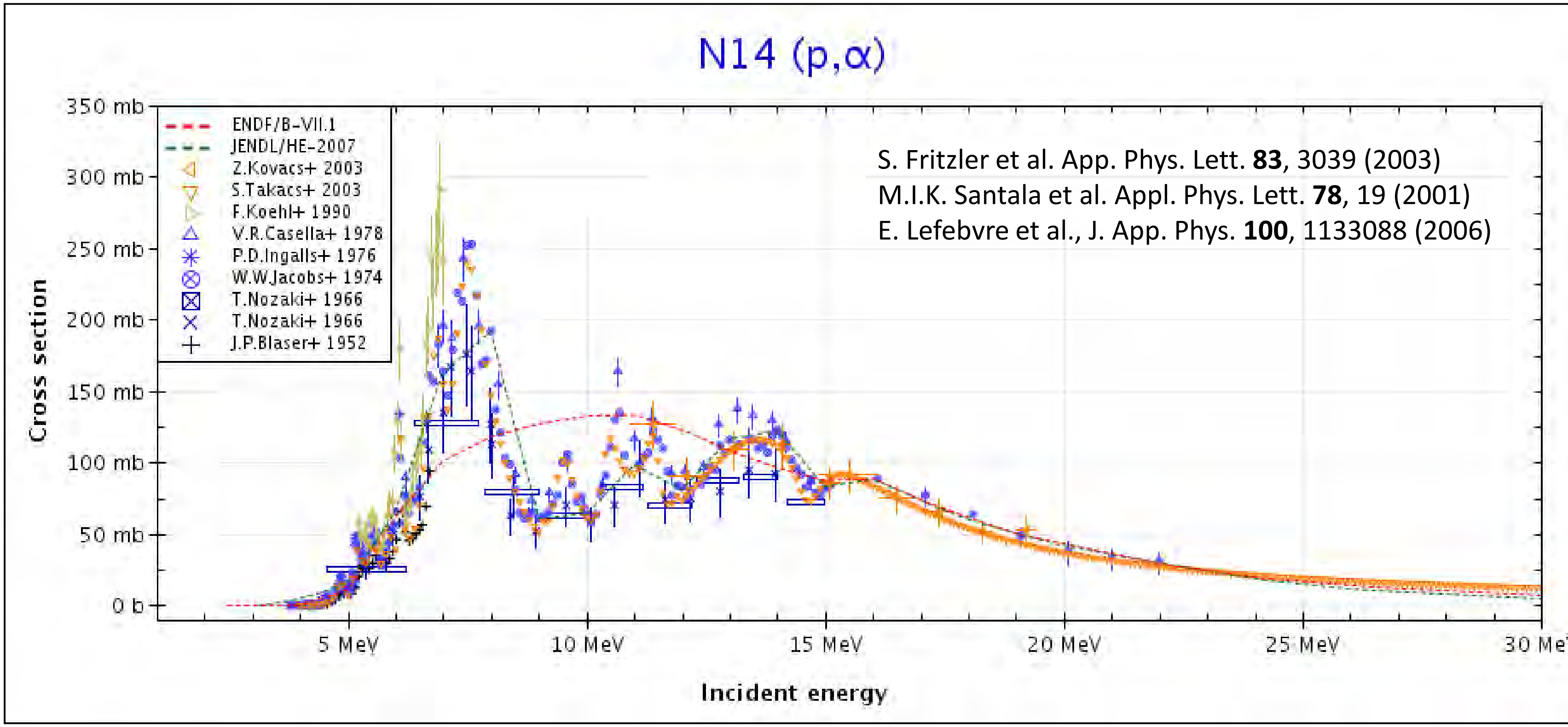

- Positron emission tomography (PET) exploits radioisotopes such as C^{11} ($\tau_{1/2} = 20\ min$) and F^{18} ($\tau_{1/2} = 109\ min$) for medical imaging

- A laser driven ion source delivering > 5 MeV protons with high average flux could be a viable PET isotope source

High density gas jet

- Cryogenically cooled solenoid valve with 100µm needle nozzle

$$N = \frac{P}{kT}$$

- H_2 gas densities near the nozzle approach critical density for backing pressures of 1000psi

- Gas profiles have 250µm FWHM at distance ~200µm above the nozzle

- Already interesting for electron acceleration with low power lasers

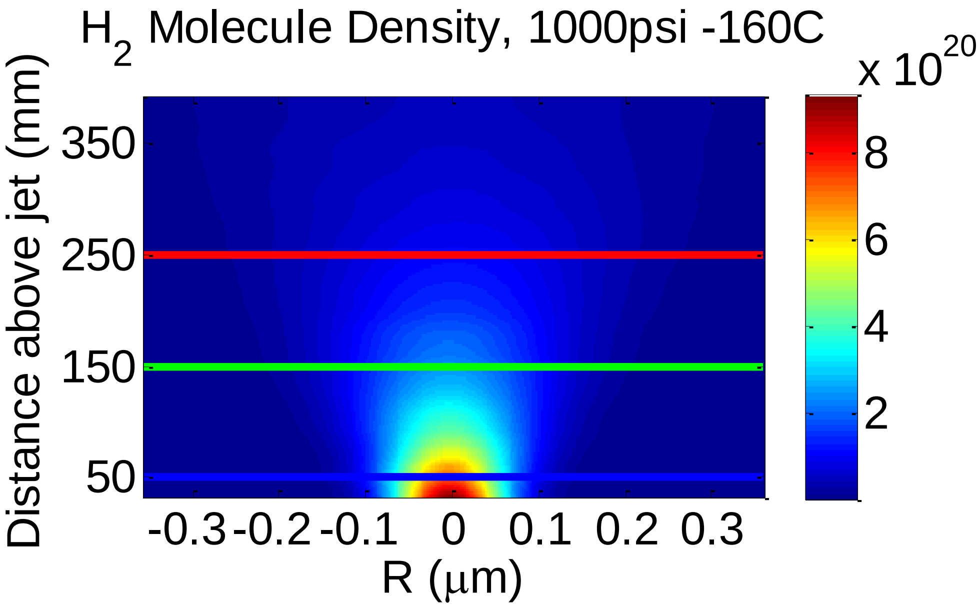

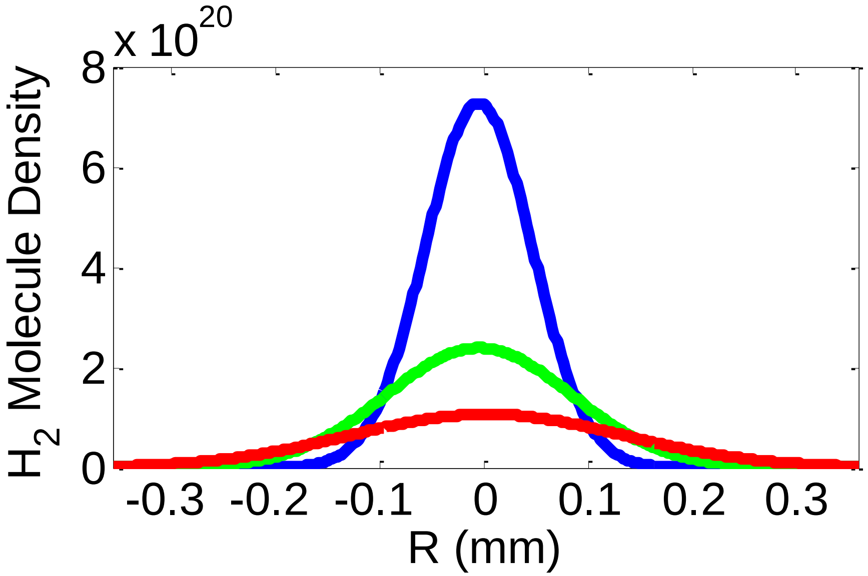

Goers et al., PRL **115**, 194802 (2015)

Ion acceleration from underdense targets

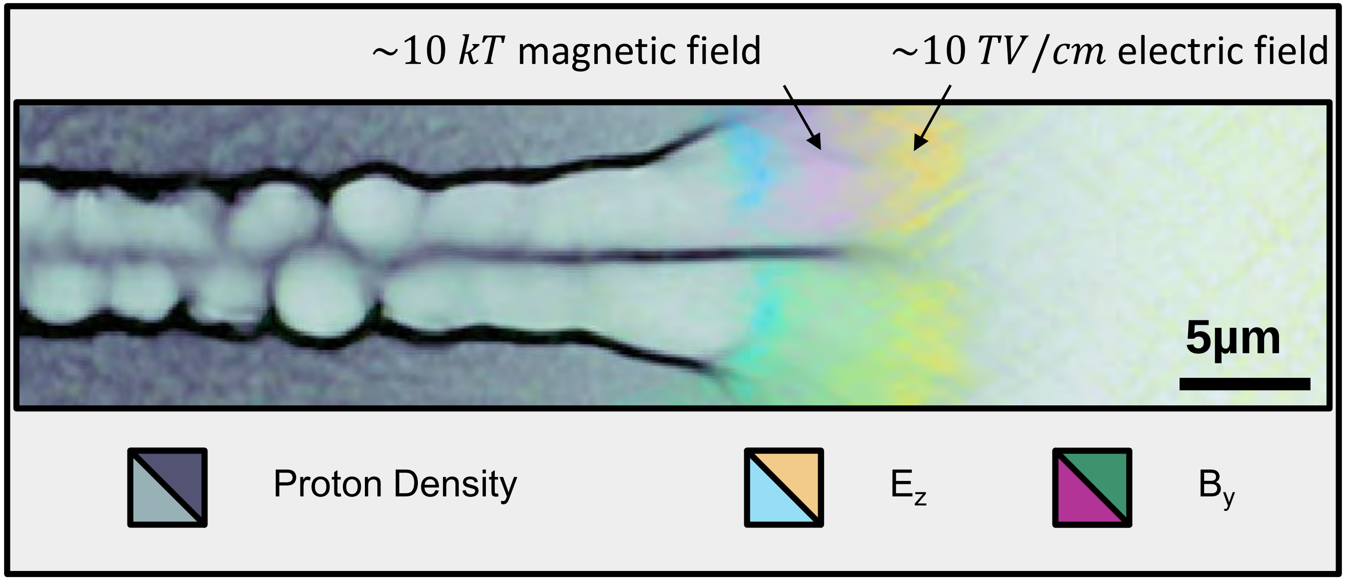

- 2D PIC
- $a_0 = 4,$
- $\tau = 40fs$
- $w_0 = 1.6\ \mu m$
- $N_e = 0.15\ N_{crit}$
- $50\ \mu m$ target

- Intense laser pulse bores a channel through an underdense target
- Ponderomotive force drives a strong current which generates ~10 kT magnetic fields
- Magnetic field expansion at the back side of the target can generate slowly expanding quasi-static fields which accelerate protons

Ion acceleration from underdense targets

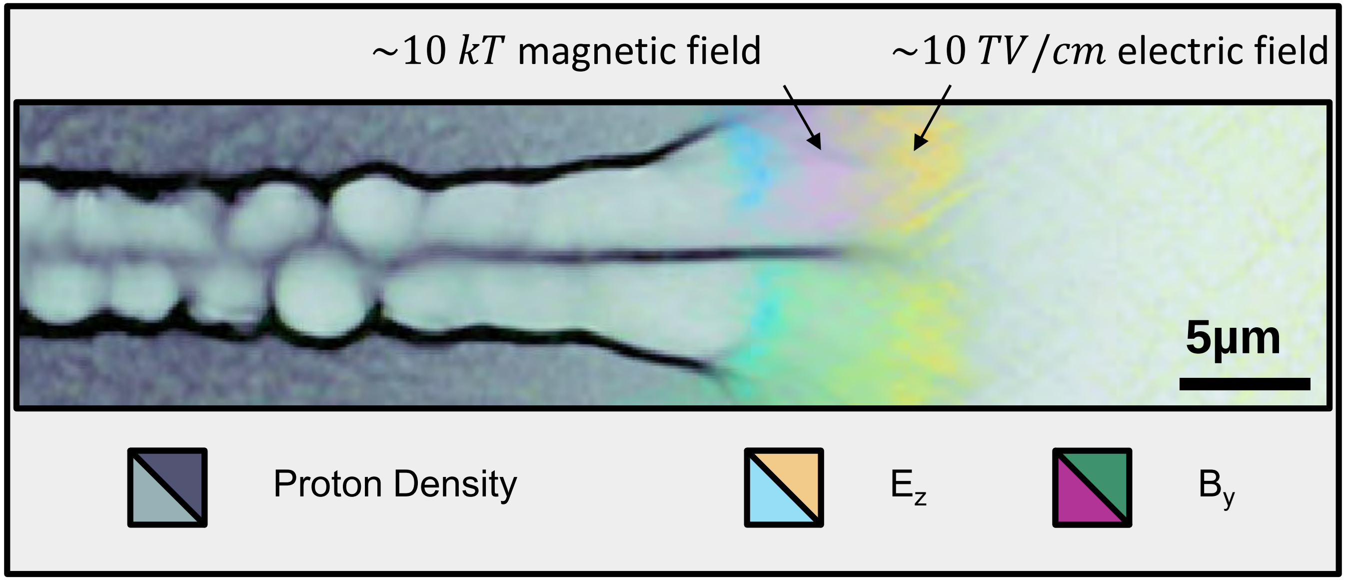

- 2D PIC
- $a_0 = 4,$
- $\tau = 40fs$
- $w_0 = 1.6\ \mu m$
- $N_e = 0.15\ N_{crit}$
- $50\ \mu m$ target

- Intense laser pulse bores a channel through an underdense target
- Ponderomotive force drives a strong current which generates ~10 kT magnetic fields
- Magnetic field expansion at the back side of the target can generate slowly expanding quasi-static fields which accelerate protons

A. Macchi, M. Borghesi, and M. Passoni, Rev. Mod. Phys. **85** (2013)

2D Simulations

2D SLAB Geometry

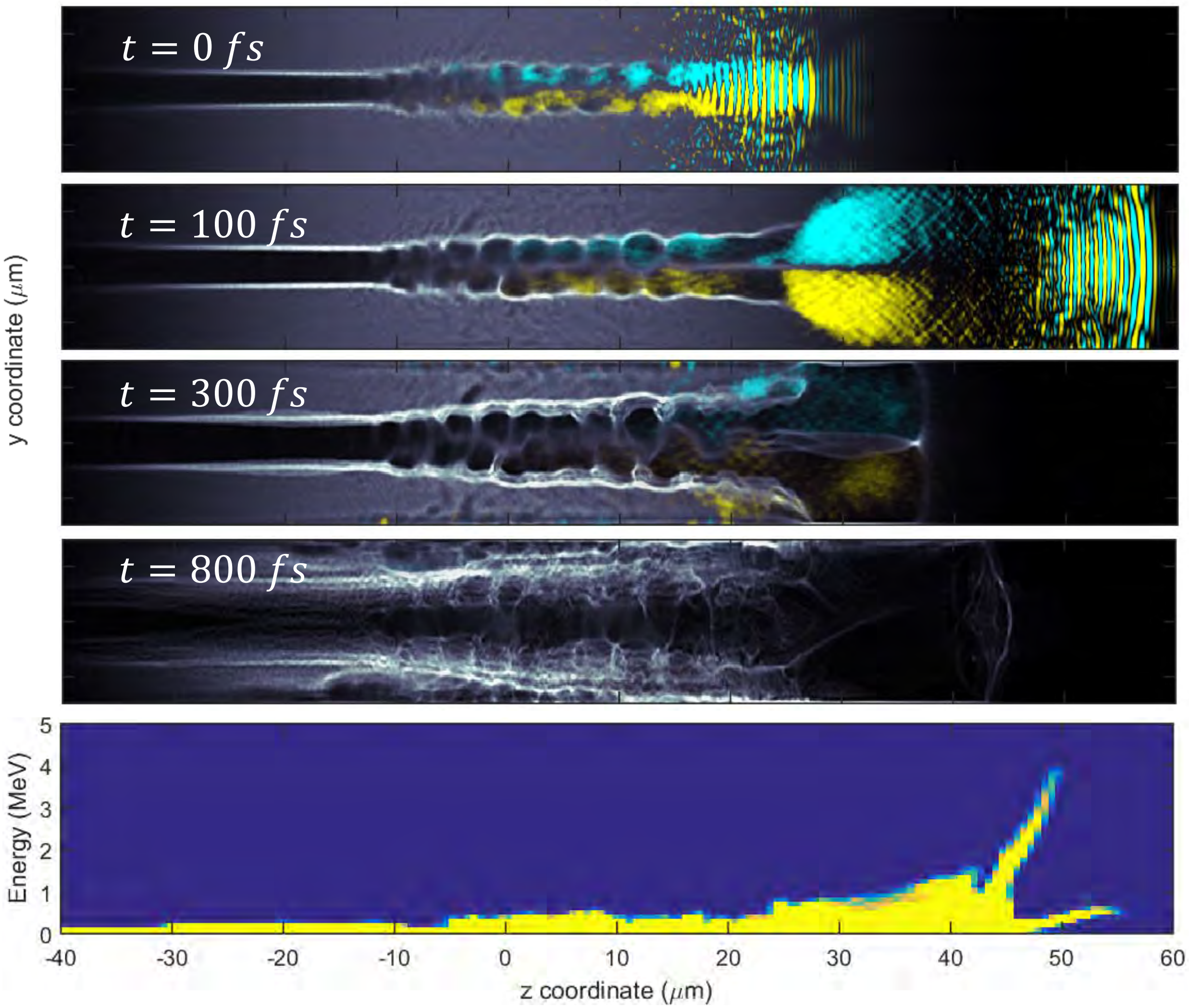

2D simulations can be optimized to generate MeV scale ions by tuning plasma density and shape.

- a_0= 4
- Linear polarization
- Spot size=3 µm
- Pulse length=40 fs

- Peak density=0.15 n_{crit}
- Plasma profile=50 µm FWHM

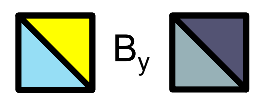

Proton acceleration up to 4MeV!

3D Simulations

Full 3D Geometry

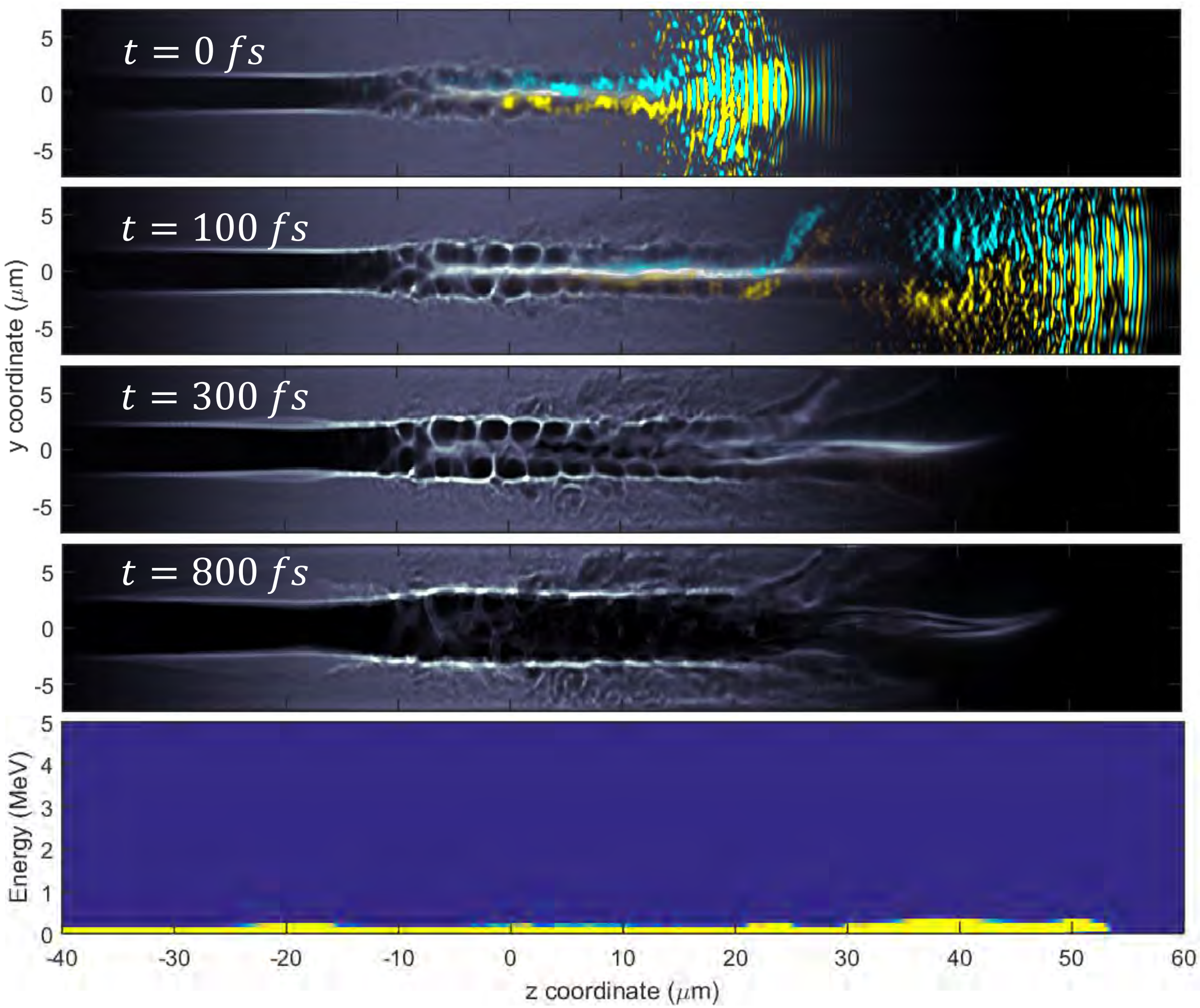

3D simulations of the same parameters, however, do not yield the same degree of proton acceleration, if any.

- a_0= 4
- Linear polarization
- Spot size=3 µm
- Pulse length=40 fs

- Peak density=0.15 n_{crit}
- Plasma profile = 50 µm FWHM

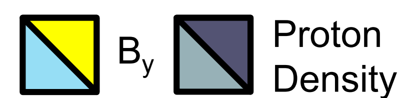

Little proton acceleration

Optimization in 3D

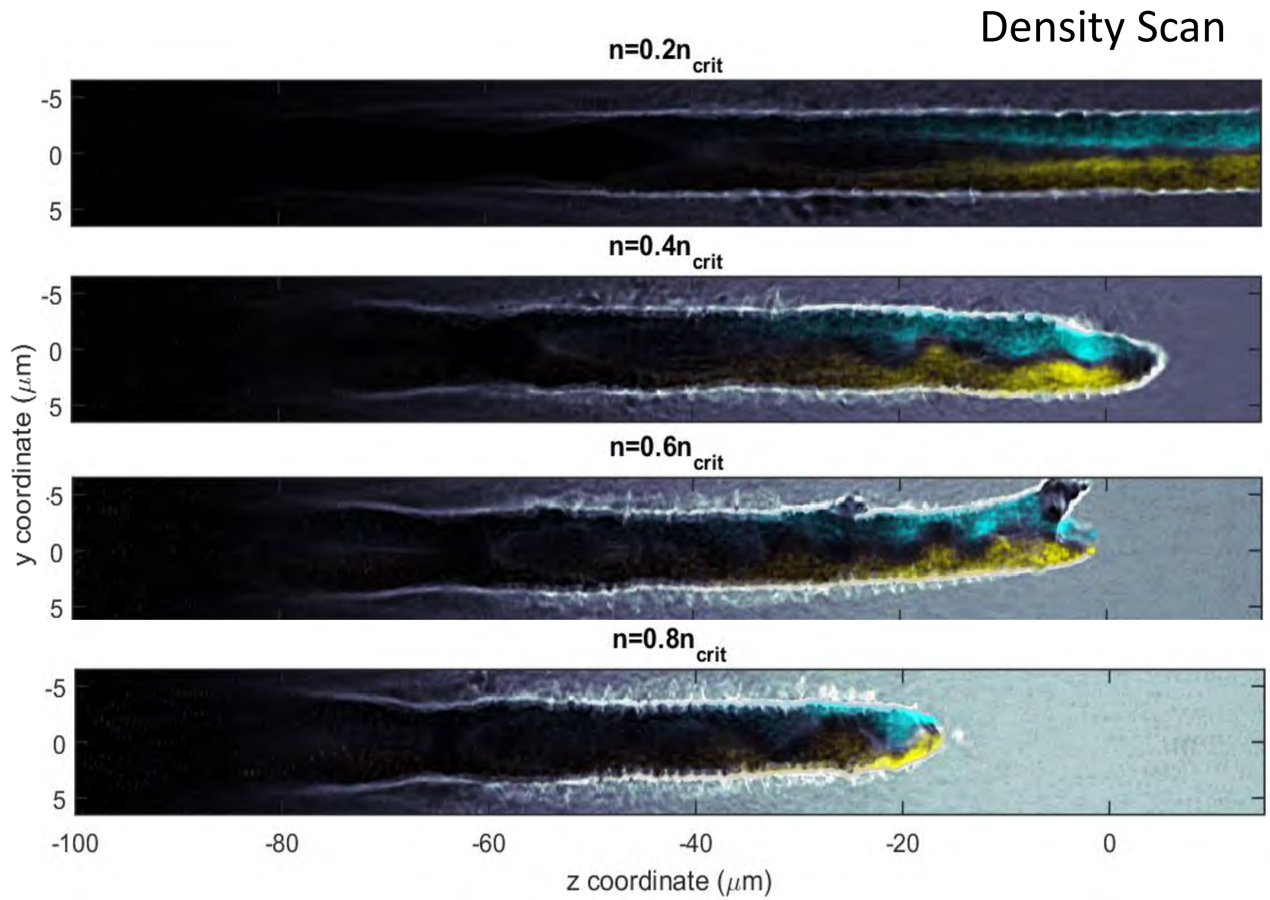

- a_0= 3.5
- Circular polarization
- Spot size=4.5 μm
- Pulse length=100 fs

- Plasma Profile = 100 μm FWHM

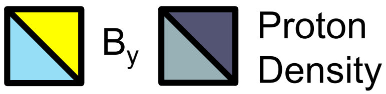

Optimization in three dimensions can be used to find the conditions desirable for ion acceleration. First the density of a 100μm plasma is tuned such that the laser depletes at the peak of the plasma density.

Simulations

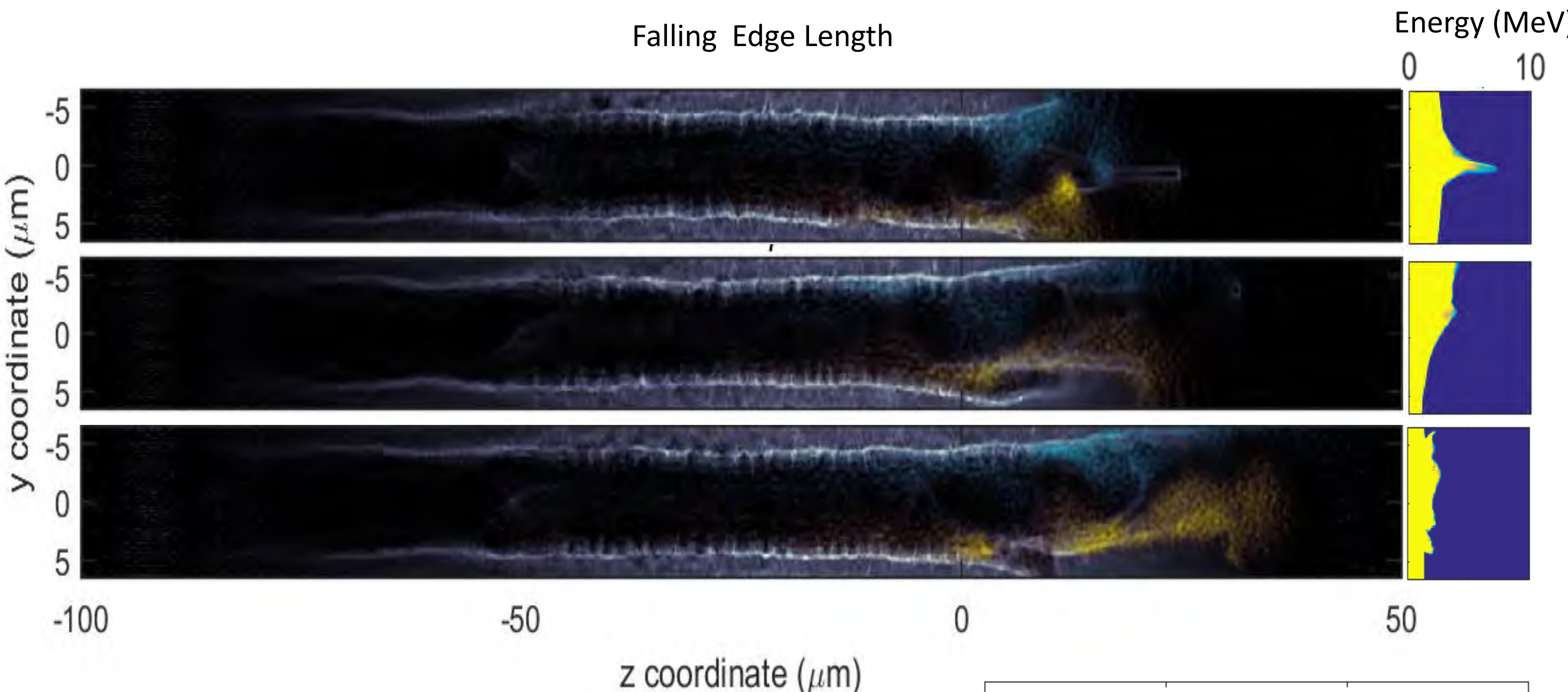

The proton yield can be optimized by sharpening the downramp of the density profile. MeV protons start to appear ~20 μm downramp.

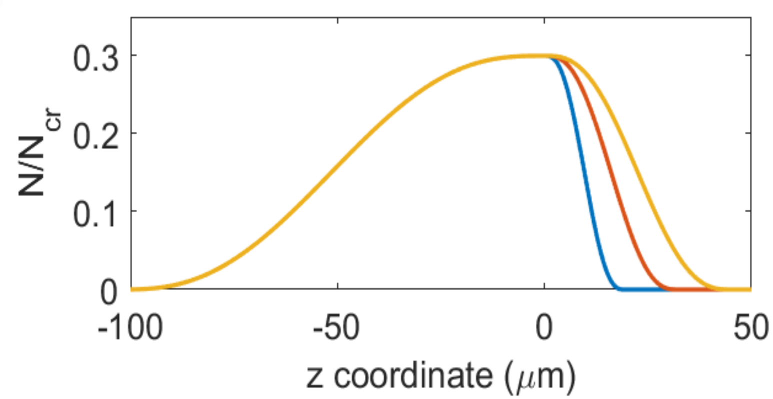

Experimental setup

- 850 mJ, 50 fs pulse
- F/3 OAP focuses to a 3 micron FWHM spot size
- Two color transverse interferometer
- 8 slot CR39 and scintillator diagnostic wheel
- Permanent magnet proton spectrometer

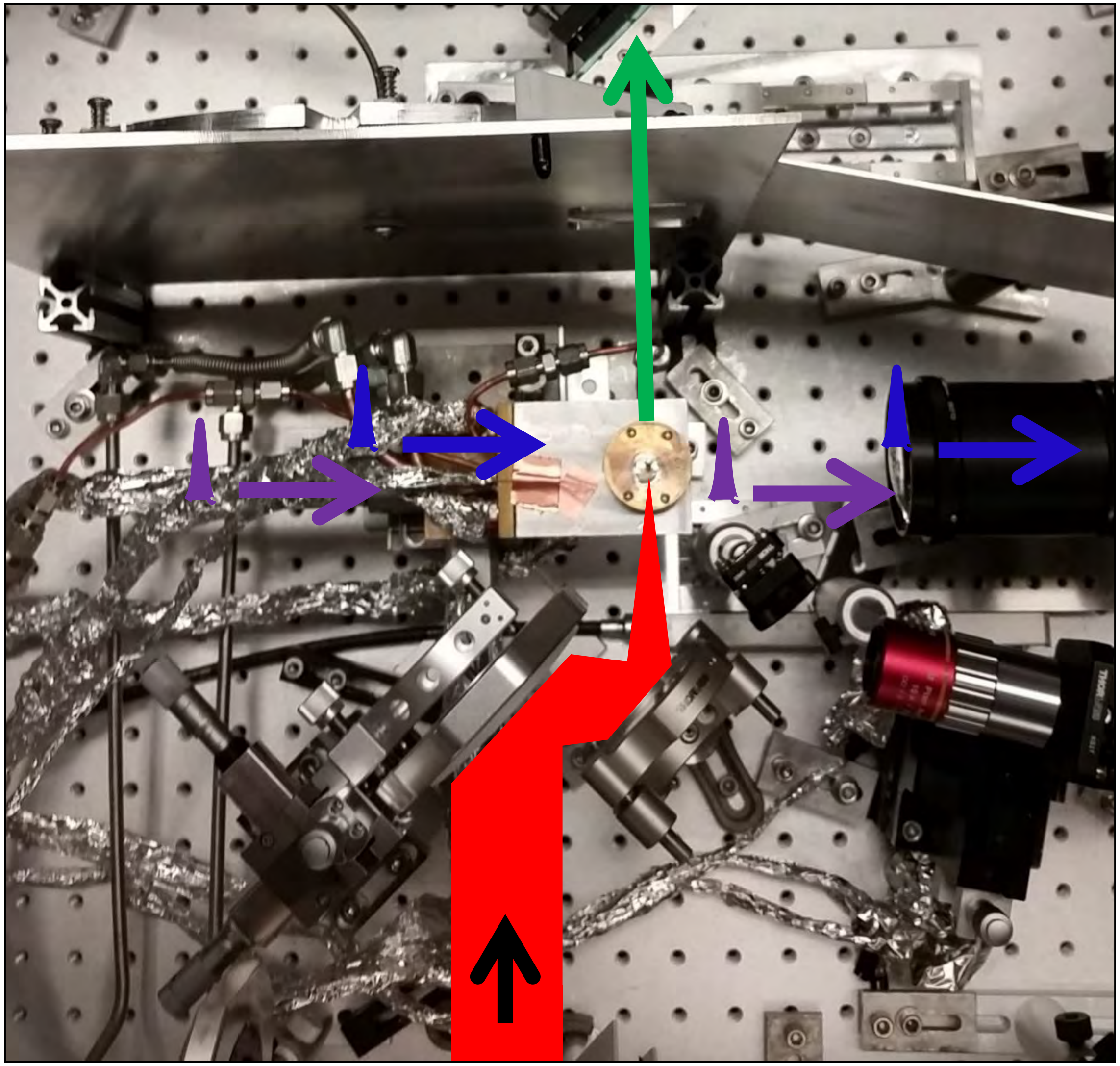

Interferometry diagnostics

266 nm interferogram

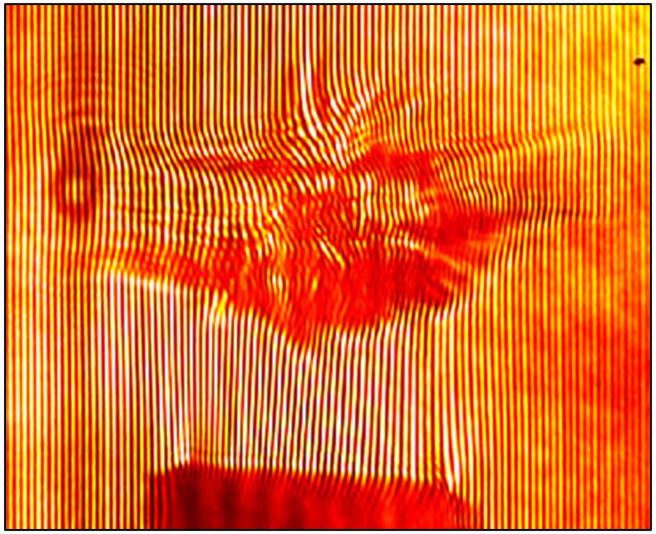

400 nm interferogram

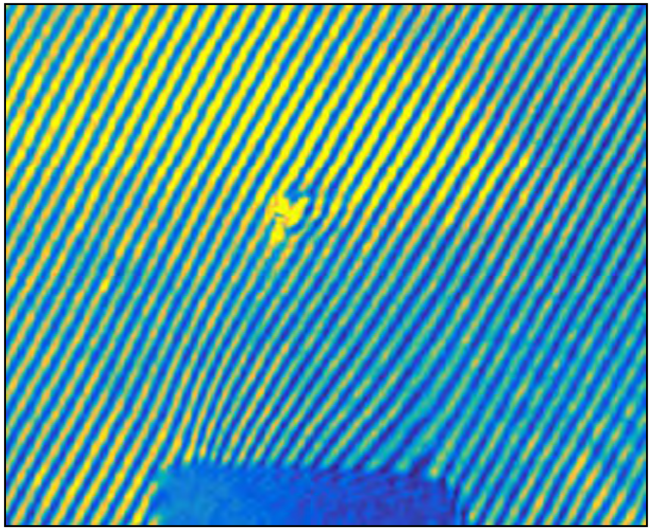

Collinear THG yields co-propagating, femtosecond probe pulses at 400 nm and 266 nm, with pulse separation controlled by placing glass before the interaction and absolute delay controlled by an optical delay line

$$\Delta\tau = L * \left(\frac{1}{v_{g,2\omega}} - \frac{1}{v_{g,3\omega}}\right) \qquad v_g = c * \left(n - \lambda_0 \frac{dn}{d\lambda_0}\right)^{-1}$$

Fused silica:

$$\frac{v_g}{c}(400nm) = 0.661,\ \frac{v_g}{c}(266nm) = 0.619,\ L = 12.7\ mm\ \rightarrow \Delta\tau = 4.28\ ps$$

Problem of pernicious pre-pulse

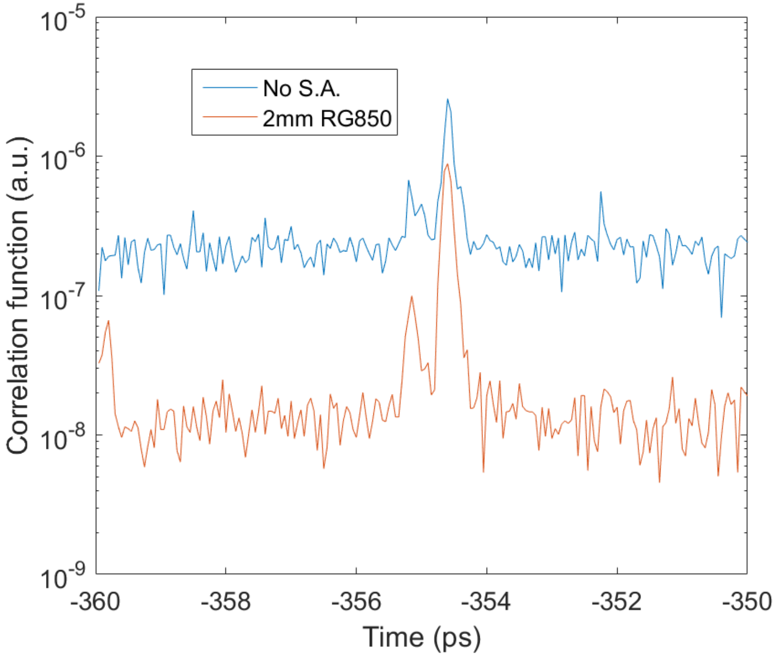

400 nm interferogram

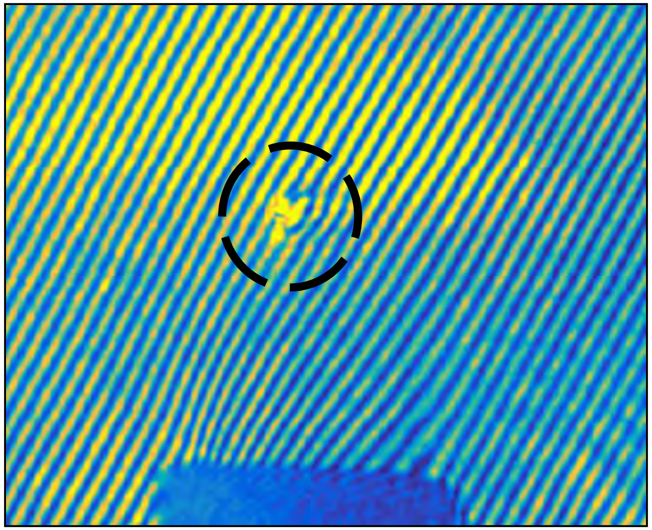

- Pre-pulses and ASE cause pre-ionization of the high density jet
- A 2mm RG850 saturable absorber was implemented to reduce ASE and prepulse levels
- Total energy on target is still limited by pre-plasma from a pre-pulse 355 ps before the main pulse

Evidence of channeling?

>2 MeV Electron Beam Profiles | Side scatter

150 fs, 500 mJ

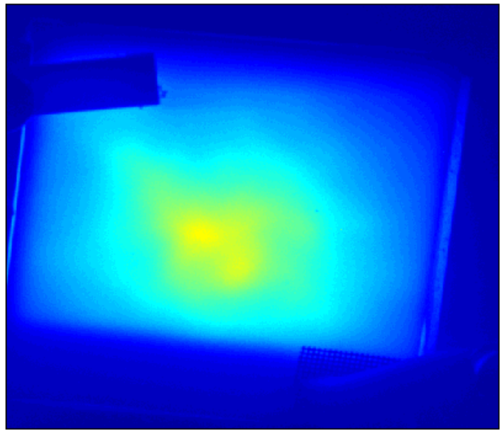

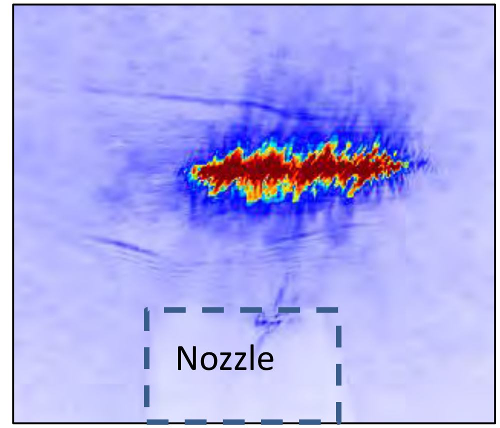

300 fs, 500 mJ

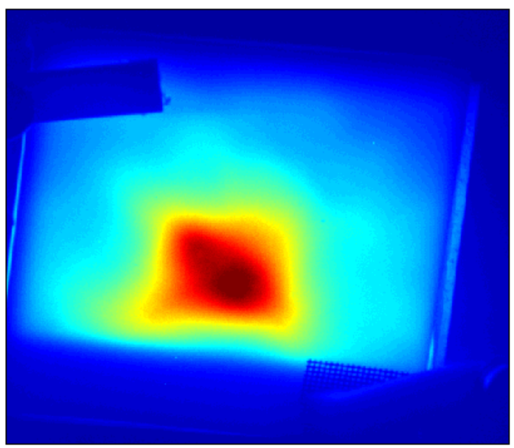

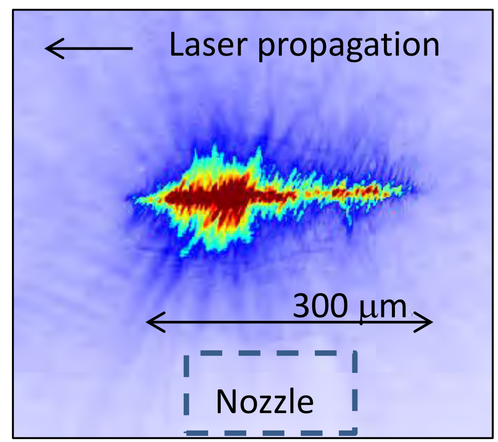

- Forward directed electron flux increases with longer pulse lengths
- Bright side scattered light observed to depend on pulse length, possibly indicative of pulse channeling

Preliminary Protons?

Full 43mm x 43 mm stitched CR39

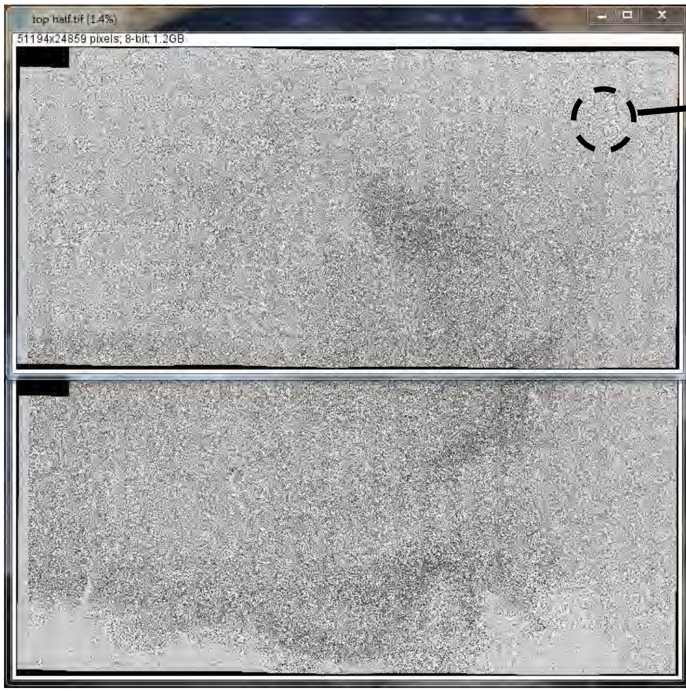

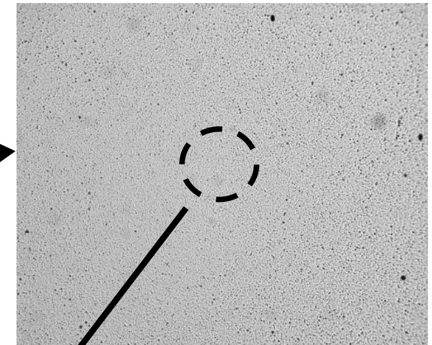

Single 1.7mm x 1.4mm image

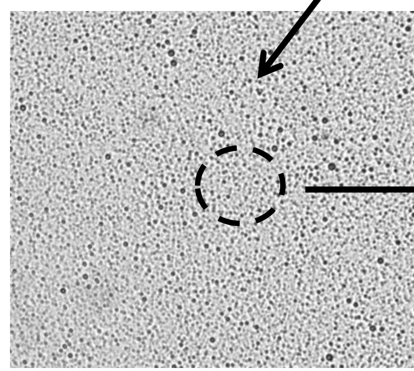

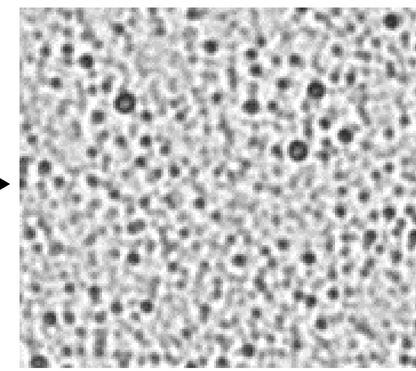

- No significant ion flux in the FORWARD direction
- TRANSVERSE ion flux measured with energy < 700 keV using CR39 placed 5 cm from the plasma transverse to the pump laser propagation

Summary

- We are interested in laser driven proton acceleration from a near critical density target with application to generating PET isotopes
- 2D PIC simulations overestimate the proton acceleration and cannot be directly translated to 3D results
- 3D PIC simulations with optimized peak density and gradient show few MeV proton acceleration with < 1 J pulses
- Experiments are underway… stay tuned.

Appendix 4:
Ion Acceleration in an Underdense Plasma

3D Particle-in-cell simulations

Overview of the acceleration mechanism

George Hine 12/2016

The Target

We start with a plasma with a Gaussian longitudinal profile, with a full width at half maximum of 50 microns, and a peak density of $0.3 x n_{crit}$. This is attainable in our experiment, provided that the laser beam waist is extremely close to the nozzle orifice (close enough to damage it in a single high energy shot).

The target is fully ionized hydrogen and is initially uniform in the transverse (x and y) direction.

I have imposed a "background" of plasma at 0.27% of the peak density (taken as a baseline for the Gaussian). This background increases the number of protons available for acceleration in the profile's exit edge (while maintaining the exit edge's slope, preventing the B-field from expanding too quickly). In general, this is the scenario that favors magnetic vortex acceleration.

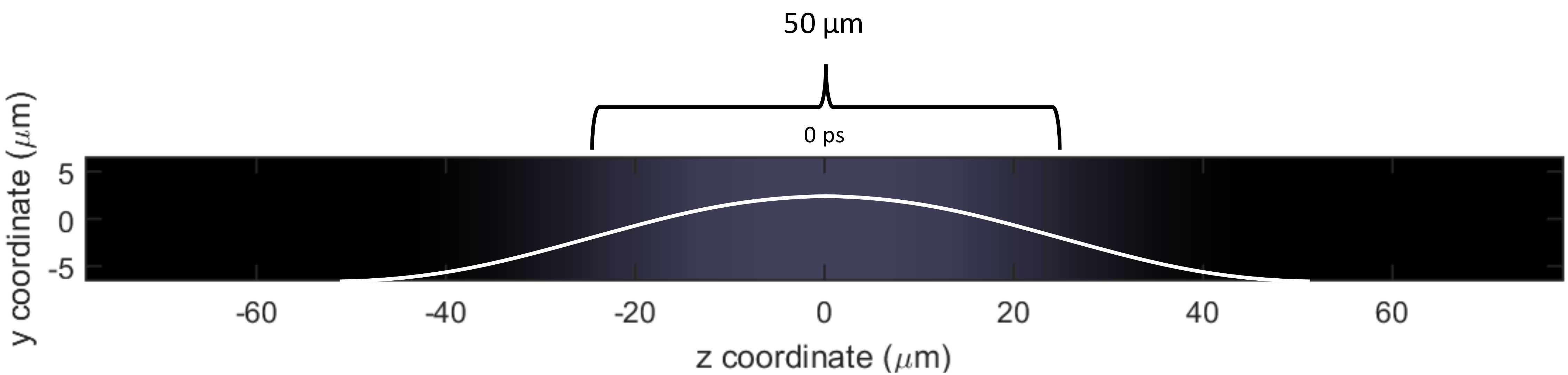

The Laser

A circularly polarized laser pulse is injected with an 810 nm wavelength, focused to a 3 micron spot size.

The laser self focuses in the medium, boring a channel in the electron and proton density.

The laser pulse length was varied, keeping the peak laser field constant at a_0=3.5. This is equivalent to saying that the energy in the laser was varied, keeping the peak field, and spot size fixed.

A toroidal magnetic field is generated by the laser, which is responsible for the acceleration of ions.

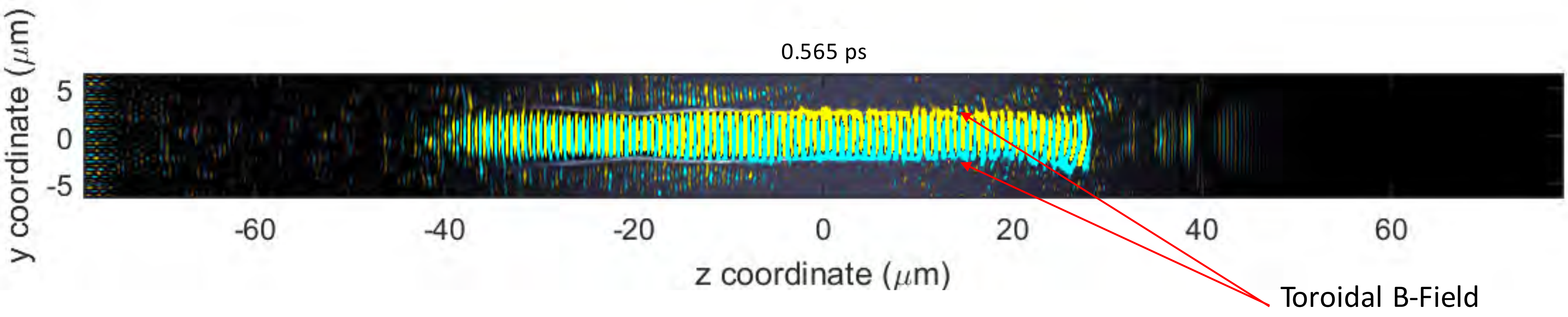

The Mechanism

As the laser propagates in the plasma, it generates a toroidal magnetic field which accompanies it.

When the laser exits the plasma, the toroid is left behind in the plasma, and transforms as dictated by electron magnetohydrodynamics (highly magnetized electrons, unmagnetized ions)

Expansion of the toroid pinches and pushes electrons which drag ions, accelerating them.

A core of protons is produced, the tip of which is accelerated to the MeV scale.

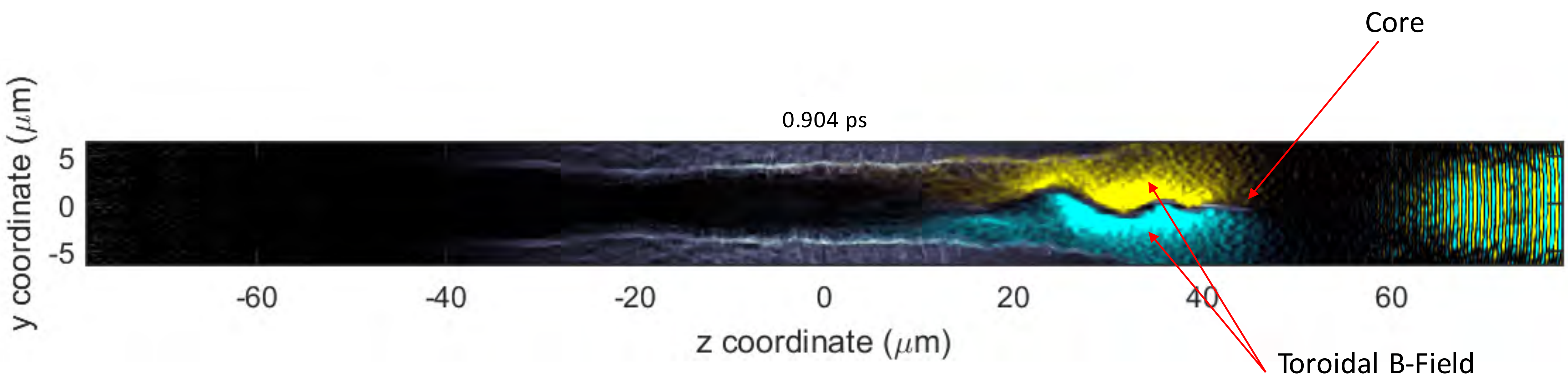

The Mechanism

As the laser propagates in the plasma, it generates a toroidal magnetic field which accompanies it.

When the laser exits the plasma, the toroid is left behind in the plasma, and transforms as dictated by electron magnetohydrodynamics (highly magnetized electrons, unmagnetized ions)

Expansion of the toroid pinches and pushes electrons which drag ions, accelerating them.

A core of protons is produced, the tip of which is accelerated to the MeV scale.

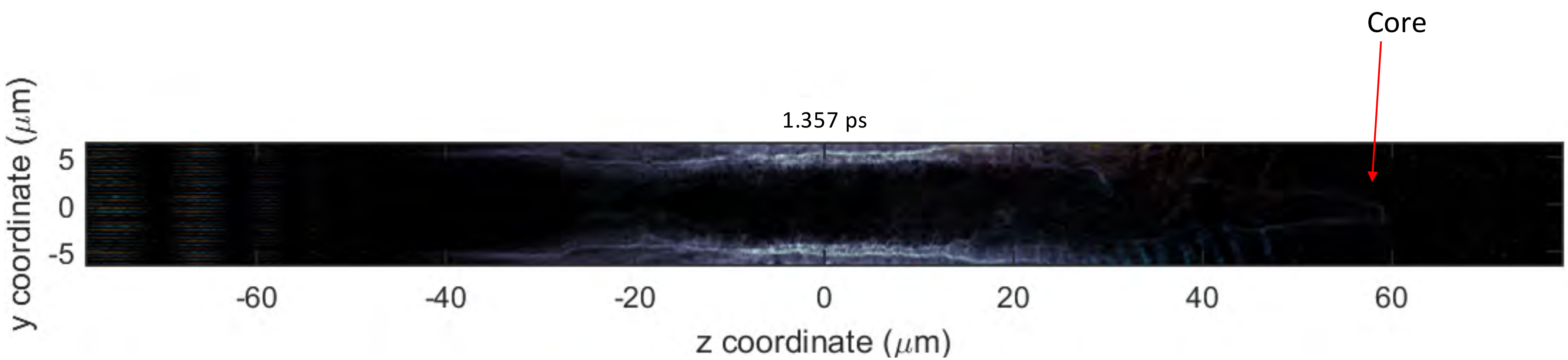

The Mechanism

As the laser propagates in the plasma, it generates a toroidal magnetic field which accompanies it.

When the laser exits the plasma, the toroid is left behind in the plasma, and transforms as dictated by electron magnetohydrodynamics(highly magnetized electrons, unmagnetized ions)

Expansion of the toroid pinches and pushes electrons which drag ions, accelerating them.

A core of protons is produced, the tip of which is accelerated to the MeV scale.

With the contrast adjusted, the exploding core is more visible.

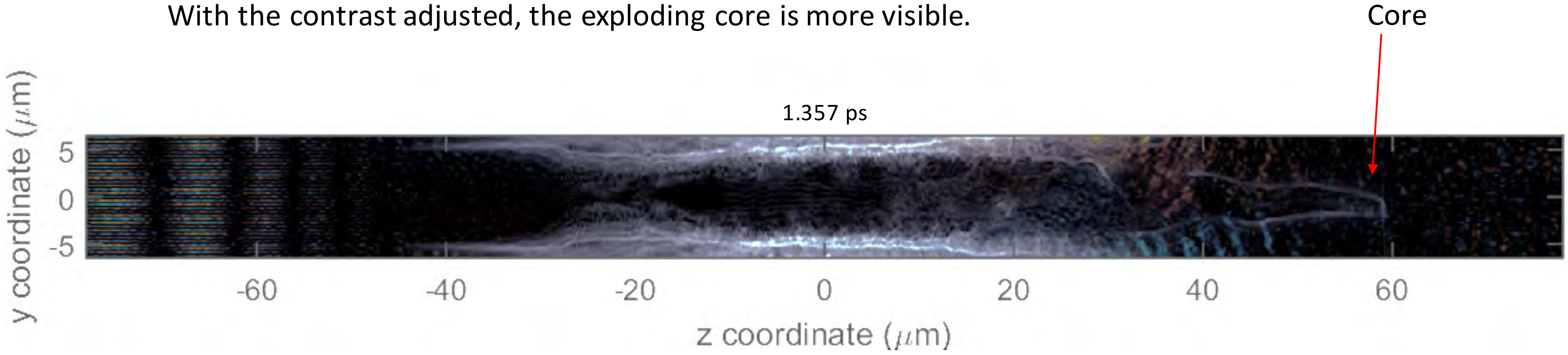

Varying the pulse length and energy, it is seen that a Ti:Sapphire laser with ~400-900mJ of energy can produce protons between 4 and 8 MeV.

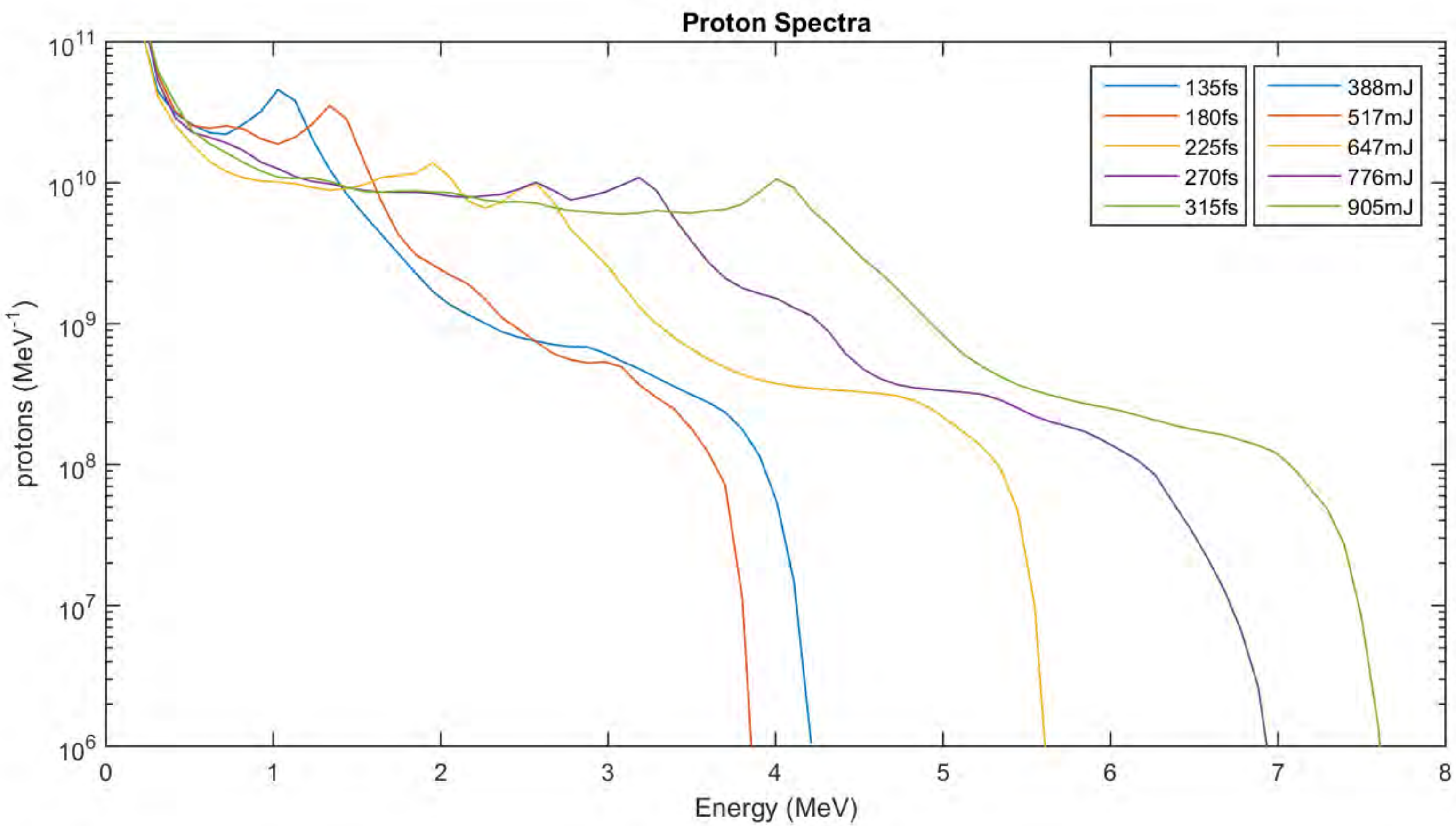

This spectrum can be integrated to give absolute numbers of protons in an energy range.

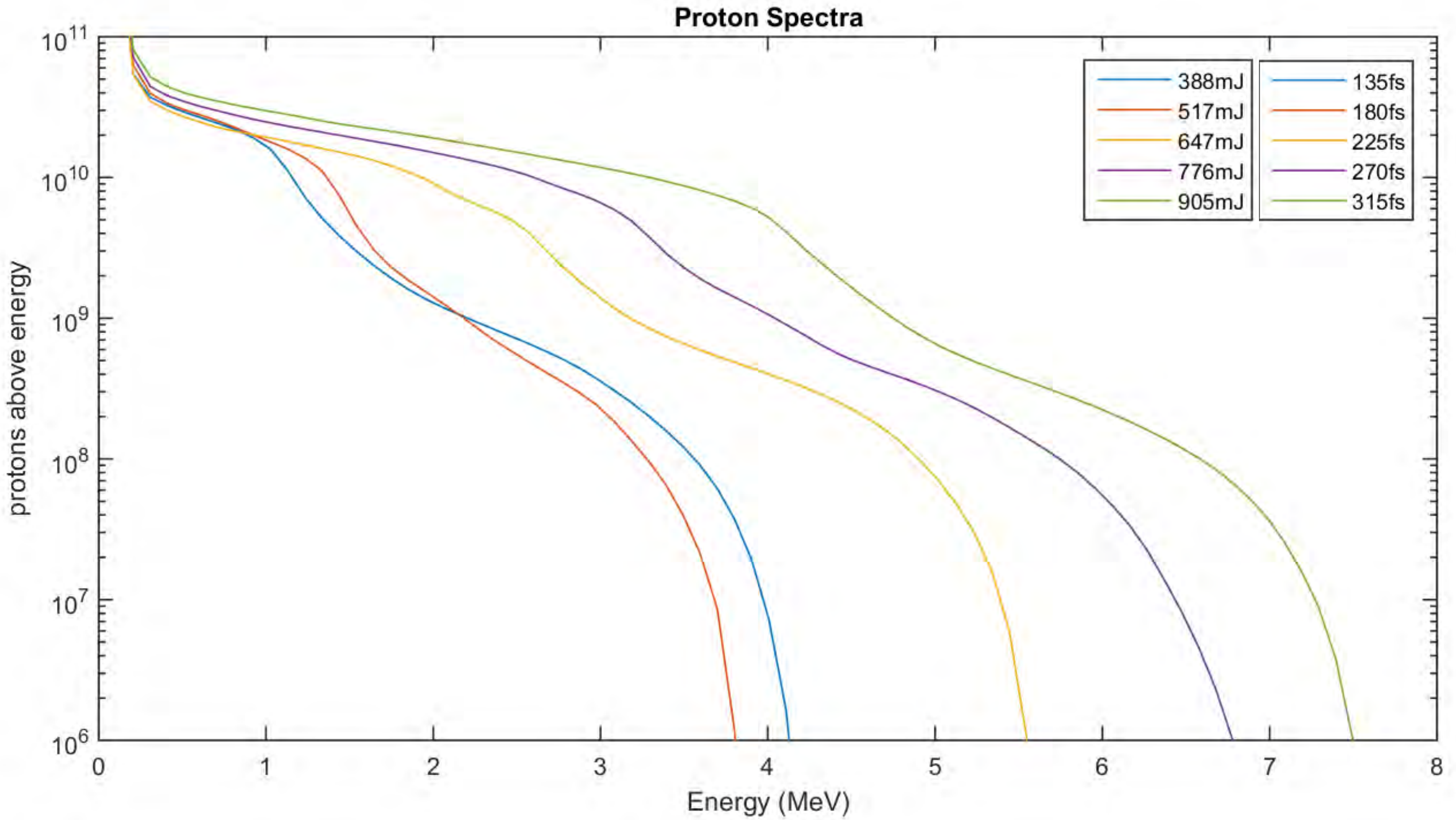

Summary

We have 3D pic simulations showing ion acceleration of 10^9-10^{10} protons up to 7.5 MeV using laser parameters and target parameters which are reasonably accessible to our experiment.

The target parameters used may take considerable effort to achieve, given that they would require operating very close to the gas jet nozzle.

Note that it is assumed that there is no laser prepulse, which might negatively affect the results. Directly simulating a prepulse could make the simulation prohibitively expensive, depending on the timescale of the prepulse. To make progress on this question, we will simulate the interaction of a single pulse with a preformed density profile informed by interferometric measurements of the prepulse-heated hydrogen plasma.